Investigating Paleogene strata from the tropical low latitudes; new insights from integrated chemostratigraphy, sedimentology, and biostratigraphy

Charlotte Beasley

2021

Submitted by Charlotte Beasley to the University of Exeter
as a thesis for the degree of
Doctor of Philosophy in Geology
in March 2021

I certify that all material in this thesis which is not my own work has been identified and that no material has previously been submitted and approved for the award of a degree by this or any other University.

Signature: ……

Abstract

The Paleogene (66–23 Ma) was characterised by warming and cooling trends, on the scales of tens-of-thousands to millions of years, ultimately driven by tectonic processes (e.g., Zachos et al., 2001; Westerhold et al., 2020). Shorter period variability occurs due to changes in the Earth's orbital configuration, known as Milankovitch cyclicity, driving changes in the climate and carbon cycle. This high frequency variability is well-known from increasingly detailed sedimentological and geochemical records primarily from deep sea sedimentary archives; however, there are relatively fewer records from shallow and intermediate water depths or low latitude areas. In addition to these quasi-periodic Milankovitch cycles a number of significant global climate perturbations are recorded in the Paleogene rock record including the well-known Paleocene–Eocene thermal maximum (PETM; ~56 Ma), where global sea surface temperatures are thought to have increased by ~3–4°C (e.g., McInerney & Wing, 2011). Low latitude areas, such as the Middle East and Arabian Sea, are thus far relatively understudied in terms of their combined palaeoenvironmental and biostratigraphic records through the Paleogene. As such, further high-resolution records from low latitude, shallow water and intermediate depth sites are important to discern orbital-scale variability and constrain how these regions responded to geologically rapid climate changes.

This project applies a number of varied geochemical, sedimentological, and palaeontological techniques to material from both onshore shelf sea settings (Jordan and the United Arab Emirates) and open ocean (Arabian Sea) sediment cores. The overarching aim of the project is to analyse the changes in palaeoenvironment, palaeoclimate, and palaeoecology in low latitude, tropical environments of the Middle East and Arabian Sea through the Paleogene. The PETM is shown to have a limited impact on the oceanography and biota of this area, with the long-term warming from the late Paleocene to early Eocene instead causing shifts in biodiversity and influences of specific water masses. Similarly, the Oligocene–Miocene transition is shown to have an important role in the long-term evolution of the Arabian Sea region and proto-South Asian monsoon system.

Acknowledgements

So many people made this thesis possible, and I'd like to thank every single one of them for their comments, suggestions, discussions, and general interest in my PhD research.

Firstly, to the team of supervisors I had supporting me: Kate Littler, Sev Kender, Steve Hesselbo, Laura Cotton and Aisha Al Suwaidi – this thesis wouldn't have been finished without all of you, so thank you. A huge shout out to Kate specifically whose support was unwavering throughout this whole process, and who simultaneously grew two human beings: some mean feat. Also, thanks go to Laura and Aisha who both welcomed me into their homes whilst visiting for lab work (Laura, I hope Hank and Nina have forgiven me).

Secondly, to all the incredible collaborators I have been fortunate enough to work with through lab work and writing up subsequent manuscripts. The papers I have produced would not have happened without all of you: Clemens Ullmann, Pallavi Anand, Clara Bolton, Leah LeVay, Liviu Giosan, Alex Dickson, Dan Parvaz, Katrina Nilsson-Kerr, Appy Sluijs, Mel Leng.

And finally, to all my friends and family who only asked me 12,363,761 times if I'd finished this yet.

Table of Contents

Abstract 4

Table of contents 6

Chapter 1 – Introduction

1.1 Thesis structure 11

1.2 Literature review and PhD project summary 12

1.2.1 Setting the scene: Paleogene (and earliest Neogene) palaeoclimate and palaeoceanography 12

1.2.2 Microfossils and their use in studying past climates 17

1.2.3 Geochemical proxies in past climate studies 18

1.2.4 PhD project summary 19

1.3. Research questions 22

Chapter 2 – Triumph and tribulation for shallow water fauna during the Paleocene–Eocene transition; insights from the United Arab Emirates

2.1 Abstract 24

2.2 Introduction 25

2.3 Geological setting of study area 31

2.4 Methods 31

2.4.1 Microfossils 31

2.4.1.1 Larger benthic foraminifera 31

2.4.1.2 Calcareous nannofossils 32

2.4.1.3 Palynomorphs 33

2.4.2 Carbon and oxygen isotope analysis 34

2.4.3 Percentage calcium carbonate analysis 35

2.4.4 Inductively couple plasma optical emission spectroscopy 35

2.4.5 Optical cathodoluminescence microscopy 36

2.4.6 Wireline logging 37

2.5 Results 37

2.5.1 Sedimentology 37

2.5.2 Micropalaeontological results 38
2.5.2.1 The larger benthic foraminiferal assemblages 38
2.5.2.2 Calcareous nannofossil biostratigraphy 42
2.5.2.3 Palynology 45
2.5.3 Bulk carbonate carbon and oxygen isotopes 45
2.5.4 Percentage calcium carbonate 48
2.5.5 Gamma ray 49
2.6 Discussion 49
2.6.1 An integrated age model for the late Paleocene to early Eocene of the central UAE 49
2.6.2 Paleocene–Eocene palaeoenvironmental and biotic trends 54
2.6.2.1 The Paleocene–Eocene transition 56
2.6.3 Response of shallow marine biota to Eocene warmth 58
2.6.4 The early Paleogene vs anthropogenic climate change in the shallow water realm 61
2.7 Conclusions 62

Chapter 3 – Liberating microfossils from indurated carbonates: comparison of three disaggregation methods
3.1 Abstract 64
3.2 Introduction 65
3.3 Materials and methods 66
3.3.1 Method 1: Calgon 68
3.3.2 Method 2: Acetic acid 71
3.3.3 Method 3: Electric pulse fragmentation 72
3.3.4 Normalising number of liberated microfossils 75
3.3.4.1 Larger foraminifera per gram 75
3.3.4.2 Percentage fossiliferous fraction 75
3.3.5 Scanning electron microscope and energy dispersive spectroscopy 75
3.4 Results 76
3.4.1 Calgon 76
3.4.2 Acetic acid 76
3.4.3 Electric pulse fragmentation 77

3.4.4 Poor disaggregation 79
3.5 Discussion 79
3.6 Conclusions 83

Chapter 4 – Evidence of a South Asian proto-monsoon during the Oligocene–Miocene transition
4.1 Abstract 85
4.2 Introduction 86
4.3 Modern Arabian Sea oceanography 91
4.4 Materials and methods 92
4.4.1 Sampling and sample preparation 93
4.4.1.1 Foraminifera 94
4.4.1.2 Calcareous nannofossils 94
4.4.2 Foraminiferal stable isotope analysis 95
4.4.3 Planktic foraminiferal trace element analysis 95
4.4.3.1 Converting Mg/Ca to temperature 96
4.4.3.2 Calculating upper water column $\delta^{18}O$ ($\delta^{18}O_{sw}$) 97
4.4.4 Core scanning X-ray fluorescence (XRF) 98
4.4.5 Inductively coupled plasma optical emission spectroscopy 98
4.4.6 Scanning electron microscope (SEM) 99
4.4.7 Terrigenous flux 100
4.5 Results 100
4.5.1 Age model 100
4.5.2 Percentage coarse fraction (%CF) and percentage calcium carbonate 102
4.5.3 Foraminiferal stable isotope analysis 105
4.5.4 Planktic foraminiferal trace element analysis 106
4.5.4.1 Mg/Ca-temperature calibrations 107
4.5.4.2 Upper water column $\delta^{18}O$ ($\delta^{18}O_{sw}$) 107
4.5.5 XRF core scanning 107
4.5.6 Terrigenous flux 109
4.6 Discussion 110
4.6.1 Change in Dentoglobigerina venezuelana *depth habitat* 110

4.6.2 Oligocene–Miocene upper water column temperature evolution 111
4.6.3 The early phase of the Oligocene–Miocene transition (23.7–23.0 Ma) 112
4.6.3.1 Tectonic changes over the Oligocene to early Miocene 116
4.6.4 The late phase of the Oligocene–Miocene transition (23.0–22.7 Ma) 117
4.6.5 Long-term shift in sedimentology at Site NGHP-01-01A 121
4.7 Conclusions 123

Chapter 5 – Palaeoceanography of the Tethyan corridor over the Paleocene–Eocene transition
5.1 Abstract 125
5.2 Introduction 125
5.2.1 Neodymium isotopes as ancient water mass tracers 126
5.2.2 Neodymium isotope records across the PETM 129
5.3 Materials and geological setting 131
5.4 Methods 132
5.4.1 Sample preparation 132
5.4.2 Neodymium isotope analysis 133
5.4.3 Age model construction 134
5.5 Results 135
5.5.1 Neodymium isotopes 135
5.6 Discussion 137
5.6.1 Neodymium data record regional end-member water mass mixing processes 137
5.6.2 Neodymium data record local environmental processes 138
5.6.2.1 Neodymium data controlled by internal cycling processes (boundary exchange and reversible scavenging) 140
5.7 Preliminary conclusions 141

Chapter 6 – Synthesis and conclusions
6.1 Synthesis of data and conclusions 143
6.2 Addressing research questions 147

6.3 Future work 151
6.3.1 Tailoring the EPF methodology for smaller microfossils 151
6.3.2 Constraining weathering fluxes in the Arabian Sea 152
6.3.2.1 Constraining palaeoceanographic and tectonic interactions in the Arabian Sea 152
6.3.3 Constraining Dentoglobigerina venezuelana *depth habitat* 153
6.3.4 Increasing data density of Tethyan neodymium data 153

Appendices

Appendix 1: **Beasley, C.**, Cotton, L., Al Suwaidi, A., LeVay, L., Sluijs, A., Ullmann, C. V., Hesselbo, S. P., Littler, K., 2021. Triumph and tribulation for shallow water fauna during the Paleocene–Eocene transition; new insights from the United Arab Emirates. Newsletters on Stratigraphy 54(1), 79–106. 154
Appendix 2: **Beasley, C.**, Parvaz, D. B., Cotton, L., Littler, K., 2020. Liberating microfossil from indurated carbonates: comparison of three disaggregation methods. Journal of Micropalaeontology 39, 169–181. 181
Appendix 3: Core A age model construction 194
Appendix 4: Core A calcareous nannofossil biostratigraphy 197
Appendix 5: Core A bulk ICP-OES derived Mg/Ca values 199
Appendix 6: Site NGHP-01-01A palaeodepth calculation 199
Appendix 7: Mg/Ca-temperature and $\delta^{18}O_{sw}$ estimates error propagation 200
Appendix 8: Site NGHP-01-01A supplementary figures 202
Appendix 9: Site NGHP-01-01A supplementary tables 206
Appendix 10: Core OS-28 ICP-MS standard results 207

Bibliography 208

Chapter 1: Introduction

1.1 Thesis Structure

Within this thesis each chapter is intended to act as a standalone publication, under the broad umbrella of “Investigating Paleogene strata from the tropical low latitudes”. As such, chapter specific methods and detailed literature reviews will be included within each individual data chapter (Chapters 2–5). An introduction to the aims and objectives of the overarching PhD project (Section 1.2), along with a more general literature review and project summary (Section 1.3), will follow within this first chapter. Data chapters that have already been published can be found in Appendices 7.1 and 7.2, at the end of this thesis. Co-author contribution statements are located after the abstract in each chapter. Associated name abbreviations are listed below:

CB: Charlotte Beasley
KL: Kate Littler
LC: Laura Cotton
AAS: Aisha Al Suwaidi
SPH: Stephen P. Hesselbo
CVU: Clemens V. Ullmann
AS: Appy Sluijs
LL: Leah LeVay
DBP: Daniel B. Parvaz
SK: Sev Kender
CTB: Clara T. Bolton
PA: Pallavi Anand
LG: Liviu Giosan
KNK: Katrina Nilsson-Kerr
MJL: Melanie J. Leng
AD: Alex Dickson

1.2 Literature review and PhD project summary

The purpose of this section is to describe briefly and assess the current understanding of Paleogene climate and oceanography, as well as the use of microfossils and geochemistry in studying past climates. More detailed, chapter specific, literature reviews are located in individual data chapters (Chapters 2–5). In the PhD project summary I will also detail the specific aims of each data chapter, as well as briefly outlining the main conclusions of each study.

1.2.1 Setting the scene: Paleogene (and earliest Neogene) palaeoclimate and palaeoceanography

The Paleogene Period spans from immediately after the end-Cretaceous mass extinction event (~66 Ma) to the beginning of the Neogene Period (~23 Ma). It is generally characterised by long-term secular warming and cooling trends, on the scale of tens of thousands to millions of years (Fig. 1.1) (Zachos et al., 2001a; Westerhold et al., 2020). As well as these long-timescale trends, shorter period variability in Earth's orbital configuration also drives cyclic changes in climate, known as Milankovitch cyclicity. These Milankovitch cycles refer to three orbital parameters which change as the Earth orbits and changes its angle and distance relative to the Sun. Eccentricity is the change of the Earth's orbit around the Sun from more elliptical to more circular, occurring in approximately 100 and 405 kyr cycles (Hinnov, 2004). Obliquity is the tilt of the Earth's spin axis from a high angle of 24.5° to a low angle of 22°. This angle changes in ~41 kyr cycles, with a high angle tilt increasing the high latitude seasonal contrast (Zachos et al., 2001a; Hinnov, 2004). Axial precession is the "wobble" of the axis of rotation, which occurs on timescales of ~19 and ~23 kyr and has an effect on the relative position of the equinoxes relative to perihelion/aphelion of the Earth's orbit (Hinnov, 2004). The interactions between, and dominance of, these different cycles changes the amount of insolation the Earth's surface receives both in totality and at various latitudes, in turn driving changes in global and regional climate (Laskar et al., 1993; 2004; 2011). Such orbitally driven trends in the climate and carbon record of the Paleogene are well-known from increasingly detailed records from the deep sea sedimentary archive (e.g., Zachos et al., 2008; McInerney & Wing, 2011; Westerhold et al., 2011; Littler et al., 2014; Westerhold et al., 2020).

However, there is a dearth of high-resolution data from both shallow water sites and/or low latitude areas, particularly in the Middle East and Arabian Sea, where data are of limited temporal and spatial resolution. Most studies from these strata are based on outcrop sections, which can be limited by lack of exposure and diagenesis. As such, further high-resolution records from low latitude sites are important to discern both long-term and orbital-scale variability in these biodiverse environments. This will help in constraining how these regions responded to both geologically rapid changes and longer timescale perturbations during the Paleogene and earliest Neogene.

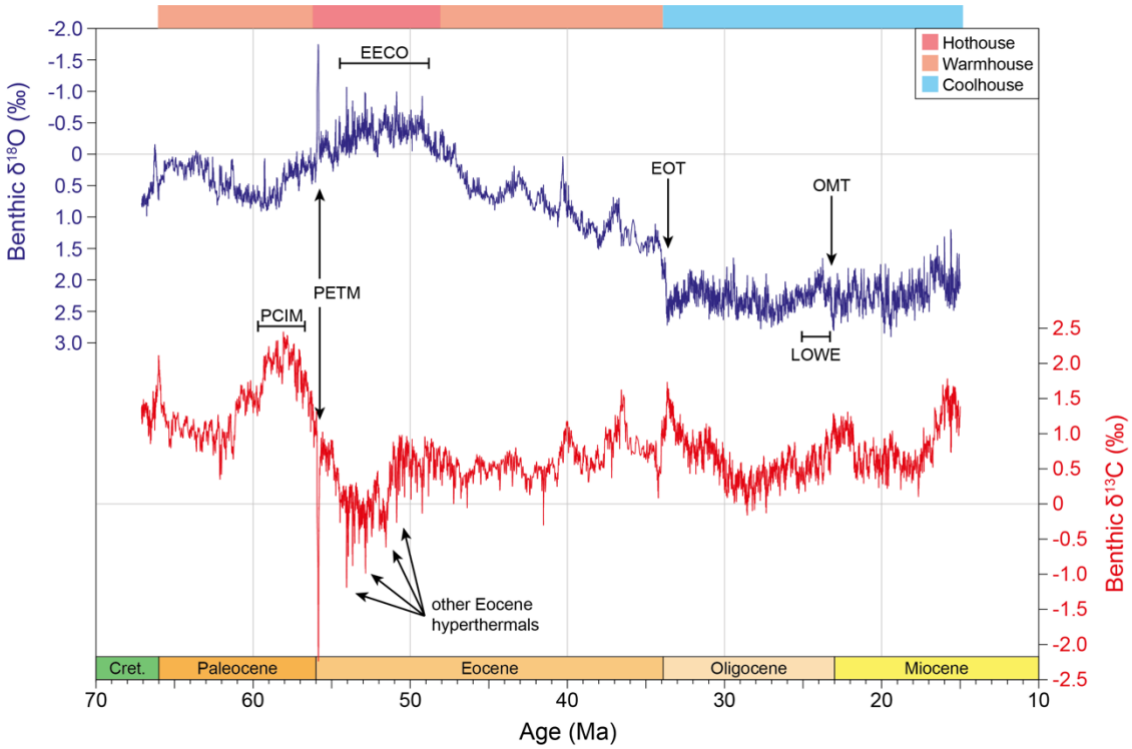

Figure 1.1: *Evolution of global climate from the beginning of the Paleogene to Miocene (~66–15 Ma). Stacked deep sea benthic foraminifera $\delta^{18}O$ and $\delta^{13}C$, obtained from a number of Ocean Drilling Project (ODP) and Deep Sea Drilling Project (DSDP) sites (adapted from Westerhold et al., 2020). This figure displays the events described within the text. PCIM is the Paleocene Carbon Isotope Maximum; PETM is the Paleocene–Eocene thermal maximum; EECO is the Early Eocene Climatic Optimum; LOWE is the Late Oligocene Warming Event; EOT is the Eocene–Oligocene Transition; OMT is the Oligocene–Miocene Transition.*

Stable isotope (carbon and oxygen) records compiled from the deep sea sedimentary archive track both long-term and orbital-scale evolution of climate and the carbon cycle across the Cenozoic (e.g., Zachos et al., 2001a; Westerhold et al., 2020) (Fig. 1.1). The earliest Paleocene Epoch (~66–63 Ma) was a time of relative warmth, which was followed by a long-term cooling trend from ~63 to 59

Ma (Fig. 1.1). The peak in this cooling trend is broadly coincident with the Paleocene Carbon Isotope Maximum (PCIM; ~59–56 Ma), as seen in $\delta^{13}C$ records. The increase in carbon isotopes is thought to be driven by sequestration of isotopically light carbon, likely in widespread terrestrial coal swamps and peat bogs rather than exclusively in the marine realm (e.g., Corfield, 1994; Zachos et al., 2010). Following the PCIM a distinct long-term trend towards a global "hothouse" is observed (Fig. 1.1; Westerhold et al., 2020), which peaks at the Early Eocene Climatic Optimum (EECO; ~52–50 Ma; Cramwinckel et al., 2018), the most recent period of significant sustained global warmth (Zachos et al., 2001a; 2008; Littler et al., 2014; Anagnostou et al., 2016; Barnet et al., 2019). This multi-million year warming trend is observed in both high latitude deep sea temperatures and low latitude sea surface temperature records (Cramwinckel et al., 2018; Westerhold et al., 2020), and is thought to have been driven by increased volcanic activity in the North Atlantic igneous province (NAIP) releasing large volumes of isotopically light carbon into the atmosphere-ocean system (Komar et al., 2013; Barnet et al., 2019).

Within this general warming trend in the late Paleocene and early Eocene there were periodic, transient fluctuations in both carbon and oxygen isotope values (Galeotti et al., 2010; Littler et al., 2014; Westerhold et al., 2018). These constitute the background 'heartbeat' of the climate-carbon cycle system and were predominantly paced by the eccentricity cycle (~100 and 405 kyr) through the modulation of precession (Cramer et al., 2003; Lourens et al., 2005; Westerhold et al., 2008; Zachos et al., 2010; Westerhold & Röhl, 2013; Littler et al., 2014; Lauretano et al., 2015; Zeebe et al., 2017; Barnet et al., 2019; Westerhold et al., 2020). The largest of these perturbations are known as 'hyperthermal' events as they are often associated with elevated temperatures relative to background conditions. Some of these negative excursions have a characteristic double spike due to the occurrence of two 100 kyr eccentricity maxima broadly coeval with the 405 kyr maximum (Barnet et al., 2019). The largest and most well-studied of these hyperthermal events is the Paleocene–Eocene Thermal Maximum (PETM; ~56 Ma). Contrary to other hyperthermal events, the PETM is thought to be out of phase with the long eccentricity cycle, but in phase with short eccentricity (e.g., Barnet et al., 2019). This phasing combined with its large amplitude and slow recovery suggests this event was likely driven by factors other than orbital forcing,

such as a massive release of carbon dioxide from the NAIP. There were perhaps associated positive feedbacks leading to the further release of methane from either gas hydrates or permafrost (Eldholm & Thomas, 1993; Dickens et al., 1995; Bains et al., 1999; Cui et al., 2010; 2011; Dickens, 2011; DeConto et al., 2012; Komar et al., 2013; Frieling et al., 2016; Gutjahr et al., 2017; Reynolds et al., 2017; Frieling et al., 2019).

The Paleocene and Eocene Epoch hyperthermals are characterised by a large release of isotopically light carbon (either carbon dioxide or methane) into the atmosphere, causing a negative carbon isotope excursion. Additionally associated with these events are various climatic and oceanographic changes such as ocean and atmosphere warming (negative oxygen isotope perturbation), shallowing of the carbonate compensation depth (CCD) due to ocean acidification, dissolution of deep sea carbonates, and extreme warming of the low and high latitudes (Kennett & Stott, 1991; Zachos et al., 2001a; 2005; Sluijs et al., 2006; 2009; Stap et al., 2009; McInerney & Wing, 2011; Dunkley Jones et al., 2013; Aze et al., 2014; Penman et al., 2014; Sluijs et al., 2014; Frieling et al., 2017; Cramwinckel et al., 2018; Naafs et al., 2018; Komar & Zeebe, 2021). Negative excursions in the carbon cycle on average lag excursions in oxygen isotopes, suggesting that climatic changes (driven by changes in orbital configuration) led to a positive feedback release of carbon (Littler et al., 2014; Barnet et al., 2019). Despite extensive study, the causal relationship between Milankovitch cyclicity and the observed fluctuations in climate, atmospheric CO_2, and oceanic dissolved carbon is complex and still relatively poorly understood (Zeebe et al., 2017).

Following the EECO there was a gradual descent into “coolhouse” conditions throughout the remainder of the middle and late Eocene (Fig. 1.1) (Westerhold et al., 2020). Two major steps in the rate of cooling are observed in the oxygen isotope record at the Eocene–Oligocene transition (EOT; ~34 Ma) and the Oligocene–Miocene transition (OMT; ~23 Ma). Both of these events are thought to represent expansion of the East Antarctic Ice Sheet in response to declining pCO_2 and global and regional cooling, with the EOT being the first period of continental glaciation in the Cenozoic (Miller et al., 1991; Zachos et al., 1996; 2001b; DeConto & Pollard, 2003; Coxall et al., 2005; Zachos & Kump, 2005;

Pekar & DeConto, 2006; Liebrand et al., 2011; Villa et al., 2014; Liebrand et al., 2017; Greenop et al., 2019; Hutchinson et al., 2021). The Oligocene Epoch itself has a number of orbitally-paced glaciation intervals, predominantly driven by eccentricity modulation of precession (Paul et al., 2000; Wade & Pälike, 2004; Pälike et al., 2006; Liebrand et al., 2011; 2017; De Vleeschouwer et al., 2020).

The late Oligocene has an ~2 Myr long climate amelioration phase known as the Late Oligocene Warming Event (LOWE; ~25 Ma; Liebrand et al., 2017) (Fig. 1.1) marked by an ~1‰ negative excursion in benthic oxygen isotopes (Zachos et al., 2001a; Pälike et al., 2006; Pekar & DeConto, 2006; Hauptvogel et al., 2017; Liebrand et al., 2017) and associated marine transgression (Van Simaeys, 2004). Unlike the EOT and OMT, the LOWE is thought to be decoupled from atmospheric CO_2 changes, with stomatal (Grein et al., 2013; Roth-Nebelsick et al., 2014) and alkenone (Zhang et al., 2013a) proxy records suggesting pCO_2 did not increase during this period. Despite this event apparently representing one of the few Cenozoic cool to warm transitions, precise causes of the LOWE are undetermined. It has been suggested that a warm water mass bathed mid and low latitude sites over the LOWE, seen from a significant temperature gradient between deep ocean basins (Pekar & DeConto, 2006). There is little evidence for a major deglaciation on Antarctica itself during this interval, suggesting perhaps a well-established Antarctic circumpolar current protected it from this warmer water mass (Hauptvogel et al., 2017).

Terminating the LOWE is the OMT glaciation event, which is thought to have been driven by orbital cyclicity (Zachos et al., 2001b; Liebrand et al., 2011; Mawbey & Lear, 2013; Liebrand et al., 2017; Stewart et al., 2017). This event consists of two rapid, transient ~0.5‰ increases in benthic oxygen isotopes separated by ~405 kyr of partial recovery (Lear et al., 2004; Mawbey & Lear, 2013; Liebrand et al., 2017). The structure of this event is therefore comparable to the EOT (Coxall et al., 2005; Liebrand et al., 2017). Despite this, the link between the OMT glaciation and the carbon cycle processes driving the changes are poorly understood. It has been suggested that increased weathering of silicates (for example those of the Himalayan-Tibetan plateau [HTP]) lead to increased CO_2 sequestration (increased organic carbon burial), pre-conditioning the climate system prior to the OMT glaciation (Stewart et al., 2017). Due to a

lack of recovered marine sedimentary archives there is a dearth of data covering the Arabian Sea region over this climatic interval. In the modern, the Arabian Sea is subject to active monsoonal circulation (the South Asian monsoon); this impacts the oceanography and climate of the region with the seasonal modulation of precipitation, evaporation and ocean circulation patterns (Schott & McCreary, 2001; Gupta et al., 2020). The beginnings of the South Asian monsoon are poorly constrained, especially in the marine realm and Arabian Sea region due to a lack of suitable marine cores; current records from the Arabian Sea extend back to the middle Miocene Epoch and the nearest Oligocene age record is from the Maldives carbonate platform (Betzler et al., 2016; Pandey et al., 2016; Bialik et al., 2020; Yang et al., 2020). A number of terrestrial records suggest that the late Oligocene to early Miocene may have been a significant time in the evolution of the regional monsoonal climate (Clift & Vanlaningham, 2010; Srivastava et al., 2012; Jean et al., 2020), possibly due to the uplift of the HTP to a critical height to impact atmospheric circulation (Kutzbach et al., 1993; Clift et al., 2002; Tang et al., 2013). However, modelling also suggests that the HTP may not be required in order for there to be active monsoonal circulation (Boos & Kuang, 2010; 2013; Ding et al., 2017; Spicer, 2017; Acosta & Huber, 2020). Interactions between the changing tectonic regime of this region with global climatic events such as the LOWE and OMT are therefore poorly understood.

1.2.2 Microfossils and their use in studying past climates

Microfossils are widely used within the study of past climates. Biostratigraphy of microfossils such as foraminifera and calcareous nannofossils is useful to build up age models at a site. Without proper age constraint, any study of a site is not able to fit into a wider geographical and temporal context. Several microfossil groups are also useful tools in palaeoecology, where whole assemblages of genera or species can be examined to determine the specific ecological setting in which sediments were deposited. Finally, groups such as foraminifera are useful tools for geochemical analysis, further details of which are discussed below. Due to the wide utility of microfossils within palaeoclimate research, both foraminifera (larger and smaller) and calcareous nannofossils are utilised within this thesis for biostratigraphy, assemblage analysis, and geochemical analysis.

1.2.3 Geochemical proxies in past climate studies

To identify fluctuations in the Cenozoic climate record a number of different proxies can be used and a multi-proxy approach is key to understanding the dynamics of climate and oceanographic systems. Stable carbon and oxygen isotopes from both bulk carbonate sediment (implemented in Chapter 2) and species-specific foraminifera analysis (Chapter 4) can be used. The purpose of these measurements is to investigate changes in the climate and carbon systems in deep time, as both carbon and oxygen isotopes are affected by fluctuations and/or perturbations to these systems. Along with a detailed biostratigraphic age model, carbon and oxygen isotope time series are also tools for age control. Distinctive “events” in the chemostratigraphy of a study location can be used as age tie points, correlated to a well-known high-resolution stratigraphy from a different (deep marine) site. This integrated approach of using both bio- and chemostratigraphy to build an age model has been used in Chapters 2, 4, and 5.

Sample trace element analysis can be used at a variety of analytical scales, from bulk trace element analysis (Chapter 2) and high-resolution core-scanning trace element analysis (Chapter 4) to species-specific foraminifera trace element analysis (Chapter 4). Within this thesis bulk trace element analysis was implemented to observe changes in sediment inputs to the marine successions being investigated. For example, an increase in riverine-derived sediments to a marine basin, through either increased riverine discharge or a decrease in sea level, would result in mud-dominated sediments being delivered to the basin; in the trace elements this may be seen as an increase in weathering-derived elements such as titanium (Rothwell & Croudace, 2015). Foraminiferal trace element analysis can be used for several purposes, from changes in the oxygenation state of a water mass (e.g., Bialik et al., 2016) to changes in water mass temperature/salinity (Elderfield & Ganssen, 2000; Anand et al., 2003), both of which are applied in Chapter 4. Isotopic analysis of the trace element neodymium is used in geochemistry as a water mass tracer, due to its homogeneity across ocean basins (Piepgras et al., 1979). Neodymium isotopes are used in Chapter 5, and a detailed explanation of the systematics of this geochemical tracer can be found in Section 5.2.1.

1.2.4 PhD project summary

The overarching aim of this PhD thesis was to investigate regional palaeoenvironmental and palaeoclimatic change in the tropical low latitudes through the Paleogene and earliest Neogene (Fig. 1.2). The focus was the Middle East and Arabian Sea, with a view to improve our understanding of how these regions responded to both transient, rapid and longer-term climatic events. As described above, the Paleogene was a period of both long-term climate variability and ephemeral perturbations, meaning it can provide insight into how climate systems and biota are affected by palaeoenvironmental changes on a variety of timescales.

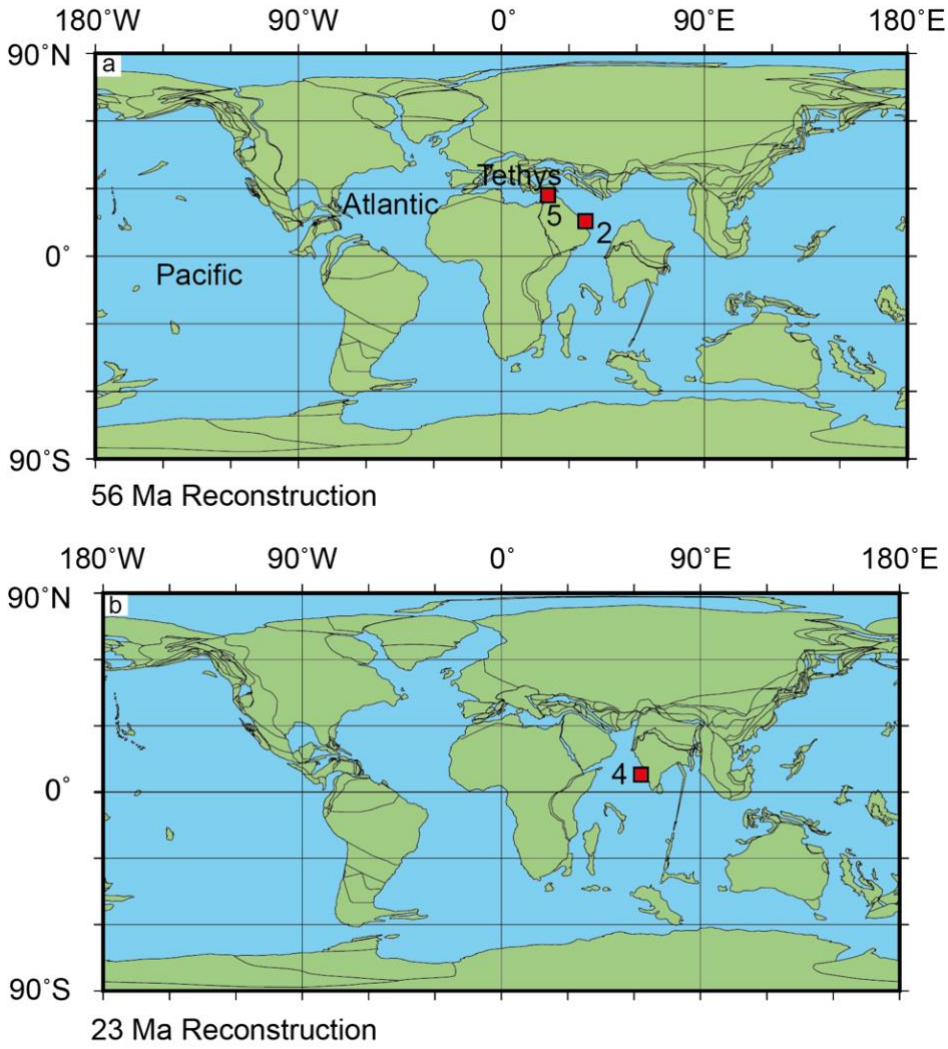

Figure 1.2 *Palaeogeographical maps of (a) the Paleocene–Eocene interval (~56 Ma) and (b) the Oligocene–Miocene interval (~23 Ma). Site locations studied in this thesis are shown by the red squares, numbers denote the related chapter. Note the narrowing of the eastern Tethys Ocean gateway through time and the northward movement of the Indian subcontinent.*

In Chapter 2 a shallow marine, carbonate-rich sedimentary sequence from the United Arab Emirates was investigated (Fig. 1.2a). Detailed analyses of the geochemistry, sedimentology, and biostratigraphy (larger benthic foraminifera [LBF] and calcareous nannofossils) were conducted in order to reveal new insights into shallow water (<100 m), low latitude environments over extreme, transient climate warming events, such as the PETM. Further to this, the long-term impact of early Paleogene warming on the palaeoecology and palaeoenvironment at the site was also examined.

High-resolution investigation of the LBF assemblage revealed that there was a major turnover event (i.e., multiple first and last occurrences in a short stratigraphic interval), however the assemblage remained stable over the onset of the PETM perturbation itself. It was concluded that this turnover was caused by long-term early Paleogene warming and the crossing of a long-term climatic and oceanographic threshold. This was also the main driver behind the overall loss of biodiversity from the shallow marine assemblage, with the diverse marine biota of corals, bivalves, and gastropods from the Paleocene not surviving into the early Eocene.

While processing samples for Chapter 2 the issue of disaggregating heavily indurated samples was encountered; when samples are strongly cemented, through burial and diagenesis, it becomes extremely hard to liberate microfossils effectively for identification and analysis without causing damage. In Chapter 3, three methods of retrieving foraminifera (primarily LBF) from indurated carbonates were compared and contrasted. These methods were two “traditional” methods (i.e., well-documented within current literature), Calgon and acetic acid, and a novel method of electric pulse fragmentation (EPF). It was shown that the EPF method was extremely effective and efficient at liberating LBF from the samples, especially compared to Calgon. Acetic acid also liberated a number of LBF specimens; however, scanning electron microscope analysis showed that preservation of these specimens was compromised by the strong acid.

In Chapter 4, foraminifera-nannofossil oozes from intermediate depths of the Arabian Sea were analysed over the Oligocene to early Miocene interval (Fig. 1.2b). Previously this interval has been relatively understudied, in part due to the

lack of recovery of continuous marine sediment cores of this age. More data are needed in order to reveal insights into the impacts of the long-term oceanographic and climatic changes occurring through this time, such as the LOWE and the glaciation at the OMT. A multi-proxy approach was adopted including species-specific planktic and benthic foraminiferal stable isotope and trace elements analyses, bulk sediment elemental analyses using ICP-OES and core-scanning XRF, and measurements of percentage coarse fraction. XRF-derived elemental ratios of Ti/Ca showed a step-change to higher values over the OMT. The geochemical data reveal a transient perturbation associated with the OMT glaciation interval, during which there was increased water mass mixing, possibly caused by intensified winter monsoon-like atmospheric circulation (winds flowing from the Asian landmass towards the Indian Ocean). During the latter part of the OMT there was a transition out of the glaciation phase, which resulted in a long-term initiation or intensification of a proto-South Asian monsoon system, with an associated intense oxygen minimum zone present over this eastern Arabian Sea site. The possible causes of this long-term change in atmospheric circulation and oceanography are discussed in the context of global and regional climate.

Lastly, in Chapter 5, an organic-rich succession spanning the PETM interval from onshore Jordan was investigated. This core is located in a key area of Tethyan through-flow in the eastern Paleogene Tethys Ocean (Fig. 1.2a); it was therefore hypothesised that a high-resolution investigation of oceanographic conditions over a rapid, transient warming event could be conducted. In order to do this, neodymium isotope data were generated from fossil fish teeth extracted from the core. Unfortunately, due to the Covid-19 pandemic, the results for this chapter are incomplete. However, preliminary data show there to be no discernible change in neodymium isotopes associated with the PETM itself. The long-term record shows a distinct change in neodymium isotopes to more negative (less radiogenic) values during the early Eocene. It was hypothesised that this could have been caused by a change to end-member water mass mixing in the Tethys, with an increased contribution of a more negative Atlantic or Indian Ocean water mass. Alternatively, a long-term change in internal cycling processes of neodymium may have driven this overall change to more radiogenic neodymium values. Additional lab work is required to make this chapter publishable.

A synthesis of the work contained in this thesis is provided in Chapter 6. It addresses the proposed research questions from Section 1.2 and provides possible directions for future work.

1.3 Research questions

During this PhD project I investigated regional marine sedimentary records from the Arabian Plate and Arabian Sea in order to address questions regarding the response of the tropics to both transient events and long-term palaeoclimatic perturbations of the Paleogene. Specifically, I addressed the following questions:

1) Are Paleogene hyperthermals (e.g., the PETM) preserved in the shallow water and/or low latitude sediments in this region? If so, how are the hyperthermals characterised in the investigated sediments and what does this tell us about the effects of hyperthermals on these shallow water/low latitude environments?

2) Are shallow water palaeo-fauna adversely affected by either transient climate perturbations or long-term climate change in the early Paleogene? Specifically, how do the larger benthic foraminifera (LBF) respond to long-term climate warming through this interval?

3) Are there associated palaeoceanographic changes in the study region through the late Paleocene to early Eocene time interval? It has been suggested that the PETM caused transient palaeoceanographic circulation changes; do we detect this in the study region?

4) Can we improve the currently available methods for disaggregating heavily indurated carbonate samples to retrieve LBF effectively and efficiently (and possibly other micro- and macrofossils)?

5) What are the impacts of the transient, global cooling events (e.g., the Oligocene–Miocene transition glaciation event) in the same low latitude regions? How does this long-term evolution of climate interact with this region which has active monsoonal circulation? What can this tell us about the proto-South Asian monsoon?

6) Can the effects of contemporaneous tectonic and climatic shifts be disentangled through sedimentological and geochemical analyses?

Chapter 2: Triumph and tribulation for shallow water fauna during the Paleocene–Eocene transition; insights from the United Arab Emirates

2.1 Abstract

The Paleocene–Eocene transition was a time of short-term rapid climatic and biotic change, superimposed on a long-term warming trend. The response of shallow tropical carbonate systems to past rapid warming is important to understand in the context of ongoing and future anthropogenic global warming. Larger benthic foraminifera (LBF) were abundant and important components of shallow water ecosystems throughout the early Paleogene and are sensitive to environmental change, making them ideal organisms to track shallow marine biodiversity. Furthermore, through the use of integrated bio- and chemostratigraphy it is possible to correlate the shallow (<100 m) and deep water realms to create a regional stratigraphic framework for the time period. Here we present a new LBF biostratigraphic and high-resolution carbonate carbon isotopic record spanning the Paleocene–Eocene transition from the onshore sub-surface of the United Arab Emirates (UAE). Results show a turnover event in the LBF assemblage during the early Eocene, wherein there are a number of first and last occurrences of species. However, assemblages remain generally stable coincident with the large negative carbon isotope excursion interpreted to be the onset of the Paleocene–Eocene thermal maximum (PETM). Turnover in the LBF assemblage in the early Eocene likely occurred due to the crossing of a long-term climatic and oceanographic threshold. The impacts of this long-term climatic change on the overall biotic assemblage at this site are significant, with LBF outcompeting a previously diverse community of corals, gastropods, and bivalves to become the dominant carbonate producers through the Paleocene–Eocene transition. Despite this, modern studies suggest that LBF are not immune to impacts of anthropogenic climate change, perhaps due to the significantly higher rates of change in the modern compared to the Paleocene–Eocene transition.

This chapter is published as a paper in *Newsletters on Stratigraphy* as: **Beasley, C.**, Cotton, L., Al Suwaidi, A., LeVay, L., Sluijs., A., Ullmann, C. V., Hesselbo, S. P., Littler, K., 2021. Triumph and tribulation for shallow water fauna during the Paleocene–Eocene transition: new insights from the United Arab Emirates.

Newsletters on Stratigraphy 54(1), 79–196. This is a modification of the published version as supplementary figures and tables have been inserted into the main text (see Appendix 1 for published version).

Co-author contributions: CB collected bulk samples and logged the core, with assistance in the UAE from AAS. CB analysed thin sections for LBF with assistance from LC. LL analysed calcareous nannofossil assemblages. AS analysed dinoflagellate cyst assemblages. CB ran geochemical analyses with assistance from CVU. CB constructed the chapter/manuscript, with edits from KL, LC, SPH, AAS, AS, CVU, and LL.

2.2 Introduction

The Paleocene and early Eocene (~66–50 Ma) interval is characterised by long-term warming associated with changes in the carbon cycle (e.g., Eldholm & Thomas, 1993; Zachos et al., 2008; Komar et al., 2013; Anagnostou et al., 2016). Shorter period Milankovitch cyclicity, changes in Earth's orbital configuration (i.e., eccentricity, obliquity and precession), also drove both variations in climate and perturbations to the carbon cycle during this period (Cramer et al., 2003; Lourens et al., 2005; Westerhold et al., 2011; Littler et al., 2014; Westerhold et al., 2017; Barnet et al., 2019). Against the background of warming during the late Paleocene to early Eocene, several transient global warming phases, so called 'hyperthermal' events of varying severity and duration, occurred that are likely to have been paced by Milankovitch cyclicity (e.g., Cramer et al., 2003; Lourens et al., 2005; Zeebe & Lourens, 2019). These hyperthermals are associated with ocean acidification (Zachos et al., 2005; Stap et al., 2009), and negative carbon and oxygen isotope excursions as recorded in carbon bearing phases in both marine and terrestrial archives (Kennett & Stott, 1991; Koch et al., 1992; Thomas & Shackleton, 1996; Bolle et al., 2000; Lourens et al., 2005; Sluijs et al., 2009), providing strong evidence of rapid and massive injections of carbon into the ocean-atmosphere system (Dickens et al., 1995; 1997). During the largest of these hyperthermal events, the Paleocene Eocene Thermal Maximum (PETM; ~56 Ma), global climate rapidly warmed by ~5°C, with limited extratropical amplification (Dunkley Jones et al., 2013; Zeebe et al., 2014; Frieling et al., 2017). The PETM is recognised in geochemical records by a sudden negative carbon

isotope excursion (CIE), followed by the 'body' of the CIE and relatively more gradual recovery to background levels, all of which is thought to have taken ~170 kyr (Röhl et al., 2007) but possibly more than 200 kyr (Zeebe & Lourens, 2019). In many deep sea sites, the magnitude of this negative excursion, as recorded in marine carbonates by benthic foraminifera, is ~2–3‰ (Kennett & Stott, 1991; Bains et al., 1999; Zachos et al., 2003). However, some bulk marine organic matter records show a negative excursion of up to ~8‰ in magnitude (Sluijs et al., 2006; Cohen et al., 2007; McInerney & Wing, 2011). The differences in size and shape of the CIEs measured on specific substrates and regions are thought to relate to changes in the relative abundance of mixed components with different $\delta^{13}C$ values within a measured substrate, changes in isotopic fractionation through physiological changes, changes in the isotope composition of the carbon source, and possibly effects of diagenetic alteration (Sluijs & Dickens, 2012).

Following the PETM, the general warming of early Paleogene global climate continued, peaking at the early Eocene climatic optimum (EECO) between ~52–50 Ma (Zachos et al., 2001a; 2008; Bijl et al., 2009; Cramwinckel et al., 2018). High-resolution records of benthic foraminifera oxygen isotope values document a number of hyperthermal events within this early Eocene general warming trend (Galeotti et al., 2010; Littler et al., 2014; Lauretano et al., 2015; 2016; Westerhold et al., 2018; Barnet et al., 2019). These events include Eocene Thermal Maximum (ETM) -2 (also referred to as Elmo or H-1; Lourens et al., 2005; Sluijs et al., 2009; Stap et al., 2010) at ~53.7 Ma and ETM-3 (or the "X" event; Agnini et al., 2009; Thomas et al., 2018) at ~52.5 Ma. Many of these early Eocene hyperthermals are thought to be orbitally paced by both the long (~405 kyr) and short (~100 kyr) eccentricity cycles, and the precession (~21 kyr) cycle (Cramer et al., 2003; Lourens et al., 2005; Galeotti et al., 2010; Zachos et al., 2010; Littler et al., 2014; Galeotti et al., 2019; Zeebe & Lourens, 2019).

Throughout this early Paleogene interval larger benthic foraminifera (LBF) were abundant in tropical, shallow (<100 m) waters (Hottinger, 1998; BouDagher-Fadel, 2008). LBF are single-celled organisms which form more complex tests (shells) than smaller foraminifera (BouDagher-Fadel, 2008). Many genera of LBF possess algal photosymbionts, similar to corals, restricting them to the marine photic zone (Haynes, 1965). LBF are sensitive to environmental change, making

them ideal organisms to study the effects of sudden global warming events, such as the PETM (Hallock & Glenn, 1986). From the late Paleocene into the early Eocene LBF were increasingly important shallow water calcifiers, becoming the dominant carbonate producers in shallow oligotrophic environments as corals underwent decline (Scheibner & Speijer, 2008a; Afzal et al., 2011; Zamagni et al., 2012). Coral reefs declined from the late Paleocene to early Eocene, possibly due to a number of stressors which include increased water temperatures and an increase in sediment load/nutrient supply (Zamagni et al., 2012). Over the Paleocene–Eocene transition, LBF underwent gradual turnover, as expressed in multiple low latitude sites including Spain, Egypt and Tibet (Scheibner et al., 2005; Pujalte et al., 2009; Zhang et al., 2018). LBF also experienced species diversification and increases in adult dimorphism and test size at this time (Hottinger, 1998; Scheibner et al., 2005; Zhang et al., 2018); these changes are termed the larger foraminifera turnover (LFT). It remains uncertain whether this LFT event coincides with, and is therefore likely to be causally related to, the PETM (Pujalte et al., 2009; Scheibner & Speijer, 2009), or if it predates this event and is therefore unrelated (Hottinger, 1998; Zhang et al., 2013b). The correlation of the LFT event to global biostratigraphy and chemostratigraphy would tie together shallow and deep water stratigraphies; however, most sites where the LFT is well expressed lack the additional stratigraphic control to link to the global expression of the PETM definitively (e.g., Pakistan; Afzal et al., 2010). Continued diversification of the LBF through the Paleogene created "hotspots" of high generic and species-level diversity which moved eastwards through this interval, from the Tethys to the current hotspot in the Indo-Pacific (Renema et al., 2008). Absolute timing and location for the beginning of this upturn in diversity is debated, with some suggesting that it started earlier in the late Paleocene to early Eocene in the eastern Tethys (Scheibner et al., 2005; Hottinger, 2014), and others proposing a later start during the late middle Eocene in the western Tethys (Renema et al., 2008).

Contrary to this more gradual turnover and diversity increase of LBF in the shallow water domain, smaller benthic foraminifera in the deep water domain experienced a major extinction. Known as the benthic foraminifera extinction event (BEE; Thomas, 1989; Thomas & Shackleton, 1996; Thomas, 1998; Alegret & Ortiz, 2006), 30–50% of known deep sea smaller benthic foraminifera species

did not survive into the Eocene (Schmitz et al., 1996; Thomas, 1998; 2007). It is suggested that the recorded ~5°C of bottom water warming could have caused the BEE (Thomas et al., 2000; Winguth et al., 2012), either through warming of surface waters in regions of bottom water formation, or due to a switch of bottom water formation to lower latitudes (Thomas & Shackleton, 1996). Additional factors affecting the smaller benthic community were marine waters that were increasingly corrosive to $CaCO_3$, decreased oxygenation, and changes in productivity (Thomas, 1998; 2007). It has also been suggested that the rapidity of the climate perturbations at the PETM, rather than the magnitude itself, caused the BEE (Thomas, 2007). Across the gradual (~500 kyr) global cooling at the Eocene–Oligocene transition, abyssal and bathyal benthic foraminifera show little change associated with the boundary itself, in contrast to the PETM (Coxall & Pearson, 2007). This suggests an ability to adapt to such gradual changes and an inability to cope with the sudden change in palaeoenvironment at the onset of the PETM.

It is increasingly clear that hyperthermal events such as the PETM have a spatially heterogenous expression, where different regions experienced contrasting shifts in temperature (Sluijs et al., 2006; Aze et al., 2014; Sluijs et al.. 2014; Frieling et al., 2017) and hydrology (Bolle & Adatte, 2001; Bowen et al., 2004; Schmitz & Pujalte, 2007; Bowen & Bowen, 2008; Carmichael et al., 2017), as well as differing biological responses to these conditions (Speijer et al., 2012). For example, general circulation model (GCM) simulations for the PETM indicate that some regions, such as the eastern US coast and a number of localities around the Tethys, likely experienced increased precipitation, while the western US and the Angola Basin experienced aridification over the same interval (Carmichael et al., 2017). It is therefore important that the proxy record also has broad spatial coverage, both in terms of latitude/longitude and depth in the oceans.

Although there are excellent representative deep sea marine records of the late Paleocene to early Eocene from most of the major ocean basins, more multi-proxy records from the low latitudes and tropics are required in order to test these models. In particular, there is a dearth of data from shallow marine (<100 m), low latitude areas (Fig. 2.1). Although geochemical, sedimentological,

palaeogeographical, and palaeobiological data spanning this interval are available from other east Tethyan sections (Nolan et al., 1990; Keen & Racey, 1991; Alsharhan & Nairn, 1995; Racey, 1995; Schmitz et al., 1996; Charisi & Schmitz, 1998; Speijer & Schmitz, 2000; Speijer & Wagner, 2002; Dupuis et al., 2003; Alegret & Ortiz, 2006; Beavington-Penney et al., 2006; Dill et al., 2007; Khozyem et al., 2015; Serra-Kiel et al., 2016a; Giraldo Gómez et al., 2018) comparable data from the United Arab Emirates (UAE) is of limited spatial and temporal resolution (Dill et al., 2007; Faris et al., 2014; Tomas et al., 2016). Importantly, the UAE is significantly further south (by ~5°) and further east than most of these existing sites (Fig. 2.1). High-resolution, integrated geochemical and palaeoecological records from low latitude, shallow water sites of this age are important to constrain how these regions responded to both long-term changes in the climate and carbon cycle and geologically rapid events such as the PETM. A multi-proxy, integrated approach is key in order to be able to tie local stratigraphy to a global stratigraphic model, allowing for correlation from the shallow to the deep oceans.

Presented here is an integrated high-resolution LBF record with stable isotope and calcareous nannofossil stratigraphy from the subsurface of onshore United Arab Emirates (UAE) covering the late Paleocene into early Eocene interval. This area previously lacked integrated, high-resolution palaeoclimatic data from this globally important time interval (Fig. 2.1). The core investigated in this study provides an opportunity to examine a long-ranging interval in which the LBF response to global climate change can be tied to the global isotope and biostratigraphy. The response of the low latitude and shallow water domains to past climate perturbations provides important insight for the future response of these fragile ecosystems to anthropogenic climate change.

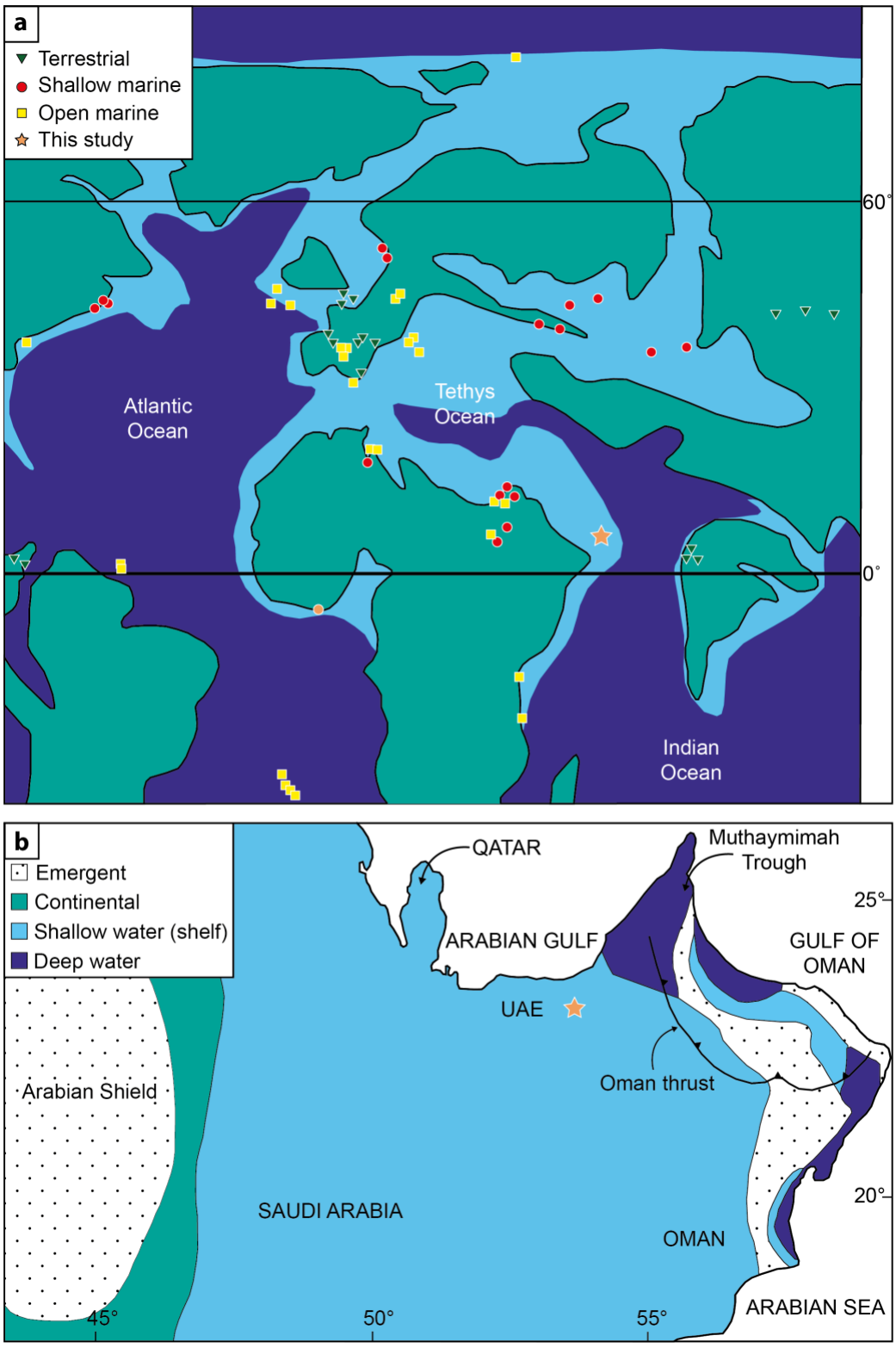

Figure 2.1: *Modern location and palaeoceanographic setting of study site and other PETM records. (a) Map of late Paleocene (~56 Ma) palaeogeography (adapted from Dickson et al., 2015) displaying locations of PETM records (modified from McInerney & Wing, 2011). Shallow marine defined as <200 m water palaeodepth, open marine defined as 200 m to pelagic. Note the lack of sections from the southern and eastern Middle East, and the Arabian Sea. (b) Palaeogeography of the Arabian Plate during the late Paleocene to early Eocene showing relationships between shallow and deeper water facies (modified from Ziegler, 2001; Haq & Al-Qahtani, 2005). Orange star indicates Core A location in both figures.*

2.3 Geological setting of study area

In order to address the outstanding questions surrounding the response of the shallow marine realm to the climatic changes during the late Paleocene to early Eocene, new geochemical and palaeontological records from “Core A”, onshore UAE (Fig. 2.1), were produced. Core A was recovered by Abu Dhabi National Oil Company (ADNOC) and may have economic significance, and as such the specific core name and precise locality cannot be published. Located in the western UAE, Core A is from an area otherwise dominated by sandy desert with no available outcrop. Core A was logged at a high-resolution along the entirety of its length revealing the core consists of ~383 m of dominantly shallow (<100 m) marine carbonate sediments, rich in bioclasts. The examined core was previously split and slabbed, allowing for sedimentary structures and biota to be observed. The top of the core starts at approximately 985 m depth below surface (mbs), extending to ~1350 mbs at the base of the core. For the purpose of this study 985 mbs was used as the zero level and will be referred to as such for the rest of the text.

2.4 Methods

2.4.1 Microfossils

2.4.1.1 Larger benthic foraminifera

A total of 48 samples were analysed for LBF biostratigraphy through the use of 56 petrological thin sections. Multiple thin sections were made for some samples in order to aid identification of LBF; identification to species level requires the specimen to be orientated with the section passing through the first chamber (proloculus), thus duplicate thin sections were made in key intervals at right angles to one another. Standard petrographic thin sections were used for identification of LBF taxa and ground to a thickness of 50 µm in order to ensure skeletal grains were identifiable. Samples were taken approximately every 20 m for the lower part of the core, increasing to a ~5 m resolution from ~50 m depth to the top of the core. Transects of the slide were made until the complete slide had been viewed. Specimens were identified to at least genera level, or species

level where possible. If this was not possible these were marked as an unidentified LBF occurrence. Taxonomy follows that of Hottinger (2014).

The LBF assemblages were examined throughout Core A to construct the basis of an age model and determine palaeoecological changes through the Paleocene–Eocene interval. Biostratigraphy of LBF uses regional schemes; within the Tethyan region this is the shallow benthic zonation (SB) scheme (Papazzoni & Pignatti, 2019), which is the closest and most widely used in the Arabian Peninsula region. To create the biostratigraphic model the SB Zonation scheme constructed in the Tethyan region and updated and modified in nearby areas of the Arabian Plate were utilised (Serra-Kiel et al., 1998; Scheibner & Speijer, 2009; Serra-Kiel et al., 2016a; 2016b).

2.4.1.2 Calcareous nannofossils (conducted by LL)

Sixteen samples from between 5.8–372.6 m were studied in order to provide a biostratigraphic framework. Samples that contained a higher percentage of marl were chosen for analysis on the basis that preservation was likely to be better in the finer grained sediment. Smear slides were prepared using standard techniques (Bown & Young, 1998) and the slides used 24 mm x 40 mm cover slips. Transects across the cover slip were made at x630–1000 magnification using a Zeiss Axioscope A1. The transects were intended to capture the whole cover slip, but some fields of view may have been missed.

Total nannofossil abundance in the slide was visually assessed using the following criteria (Clemens et al., 2016): D = dominant (>90% of sediment particles in a field of view); A = abundant (50–90% of sediment particles); C = common (10–50% of sediment particles); F = few (1–10% of sediment particles); R = rare (<1% of sediment particles); B = barren (no specimens present).

The relative abundance of nannofossil species was not collected due to the overall rarity of fossils. In figures, the presence of a species is denoted with an ‘X’, and questionable species occurrences due to poor preservation are marked with a ‘?’.

The preservation state of the nannofossils was qualitatively described using the categories (Clemens et al., 2016): VG = very good (no evidence of dissolution and/or recrystallisation, no alteration of primary morphological characteristics, and specimens identifiable to species level); G = good (little evidence of dissolution and/or recrystallisation, primary morphological characteristics only slightly altered, and specimens identifiable to species level); M = moderate (specimens exhibit some etching and/or recrystallisation, primary morphological characteristics somewhat altered, and most specimens identifiable to species level); P = poor (specimens severely etched or overgrown, primary morphological characteristics largely destroyed, fragmentation has occurred, and specimens could not be identified to species and/or genus level).

The biostratigraphic classification of the study succession is based upon the Martini (1971) NP zonation (Agnini et al., 2007; 2014). Nannofossil taxonomy follows Perch-Nielsen (1985) and the Nannotax database (Young et al., 2019).

2.4.1.3 Palynomorphs (conducted by AS)

Three samples were processed for palynology. These samples bordered the Paleocene–Eocene boundary, with slides at 7.4 m, 8.2 m, and 153.3 m from the top of the core. Palynological slides were prepared at the National Oceanography Centre, University of Southampton. Approximately 5 g of roughly crushed rock was treated with 30% HCl to remove carbonates, followed by decant washing to a neutral pH. Samples were further demineralised in 60% HF followed by decant washing again to a neutral pH and sieved at 15 µm. Samples were then placed in glass beakers and briefly boiled in 30% HCl to solubilise neoformed fluorides that were then removed by diluting into a large volume of water and re-sieving. Residues were then vialed, with strew slides made and mounted in Elvacite 2044™. Residues were analysed at Utrecht University, Laboratory of Palaeobotony and Palynology for general palynological content, with emphasis on dinoflagellate cysts (dinocysts) following the taxonomy of Williams et al. (2017).

2.4.2 Carbon and oxygen isotope analysis

To generate an age model for the stratigraphic interval studied, and to identify the timing of faunal changes in LBF relative to the onset of the PETM, the stable carbon and oxygen isotope composition of the bulk carbonate fraction of 710 samples was determined. This consisted of 379 samples from the top 79 m of Core A, at a resolution of 10 cm, and 331 samples from the remaining ~300 m, at a resolution of approximately 1 m. These samples were drilled using a micro-drill, choosing fresh surfaces and avoiding macrofossil material. The bulk rock powder was weighed at 500 ± 50 µg for each sample and subsequently analysed for $\delta^{13}C$ and $\delta^{18}O$ values using a SerCon 20-22 Gas Source Isotope Ratio Mass Spectrometer (GS-IRMS) in the Environment and Sustainability Institute, University of Exeter. Samples were weighed using a MSE3.6P-000-DM Sartorius Cubis® Micro Balance. Standards and samples are reported in δ-notation relative to VPDB (Vienna Pee Dee Belemnite). Each complete run of analysed samples consisted of 80 samples plus 22 aliquots of the in-house standard CAR (Carrara Marble, $\delta^{13}C$ = +2.10‰ VPDB; $\delta^{18}O$ = –2.03‰ VPDB) and 8 aliquots of the in-house standard NCA (Namibia Carbonatite, $\delta^{13}C$ = –5.63‰ VPDB; $\delta^{18}O$ = –21.90‰ VPDB). Standards were also weighed at 500 ± 50 µg.

All samples were flushed with He for 80 seconds before manual injection of ~100 µL of nominally anhydrous phosphoric acid. Samples were measured alternating with a reference gas in continuous flow mode (Spötl & Vennemann, 2003). For the results shown in this report the average 2 sd repeatability of CAR was found to be 0.06‰ for $\delta^{13}C$ and 0.14‰ for $\delta^{18}O$ and average 2 sd repeatability of NCA was 0.09‰ for $\delta^{13}C$ and 0.30‰ for $\delta^{18}O$ (Table 2.1).

Table 2.1: *2 standard deviation repeatability for standards Carrara Marble (CAR) and Namibia Carbonatite (NCA) used in stable isotope analyses.*

	CAR		NCA	
	$\delta^{13}C$	$\delta^{18}O$	$\delta^{13}C$	$\delta^{18}O$
2sd of analyses	0.07	0.17	0.11	0.33
	0.06	0.15	0.10	0.28
	0.07	0.13	0.06	0.36
	0.05	0.13	0.08	0.25
	0.06	0.16	0.09	0.28
	0.07	0.12	0.10	0.33
	0.04	0.16	0.09	0.21
	0.04	0.12	0.13	0.29
	0.07	0.10	0.06	0.41
Average 2sd	**0.06**	**0.14**	**0.09**	**0.30**

2.4.3 Percentage calcium carbonate analysis

To observe relative changes in the carbonate vs. terrigenous fraction in the core, percentage calcium carbonate (%$CaCO_3$) data were determined as a by-product of the carbonate carbon and oxygen isotope analysis detailed in Section 2.4.2. Bulk sediment samples were weighed before analysis (as above), and this known amount was dissolved using anhydrous phosphoric acid. Once dissolved the samples release CO_2, and through calibration of the size of this CO_2 peak relative to known standards, the %$CaCO_3$ could be determined for each sample, yielding a 2 sd reproducibility of ± 2.3% for the in-house standard NCA (n=79) (e.g., Razmjooei et al., 2020).

2.4.4 Inductively coupled plasma optical emission spectroscopy (ICP-OES)

A total of 34 bulk carbonate samples were analysed using ICP-OES, at a resolution of approximately 10 m, for their trace element signal. This was to assess for possible diagenesis in the core. Bulk samples were micro-drilled, choosing fresh surfaces and avoiding macrofossil material. Bulk rock powder was weighed at 850 ± 100 µg using a MSE3.6P-000-DM Sartorius Cubis® Micro Balance. The samples were dissolved using 2% nitric acid and diluted to a nominal Ca concentration of 25 µg/g. These solutions were run on an Agilent 5110 Series machine at the University of Exeter Penryn Campus with three multi-elemental standards consisting of 12 JLS-1, 8 AK and 4 BCQC. Table 2.2 shows

the suite of analysed elements with their 6 sd quantification limits. Data repeatability (2 relative standard deviations) is generally better than the larger value of either quantification limit (for low element/Ca ratios) or 1% of the measured element/Ca ratio (for high element/Ca ratios).

Table 2.2: *Suite of analysed elements using ICP-OES, wavelengths (nm) and 6sd baseline variability in ng/g and converted to equivalent molar ratios (mmol/mol) given a nominal Ca concentration of 25 µg/g in analysed solution.*

Element	Wavelength (nm)	6sd Baseline Variability (ng/g)	6sd Baseline Variability (mmol/mol)
Ca	317.993	1.1	0.017
Ca	422.673	0.8	0.013
Fe	238.204	0.7	0.008
Fe	259.940	0.3	0.004
Li	670.783	0.4	0.040
Mg	279.553	0.09	0.002
Mg	280.270	0.13	0.003
Mg	285.213	0.41	0.011
Mn	257.610	0.05	0.001
Mn	259.372	0.15	0.002
P	213.618	7.58	0.160
S	181.972	5.65	0.110
Sr	407.771	0.01	0.0001
Sr	421.552	0.02	0.0002

2.4.5 Optical cathodoluminescence microscopy

To assess for diagenetic alteration, three representative thin sections from Core A were observed using a Nikon Eclipse LV100ND with CITL Analytical Instruments MK 5-2 cold cathodoluminescence microscope. Investigated samples were from ~0.2 m, ~16.1 m, and ~85.6 m, within bioclastic facies dominated by LBF. Impurities within the carbonate rocks affect the luminescence of the material, with Mn^{2+} activating luminescence and Fe^{2+} quenching it. The ratio of these elements, therefore, control the intensity of luminescence in a material (Adams & MacKenzie, 1998).

2.4.6 Wireline logging

Wireline logging data, collected during drilling operations, were obtained from ADNOC. The wireline undifferentiated gamma ray data has been used in this study; spectral gamma ray was not available. Measurements were taken approximately every 15 cm downcore.

2.5 Results

2.5.1 Sedimentology

Within the core there are three distinct lithofacies (Fig. 2.2): 1) Marl with few or no bioclasts; 2) LBF-rich bioclastic wackestone/packstone and; 3) Bioclastic grainstone with LBF, gastropods, bivalves, and solitary corals. In the lower part of the core, from 285–383 m, facies type 1 dominates with occasional thin-shelled bivalves and rare or absent photosymbiont bearing organisms, such as corals or LBF. This lower interval transitions up into facies type 3 from ~185–285 m. From ~173 m upwards in the core there are a series of shallowing-up parasequences on the order of 10's of metres (core log, Fig. 2.3). Marls with thin-shelled bivalves and LBF, suggestive of a low energy environment, grade upwards into more bioclastic facies (facies type 2) with thicker shelled bivalves, occasional gastropods and abundant LBF. Within these parasequences there are intermittent grainstone beds composed of broken up, poorly sorted bioclasts (Fig. 2.3). The nature of these beds is suggestive of storm-influenced deposits.

Within the observed sedimentary sequence there is no evidence of sub-aerial emergence of the platform indicating that there is an absence of large regression episodes on the platform. However, there are large gaps in the record at the top of the core where no sediments were recovered during drilling.

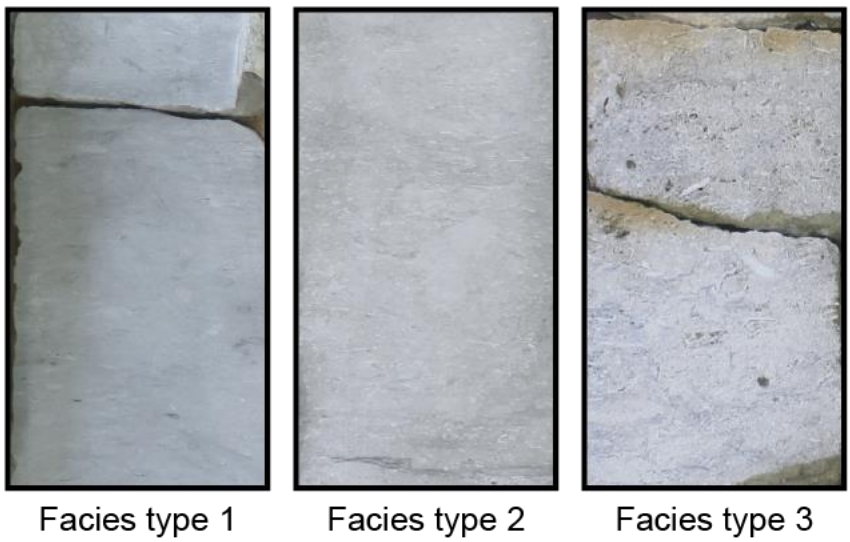

Figure 2.2: *Key facies types of core A. Facies type 1: Marl with few or no bioclasts. Facies type 2: LBF-rich bioclastic wackestone/packstone. Facies type 3: Bioclastic grainstone with LBF, gastropods, bivalves, solitary corals.*

2.5.2 Micropalaeontological results

2.5.2.1 The larger benthic foraminiferal assemblages

The LBF assemblage in Core A consists largely of the genera *Daviesina*, *Kathina*, *Lockhartia*, *Miscellanea*, *Sakesaria*, *Ranikothalia*, and *Nummulites*, all of which are typical for the region. From the bottom of Core A to ~50 m the LBF assemblages are composed primarily of the genera *Daviesina*, *Miscellanea, Kathina* and *Dictyokathina*, diagnostic of Zones SB 3 and SB 4, which broadly correlate to a mid to late Paleocene age (Serra-Kiel et al., 1998). The first occurrence (FO) of *K. major* and *K. delseota* (Hottinger, 2014) and the FO of *M. dukhani* (Hottinger, 2009) occur at ~193 and ~134 metres respectively, placing the Zone SB 3–4 boundary at approximately 193 m (Fig. 2.3). Between 134 and 46 m the assemblages remain relatively stable, with 5 first occurrences and 4 last occurrences recorded. There is then a core gap between ~27–46 m.

Above ~27 m in the core genera *Sakesaria* and *Nummulites* along with small rotaliids and miliolids dominate the assemblages, indicative of Zone SB 5 and higher, approximately correlating to the early Eocene (Serra-Kiel et al., 1998; Scheibner & Speijer, 2009). A more precise SB Zone cannot be determined due

to a lack of age diagnostic species in these samples. Following Serra-Kiel et al. (1998), Scheibner et al. (2005) and Scheibner & Speijer (2009) the Zone SB 4–5 boundary is defined by the last occurrence (LO) of *D. simplex* and all representatives of the genus *Miscellanea*, along with the FO of *S. cotteri*, *R. nuttalli*, *Rotalia* spp. and *Nummulites* spp. This suggests the boundary between Zone SB 4 and 5 is between 27 and 16 metres, within which *R. nuttalli*, *Sakesaria* spp. and *Nummulites* spp. all have first occurrences preceding the last occurrences of *D. simplex* and the genus *Miscellanea*.

Within the defined Zone SB 4–5 interval (16–27 m; Fig. 2.3), LBF species richness increases over approximately 10 m of stratigraphy. The assemblages from the bottom of the core to ~45 m is relatively uniform, with 6 genera and 7 species in SBZ 3 and 9 genera and 9 species in SBZ 4. From ~45 m, SBZ 5 and higher, the number of genera increases to 11 and the number of species increases substantially to 16.

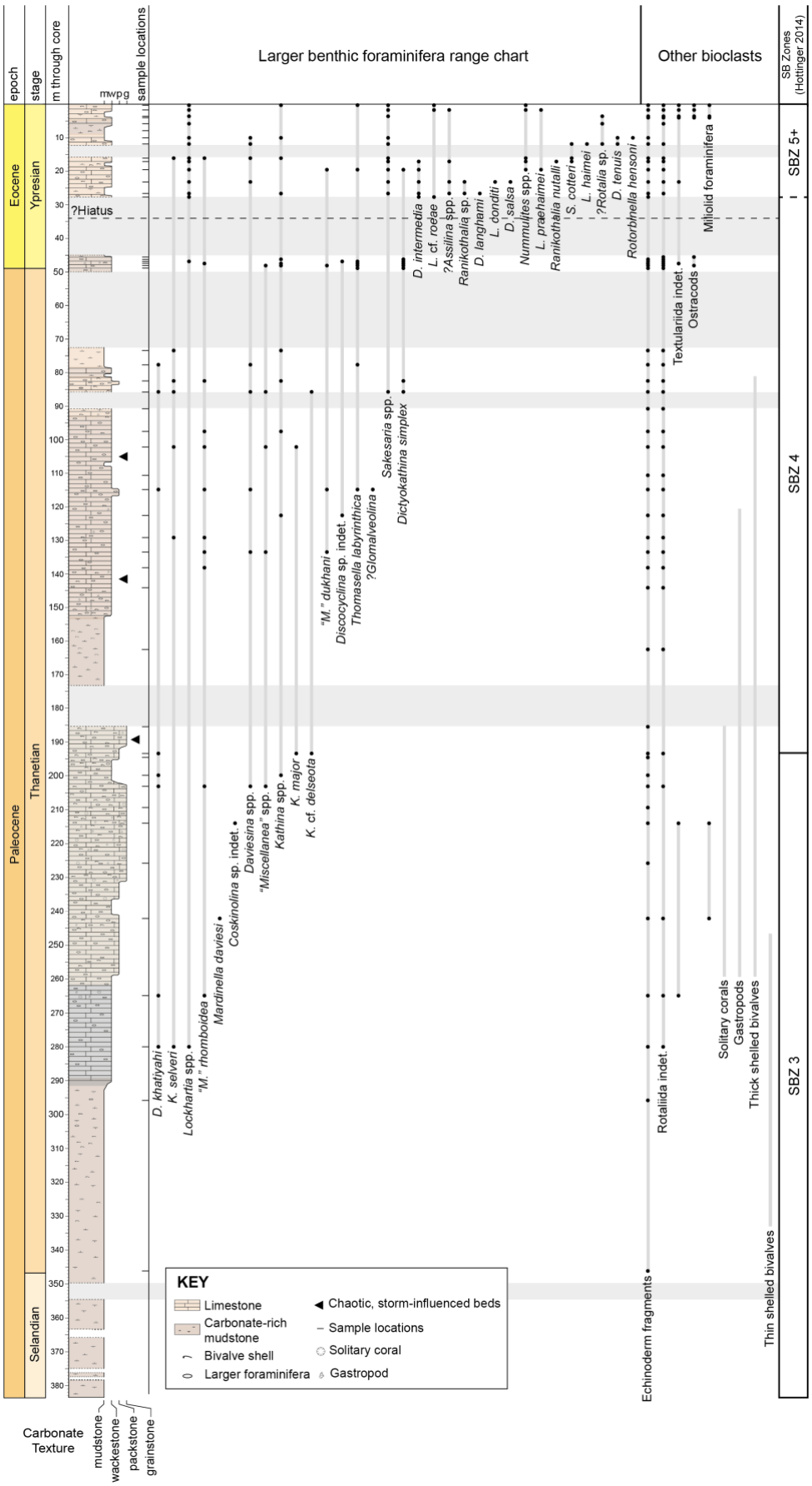

Figure 2.3: *Log of Core A and range chart of LBF species and genera observed, arranged by first occurrence in the core. Also included are other bioclasts observed in the core. Shallow benthic (SB) zonation scheme from Hottinger (2014). Colours of log directly reflect changes in lithology colour of core. Horizontal grey boxes mark core gaps.*

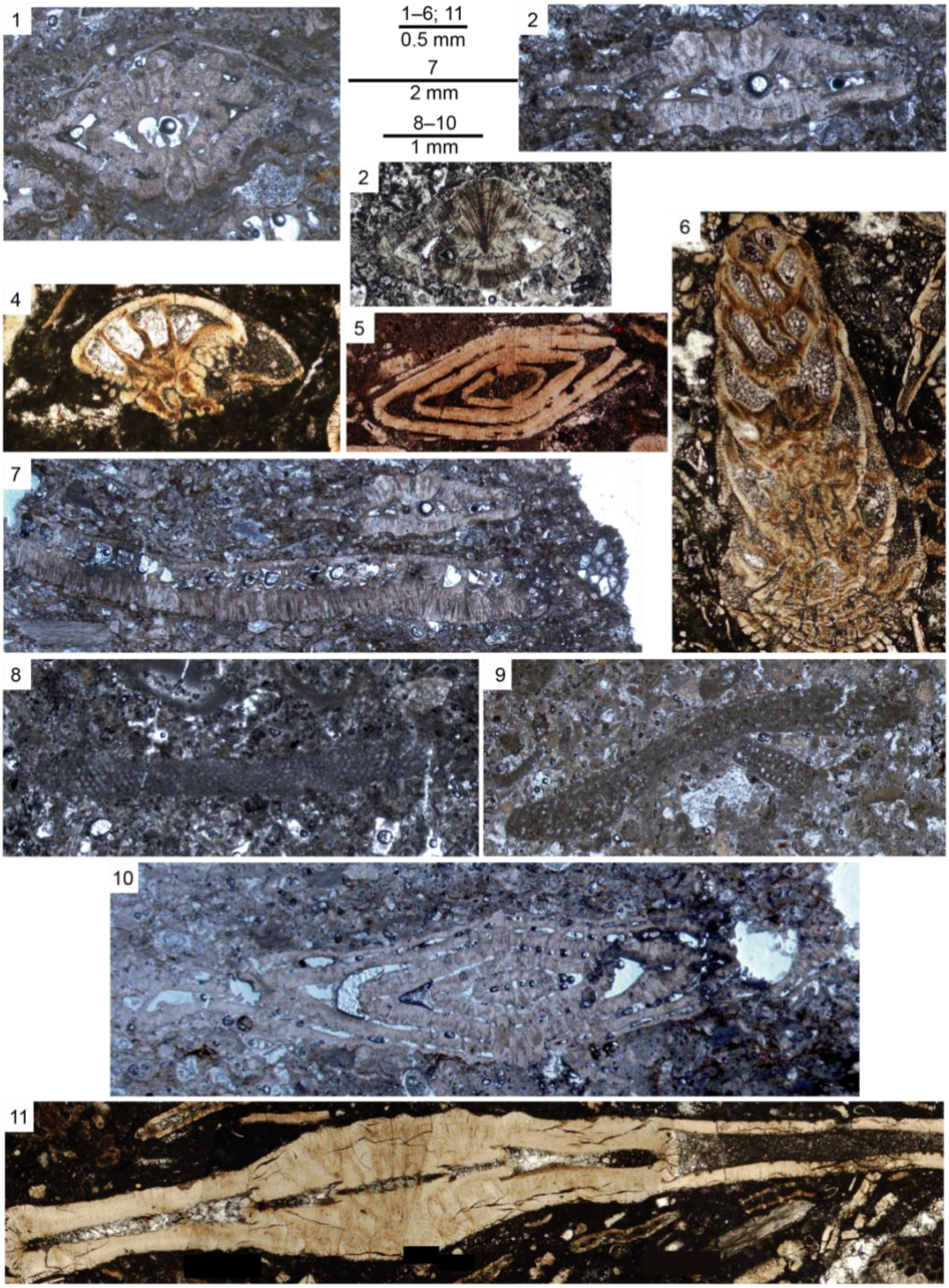

Figure 2.4: *Selected late Paleocene to early Eocene LBF from Core A.*
1) Miscellanea “rhomboidea” *Kuss and Leppig 1989, range undefined, 133.5 m.*
2) Daviesina khatiyahi *Smout 1954, SBZ 3–4, 194.6 m.*
3) Kathina selveri *Smout 1954, SBZ 3–4, 280 m.*
4) Lockhartia *cf.* conditi *(Nuttall 1926), SBZ 4–8, 23.1 m.*
5) Nummulites *sp., SBZ 5+, 16.1 m.*
6) Sakesaria cotteri *Davies and Pinfold 1937, SBZ 5–7, 17.1 m.*
7) Dictyokathina simplex *Smout 1954, SBZ 3–4, 194.6 m.*
8) Mardinella daviesi *(Henson 1950), SBZ (?–)4, 242.1 m.*
9) Thomasella labyrinthica *Grimsdale 1952, SBZ 4(–5?), 115 m.*
10) Miscellanea dukhani *Smout 1954, SBZ 4–5, 133.5 m.*
11) Ranikothalia nuttalli *(Davies 1927), SBZ 4, 17.1 m.*

2.5.2.2 Calcareous nannofossil biostratigraphy (conducted by LL)

In general, nannofossils are poorly preserved (Fig. 2.5) and have abundances ranging from rare to few when present (Fig. 2.6). A total of 29 species plus 7 undifferentiated genera are recognised (Fig. 2.6). The estimated age assignments are primarily based upon the assemblage and documented ranges of non-marker species, as few marker species are present in the samples. We caution that the presented zones are estimates that provide age constraints and, without the presence of marker taxa, cannot be regarded as precise. The samples range from middle Paleocene (Zone ~NP 4–6) to the early Eocene (~NP 11). Calcareous nannofossils were present in 14 of the 16 smear slides analysed and of these 14 samples, biozone ranges are assigned to 9 of them. Where approximate ages are stated, they are calibrated to GTS2012 (Gradstein et al., 2012).

The base of the core (~370 m) contains *Lithoptychius janii*, which constrains the age of these sediments to likely be within the NP 4–6 biozones (Varol, 1989; Young et al., 2019) and corresponds to the middle Paleocene. Below the large gaps in the core, at ~78 m, the first appearance of the robust marker species *Discoaster multiradiatus* is present indicating late Paleocene age (marker species for the base of Zone NP 9; Martini, 1971). The top of the core (~27 m and above) contains *Camplyosphaera eodela, D. multiradiatus, D. barbadiensis, Coccolithus latus* and *Sphenolithus orphaknollensis*. This assemblage suggests this sample likely falls within or near Zone NP 11 (Agnini et al., 2007; Shamrock & Watkins, 2012) correlating to the early Eocene. The primary marker for the base of NP 11, *Tribrachiatus contortus*, is absent, which may be due to poor preservation or ecological exclusion. The change in biozones from ~NP 9 to NP 11 that occurs between ~78 m and ~28 m, suggests either a hiatus in sedimentary deposition or that stratigraphic condensation occurred. More detailed descriptions of the calcareous nannofossil assemblages are given in Appendix 7.4.

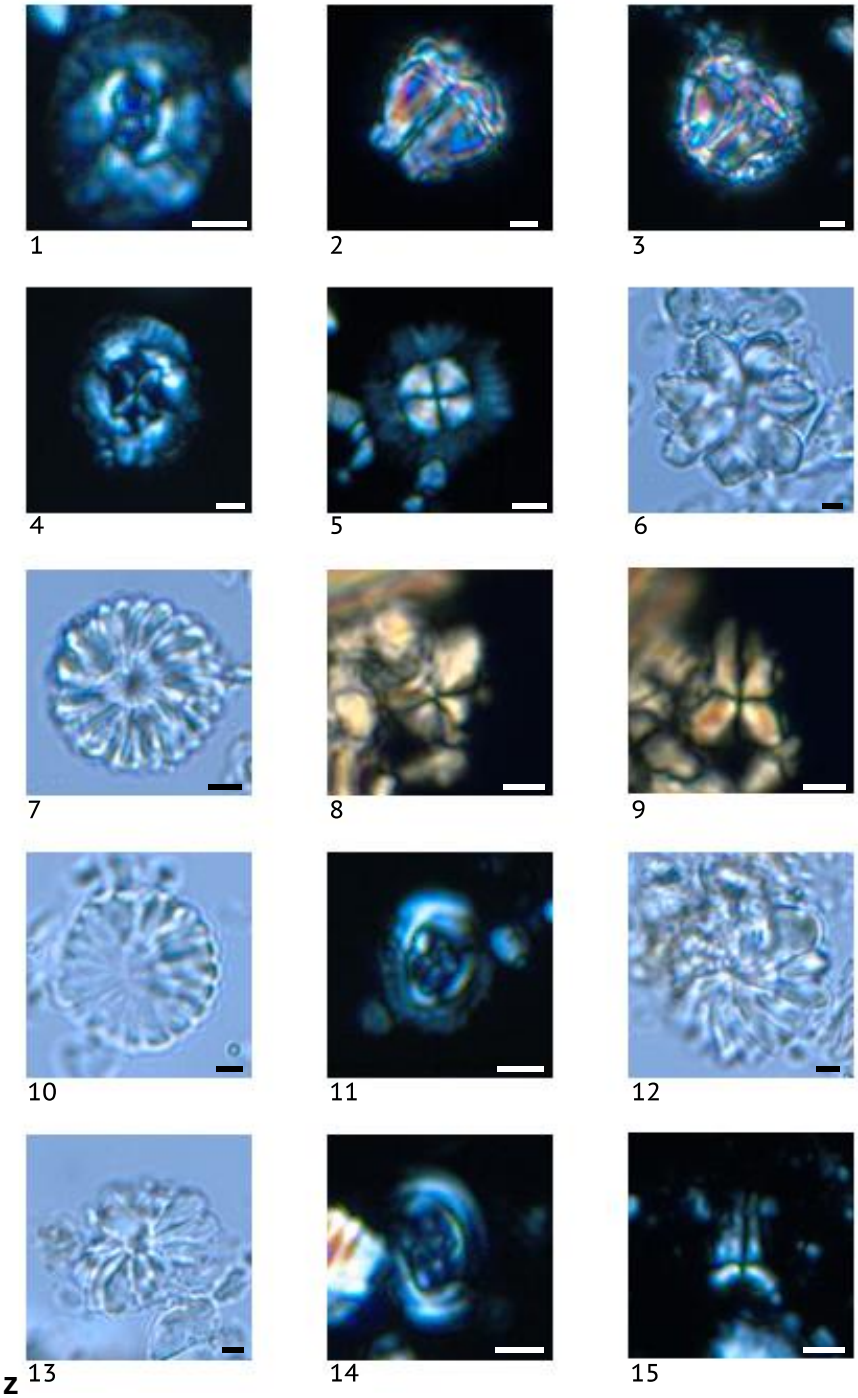

Figure 2.5: *Select nannofossils from Core A. The horizontal scale bar is 2 µm.*
1) Chiasmolithus nitidus *? Perch-Nielsen 1971, 372.6 m.*
2, 3) Lithoptychius janii *Perch-Nielsen 1971, 372.6 m.*
4) Chiasmolithus consuetus *(Bramlette & Sullivan 1961), Hay & Mohler 1967, 368.6 m.*
5) Bomolithus megastypus *(Bramlette & Sullivan 1961), Bown 2010, 170.2 m.*
6) Discoaster nobilis *? Martini 1961, 170.2 m.*
7) Discoaster multiradiatus *Bramlette & Riedel 1954, 77.7 m.*
8, 9) Sphenolithus apoxis *? Bergen & de Kaenel 2017, 77.7 m.*
10) Discoaster multiradiatus *Bramlette & Riedel 1954, 27.7 m.*
11) Campylosphaera eodela *Bukry & Percival 1971, 27.7 m.*
12, 13) Discoaster barbadiensis *Tan 1927, 16.1 m.*
14) Campylosphaera eodela *Bukry & Percival 1971, 16.1 m.*
15) Sphenolithus orphanknollensis *Perch-Nielsen 1971, 11.9 m.*

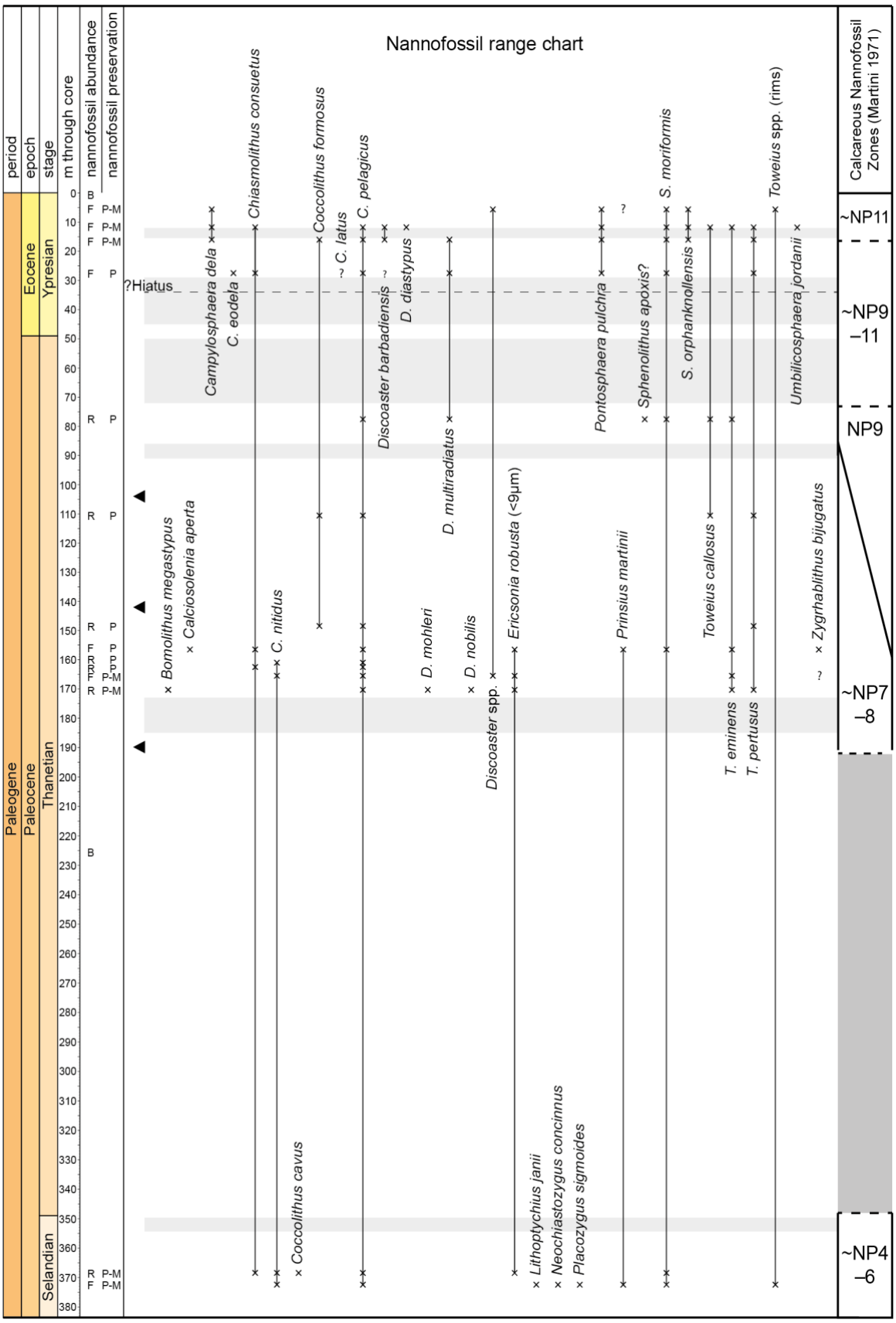

Figure 2.6: *Calcareous nannofossil range chart with estimated calcareous nannofossil zones (Martini, 1971). Other than Zone NP 9, all other calcareous nannofossil zones are approximated as the marker species for these zones are absent; discussion of the assemblages these estimates are based on is provided in Section 2.5.2.2. Grey boxes mark core gaps. Black triangles indicate location of chaotic, storm-influenced beds.*

2.5.2.3 Palynology (conducted by AS)

In the three samples analysed for palynology the main component is AOM, most likely of marine origin, with abundant organic linings of benthic foraminifera, sometimes abundant phytoclasts and only very small contributions of dinoflagellate cysts and pollen. Only one sample, at ~153 m, contains significant numbers of marine palynomorphs; these consist largely of the dinocyst genera *Operculodinium*, *Spiniferites*, *Hafniasphaera*, and *Cordosphaeridium*. The sample at 8.2 m contains mainly AOM, of a presumed dominantly marine origin due to the lack of structures assignable to components of terrestrial plants with high preservation potential, as well as increased amounts of terrestrial phytoclasts relative to the sample at 153 m. The sample at 7.4 m is dominated by AOM, with few terrestrial phytoclasts. Two dinocysts were observed in this sample, both *Polysphaeridium* spp. Detailed palynological assemblages are shown in Table 2.3.

Table 2.3: *Detailed analyses of the palynomorph assemblages from Core A. The dominant component of all three samples analysed was amorphous organic matter (AOM), likely of a marine origin.*

Depth (m)	Amorphous organic matter	Phytoclast (terrestrial)	Cuticle	Pollen	Fungal spore	Marine palynomorph	*Apectodinium* spp.	*Cordosphaeridium multispimum*	*Cordosphaeridium fibrospinosum* cpx. (pars)	*Hafniasphaera septata*	*Hystrichokolpoma* spp.	*Glaphyrocysta* cpx.	*Operculodinium* spp. cf. *centrocarpum*	*Polysphaeridium* spp.	*Spiniferites* spp.	*Dinocyst* spp.	Benthic foraminifera lining (3+ chambers)	Marine palynomorph (pars)	Reworked dinocyst
7.3	230	6				2								2					
8.2	80	35	2	1	1	22			1			1			6		8	6	1
153.3	800	10		10		94	1	7	1	4	1	2	19		3	3	50	3	

2.5.3 Bulk carbonate carbon and oxygen isotopes

The bulk carbon isotope record (Fig. 2.7e) of Core A can be split into two distinct intervals. Firstly, below 70 m the record is relatively stable, with $\delta^{13}C$ values

around +3‰ comparable to the bulk carbonate record of other late Paleogene shallow water (Zhang et al., 2017) and deep water (Barnet et al., 2019) sites. Within this lower part of the record there are two long-term cycles (occurring over 100's of metres) in the carbon isotope record with an amplitude of ~0.5 to 1‰. The first of these cycles runs from 380 m (the bottom of the core) to 200 m, with values peaking at around +3‰. The second cycle runs from 200 m to ~50 m, with values peaking at +3.5‰ at ~130 m.

Between approximately 46 m and 50 m there is a carbon isotope excursion (CIE), with values dropping rapidly (within 4 m) from +3‰ to +2‰ (Fig. 2.7e). A core gap between 27–45 m potentially cuts off a large section of the recorded carbon isotope record. The initial decrease in carbon isotope values occurs in the upper part of Zone SB 4 and between the Zones NP 9–11, suggesting this is the Paleocene–Eocene transition. Subsequent values from 27 m upwards are significantly more negative, with values from 0‰ to –1‰ recorded. These values occur in Zone NP 11, suggesting this part of the record is early Eocene in age.

The oxygen isotope record of Core A (Fig. 2.7f) is characterised by values of approximately –3.5‰ to –4.5‰. These values do not suggest that the core has been extensively diagenetically altered by interaction with meteoric water, whereby values would be much more negative (e.g., Knauth & Kennedy, 2009; Ullmann & Korte, 2015; Schobben et al., 2016). The cross-plot of pre-CIE $\delta^{13}C$ vs. $\delta^{18}O$ (Fig. 2.8) in which the R^2 value of the data is low ($R^2 = 0.0231$), indicates that there is little correspondence between these data sets, excluding a high degree of meteoric diagenesis. All the data also plot within values expected for a primary marine-derived carbonate (Arthur et al., 1983). In addition, cathodoluminescence analysis (Fig. 2.8) did not show the foraminifera or surrounding sediment to be luminescent, which would be an indication of possible alteration. Mg/Ca ratios from ICP-OES analysis are slightly higher than average values for a normal marine-derived carbonate (average Core A bulk sediment values of 29.6 mmol mol^{-1}; Appendix 7.5). However, this can be explained by the high abundance of echinoid fragments as seen in the LBF biostratigraphic log (Fig. 2.3) which have a naturally high Mg/Ca ratio (Riechelmann et al., 2018; Ullmann et al., 2018). Shell remains of echinodermata typically rapidly

recrystallise to low-Mg calcite, supplying excess Mg to diagenetic fluids which in turn would likely favour the formation of Mg-enriched carbonate cements.

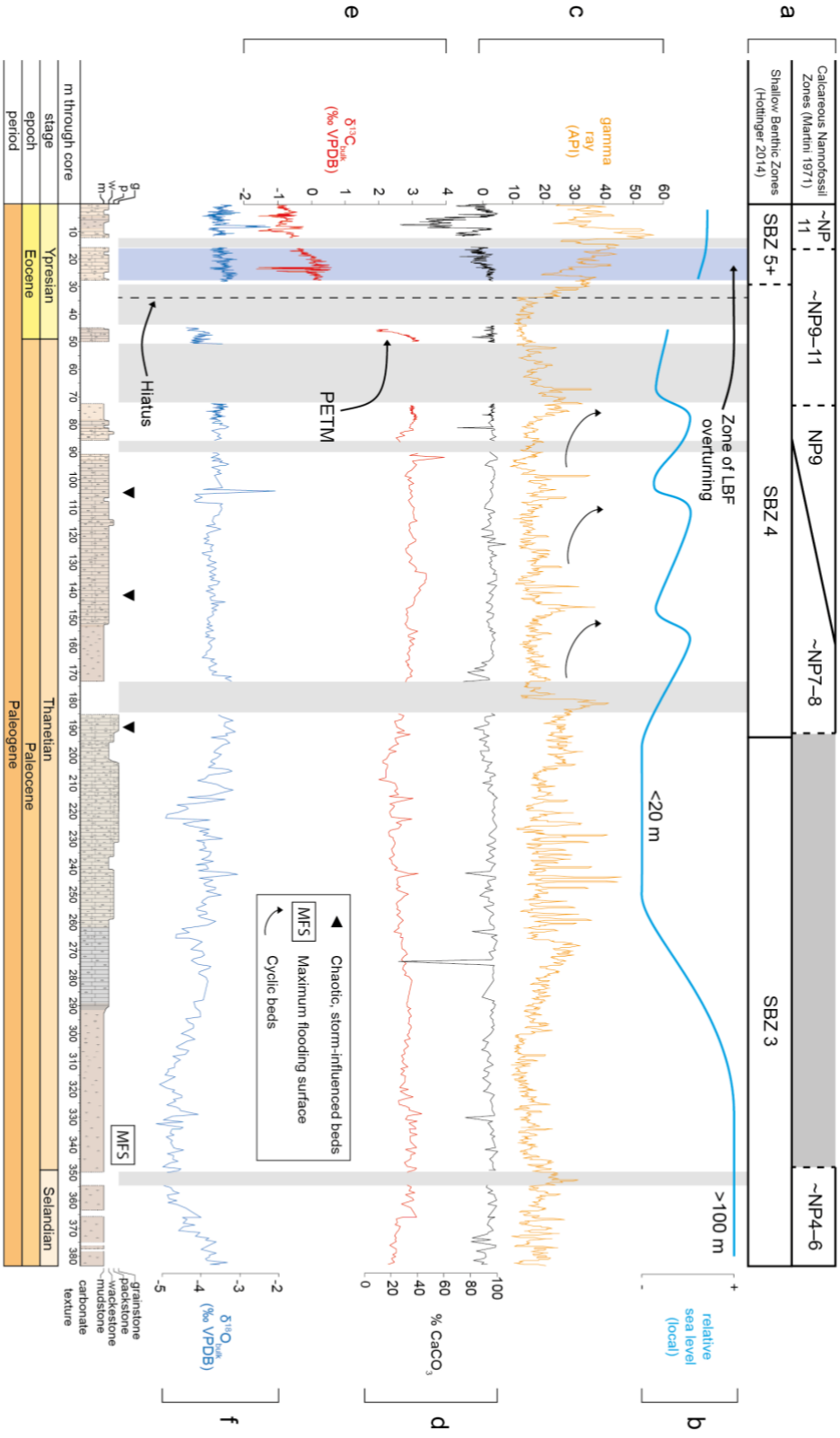

Figure 2.7: *(a) SBZ and calcareous nannofossil zonations; (b) Relative sea level curve derived from sedimentology and palaeoecology of faunal assemblages; (c) Gamma ray*

data from wireline log; (d) %$CaCO_3$; (e) Bulk carbonate carbon isotopes; (f) Bulk carbonate oxygen isotopes. Blue box depicts zone of turnover in LBF record (Section 2.5.2.1 and 2.6.2). Grey box indicates core gap within which hiatus/condensation occurs, with dashed black line indicating possible of hiatus location based on rapid increase on the gamma ray record (Section 2.6.1).

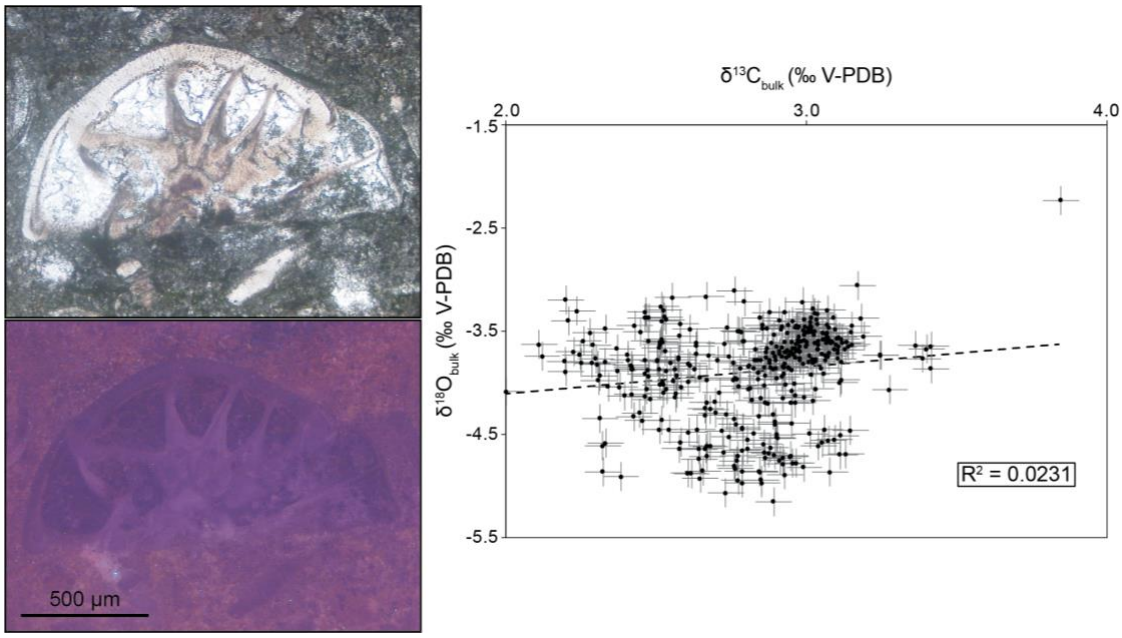

Figure 2.8: *Left hand side shows reflected light vs. cathodoluminescence images of* Lockhartia *sp. (taken from sample at ~0.2 m) showing little luminescence within LBF or surrounding sediment. Right hand side shows $\delta^{13}C$ vs. $\delta^{18}O$ cross-plot of pre-CIE values (below ~70 m), which shows a low R^2 value thus suggesting meteoric diagenesis has not affected the bulk isotopic values in a systematic manner. Error bars are 2sd of the standard CAR (Table 2.1).*

2.5.4 Percentage calcium carbonate

Percentage calcium carbonate values are generally very high and stable throughout the majority of the core, fluctuating between ~80–100% (Fig. 2.7d). There does not seem to be a close correspondence between described lithology as displayed in the sedimentary log and %$CaCO_3$, with all lithologies clearly dominated by carbonate phases regardless of texture and fossil content. There is a significant drop in average %$CaCO_3$ between 5–10 m, with values reaching as low as ~30%, indicating a terrigenous fraction dominates the sedimentology towards the very top of the core.

2.5.5 Gamma ray

The gamma ray record shows a degree of variability, with values ranging from ~10–55 API, but with most values between ~10–40 API throughout the majority of the core below 35 m. Average values increase to ~30–50 API at the top of the core between ~0–35 m. There appears to be cyclicity in certain parts of the record, particularly between ~180 and 70 m, where ~3 cycles can be visually identified with a wavelength of ~30–40 m (Fig. 2.7c). A sharp change in gamma ray values at ~35 m suggests this may be the location of a hiatus.

2.6 Discussion

2.6.1 An integrated age model for the late Paleocene to early Eocene of the central UAE

LBF biostratigraphy (e.g., the SB Zone scheme) is critically important for providing age models in Paleogene-aged shallow water strata, which form extensive hydrocarbon reservoir rocks in the Middle East. Other marine taxa, such as calcareous nannofossils or planktonic foraminifera, are often absent due to differing environmental preferences. As a result of this mutual environmental exclusion of other taxa, it is often difficult to tie LBF biostratigraphy to global stratigraphy, which is key for correlating the stratigraphy of the deep and shallow water domains and for understanding responses to global climatic events. Exceptionally, in the new Core A section we have records of both LBF and calcareous nannofossil biostratigraphy from the same samples, as well as high resolution chemostratigraphy, which allows for correlation to global stratigraphy (Fig. 2.9) and estimation of sedimentation rates (Fig. 2.10).

In order to tie local and global, shallow and deep water stratigraphies together it is important to analyse variations in species ranges between localities. Improved knowledge of such discrepancies will allow for more precise and robust age models to be constructed based upon biostratigraphic horizons. In general, the LBF assemblages in this study are in good agreement with other published literature from the Arabian Plate region (e.g., Pignatti et al., 1998; Serra-Kiel et al., 1998; Hottinger, 2014) and are consistent with carbon isotope stratigraphies

developed from deep sea records through this interval (Fig. 2.9 and Barnet et al., 2019). The broad trend, of more positive $\delta^{13}C$ values in the late Paleocene and more negative values in the early Eocene, is coherent between the ODP Site 1262 reference section and the new Core A record, although there are discrepancies in the fine detail. Offsets in absolute values between the deep sea and shallow water bulk carbon isotope records (Fig. 2.9) may be influenced by the differing composition of biogenic carbonates in the shallow and deep sea (e.g., differing proportions of carbonate-secreting taxa), or differing isotopic compositions of the (bottom) waters due to the relative age and organic matter content of the water masses (Sluijs & Dickens, 2012). Further to this, discrepancies in trends between the two bulk carbonate records could be due to a number of factors; for example, the two sites are from different ocean basins (ODP Site 1262 is from the South Atlantic) and coeval carbon isotope records from different regions are rarely exactly the same due to differences in oceanic setting and productivity (e.g., Giusberti et al., 2007; Cramer et al., 2009; Westerhold et al., 2011; Slotnick et al., 2012; Agnini et al., 2016). The composition of the bulk material also differs, with ODP Site 1262 sediments composed of a nannofossil-foraminifera ooze with minimal diagenetic overprint, while Core A sediments are composed of both macro- and microfossil material with significant diagenetic cements in places. Finally, the two sites represent deposition at very different palaeodepths; Paleocene–Eocene-aged sediments at ODP Site 1262 were deposited at ~3000–3500 m water depth, while coeval sediments at Core A were deposited in <100 m water depth. The potential differences in effects of burial and diagenesis in such different settings cannot be discounted. Alternative age models, based on tying the $\delta^{13}C$ data between the sites more closely, yielded unrealistic sedimentation rates and do not agree with the LBF biostratigraphy of Core A, therefore they are not taken as the preferred option here (see Appendix 7.3 for further discussion).

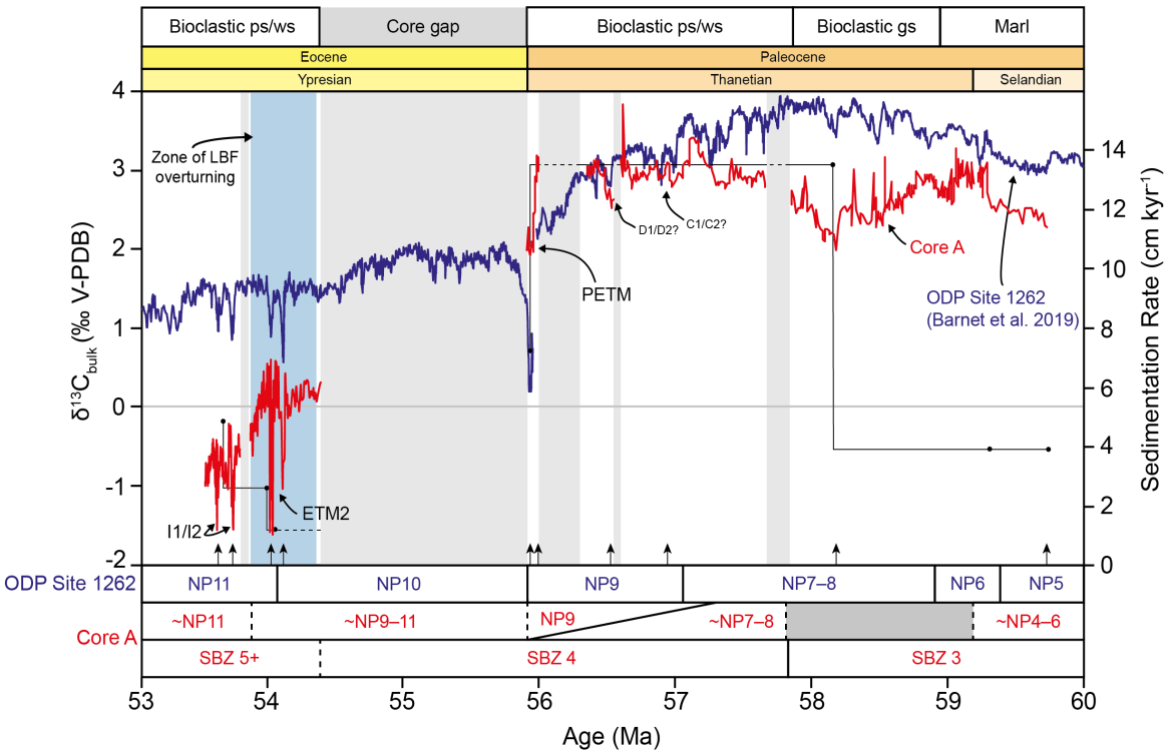

Figure 2.9: *Carbon isotope data from Core A (red) placed onto the latest orbitally-tuned age model by comparison to bulk carbon isotope data from South Atlantic ODP Site 1262 (blue; Barnet et al., 2019). Constraints from biostratigraphy (primarily calcareous nannofossils) and matching of characteristic shapes in the $\delta^{13}C_{bulk}$ record have been used to tune the Core A record. Sedimentation rates are shown with black circles and solid/dashed black lines. Tie points used to create the age model are shown with vertical black arrows. For further details on tie points and construction of this age model see Appendix 7.3. The calcareous nannofossil zonations of both records are shown in red (Core A) and blue (Barnet et al., 2019), along with the Core A shallow benthic (SB) zonations. Core gaps are shown with grey boxes. Note the gap in data between ~54.4 to ~55.8 Ma (grey shaded area), which is partly the result of a coring gap in the Core A record, and partly the result of an apparently genuine hiatus/sedimentary condensation in this record. Potential hyperthermal events captured in the Core A record are annotated. Facies types are shown at the top of the figure: ps = packstone; ws = wackestone; gs = grainstone.*

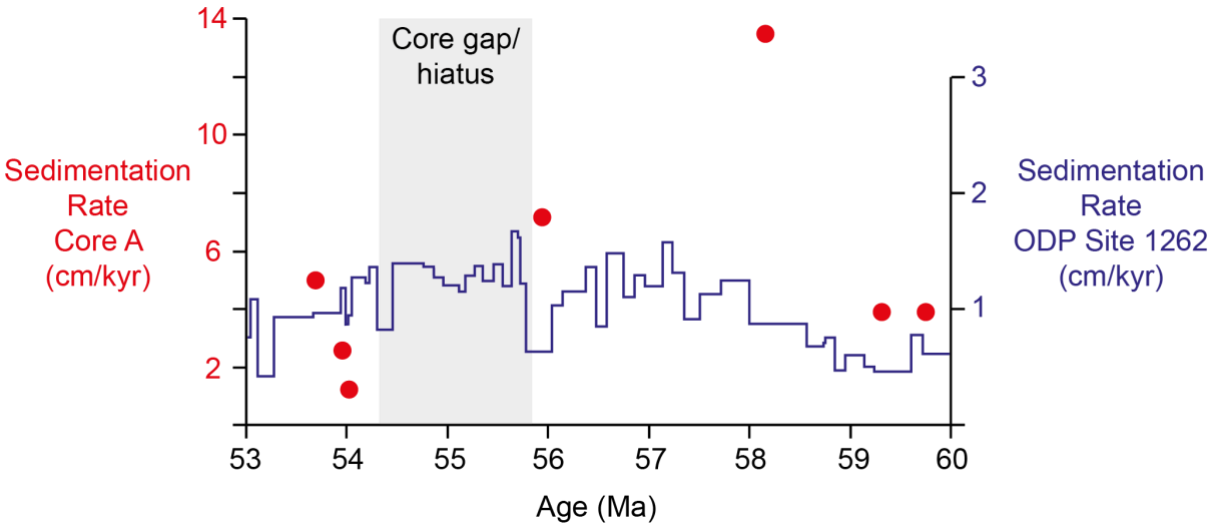

Figure 2.10: *Core A sedimentation rates in red circles calculated by tying the Core A stratigraphy to that from orbitally tuned deep sea ODP Site 1262 (Fig. 2.9). The high-resolution sedimentation rates of South Atlantic ODP Site 1262 (Barnet et al., 2019) are shown with a blue line. Site 1262 data shows an increase into the early Eocene, after the decline at the PETM. A relative increasing trend in the early Eocene observed in the Core A record.*

The late Paleocene Zone SB 3–4 boundary within Core A is no younger than the calcareous nannofossil Zone NP 8 (Fig. 2.9). This agrees in general with the correlation in previous studies (Serra-Kiel et al., 1998; Scheibner et al., 2005) where the Zone SB 3–4 transition occurs at the end of Zone NP 8. However, results from this study place the Zone SB 3–4 boundary in the middle of Zones NP 7–8 rather than at the end (Fig. 2.9). Due to the uncertainty in the nannofossil stratigraphy at Core A, we consider this to be consistent with previous studies.

Previous studies from the Arabian Plate region (Serra-Kiel et al., 1998; Scheibner et al., 2005) place the Zone SB 4–5 boundary younger than Zone NP 8–9 boundary; however, in this study the Zone SB 4–5 boundary is located after the first occurrence of *Discoaster multiradiatus* (base of NP 9) and within the Zones NP 9–11. Some difficulties arise when positioning the Zone SB 4–5 boundary primarily due to the occurrence of a hiatus/condensation in the sedimentary sequence (discussed below; Fig. 2.9). This problem is confounded by the lack of some Arabian Plate Eocene marker species and genera in the assemblage, such as the alveolinids (cf. Serra-Kiel et al., 1998; Scheibner & Speijer, 2009). This could be due to Core A recording a relatively deeper shelf environment over this transition, indicated by the presence of *Nummulites* spp. and *Assilina* spp. which are thought to have resided below fair-weather wave base (Racey, 1995). The

precise location of the Zone SB 4–5 transition, and its correlation to the calcareous nannofossil biozones, is important when discussing the PETM and the larger foraminifera turnover (LFT) event. Whether the LFT coincides with the PETM (Pujalte et al., 2009; Scheibner & Speijer, 2009) or predates the PETM (Hottinger, 1998; Zhang et al., 2013b) is important for the applicability of the global stratigraphic horizon that the LFT creates, as well as the mechanisms driving the LFT. If, for example, the LFT denotes the Zone SB 4–5 transition, which in turn correlates to Zone NP 9, this creates a correlative surface across the breadth of Tethyan fauna as well as an easily recognisable change on which to base the biostratigraphy of the region. Results from this study suggest that the LFT event can be utilised to define the Zone SB 4–5 transition, which in turn correlates to calcareous nannofossil Zones NP 9–11 (Fig. 2.9).

Further to these potential discrepancies in biozone boundary correlations, the biostratigraphic ranges of some species at this site are different to those suggested in published literature (Fig. 2.11). In Core A the ranges of *Lockhartia praehaimei*, *L. roeae*, *Kathina selveri*, *Dictyokathina simplex*, *Daviesina tenuis*, and *Thomasella labyrinthica* extend to younger ages than previously recorded in literature from the Arabian Plate region (Pignatti et al., 1998; Serra-Kiel et al., 1998; Hottinger, 2014). *Miscellanea "rhomboidea"* and *Mardinella daviesi* extend into older strata than currently recorded (Pignatti et al., 1998). Proposed expansions to these species biostratigraphic ranges are shown in Figure 2.11. These differences in ranges of some species could be due to a number of reasons, for example, variability in local environmental conditions, diachroneity of speciation/extinction, or incomplete outcrop sections. Shallow, reef associated LBF assemblages today are typically regionally heterogenous, with significant differences in the dominant taxa present (Hallock, 1984; Hallock & Glenn, 1986). This heterogeneity seems to be largely depth controlled, due to subsequent differences in light and nutrient availability, water energy, and substrate (Hottinger, 1983). It is such spatial variability in LBF records that necessitates the application of integrated stratigraphic techniques and investigation of a range of localities.

All three stratigraphic indicators suggest there is a hiatus or sediment condensation in the core gap between 27–45 m (Fig. 2.9), as evidenced by

missing biozones and the step change in carbon isotopes to significantly more negative values (Fig. 2.7e). The core gap itself results in ~1.4 million years of strata missing, with the possible hiatus/condensation within this core gap totalling an unknown amount of this time. The precise location of the hiatus within the core gap may be ~34 m, as denoted by the rapid increase in the (continuous) down-hole gamma ray values. Importantly, the initial drop in carbon isotopes ratios between 46–50 m occurs within a core section where there is no sedimentological evidence for a hiatus. This suggests we have captured one of the late Paleocene hyperthermal events, most likely the PETM CIE based upon reasonable estimates of sedimentation rates in such settings as well as the sedimentological and LBF biostratigraphic evidence (Fig. 2.9).

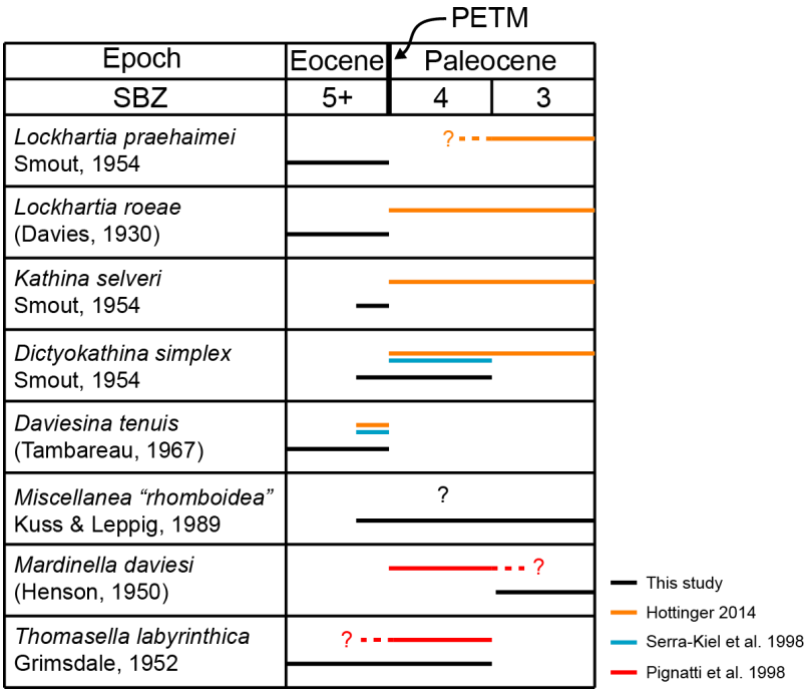

Figure 2.11: *Differences in biostratigraphic ranges between Core A and published literature.*

2.6.2 Paleocene–Eocene palaeoenvironmental and biotic trends

The late Paleocene sedimentary sequence preserved in Core A is indicative of a shallow (<100 m), low-energy, storm-dominated epeiric platform setting (Tucker & Wright, 1990; Sharland et al., 2001) within the easternmost Paleogene Tethys Ocean (Fig. 2.1). Through the late Paleocene at this site there was a broad-scale change in the biotic assemblage, occurring across a number of genera, coupled to changing palaeoenvironmental settings. The lowermost facies (285–383 m) of

marl is likely to represent a relatively deeper water (Fig. 2.7a), low energy environment, below storm wave base, as indicated by the presence of thin-shelled bivalves and rare or absent photosynthetic organisms such as corals or LBF. This is interpreted as being locally representative of the regional maximum flooding surface recognised at ~59.5 Ma (re-calibrated to GTS2012; Fig. 2.7a) (Sharland et al., 2001; Haq & Al-Qahtani, 2005); this is supported by the sedimentation rate through this interval being among the lowest in the record (Fig. 2.10; ~3.9 cm kyr^{-1}), which agrees well with the observed sedimentological sequence.

As the shallower water facies prograded over these deeper water sediments, shallow water fauna including solitary corals, gastropods, bivalves, and LBF became abundant (~185–260 m). This fauna represents a diverse shallow water reef assemblage, a highly productive “carbonate factory” likely deposited at <15 m water depth (cf. Tucker & Wright, 1990). Sedimentation rates through this time increase significantly up to ~13.5 cm kyr^{-1} (Figs. 2.9 and 2.10). This is interpreted as the Arabian Plate carbonate platform prograding out into the adjacent deeper water Muthaymimah Trough sub-basin to the north-east (Fig. 2.1b). Progradation occurs due to rapid subsidence in this region during the early Paleogene initiated by the cessation of Semail ophiolite obduction to the east (Ziegler, 2001). This rapid tectonic deepening is also enhanced by eustasy (Sharland et al., 2001). As the carbonate platform filled the available accommodation space, with inferred accelerating carbonate production, an overall shallowing-up sequence is observed. From ~173 m upwards a series of cyclic shallowing-up parasequences are observed in both the sedimentology and the gamma ray signal (Fig. 2.7). Three cycles can be observed in the record with a wavelength of ~30–40 m. The top of each parasequence is marked by a chaotic, storm-influenced bed with broken bioclasts (Figs. 2.3 and 2.7), due to a relative decrease in sea level, bringing Core A to above storm-wave base, suggesting these may be a series of 4^{th} order sea level cycles. From the orbitally tuned age model (Fig. 2.9) these cycles cover ~57.6 Ma to 56.3 Ma, a period of approximately 1.3 Myr, making these cycles roughly 400 kyr in duration. As such, these cycles could reflect the long eccentricity (405 kyr) cycle. High-resolution orbitally tuned stable isotope records from the late Paleocene of the South Atlantic (Zachos et al., 2010; Littler et al., 2014; Barnet et al., 2019) and Pacific Ocean (Westerhold et al., 2008) show

long eccentricity as the dominant frequency expressed in both climate and carbon-cycle records.

From ~152 m upwards in the core there is the systematic loss of corals and gastropods (Fig. 2.3). This gradual transition through the core, with the loss of the diverse biotic assemblage but increases in LBF diversity, suggests that the environment became more favourable to the rapidly calcifying LBF (Scheibner et al., 2005). This could be forced by a number of factors, such as an increase in nutrient input disturbing the previously stable oligotrophic environment and creating a more meso- to eutrophic environment (Scheibner & Speijer, 2008b; Zamagni et al., 2008), or increases in pCO_2 through this interval adversely affecting the growth of calcareous macro-organisms (Shirayama & Thornton, 2005). Alternatively, this gradual change could be due to an overall deepening in the sequence, losing the diverse fauna present on the reef and moving towards an open shelf setting (Hallock & Glenn, 1986). This latter hypothesis is supported for the upper part of the core, after the core gap (Fig. 2.3), by the presence of generally deeper dwelling nummulitids (Racey, 1995).

2.6.2.1. The Paleocene–Eocene transition

The partial record of the PETM onset recovered within Core A spans ~4 m of stratigraphy and is therefore relatively expanded compared to many other PETM records from deeper water sites. Such expanded PETM sections have also been recorded in other marginal marine sites, such as Svalbard (Cui et al., 2010), the New Jersey margin (Zachos et al., 2006; Sluijs et al., 2007; Kopp et al., 2009), the Northern Tethys (Giusberti et al., 2007), and Tibet (Zhang et al., 2017). Unlike deep sea records, this very shallow marine (~<20 m water depth) environment is unaffected by shoaling of the carbonate compensation depth (CCD). Over the expanded section of the PETM onset, high resolution sample intervals (approximately every ~0.8 m; Fig. 2.3) allow us to assess changes in the LBF assemblage during this interval. Despite a major perturbation to the carbon cycle shown by the rapid decline in carbon isotope values (Fig. 2.7e) the LBF assemblage is stable throughout this 4 m of stratigraphy (Fig. 2.3), with 9 of the 11 species present in the latest Paleocene also present after the Paleocene–Eocene boundary. The two exceptions are *Discocyclina* sp. and *Miscellanea* sp.,

with last occurrences at ~47 m; however, as this is the start of the coring gap it could be that the continued record of these genera has not been captured.

Above the hiatus/condensation in sedimentary deposition, occurring in the core gap between 27–45 m (Fig. 2.7; likely ~34 m), the sediments are likely within Zone NP 11, correlating to the early Eocene. After the core gap, carbon isotope values decrease further from 0‰ to –1‰. These values, therefore, likely represent the decline towards the early Eocene climatic optimum (EECO; ~52–50 Ma), the peak of Paleogene warmth (Zachos et al., 2001a; 2008; Cramwinckel et al., 2018). Prior to the EECO there are a number of orbitally paced hyperthermal events observed in the carbon isotope record, on the order of ~–1‰ (Cramer et al., 2003; Zachos et al., 2010; Littler et al., 2014; Barnet et al., 2019). Within the Core A record there are three CIEs stratigraphically above 27 m. These occur at 23 m, 10 m, and 4 m and are –1.5‰, –1‰ and –0.8‰ in magnitude, respectively. Located within Zones NP 9–11, it is likely that these negative excursions are expressions of hyperthermal events, such as Eocene thermal maximum 2 (ETM-2 at ~53.7 Ma; Lourens et al., 2005; Stap et al., 2010). As with the PETM interval at this site, there would be no expected dissolution during these events due to the shallow shelf setting located far above the CCD. Calculated sedimentation rates here fit with this interpretation; approximate average rates of 2.9 cm kyr^{-1} at the top of the core (Figs. 2.9 and 2.10) would equate to the top 27 m the core covering a ~925 kyr period from ~54.4 Ma, which is the time period and scale on which these hyperthermals occur (Barnet et al., 2019).

There is no increase in gamma ray values throughout the putative PETM interval (Fig. 2.7c), commensurate with the LBF evidence for a relatively stable local environment during this time. However, there is a significant increase in gamma ray values after the hiatus/sedimentary condensation (~30 m) within the coring gap and into the early Eocene (Fig. 2.7c). As gamma ray values represent the combined abundance of radioactive K, U and Th, an increase is indicative of either an increase in organic matter within the sediments, or of increasing clay content in the core (Bigelow, 2002), both of which can contain incorporated radioactive elements. There is no evidence for glauconite in the core, which can also elevate total gamma ray values through elevated K content (e.g., Hesselbo,

1996). The %$CaCO_3$ values through this interval also decrease (Fig. 2.7d), potentially due to dilution from increased terrigenous input (Slotnick et al., 2012). Taken together, these trends suggest that through the early Eocene interval prior to the EECO, there may have been increased humidity and/or rainfall in this part of the Arabian Peninsula. This humidity could have caused either enhanced input of riverine transported clay material derived from the areas of emergence to the east and west of the Core A locality (Fig. 2.1), and/or elevated organic matter burial through increased nutrient-driven algal productivity potentially coupled with increased anoxia. The former argument is supported by the increase in abundance of terrestrially derived phytoclasts, most likely dominantly river transported, in the sediments during the early Eocene (~8 m; Table 2.3) relative to the late Paleocene (Hollis et al., 2005; Slotnick et al., 2012). Calculated sedimentation rates through this interval also show an increase from ~1.2 to 5 cm kyr^{-1} (Fig. 2.11), which is consistent with elevated terrestrial input in this setting. This matches trends seen in open ocean sites, such as ODP Site 1262 in the South Atlantic (Barnet et al., 2019), and shelf sites, such as Mead Stream in New Zealand (Slotnick et al., 2012), where sedimentation rates also show an increase into the Eocene.

2.6.3 Response of shallow marine biota to Eocene warmth

Following the PETM CIE there is a gradual turnover in the LBF assemblage at Core A, within a broadly consistent lithology suggesting the depositional environment is largely unchanging. The larger foraminifera turnover (LFT) event is preceded by a major perturbation to the carbon cycle and elevated terrestrial input to the Core A site. Despite these perturbations to the environment, during the PETM onset the LBF assemblage is stable (Fig. 2.3), with the turnover occurring later in the early Eocene. This suggests long-term warming into the early Eocene may have been the trigger for the LFT, rather than the PETM itself. From ~16 m to ~27 m, above the core gap, there is a step-change in the assemblage, with an increased dominance of less-specialised and smaller fauna that are better able to inhabit/colonise perturbed environments, and/or are more tolerant to a wider range of oceanographic conditions. Examples of such genera include *Rotalia* spp. and *Sakesaria* spp. (Fig. 2.3). Through the early Eocene interval there is also an increase in the genera and species richness of the LBF

assemblage. One way to facilitate increases in species diversity is known in modern ecology as the intermediate disturbance hypothesis (IDH). The IDH theory suggests that when there is increasing ecological disturbance to an environment there may also be increasing species diversity (Townsend et al., 1997). Once an intermediate level of disturbance is reached both rapid opportunistic colonisers and species which are more competitive are able to co-occur (Townsend et al., 1997). The changes observed in the Core A LBF assemblage, from 16–27 m, could therefore be due to an intermediate level of disturbance to the environment having been reached, creating a "sweet spot" for increased biodiversity. This increase in genera and species richness over the Paleocene–Eocene interval is also seen in other areas of the shallow Tethys Ocean (Scheibner & Speijer, 2008b). Known as the *Lockhartia* Sea (Hottinger, 2014), this was a biogeographic region defined by increased generic diversity in "hot spots" (geographic regions of maximum biodiversity in a given time interval) which migrate around the Paleogene Tethys Ocean (Fig. 2.12) (Renema et al., 2008; Hottinger, 2014). Prior to the PETM, the environment was characterised by stable, low-diversity conditions, as demonstrated by the relatively unchanging sediments (Fig. 2.3), LBF assemblage, and the dominance of *Cibicides* spp. in the smaller benthic foraminiferal assemblage (Boscolo-Galazzo, pers. comm.). The disturbance to the ecosystem precipitated by the PETM, and likely continuing into the early Eocene (section above the core gap) may have triggered the concurrent increase in diversity and dominance of LBF.

Table 2.4: *Summary table of changes in specific- and generic-level diversity changes through time described in the text.*

Location	Number of genera/species	Approximate age	Reference
Oman	8 genera	mid to late Paleocene	Serra-Kiel et al. 2016a
UAE	9 genera, 9 species	late Paleocene	This study
UAE	11 genera, 16 species	early Eocene	This study
Oman	18 genera	mid Eocene	Serra-Kiel et al. 2016a
South east Arabian Plate	5–8 genera	mid Eocene	Renema et al. 2008
Western India	29 species	Eocene	Cotton et al. 2019
Western India	2 species	Oligocene	Cotton et al. 2019
South east Arabian Plate	9–12 genera	Miocene	Renema et al. 2008

A number of studies have measured LBF diversity or species richness on or near the Arabian Plate during the Paleogene; however, estimates of generic and

specific level diversity vary across locations (Table 2.3). In the mid to late Paleocene the number of LBF genera in Oman was shown to be n=8 (Serra-Kiel et al., 2016a), increasing to n=18 in the mid-Eocene (Serra-Kiel et al., 2016b). In the nearby offshore India province the number of species/morphotypes in the Eocene was measured at n=29, with this significantly decreasing to n=2 in the Oligocene, although few Oligocene samples were available (Cotton et al., 2019). Contrary to these estimates Renema et al. (2008) suggest that the number of genera in the south-eastern Arabian Plate was as low as n=5–8 in the mid Eocene, increasing to its maximum of n=9–12 in the Miocene. This study suggests that the modern hotspot in the Indo-Pacific region evolved due to the eastward movement of generic level alpha biodiversity (number of genera in a single location) from the Tethys in the middle Eocene (Fig. 2.12 and Renema et al., 2008). Our data from the UAE suggests that the increase in generic and species richness in this region actually began as early as the early Eocene (Fig. 2.12), which is in agreement with other more recent studies from the broader region (Serra-Kiel et al., 2016b; Cotton et al., 2019). It has been suggested that changes in tectonic configuration of continents, creating and destroying numerous shallow water habitats, is the main driving force behind these changes in biodiversity (Renema et al., 2008). However, the timing of these biodiversity increases, coincident with or following on from the PETM both in this study and others, suggests that early Eocene climate could have been a contributing factor in the upward trajectory of biodiversity (Orue-Etxebarria et al., 2001; Pujalte et al., 2009; Scheibner & Speijer, 2009).

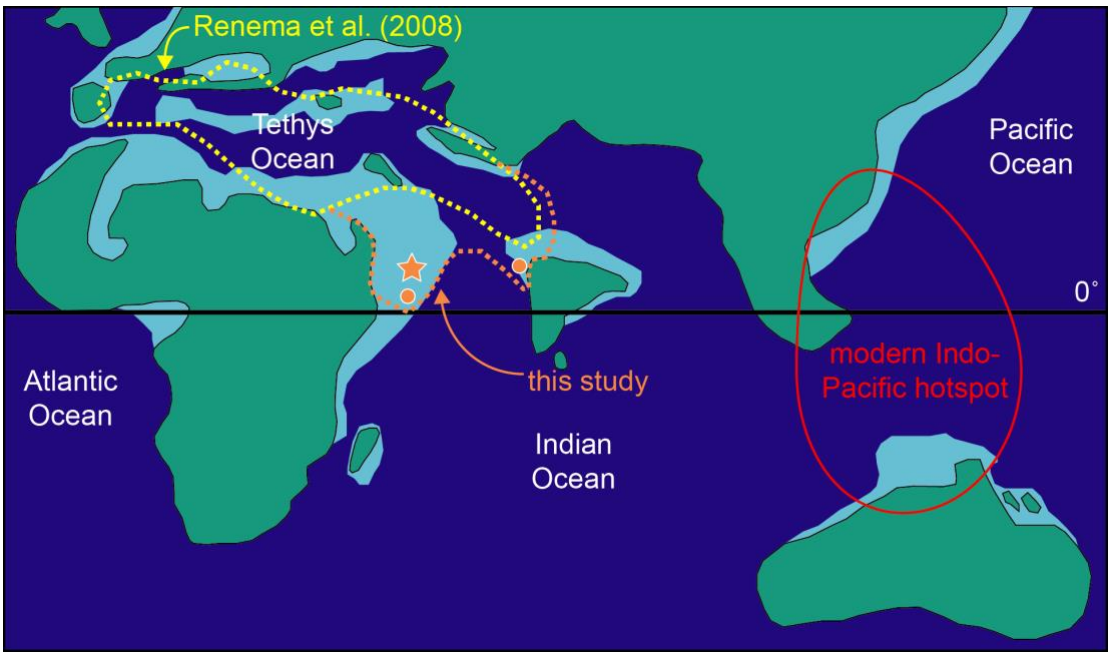

Figure 2.12: *Cartoon adapted from Renema et al. (2008) to demonstrate the extensions of the proposed hotspots through the early–middle Eocene. Yellow dashed area denotes the middle Eocene hotspot from Renema et al. (2008), orange dashed area denotes extension of this hotspot in the early Eocene from this study (orange star) and others (orange circles: Serra-Kiel et al., 2016a; Cotton et al., 2019). Red solid line indicates area of modern hotspot in the Indo-Pacific (Renema et al., 2008).*

2.6.4 The early Paleogene vs anthropogenic climate change in the shallow water realm

The results of this study suggest that the shallow water LBF community was able to turnover and subsequently thrive throughout the extreme warming experienced over the early Eocene, becoming the dominant shallow water carbonate producers of the Eocene (Scheibner & Speijer, 2008a; Afzal et al., 2011; Zamagni et al., 2012). There are, therefore, implications for the future of shallow water environments with continued anthropogenic climate change and ocean acidification. For example, will there be a shift of the dominant carbonate producers? Will modern coral reefs be replaced by a diverse fauna of LBF? Larger foraminifera at present produce 2.5% of the total $CaCO_3$ in the oceans (Langer, 2008). They are therefore important for the global climate-carbon cycle and constitute a substantial carbon sink in the shallow oceans.

Short-term (maximum 6 weeks) lab experiments suggest that LBF are unaffected by pH decrease (acidification) and temperature increase, in some cases even displaying an increase in growth yields under these conditions (Hikami et al.,

2011; Vogel & Uthicke, 2012; Prazeres et al., 2015). On the long-term, however, the effects are markedly different. In both lab and field experiments long-term changes to pH or temperature had major negative effects upon the LBF communities, with the highest impact observed in lab experiments when temperature increase and acidification acted in unison (Schmidt et al., 2014). Alternatively, in field studies conducted on shallow benthic communities close to volcanic CO_2 seeps indicate an inability to tolerate pH < 7.9. At current rates of CO_2 injection into the atmosphere, this suggests that ocean acidification will reach a threshold of major extinctions in the shallow water benthos community by 2100 (Uthicke et al., 2013). Over this long-term, coral reefs also show major disruption as a result of acidification and increased temperatures (Fabricius et al., 2011), similar to the negative effects observed in the Paleocene (Scheibner & Speijer, 2008a). Ultimately, this comparison shows us that rate of change is likely key when assessing the ability for shallow water benthos to adapt. However, with anthropogenic climate change being orders of magnitude faster than changes that occurred during the early Eocene or even the PETM, it is problematic to use the two as direct analogues for the near future.

2.7 Conclusions

Integrated LBF and calcareous nannofossil biostratigraphy and carbonate stable isotope chemostratigraphy from this easternmost Tethyan site show a step-wise shift in palaeoenvironment from the late Paleocene into the early Eocene. The Paleocene strata in this region record a relatively stable time period in terms of climate, oceanography, and palaeoenvironmental setting, allowing a diverse shallow water (<100 m) biotic assemblage to thrive through the late Paleocene. The local response to globally warmer temperatures during the Paleocene to Eocene involved the systematic loss of corals, gastropods, and bivalves. Further to this, the LBF assemblage underwent turnover in the early Eocene, with smaller and less specialised genera such as *Rotalia* spp. and *Sakesaria* spp. outcompeting the previously dominant Paleogene genera (Figs. 2.3 and 2.7). It is hypothesised that the perturbations to ocean and atmosphere temperature, the carbon cycle, run-off, and nutrient input through the early Eocene were the trigger for an increase in generic and specific level diversity at this site and others in the eastern Tethys Ocean. This was the beginning of the generic biodiversity hotspot

that developed through the Paleogene and Neogene in the Tethys, moving eastwards to its present-day hotspot in the Indo-Pacific (Fig. 2.12). Despite the success of the larger benthic community through this major palaeoclimatic change, they do not appear to be resilient to anthropogenic climate change. It is likely that the significantly faster rate of change in pH and temperature at the present, compared to the Paleocene–Eocene, is the explanation; however, the vastly different timescale lengths pertaining to these studies are conducted does not allow for a more definite conclusion.

With an integrated record of biostratigraphy and chemostratigraphy from this region it is possible to tie a local, shallow water record to global stratigraphy through the early Paleogene interval. This record suggests that the LFT event can be correlated to Zone SB 5. This stratigraphic interval, recorded in the shallow water domain, can be tied to calcareous nannofossil Zones NP 9–11. These integrated records allow for the correlation of the shallow and deep water domains and provide important and easily recognisable stratigraphic horizons which tie directly to a bio- and chemostratigraphic age model.

Chapter 3: Liberating microfossils from indurated carbonates: comparison of three disaggregation methods

3.1 Abstract

Three disaggregation methods (Calgon, acetic acid, and electric pulse fragmentation [EPF]) have been applied to a range of heavily lithified, carbonate-rich sedimentary rock samples of Paleogene age. Samples are predominantly from the carbonate-rich, shallow water domain (<250 m palaeo-water depth) of Tanzania, Malta and the United Arab Emirates (Paleogene Tethys Ocean). The effectiveness and efficiency of each method has been compared, as well as the preservation of the resultant liberated microfossil material (primarily larger benthic foraminifera; LBF). Of the three methods, the most efficient and effective was EPF, which liberated the largest number of LBF in a very short processing time and resulted in the best preservation. Samples with calcitic, silicic, and clay matrices and cements were successfully disaggregated using EPF. In this study, recovered microfossils were largely >500 µm suggesting this technique may be more appropriate for liberating larger microfossils (e.g., LBFs). However, nuances to the method are discussed which would allow for more effective recovery of smaller microfossil specimens. The more traditional acetic acid method was also able to disaggregate a number of the samples. However, preservation of the LBF was compromised. A best practice methodology for implementing EPF in micropalaeontological studies is suggested.

This chapter is published as a paper in *Journal of Micropalaeontology* as: **Beasley, C.**, Parvaz, D. B., Cotton, L., Littler, K., 2020. Liberating microfossils from indurated carbonates: comparison of three disaggregation methods. Journal of Micropalaeontology 39, 169–181. This chapter is a reproduction of this published work (see Appendix 2).

Co-author contribution: CB conducted acetic acid and Calgon treatments, DBP performed EPF treatment. CB picked and analysed all samples using thin sections and EDS-SEM. CB and LC provided sample material. CB constructed the chapter/manuscript, with edits from DBP, LC and KL.

3.2 Introduction

Indurated carbonate-rich sedimentary rocks (e.g., limestones) are notoriously difficult to disaggregate, something that is essential when liberated microfossils are required for taxonomic or geochemical analyses. 'Traditional' methods (i.e., those well documented within current literature) used for disaggregation of deep-sea sediments, such as Calgon, cannot break apart the well cemented matrix and methods utilising stronger acids risk damaging microfossils which are themselves often composed of calcium carbonate. Alternative techniques are therefore required to liberate successfully microfossils in such indurated carbonates. The biostratigraphic study of larger benthic foraminifera (LBF) in these rocks is more commonly achieved through the use of thin sections or acetate peels, however the resultant "cut" through the rock may not allow for successful identification to specific or generic level. In order to identify LBF to species level the specimen must be orientated either on its axial or equatorial axis (Fig. 3.1). As such, liberated specimens from which individual thin sections can be made are preferred. Similarly, it is extremely difficult to identify smaller foraminifera accurately from thin sections, as various aspects of their external morphology (e.g., the surface of their tests) need to be assessed for species-level identification.

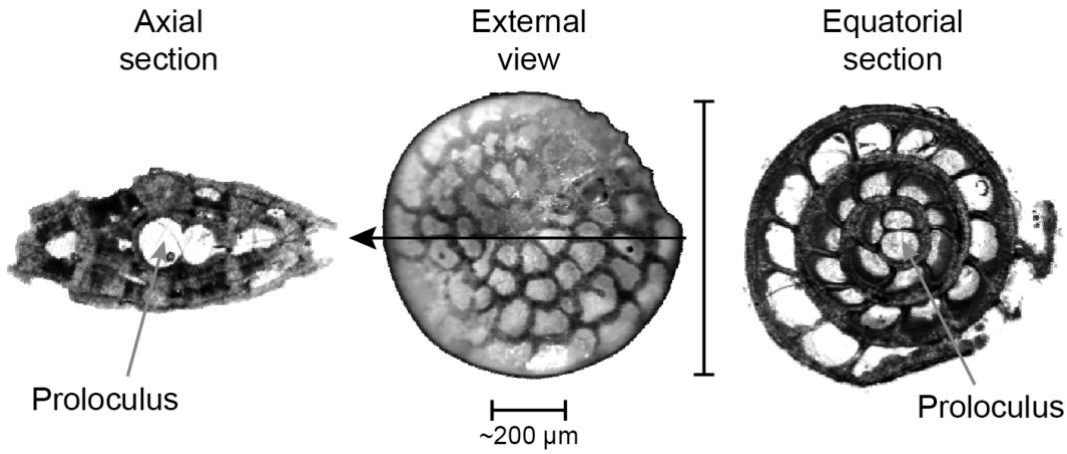

Figure 3.1: *The equatorial and axial orientation of larger benthic foraminifera thin section samples (foraminifera images from Cotton, 2012).*

The difficulty in liberating microfossils from indurated carbonates is a widespread problem which is especially ubiquitous when studying outcrop samples which have often been subjected to weathering and enhanced cementation. However,

there is a wealth of information to be gained from detailed study of ancient shallow-water carbonate settings, which are often exposed as outcrops rather than cores. As such, electric pulse fragmentation (EPF) is investigated as a possible improvement over traditional rock disaggregation techniques to aid microfossil recovery in these lithologies. Commonly used for liberation of coarse zircon grains for geochronological studies, EPF as a tool for microfossil liberation was proposed by Saini-Eidukat and Weiblen (1996); this study successfully liberated a range of microfossil (conodonts, foraminifera, juvenile ammonites, ostracods) and macrofossil (belemnite tip, fossil moulds, fish teeth) material from shales and sandstones. Liberated material was composed of moulds. Despite further industrialisation and more commercially available EPF systems, this technique has not yet been investigated further. More specifically, this method has not previously been applied to any carbonate sediments, within which micro- and macrofossil material can be abundant.

In an initial pilot study, LBF were successfully liberated from surrounding carbonate cement in one sample from the United Arab Emirates (UAE) shallow water Umm Err Radhuma formation; an indurated, bioclastic Paleogene carbonate (Parvaz et al., 2018). To test the effectiveness of EPF in LBF liberation further, it is compared against two traditional methods: Calgon and acetic acid. These two methods were chosen as they represent use of an acid (acetic acid) and a surfactant (Calgon) to disaggregate samples; these are categories into which most other disaggregation techniques fall into (Hodgkinson, 1991). They are therefore representative for comparison across a wide range of techniques. The effectiveness and efficiency of each of these methods in liberating LBF from carbonate-rich lithologies is assessed by comparing disaggregation time, percentage fossiliferous fraction, and number of liberated specimens.

3.3 Materials and methods

A total of nine field samples from strata of Paleogene age were investigated; each was subjected to disaggregation using three different techniques. Samples were collected on field campaigns in Tanzania, Malta, and the UAE; they consisted dominantly of carbonate-rich, bioclastic grainstones with extensive diagenetic cements of varying composition (Table 3.1). All samples were deposited in a

dominantly shallow water environment (<250 m) with a diverse assemblage of shallow water biota present (LBF, ostracods, bryozoans, red and green algae). Samples have undergone various stages of diagenesis and are therefore highly lithified with diagenetic cements. The details of the field samples are shown in Table 3.1. Hand specimen and thin section images are shown in Figures 3.2 and 3.3 respectively.

Table 3.1: *Details of the different samples used in this study. The details of the biota were identified in thin sections, shown in Figure 3.2.*

Sample name	Locality (latitude, longitude)	Bioclasts	Type of cement/matrix	Facies type; approximate age	References and formation names
K05	Kilwa, Tanzania (08° 55' S, 039° 30' E)	LBF (*Discocyclina* spp., *Nummulites* spp., *Assilina* spp.), complex miliolids, green algae.	Coarse-grained quartz grains within clay matrix infilling porosity.	LBF packstone; Eocene	Kilwa group, Masoko Formation (e.g., Nicholas et al., 2006)
K09	Kilwa, Tanzania (08° 55' S, 039° 30' E)	LBF (*Discocyclina* spp., *Nummulites* spp., other orthophragmines).	Fine-grained quartz grains within clay matrix infilling porosity.	LBF packstone; Eocene	Kilwa group, Masoko Formation (e.g., Nicholas et al., 2006)
K16	Kilwa, Tanzania (09° 16' S, 039° 31' E)	LBF (*Discocyclina* spp., *Nummulites* spp., *Assilina* spp., other orthophragmines).	Fine-grained quartz grains and sporadic clay matrix infilling porosity.	LBF packstone-grainstone; Eocene	Kilwa group, Masoko Formation (e.g., Nicholas et al., 2006)
L05	Near Mbanja, Tanzania (09° 52' S, 039° 44' E)	LBF (miogypsinids, lepidocyclinids, *Sphaerogypsina* spp.), red algae.	Thin calcitic meniscus cement between bioclasts. Clay lining pores.	LBF packstone; Miocene	Miocene; not formally described in literature (Nicholas et al., 2006)
LCL	Il Mara, Malta (35° 48' N, 14° 31' E)	LBF (lepidocyclinids, nummulitids).	Fine-grained secondary calcite cement. Quartz grains within clay matrix.	LBF packstone; Oligocene	Lower Coralline limestone Formation (e.g., Pedley, 1975)
JB1	Jebel Buhays, UAE (25° 01' N, 55° 47' E)	Smaller benthic foraminifera, complex miliolids.	Coarse-grained secondary calcite cement.	Bioclastic wackestone; Paleocene/ Eocene	Muthaymimah/Rus Formation (e.g., Abdelghany & Abu Saima, 2013)
JB3	Jebel Buhays, UAE (25° 01' N, 55° 47' E)	LBF (nummulitids, orthophragmines), red algae.	Primary isopachous crust, secondary fine-grained calcite cement.	Bioclastic wackestone; Paleocene/ Eocene	Muthaymimah/Rus Formation (e.g., Abdelghany & Abu Saima, 2013)
JF2	Jebel Faiyah, UAE (25° 05' N, 55° 49' E)	Smaller benthic foraminifera, algae.	Coarse-grained secondary calcite cement.	Bioclastic grainstone; Paleocene/ Eocene	Muthaymimah Formation (e.g., Nolan et al., 1990)
JH1	Jebel Hafeet, UAE (24° 03' N, 55° 45' E)	LBF (*Nummulites* spp., alveolinids), complex miliolids, smaller benthic foraminifera.	Fine-grained secondary calcite cement.	Foraminifera wackestone; early Eocene	Dammam Formation (e.g., Abdelghany, 2002)

Two traditional methods (Calgon and acetic acid) used in disaggregating carbonates were employed in order to compare against the new technique (EPF). Each of the nine bulk samples were first imaged (Fig. 3.2), and one thin section of each sample was made (Fig. 3.3). Then, three equal sized amounts of the rocks were broken off from each sample. The resultant amount was dependent

upon the initial size of the sample, but each was at least 20 g. Once the samples were disaggregated using each of the three methods below a selection of liberated microfossil material from each method was imaged using a scanning electron microscope.

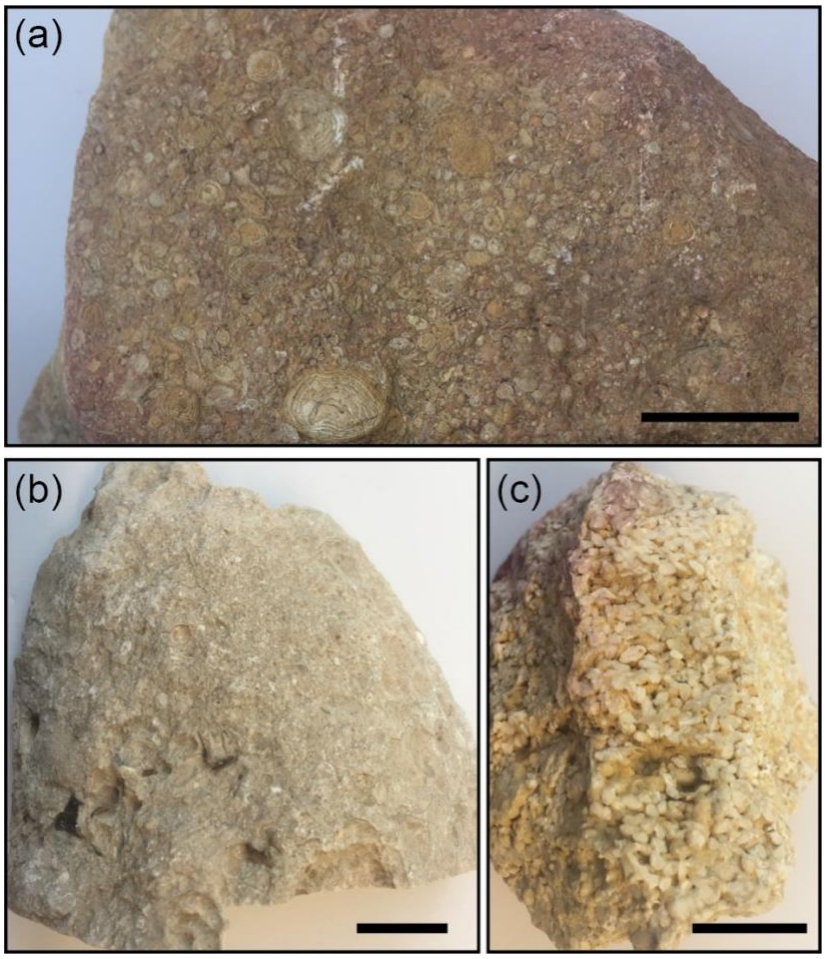

Figure 3.2: *Hand specimen images of three samples. These show the range of fossiliferous carbonate sediments that were tested with the three disaggregation methods. (a) LBF packstone-grainstone (sample K16); (b) Bioclastic wackestone (sample JB1); (c) LBF packstone (sample L05). Scale bars are 2 cm.*

3.3.1 Method 1: Calgon (modification of Riding & Kyffin-Hughes, 2004)

Immersion in cold Calgon is a technique often used to disaggregate less well indurated calcium carbonate samples (e.g., deep-sea oozes, chalks) for the study of smaller microfossils (e.g., Barnet et al., 2019; their Supplement). Within these lithologies this technique can be extremely effective at disaggregating the microfossiliferous content from the carbonate/clay matrix. Although extensively used, this modified technique for use on calcareous foraminifera has rarely been described in full (Riding & Kyffin-Hughes, 2004), as such it is described in full

below. The technique requires a buffered (pH controlled) solution of sodium hexametaphosphate ($[NaPO_3]_6$) to limit the damage that a stronger acid can have on dissolution susceptible calcium carbonate tests (Hodgkinson, 1991). This is achieved by adding sodium carbonate (Na_2CO_3) to the solution in the following proportion: 10 L de-ionised H_2O, 20 g $(NaPO_3)_6$, 1.4 g Na_2CO_3. The cold Calgon solution method works due to the deflocculating nature of the phosphate ions present. They reduce the coherence of clay particles by adsorbing strongly to the particle surface, breaking apart the clays due to the high ionic charges (Riding & Kyffin-Hughes, 2004).

The precise method used in this study is as follows: the samples were first broken up with a hammer into small (maximum 2 cm) chunks. Due to the heavily indurated nature of samples JB1, JF2 and JH1 it was not possible to break them down to this smaller size without fracturing the fossiliferous content. These chunks were then placed into a beaker and covered with cold Calgon (buffered sodium hexametaphosphate [$(NaPO_3)_6$]; as described above) and left for 24 hours. Samples were then washed over a 63 μm sieve with de-ionised water, put back into the beaker, covered again with Calgon and left for 48 hours. The beakers were then placed on a shaker table for 2 hours, then washed again over a 63 μm sieve, and subsequently covered again in Calgon. After 24 hours the samples were placed on a shaker table for 2 hours, washed over a 63 μm sieve and dried in an oven overnight at 50°C.

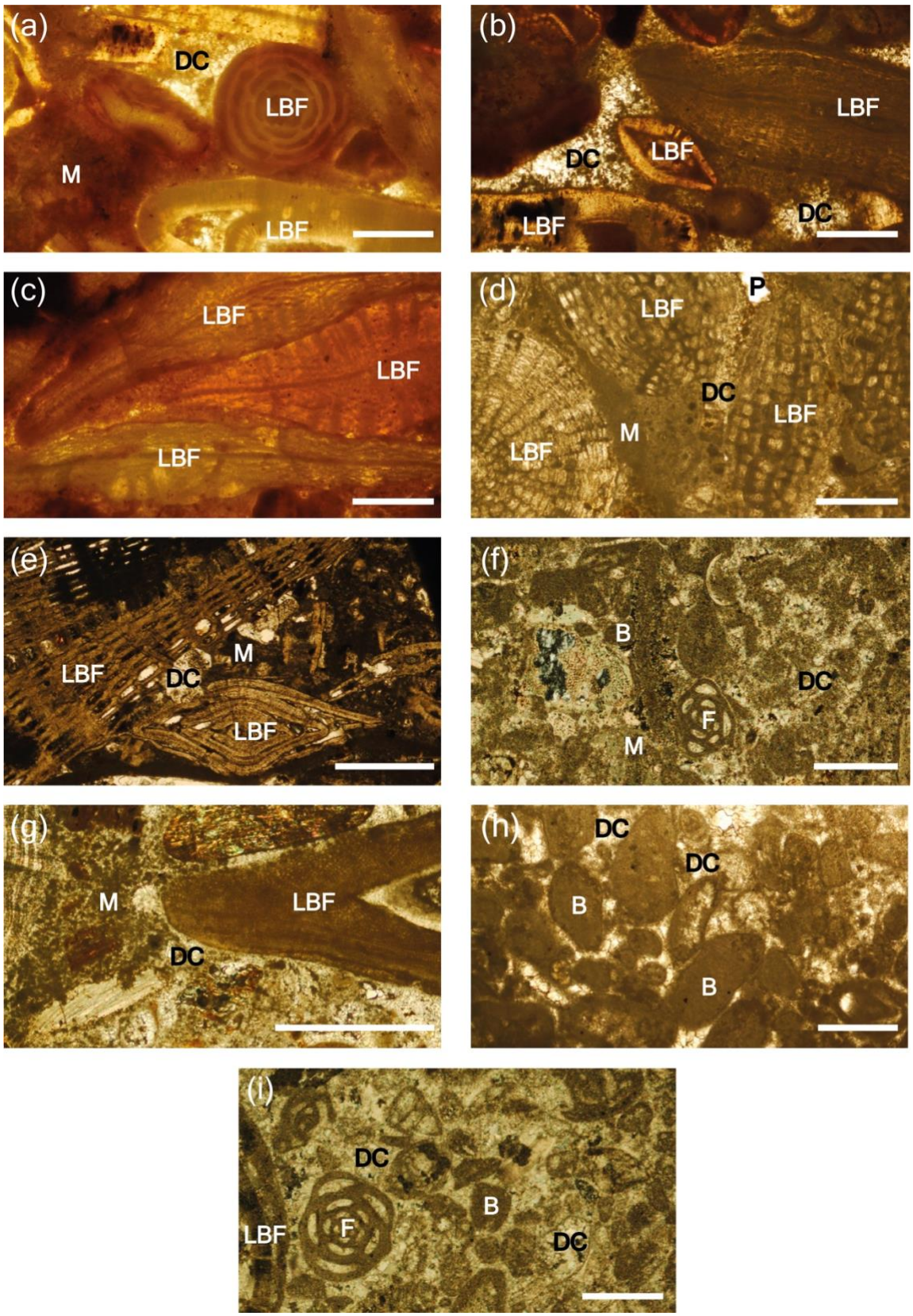

Figure 3.3: *Example thin section images of the bulk samples showing the range of biota and amount and type of cement. Images taken with transmitted light microscope, XPL = crossed polarised light, PPL = plane polarised light. White scale bars are 500 µm in each image. (a) LBF packstone (?*Alveolina *and nummulitids) with quartz grains within clay matrix (sample K05 in XPL); (b) LBF packstone (nummulitid and orthophragmine) with quartz grains within clay matrix (sample K09 in PPL); (c) LBF packstone-grainstone (orthophragmine) with quartz grains within clay matrix (sample K16 in PPL); (d) LBF*

packstone (miogypsinids and Sphaerogypsina*) with thin calcitic meniscus cement (sample L05 in PPL); (e) LBF packstone (*Lepidocyclina *and nummulitid) with calcite cement, clay matrix and quartz grains (sample LCL in PPL); (f) Bioclastic wackestone with secondary calcite cement (sample JB1 in XPL); (g) Bioclastic wackestone with secondary calcite cement (sample JB3 in XPL); (h) Bioclastic grainstone with secondary calcite cement (sample JF2 in PPL); (i) Foraminifera wackestone with secondary calcite cement (sample JH1 in XPL). LBF = larger benthic foraminifera, DC = diagenetic cement, M = matrix sediment, P = porosity, F = foraminifera, B = other bioclast. Further sample descriptions can be found in Table 3.1.*

3.3.2 Method 2: Acetic acid (after Lirer, 2000)

The cold acetic acid method proposed by Lirer (2000) has been widely used to extract microfossiliferous material from indurated rocks (e.g., Jovane et al., 2007; Falzoni et al., 2016; D'Onofrio & Luciani, 2020). The free hydrogen ions in the acid work to attack the matrix of the rock, dissolving it and breaking it apart (Hodgkinson, 1991; Costa de Moura et al., 1999). Costa de Moura et al. (1999) suggest the impurities present in the matrix of carbonate rocks provide boundaries for the acid to work on more effectively, whereas the pure biogenic carbonate of a fossil test can be considered more impermeable to the acid. However, assemblage diversity losses have been reported in planktic foraminifera after sample processing with acetic acid, showing that the acid can also attack the calcium carbonate of foraminifera tests (D'Onofrio & Luciani, 2020).

As with method 1, samples were broken into small (maximum 2 cm) chunks, except in samples JB1, JF2 and JH1 where it was not possible to break them down to this smaller size without fracturing the fossiliferous content. Samples were placed into 250 ml beakers and covered with an 80% acetic acid and 20% de-ionised water solution and left in a fume cupboard for 24 hours. After this time, samples were washed with de-ionised water over a 63 μm sieve and the residue dried overnight in an oven at 50°C. Due to there being very little organic material in the samples it was not necessary to use the "Desogen" (or neosteramina; D'Onofrio & Luciani, 2020) step in the Lirer (2000) method.

3.3.3 Method 3: Electric pulse fragmentation (EPF; Saini-Eidukat & Weiblen, 1996; Parvaz et al., 2018)

The EPF method utilises highly energetic (150–750 J per pulse) pulsed electrical discharges with a very fast voltage ramp-up time (<500 ns) to break apart composite materials submerged in a process medium along internal compositional or mechanical boundaries. Dielectric process mediums such as water are more resistive than solids when the pulse rise time is kept below 500 ns resulting in discharges preferentially grounding on the solid material (Bluhm et al., 2000). In each discharge a movement of electrons, as plasma, occurs from the working electrode to the ground electrode (Andres et al., 1999; van der Wielen, 2013). This plasma channel causes explosive expansion along the discharge pathway (electrodynamic fragmentation; Andres et al., 1999; Bluhm et al., 2000), producing a shockwave that propagates through the material.

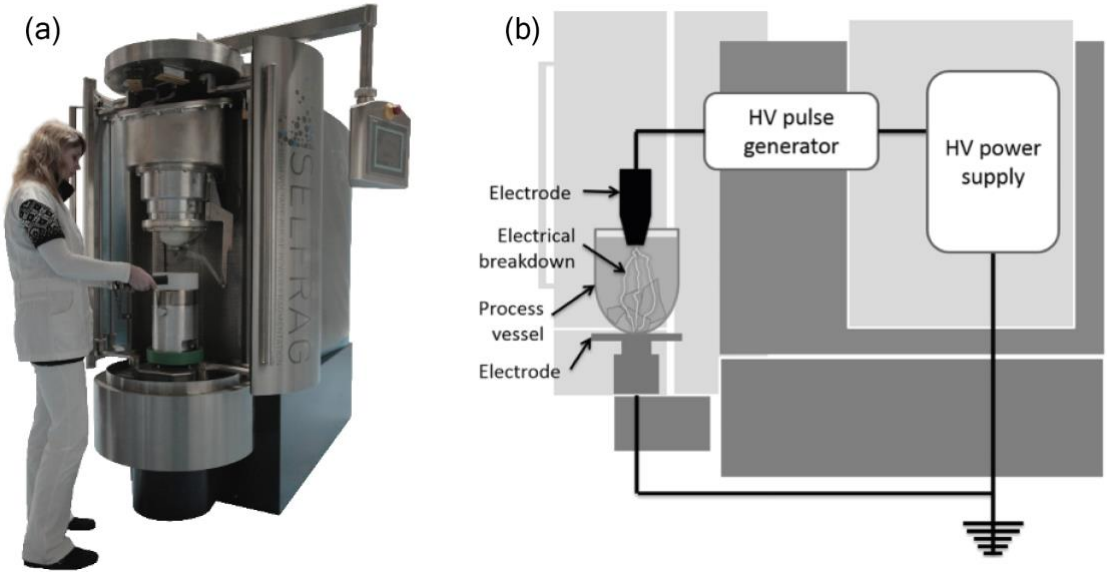

Figure 3.4: *Photograph (a) and schematic (b) of the SELFRAG Lab system (after Bru et al., 2018).*

The selectivity of the process arises from the interaction of the plasma channel and shockwaves with physico-chemical properties of the material. Discontinuities in electrical permittivity and conductivity at phase boundaries locally enhance the electric field forcing the discharge channels to these boundaries. The interaction of the shock wave with elastic and acoustic discontinuities concentrates tensile stress at phase interfaces causing local shearing and thus focussing fragmentation at these boundaries (Andres et al., 1999) allowing full liberation of

discrete components from the feed material. Applicable to a range of disciplines, EPF treatment of various mineral ores has previously shown very high liberation rates (Andres et al., 1999; Andres et al., 2001; Dal Martello et al., 2012; Wang et al., 2012; Bru et al., 2017; 2020), advocating for its potential use in micropalaeontology.

Table 3.2: *Variable parameters of the SELFRAG Lab system.*

Parameter	Range
Electrode gap	10–40 mm
Pulse retention rate	1–5 Hz
Voltage	90–200 kV
Number of pulses	1–1000
Sieve aperture	0.12–10 mm

For this study, EPF treatment was performed using a SELFRAG 'Lab' (Fig. 3.4), a laboratory scale device for the batch processing of material, manufactured by SELFRAG AG of Switzerland. The equipment is designed to process samples of up to approximately 1 kg with a top particle size of 40–45 mm in a 4L vessel filled with de-mineralised water process medium. The working electrode is immersed in the upper part of the vessel while the bottom of the vessel constitutes the counter electrode (ground). The apparatus produces high voltage electric discharges between the two electrodes. Operating parameters are presented in Table 3.2. The lab system can be operated with both a 'closed' vessel for when a fixed amount of energy is to be applied to a fixed mass of material, or an 'open' vessel where the solid lower plate is replaced with a sieve that allows material reaching the target size during crushing to fall through and be protected from further discharge events.

Samples were manually crushed to 40–45 mm to fit into the process vessel. Measurement of the LBF to be recovered guided selection of an appropriate aperture sieve for the SELFRAG open process vessel. Normally aperture diameter is ~1.5x the target particle diameter. Due to the unknown breakage behaviour of these samples, a larger diameter aperture was used in the first round of crushing and stepwise crushing process was implemented. A series of 10

pulses were applied to the sample followed by visual inspection of the remaining sample; if >10% if the sample remained above the sieve another 5–10 pulses were administered. When >90% of sample material had passed through the sieve, treatment was stopped, and the sample recovered from the process vessel collection cup (SELFRAG AG, 2012) before drying at 50°C. Process conditions and total pulses applied to each sample are found in Table 3.3.

After samples were dried, liberated LBF were manually picked from the sample and the remaining material, comprising both particles of LBF with attached matrix and only matrix, was returned to the process vessel and reprocessed (Table 3.3). A lower voltage of 160 kV was used in the second round to minimise the electrical crushing energy per pulse. Accordingly, the electrode gap was reduced to maintain the concentration of the electrical field and increase probability of successful discharges (van der Wielen, 2013).

Table 3.3: *First and second round process conditions for EPF treated samples. Sieve aperture was selected based on measurement of visible LBF. Electrode gap is smaller for K05 due to much smaller sample mass. Sample JH1 was not reprocessed as all material was processed successfully in the first processing round.*

Sample name	Processing round	Sieve aperture (mm)	Electrode gap (mm)	Pulse repetition rate (Hz)	Voltage (kV)	Total pulse count	Processing time (s)
K05	1	6	20	2	150	20	10
	2	4	20	2	160	40	20
K09	1	6	40	2	175	20	10
	2	4	20	2	160	40	20
K16	1	6	40	2	175	20	10
	2	4	20	2	160	40	20
L05	1	6	40	2	175	10	5
	2	4	20	2	160	20	10
LCL	1	6	40	2	175	20	10
	2	4	20	2	160	40	20
JB1	1	6	40	2	175	40	20
	2	4	20	2	160	40	20
JB3	1	6	40	2	175	20	10
	2	4	20	2	160	40	20
JF2	1	6	40	2	175	30	15
	2	4	20	2	160	60	30
JH1	1	10	40	2	175	30	15
	n/a	-	-	-	-	-	-

3.3.4 Normalising number of liberated microfossils

3.3.4.1 LBF per gram

Number of LBF picked in each sample was normalised per gram of original sample, due to varying size of the original sample. The entirety of each sample was picked. For the purposes of comparison, a “good disaggregation” is considered to be where more than 2 LBF per gram of sediment were liberated.

3.3.4.2 Percentage fossiliferous fraction (% FF)

Percentage fossiliferous fraction data (% FF) was obtained by first weighing the bulk disaggregated sediment ($bulk_w$), composed of chunks of non-disaggregated carbonate sediment and liberated fossils. The bulk sediment was dried in an oven at 50°C after each of the disaggregation methods were applied to ensure measured weights were accurate. The >63 μm fossiliferous fraction was then weighed once picked (FF_w). The entirety of each disaggregated sample was picked for all fossiliferous material. This mainly consisted of LBF, however a number of ostracods were also picked. In order to normalise the data to the original bulk weight of the material, the % FF was calculated using the following equation:

$$\% \, \mathrm{FF} = (\mathrm{FF_w} \div \mathrm{bulk_w}) \times 100 \qquad [\mathrm{Eq.}\, 3.1]$$

By normalising the data in this way, it removes the issues of each sample being of a different starting mass. As such, good disaggregation of samples is shown by a larger % FF.

3.3.5 Scanning Electron Microscope (SEM) and Energy Dispersive Spectroscopy (EDS)

Scanning electron microscope and energy dispersive spectroscopy (SEM-EDS) work was carried out at the University of Exeter, Penryn Campus on a TESCAN VEGA3 GMU SEM with an Oxford XMax 80 mm EDS linked to AZtec analysis software. Samples were carbon coated prior to analysis and examined at 20 kV,

at a working distance of ~11 mm for imaging and ~17 mm for EDS analysis. The EDS data was assessed in semi-quantitative mode with an acquisition time of 10 seconds. Data were used to confirm the mineralogy of diagenetic cements and matrix materials in samples (Table 3.1).

3.4 Results

3.4.1 Calgon

Despite leaving all samples in Calgon for approximately 112 hours in total, this method was not effective at disaggregating any of the samples. This is illustrated in Figures 3.5 and 3.6, where extremely few (<2 g^{-1}) or no LBF were liberated, and the percentage fossiliferous fraction was low throughout all processed samples. Where LBF were liberated, residual matrix and cement remained attached to the outside of the test (Fig. 3.7e and 3.7f). It seems unlikely that leaving the samples to sit in the Calgon for a more extended period of time would have led to a significantly improved disaggregation.

3.4.2 Acetic acid

Three samples, two LBF packstones (samples K05 and LCL) and a foraminifera wackestone (sample JH1), disaggregated well with the acetic acid method in terms of numbers of foraminifera liberated per gram (Fig. 3.5). The highest fossiliferous fraction, of 19.65%, was recorded using this method with sample K05 (Fig. 3.6); this sample is an LBF packstone of Eocene age with a clay matrix containing quartz grains. All other samples had poor recoveries of LBF using the acetic acid method (<2 LBF per gram and low % FF). In all cases, liberated LBF were not well preserved following the acetic acid method, with test surfaces having been etched by the strong acid (Fig. 3.7) likely due to any disaggregation requiring at least 24 hours of immersion.

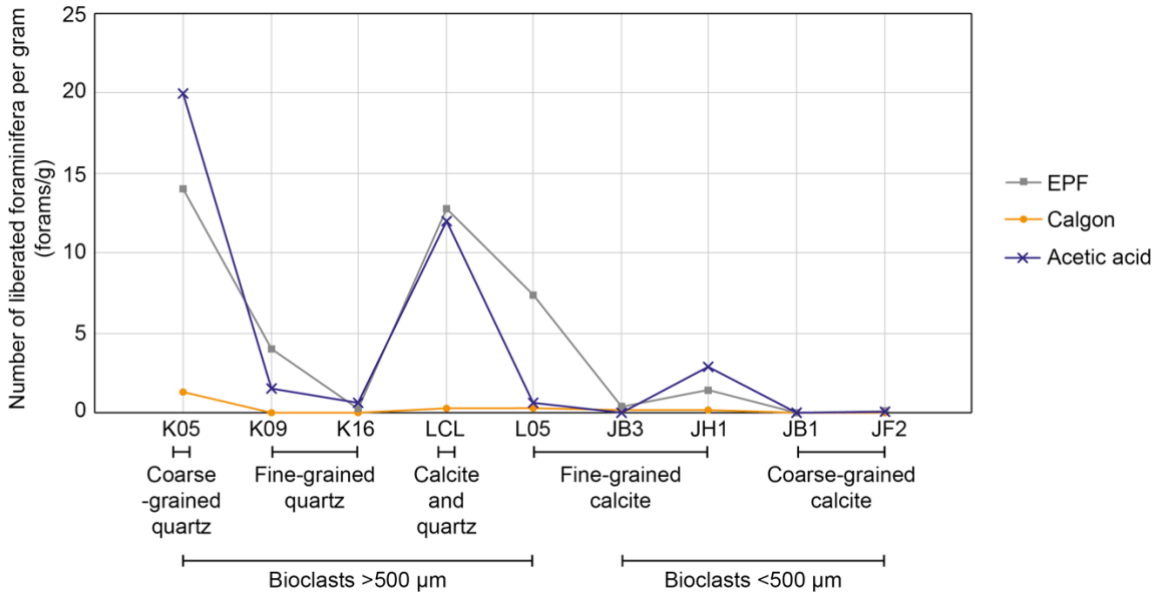

Figure 3.5: *Number of liberated larger benthic foraminifera per gram of each sample, for each of the three methods. Samples organised into types of infilling cements and sizes of bioclasts; further details can be found in Tables 3.1 and 3.4.*

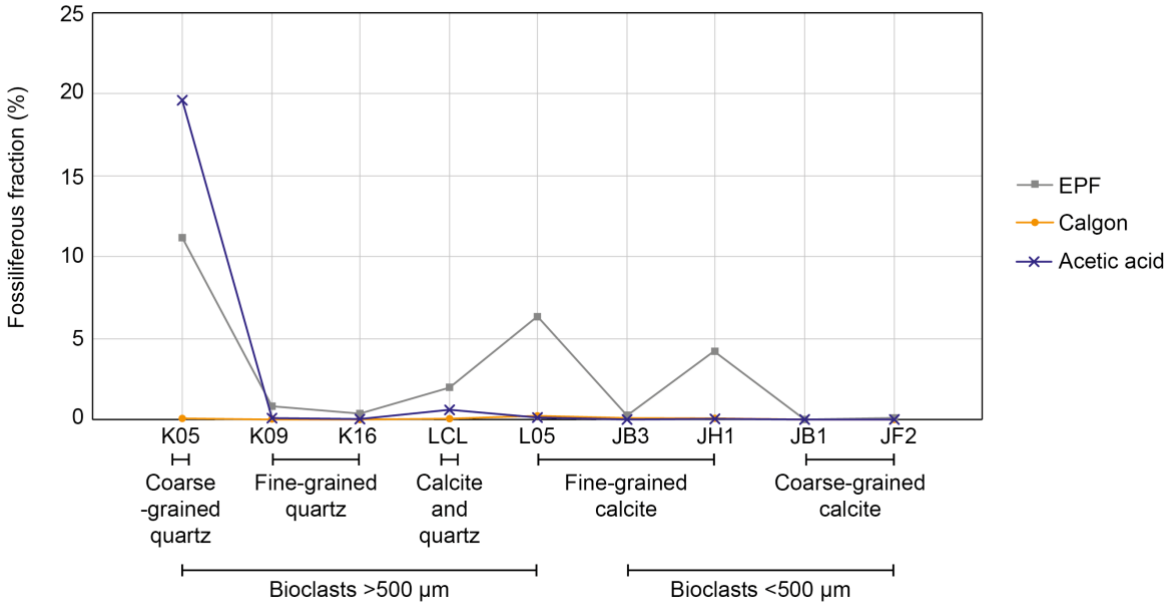

Figure 3.6: *Percentage fossiliferous fraction (>63 µm) for each sample from the three different methods. Samples organised into types of infilling cements and sizes of bioclasts; further details can be found in Tables 3.1 and 3.4.*

3.4.3 Electric pulse fragmentation

Four samples disaggregated well with the EPF method both in terms of overall numbers of LBF liberated per gram (Fig. 3.5) and percentage fossiliferous fraction (Fig. 3.6); these were LBF packstones with clay matrices containing quartz grains

(samples K05 and K09), a LBF packstone with thin calcitic meniscus cement (sample L05), and a LBF packstone with a calcite and clay matrix and small patches of quartz grains (sample LCL). All of these samples had bioclasts of 500 µm or larger (Table 3.2). Within these samples, an average of 182% more LBF per gram were liberated using EPF when compared to Calgon, and 57% more when compared to acetic acid.

Only two samples yielded more liberated LBF per gram when using the acetic acid method (Fig. 3.5); K05, a LBF packstone, yielded 35% more LBF and JH1, a foraminifera wackestone, yielded 72% more LBF. For all samples, preservation of liberated LBF using the EPF technique was good; there was minimal fragmentation, no dissolution of the test surface, and little or no matrix/cement remaining attached to the test surfaces (Fig. 3.7). EPF liberation gave some of the highest overall recoveries of LBF.

Table 3.4: *Comparison of sample properties and relative success with different disaggregation techniques.*

Sample name	Cement/ infilling	Average size of clasts	Which disaggregation method was effective?		
			EPF	Acetic acid	Calgon
K05	Quartz grains and clays	>500 µm	✓	✓	×
K09	Clays and small amount of quartz grains	>500 µm	✓	✓	×
K16	Clays and quartz grains	1–2 mm	×	×	×
L05	Calcite and thin clays around pores	>1000 µm	✓	×	×
LCL	Quartz grains and clays, calcitic crusts	>1000 µm	✓	✓	×
JB1	Coarse-grained calcite	<400 µm	×	×	×
JB3	Fine-grained calcite	<500 µm	×	×	×
JF2	Coarse-grained calcite	~50–300 µm	×	×	×
JH1	Fine-grained calcite	200–500 µm	✓	×	×

3.4.4 Poor disaggregation

Four samples did not disaggregate well with any of the three methods (Figs. 3.5 and 3.6); samples remained in large lithified chunks with little or no microfossil material liberated. These were bioclastic wackestones (samples JB1, JB3) and grainstones (sample JF2) with secondary calcite cements, and a LBF packstone-grainstone with abundant bioclasts and a clay matrix containing quartz grains (sample K16).

3.5 Discussion

The development of this new methodology, and comparison to other disaggregation techniques, aims to enable higher resolution study of the ancient low latitude, shallow water domain, which is often dominated by indurated calcium carbonate-rich sediments. Whilst there are numerous existing high-resolution palaeoclimate and micropalaeontological records from deep water settings of Paleogene age, similar resolution records in shallow water environments are comparatively rare, impeding comparisons of shallow and deep lithologies and the understanding of how these important palaeoenvironments and ecosystems, such as reefs, have evolved. The ability to break apart lithified carbonates into their constituent components enables the study of a wide variety of microfossil material, such as LBF, algae (e.g., Rhodoliths), bryozoans, fish teeth, conodonts, and more. Expansion of existing studies of evolutionary trends in individual taxa, ecophenotypic variation, species-level biodiversity trends, carbonate platform dynamics, and much more then becomes possible. Whilst other non-destructive techniques such as CT scanning are also possible (e.g., Renema & Cotton, 2015) this cannot be routinely undertaken as bioclasts need to be unfilled (e.g., the chambers must be free of cement) for optimal results and the technique is expensive and time-consuming, therefore this technique is not suitable for many samples.

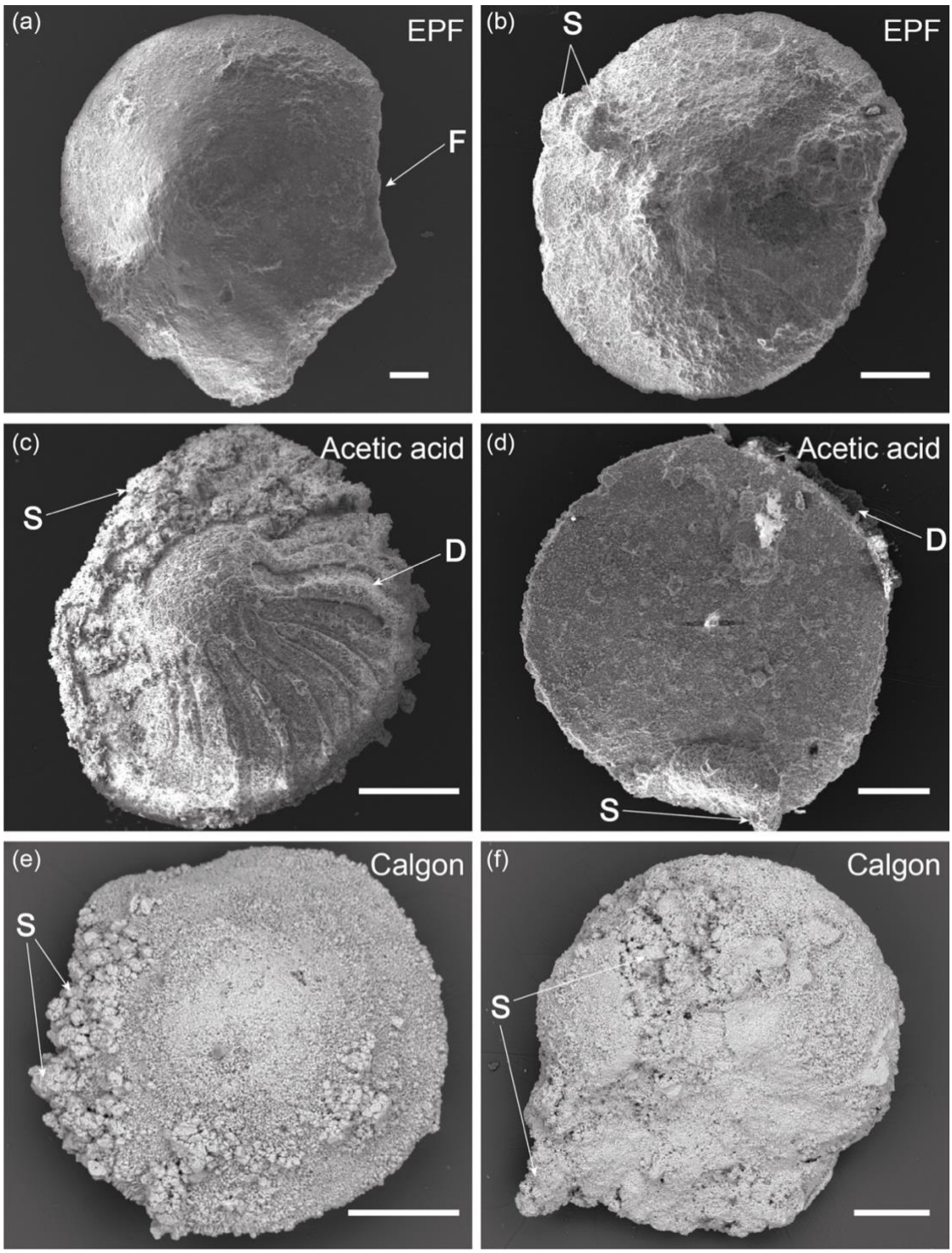

Figure 3.7 (below): *SEM and reflected light microscope images of select LBF from samples to show differential preservation from each technique. SE = image taken in secondary electron mode. BSE = image taken in back scattered electron mode. (a) K05 processed using EPF (SE), some fragmentation (breakage) of specimen has occurred; (b) LCL processed using EPF (SE), small amounts of sediment remain attached to test surface; (c) K05 processed using acetic acid (SE), dissolution has caused exposure of internal chamber walls; (d) LCL processed using acetic acid (SE), dissolution degraded periphery of test; (e) K05 processed using Calgon (BSE), clumps of sediment remain attached to test surface; (f) LCL processed using Calgon (BSE), test surface obscured by large amounts of sediment remaining attached to surface. Scale bars are 200 µm. S = sediment remaining attached to test surface, D = dissolution of test surface, F = fragmentation of specimen.*

There are also other techniques available utilising different strong acids and surfactants in order to break apart fossiliferous lithologies. One such example is Rewoquat (e.g., Jarachowska et al., 2013), the trade name for a tenside (organic detergent; Kennedy & Coe, 2014) that has been used to disaggregate both organic-rich (Jarachowska et al., 2013; Kennedy & Coe, 2014) and carbonate lithologies (Wolfgring & Wagreich, 2016). As with the Calgon and acetic acid techniques analysed in this manuscript, the Rewoquat method requires repeated rounds of processing (multiple days) for more indurated samples, with additional soaking and/or washing with hydrogen peroxide (Kennedy & Coe, 2014). The extended periods of exposure to acids and/or surfactants required with many of these techniques risks dissolution or poor preservation of recovered fossil material.

Results of this study show that, in general, the EPF method disaggregated most samples the most effectively and efficiently; this method overall gave the highest LBF recoveries compared to the acetic acid and Calgon methods (Figs. 3.5 and 3.6), whilst also liberating the best-preserved specimens (Fig. 3.7). Only samples K05 and JH1 yielded higher LBF recoveries with the acetic acid method (Fig. 3.5), however, these samples were also successfully disaggregated using EPF with significantly less damage to the fossils. The EPF treatment time varied between 10 and 30 seconds per sample (Table 3.3), however, the stepwise processing method, including inspection between cycles and cleaning, resulted in an overall processing time of around 20 minutes per sample disaggregation, compared to Calgon and acetic acid that both required multiple days.

Samples that disaggregated well with EPF contained larger (>500 µm) bioclasts (e.g., K05, K09, LCL, L05; Figs. 3.5 and 3.6). This method was effective regardless of the cement/matrix material, as samples containing calcitic, silicic, and clay matrix or diagenetic cements were disaggregated using EPF. Furthermore, Saini-Eidukat and Weiblen (1996) previously disaggregated sandstone and shale lithologies using EPF, obtaining a diverse assemblage of well-preserved microfossil moulds such as conodonts, foraminifera, fish teeth, and ammonitella. This suggests EPF is a very broadly applicable method of disaggregation in micropalaeontology.

The only sample which did not fit with the above parameters is sample K16 (LBF packstone-grainstone) which contained large bioclasts (~1–2 mm) and a clay matrix containing quartz grains but was not disaggregated using any method (Table 3.4). It is hypothesised that the bioclastic material was packed too closely together (Figs. 3.2a and 3.3c), therefore there was less cement/matrix for the disaggregation techniques to be effective on. More specifically, the EPF method was not effective on this sample as a lack of matrix/LBF boundaries reduces the contrast in electrical permittivity and conductivity between bioclasts, limiting internal boundaries on which local shearing and thus fragmentation can be focussed.

Where these larger bioclasts (>500 µm) were surrounded by a mixture of a quartz grains and clay matrix, acetic acid was also effective in disaggregating the samples (Table 3.4). It is suggested that acetic acid was able to work in these cases due to the higher surface area the fine-grained clays enabled the acid to work on. However, when acetic acid disaggregation was effective, the preservation of liberated material was compromised which reduces the utility of the microfossils for further study (Fig. 3.7).

None of the tested methods were effective at liberating fossiliferous material from samples that contained small (<500 µm) bioclasts such as planktic foraminifera or smaller benthic foraminifera (Table 3.2). Future work will aim to tailor the EPF method for use with smaller bioclasts, this could include the use of smaller sieve apertures and a greater number of processing rounds in which progressively smaller microfossil material could be collected. This would require the picking of already liberated microfossils between each processing round, increasing the time spent (and thus decreasing efficiency), but could ultimately improve the recoveries of smaller bioclasts. The EPF method could also be used as a pre-treatment step for other disaggregation techniques such as acetic acid where fractures generated from the process enhance permeability and thus acid penetration, which may reduce the amount of time that the samples need to be immersed in the corrosive liquid and hence improve preservation. In comparison to manually breaking up bulk material, the EPF method is far less likely to fragment microfossils prior to liberation due to it acting discriminately upon phase boundaries.

In terms of a best practice methodology for implementing EPF on indurated micro-fossiliferous carbonates the following methodology is suggested: microfossils should be 500 µm or larger; individual microfossils should not be touching, i.e., separated by matrix/cement; the composition of the matrix/cement is unimportant and can be fine or coarse grained and made up of calcareous, siliceous, or clay components. This technique can be used on a range of microfossil material with high specimen yields, good preservation, and a short processing time. For the recovery of smaller microfossils (<500 µm) repeated rounds of EPF processing with a gradually decreasing sieve aperture and picking of liberated material between rounds could improve recoveries, with the sacrifice of a less efficient methodology, although this remains to be experimentally tested.

3.6 Conclusions

The EPF method is highly efficient and effective as a disaggregation technique for liberating larger microfossils (>500 µm) from indurated carbonate-rich sedimentary rocks. This method indiscriminately disaggregated indurated carbonates with a mixture of calcitic, silicic, and clay matrices/cements; it has also previously been shown to liberate microfossils from sandstones and shales (Saini-Eidukat & Weiblen, 1996), showing it to be a broadly applicable method to micropalaeontology. The EPF method could be tailored to liberate smaller (<500 µm) microfossils effectively by using repeated rounds of processing and progressively smaller sieve aperture sizes, although further investigation is required.

Compared to the traditional methods of disaggregation, soaking in Calgon and acetic acid, the time required is significantly reduced and the preservation of liberated material is excellent. Acetic acid proved effective in some highly lithified samples, however, the time taken to process the samples is significantly longer and LBF preservation was compromised. Calgon was unable to disaggregate any of the carbonate samples successfully (i.e., few or no LBF were liberated) and so is unsuitable for processing these highly lithified sedimentary rocks.

Chapter 4: Evidence of a South Asian proto-monsoon during the Oligocene–Miocene transition

4.1 Abstract

The geological history of the South Asian (Indian) monsoon (SAM) before the Pleistocene is not well-constrained, primarily due to a lack of available continuous sediment archives. Previous studies have noted an intensification of SAM precipitation and atmospheric circulation during the middle Miocene (~14 Ma), but no records are available to test how the monsoon changed prior to this. In order to improve our understanding of monsoonal evolution, geochemical and sedimentological data were generated for the Oligocene–early Miocene (30–20 Ma) from Indian National Gas Hydrate Expedition 01 Site NGHP-01-01A in the eastern Arabian Sea, at 2674 m water depth. We find the initial glaciation phase (23.7–23.0 Ma) of the Oligocene–Miocene transition (OMT) to be associated with an increase in water column ventilation and water mass mixing, suggesting an increase in winter monsoon type atmospheric circulation, possibly driven by a relative southward shift of the intertropical convergence zone. During the latter part of the OMT, or 'deglaciation' phase (23.0–22.7 Ma), a long-term decrease in Mn (suggestive of deoxygenation), increase in Ti/Ca and dissolution of the biogenic carbonate fraction suggest an intensification of a proto-summer SAM system, characterised by the formation of an oxygen minimum zone in the eastern Arabian Sea and a relative increase of terrigenous material delivered by runoff to the site. With no evidence at this site for an active SAM prior to the OMT we suggest that changes in orbital parameters, as well as possibly changing Tethyan/Himalayan tectonics, caused this step change in the proto-monsoon system at this intermediate-depth site.

Co-author contributions: CB sampled and logged core, disaggregated samples, and picked foraminifera for analyses. MJL facilitated analysis of foraminiferal stable isotopes. CB conducted foraminiferal trace element analysis, with help from PA and KNK. CTB analysed samples for calcareous nannofossil biostratigraphy. LG provided XRF datasets. CB processed bulk samples for ICP-OES analysis with analytical assistance from CVU. CB constructed the chapter, with edits from KL, SK, PA, CTB, and LG.

4.2 Introduction

Today, the Arabian Sea region is strongly influenced by the modern South Asian monsoon (SAM; or Indian monsoon) system, which is a dominant vector for the transport of heat and moisture in the tropical low latitudes (Gupta et al., 2020). The initiation and intensification of the Asian monsoon systems have been hypothesised to be linked with atmospheric CO_2 levels and the uplift of the Himalayan-Tibetan Plateau (HTP) (Kutzbach et al., 1993; Clift et al., 2002; Jiang et al., 2008; Tada et al., 2016; Farnsworth et al., 2019; Thomson et al., 2021), although the timing and origin of the various Asian monsoon sub-systems and the link to HTP uplift are still debated (Boos & Kuang, 2010, 2013; Ding et al., 2017; Spicer, 2017; Acosta & Huber, 2020; Thomson et al., 2021). A number of east Asian dust records suggest that the east Asian monsoon was established prior to or during the Oligocene–Miocene interval (Guo et al., 2002; 2008; Sun et al., 2010; Licht et al., 2016). However, there are few available, continuous sedimentary records prior to the Miocene to help constrain timing of the SAM (Betzler et al., 2016; Pandey et al., 2016; Bialik et al., 2020). The available records are dominantly terrestrial and lack sufficient age constraints to place sedimentological changes into a climatic context (Reuter et al., 2013). Thus, estimates for the initiation of the SAM range from the early Paleogene (Licht et al., 2014; Farnsworth et al., 2019) to the middle/late Miocene (Gupta et al., 2015; Betzler et al., 2016; Bialik et al., 2020; Yang et al., 2020). Constraining the timing of SAM initiation is important to understand the mechanisms/processes that govern it and potentially aid in refining future predictions associated with anthropogenic climate change.

The Oligocene to earliest Miocene (~34–22 million years ago; Ma) began with the major Eocene–Oligocene transition (EOT) glaciation event (~34 Ma), thought to represent the first glaciation of Antarctica (Keigwin & Corliss, 1986; Zachos et al., 1992; 1996; Lear et al., 2000; 2004; Zachos & Kump, 2005; Lear et al., 2008; Scher et al., 2011) and ended with the transient Oligocene–Miocene transition (OMT) glaciation event (~23 Ma; Miller et al., 1991; Paul et al., 2000; Zachos et al., 2001b; Lear et al., 2004; Wade & Pälike, 2004; Pälike et al., 2006; Mawbey & Lear, 2013; Beddow et al., 2016; Stewart et al., 2017). We currently lack detailed data to infer ocean and atmosphere circulations influencing climate from

the northern Indian Ocean during this enigmatic "coolhouse" interval (Westerhold et al., 2020).

During the middle Oligocene (~28–26.3 Ma) there was a transient glacial interval coined as the middle Oligocene glacial interval (MOGI; Liebrand et al., 2017). This interval consisted of unstable but generally cooler climatic conditions. During the late Oligocene a trend towards relative global warmth, termed the late Oligocene warming event (LOWE; ~27–24 Ma), seemingly occurred during a time when proxy reconstructions suggest decreasing atmospheric CO_2 (Fig. 4.1; Zhang et al., 2013; O'Brien et al., 2020). Immediately following the LOWE is the OMT glaciation ("Mi-1" event; Miller et al., 1991). This event is marked by a 0.6–1.5‰ positive excursion in benthic foraminifera $\delta^{18}O$, thought to be caused by Antarctic ice volume expansion (Liebrand et al., 2011; 2017) and ~2°C cooling of deep waters (Mawbey & Lear, 2013; Lear et al., 2004). Sea surface temperature (SST) decreases over the same interval have also been suggested by palynological data (Egger et al., 2018), biomarker and alkenone proxies (Zhang et al., 2013; Liu et al., 2018; Super et al., 2018; Guitián et al., 2019), and modelling (Liebrand et al., 2011) for the Atlantic. However, the evolution of SST over this interval, including the magnitude of changes and spatial heterogeneity, is not well constrained (Guitián et al., 2019), with some equatorial sites showing little change in surface water oxygen isotopic values over the OMT (Fig. 4.1; Matsui et al., 2016; Stewart et al., 2017). Accompanying this global cooling was ~50–65 m of glacioeustatic sea level fall, accommodated by significant ice growth on Antarctica (Wade & Pälike, 2004; Mawbey & Lear, 2013; Beddow et al., 2016).

The OMT is superimposed upon pronounced orbitally-paced variation in ice volume/temperature with changes in $\delta^{18}O$ on the order of ~0.5–1‰ and in $\delta^{13}C$ of ~0.5‰ (Paul et al., 2000; Zachos et al., 2001a; Wade & Pälike, 2004; Pälike et al., 2006; Liebrand et al., 2011; Mawbey & Lear, 2013; Liebrand et al., 2016; 2017; Egger et al., 2018). It has been suggested that the dominant forcing on the climate/cryosphere system through the late Oligocene to early Miocene is eccentricity modulation of precession (short and long; ~110 kyr and ~405 kyr respectively), also with a strong imprint of the 2.4 Myr very long-period eccentricity (Fig. 4.1; Liebrand et al., 2016; 2017; Beddow et al., 2018; Egger et al., 2018; Greenop et al., 2019; De Vleeschouwer et al., 2020; Drury et al., 2020;

van Peer et al., 2020; Westerhold et al., 2020). The particular orbital configuration present during the OMT glaciation recovery phase (high amplitude oscillations of 110 kyr eccentricity) occurred a further four times throughout the Oligocene–Miocene interval (Liebrand et al., 2017; Greenop et al., 2019), associated with more minor cryosphere responses. Despite this, the OMT glaciation stands out from these cyclic events as a prominent, transient event terminating the LOWE (Liebrand et al., 2017). It is suggested that conditions promoting Antarctic glaciation across the OMT were a result of the long-term decline in atmospheric CO_2 rather than being triggered solely by changes in orbital parameters (Greenop et al., 2019). This multi-million-year decrease in pCO_2 observed in compiled $\delta^{11}B$ (Greenop et al., 2019) and alkenone records (Fig. 4.1; Zhang et al., 2013) may be linked to the broadly contemporaneous uplift of the HTP, leading to an increase in weathering rates subsequently sequestering atmospheric CO_2 (Raymo & Ruddiman, 1992; Zachos & Kump, 2005; Zhang et al., 2021). Despite the proximity of the Arabian Sea to the HTP there are very few long continuous records available in this region to help constrain these hypotheses of paired tectonic and climatic change (see Clift & Webb, 2019 for a review).

Core NGHP-01-01A represents a unique opportunity to investigate Oligocene–Miocene paleoceanographic dynamics at a relatively high resolution (10–40 kyr) in an oceanographically significant but otherwise data-barren area of the Arabian Sea (Fig. 4.2). Here we present new sedimentological and biostratigraphic data, paired planktic and benthic foraminiferal stable isotopes, planktic foraminiferal Mg/Ca ratios, and bulk sediment elemental ratios to reveal new insights into ocean and atmospheric circulation during this time interval. We show that the OMT was a fundamental turning point for the initiation/intensification of proto-SAM atmospheric and oceanographic circulation causing a significant step-change in the sedimentary record in the eastern Arabian Sea.

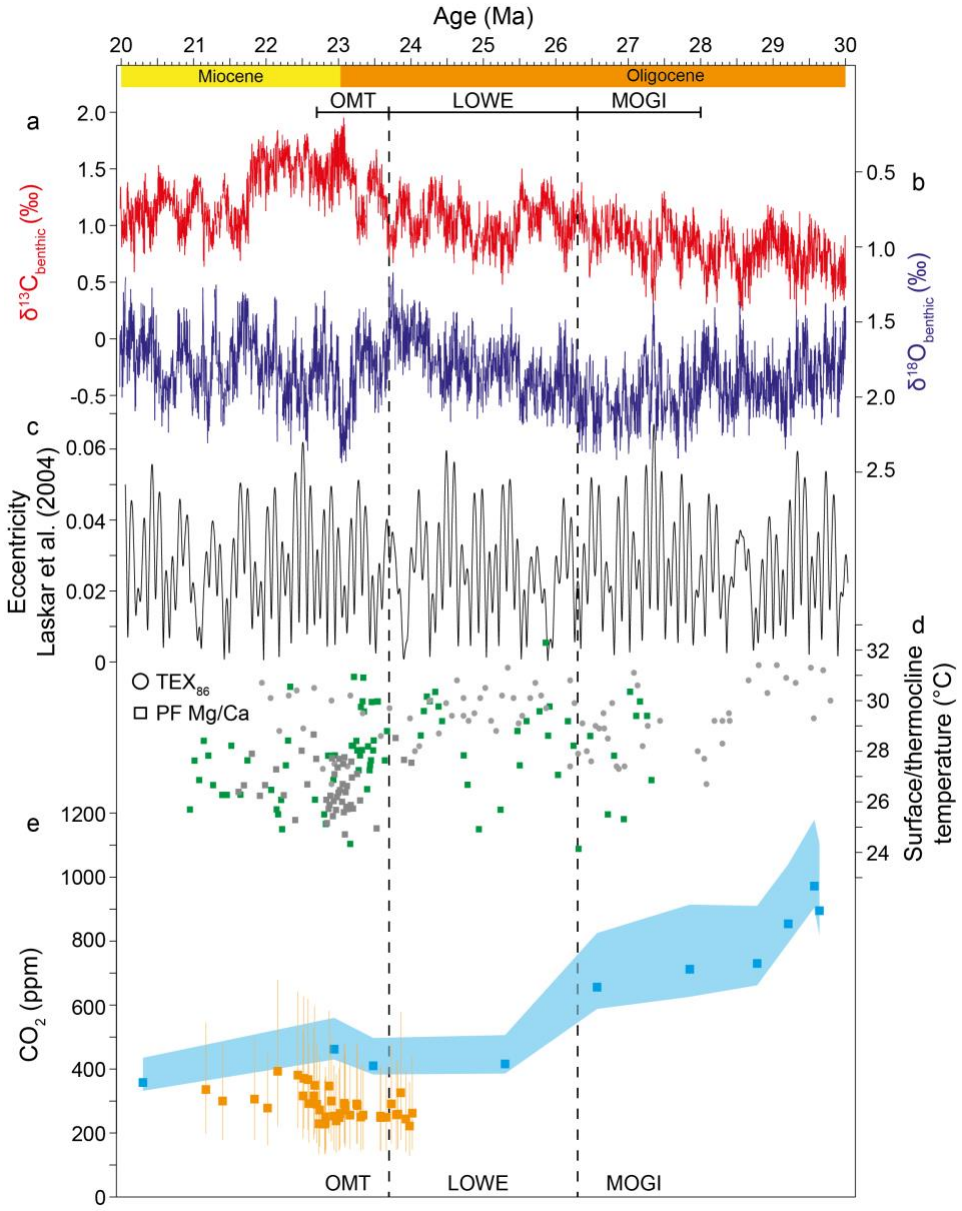

Figure 4.1: *Summary of Oligocene–Miocene climate evolution. Abbreviations from Liebrand et al. (2017) where MOGI is the middle Oligocene glacial interval, LOWE is the late Oligocene warming event, and OMT is the Oligocene–Miocene transition. (a) and (b) Benthic foraminifera carbon ($\delta^{13}C$) (a) and oxygen ($\delta^{18}O$) (b) stable isotopes from ODP Site 1264 (Liebrand et al., 2016) in the equatorial Atlantic. (c) Eccentricity variations from Laskar et al. (2004). (d) Equatorial thermocline/sea surface temperature records from the Atlantic using TEX_{86} (grey circles, ODP Site 929; O'Brien et al., 2020) and planktic foraminiferal (PF) Mg/Ca (grey squares, ODP Site 926; Stewart et al., 2017) and this study. TEX_{86} data record SST, whilst PF Mg/Ca records thermocline temperature. (e) Atmospheric CO_2 evolution derived from alkenone $\delta^{13}C$ in blue from ODP Site 925 (Zhang et al., 2013) and $\delta^{11}B$ in orange from ODP Site 926 in the equatorial Atlantic and ODP Site 872 in tropical north Pacific (Greenop et al., 2017, 2019). Error bars in alkenone record represent variability in temperature and phosphate estimates used to calculate CO_2 (see Zhang et al., 2013). Error bars in $\delta^{11}B$ record represent 2σ uncertainty.*

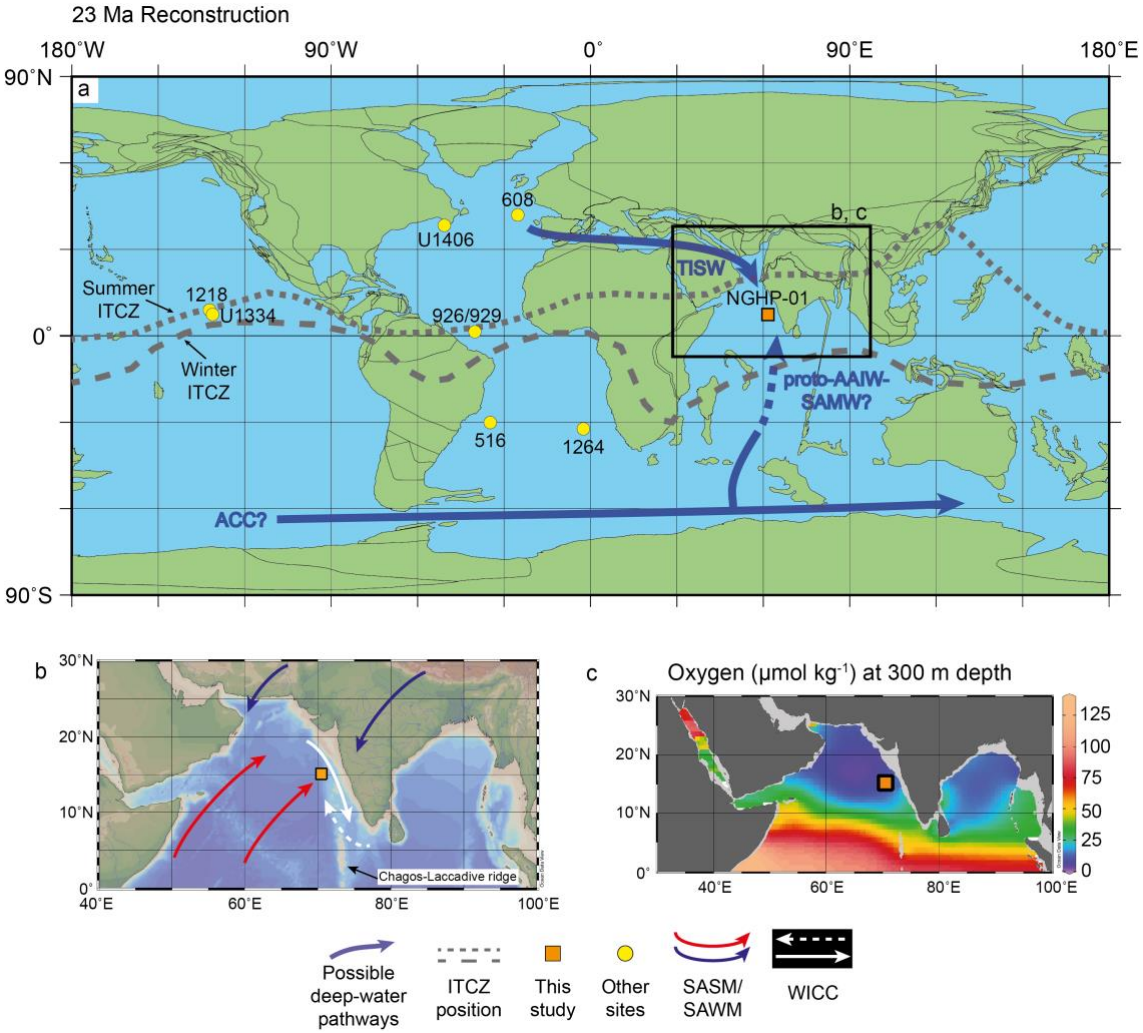

Figure 4.2: *Location of Site NGHP-01-01A shown with orange square in all maps. (a) Paleogeographic map of ~23 Ma (Oligocene–Miocene boundary). Blue arrows show potential deep-water currents affecting the NGHP-01-01A site (e.g., Böning & Bard, 2009; Hamon et al., 2013). Dotted grey line depicts the approximate modern summer position of the ITCZ, dashed grey line shows winter ITCZ position. Yellow circles show other marine core sites containing Oligocene–Miocene aged sediments for which we have comparable geochemical data. The ACC is the Antarctic Circumpolar Current; TISW is Tethyan Indian Saline Water; AAIW-SAMW is Antarctic Intermediate-Subantarctic Mode Water. Map generated through Ocean Drilling Stratigraphic Network (OSDN) Paleomap project (https://www.odsn.de/odsn/services/paleomap/paleomap.html). (b) Modern bathymetric map expanded from black square in map A. Red arrows show SASM winds, blue arrows show SAWM winds. The white arrows show West Indian Coast Current surface circulation during the SASM (solid line) and during the SAWM (dashed line). (c) Modern annual oxygen saturation (µmol kg^{-1}) at 300 m depth, also showing area expanded from black square in map A. Both maps generated with Ocean Data View (Schlitzer, https://odv.awi.de, 2020) using data from World Ocean Atlas 2018.*

4.3 Modern Arabian Sea oceanography

In the modern ocean, the Arabian Sea region is dominantly influenced by the seasonal variability of the SAM subsystem represented by the South Asian summer monsoon (SASM; or Indian summer monsoon) and South Asian winter monsoon (SAWM; or Indian winter monsoon). In the present day, the SAM is caused by seasonal temperature and atmospheric pressure contrasts between the Indian Ocean and adjacent Eurasian landmass (Schott & McCreary, 2001). During the boreal summer (SASM) moisture laden air flows from the cooler Indian Ocean (high atmospheric pressure) towards the warmer Indian landmass (low atmospheric pressure) due to the northward shift of the Intertropical Convergence Zone (ITCZ). This northward shift is controlled by heating of the Indian subcontinent combined with the HTP preventing the intrusion of cooler air from the north (Privé & Plumb, 2007; Bordoni & Schneider, 2008; Boos & Kuang, 2010; 2013; Acosta & Huber, 2020). The moisture is subsequently released as precipitation when reaching the topographic high of the Himalayas. Site NGHP-01-01A in the eastern Arabian Sea is affected by SASM precipitation both directly and via runoff from the Western Ghats, which run as a topographic high parallel to the west Indian coast (Yang et al., 2020). During the SAWM (boreal winter) the atmospheric pressure gradient is reversed, with a southward shift of the ITCZ and dominant airflow from the cooler land to the warmer ocean. This results in strong, dry, north-easterly winds originating from the Indian landmass and flowing towards the Arabian Sea (Fig. 4.2b). It is thought that the majority of lithogenic flux to the Arabian Sea occurs during the SASM from fluvial input derived from the Western Ghats; aeolian (wind blown dust) input during the SAWM constitutes a negligible percentage of mass accumulation in the eastern Arabian Sea (Clemens & Prell, 1990; 1991).

As a result of this seasonally changing atmospheric circulation, surface ocean currents also change seasonally. During the SASM surface water flow in the eastern Arabian Sea is from the north to south, via the West Indian Coast Current (Schott & McCreary, 2001). This surface water flow brings slightly higher salinity surface water from the northern Arabian Sea along the west coast of India during the SASM (Prasanna Kumar et al., 2004). During the SAWM the West Indian Coast Current switches direction and flows from south to north. These waters are

sourced from the Bay of Bengal and the northern Indian Ocean and are thought to bring fresher surface waters along the west Indian coast (Schott & McCreary, 2001; Prasanna Kumar et al., 2004).

During the SASM, strong south-westerly winds along the Somali coast, known as the Somali/Findlater jet (Findlater, 1969), induce surface water currents moving away from the Arabian Peninsula and east Africa and towards western India (deflected to the right due to the Coriolis effect). This creates a strong seasonal coastal upwelling of nutrient-rich deep waters in the western Arabian Sea and resultant high surface productivity (Anderson & Prell, 1993). Seasonally high surface productivity, coupled with a poorly ventilated thermocline, induce an intense OMZ in the Arabian Sea (Fig. 4.2c), present between ~150–1250 m depth (Reichart et al., 2002b; Lachkar et al., 2018). Within this zone oxygen levels can be as low as 2 µM (Reichart et al., 2002b) resulting in intense denitrification (Kim et al., 2018). Although the OMZ is present dominantly in the northeast and central Arabian Sea (Fig. 4.2c), the area of high biological productivity is concentrated around the basin margins and especially the western part of the Arabian Sea (Acharya & Panigrahi, 2016; Lachkar et al., 2018). Site NGHP-01-01A is located within the central-eastern part of the modern OMZ.

The Arabian Sea OMZ is thought to have been at least intermittently present since the middle Miocene (Betzler et al., 2016; Bialik et al., 2020). During Pleistocene glacials, the OMZ was periodically ventilated by incursions of southern sourced Antarctic Intermediate Water and Subantarctic Mode Water (AAIW-SAMW) (Reichart et al., 2002a; Böning & Bard, 2009). Whether similar oceanographic circulation could occur during the Oligocene–early Miocene interval, with different tectonic configuration and climate in place, is unknown as there are no published marine sediment records in the Arabian Sea prior to the early Miocene to test this (Pandey et al., 2016; Bialik et al., 2020; Yang et al., 2020).

4.4 Materials and Methods

Sediment core NGHP-01-01A from the eastern Arabian Sea (15° 18.366’N, 70° 54.192’E; Fig. 4.2) was recovered by the RV *JOIDES Resolution* funded by the

National Gas Hydrate Program (NGHP) of India Expedition-01 in 2006 from a paleodepth of ~2250 m at 25 Ma (current water depth 2674.2 m; see Appendix 6 for paleodepth calculations). The core sits on the eastern side of the Chagos-Laccadive Ridge, where the ridge meets the continental shelf (Fig. 4.2; Collett et al., 2008). The site was consistently located above the carbonate compensation depth (CCD), which was >4000 m during the Oligocene–Miocene interval (van Andel, 1975; Peterson & Backman, 1990; Campbell et al., 2018). The dominant lithology of the Oligocene–Miocene portion of the core is carbonate-rich pelagic ooze, dominated by nannofossil and foraminiferal components with a varying but significant clay component (~20–30 wt%; Johnson et al., 2014). The investigated interval of the core has low total organic carbon content (TOC <1%; Johnson et al., 2014). Importantly, there is no evidence of gas hydrates within the core (Collett et al., 2008); however, in order to ascertain gas hydrate content, periodic whole core samples were taken during shipboard operations leading to core-gaps throughout the study interval. Calcareous nannofossil biostratigraphy suggests continuous sedimentation across the late Oligocene–early Miocene period studied here (Flores et al., 2014 and this study).

4.4.1 Sampling and sample preparation

A total of 185 samples were taken from core NGHP-01-01A between the depths of 233.99 and 280.11 metres below sea floor (mbsf), spanning core sections 30X-1 to 35X-6. A robust calcareous nannofossil biostratigraphic age model for the site (Flores et al., 2014 and this study) shows this part of the core was deposited between the early Oligocene and early Miocene (~31.4 to ~20 Ma). From 262–280 mbsf samples were taken at a resolution of ~50 cm, capturing the early/middle Oligocene. The sections 243–262 mbsf and 214–224 mbsf were sampled at a ~15 cm resolution in order to target the late Oligocene and early Miocene intervals at a higher resolution. The section 224–243 mbsf, comprising the Oligocene–Miocene boundary, was sampled at an ~8 cm resolution.

Samples were freeze dried at –60°C and 0.03 mbar for 8 hours, then soaked in Calgon (buffered sodium hexametaphosphate $[NaPO_3]_6$) for 24 hours. Samples were then washed through a 63 µm sieve with de-ionised water to separate the fine fraction from the sand-sized fraction. The recovered sand-sized fraction was

then covered in Calgon again and placed on a shaker table for 2 hours. Samples were then washed over a 63 µm sieve with de-ionised water followed by methanol to evaporate remaining water and dried in an oven at 50°C.

Coarse fraction (%CF) data were obtained during processing of the samples by weighing the dried bulk sediment ($bulk_w$) after freeze drying and prior to soaking with Calgon. The >63 µm fraction (coarse fraction) was then weighed once dried (CF_w). The %CF was then calculated using the following formula:

$$\%\mathrm{CF} = (\mathrm{CF_w} \div \mathrm{bulk_w}) \times 100 \qquad [\mathrm{Eq.}\ 4.1]$$

The >63 µm CF in this core is made up almost entirely of foraminifera. CF percent abundance is therefore affected by foraminiferal productivity and/or preservation.

4.4.1.1 Foraminifera

Specimens of the planktic foraminifera species *Dentoglobigerina venezuelana* and the benthic genus *Cibicidoides* were picked from the 250–400 µm fraction for geochemical analysis. Where abundance allowed, only the species *Cibicidoides mundulus* was used for stable isotope analyses; a total of 16 samples (out of 162) used other *Cibicidoides* species in the analyses. Of these 16, nine were monospecific analyses of other *Cibicidoides* species and seven were mixtures of other *Cibicidoides* with *C. mundulus*. Planktic foraminiferal species-specific stable isotope and trace element analyses were conducted on the species *D. venezuelana*, a species that is abundant throughout the Oligocene–Miocene (Wade et al., 2018) and has been previously used for geochemical analyses for this time interval (e.g., Wade & Pälike, 2004; Stewart et al., 2012; 2017).

4.4.1.2 Calcareous nannofossils (conducted by CTB)

A total of 51 samples were studied for the presence/absence of calcareous nannofossil marker species under a cross-polarised light microscope with a rotating stage at 1000x magnification in order to provide a robust biostratigraphic framework for the core, to supplement existing lower resolution data from Flores

et al. (2014). Smear slides were prepared using standard techniques (Bown & Young, 1998). Identified calcareous nannofossil bioevents are reported in the Table 7.2 (Appendix 9) along with the bioevents used to construct the age model (Table 7.3; Appendix 9). Ages are calibrated to the timescale of Gradstein et al. (2012).

4.4.2 Foraminiferal stable isotope analysis

Paired planktic and benthic foraminiferal stable carbon and oxygen isotopes ($\delta^{13}C$ and $\delta^{18}O$) were analysed for insights into surface and bottom water oceanography. A total of 166 multi-specimen samples were analysed between the depths 233.99–280.11 mbsf. $\delta^{13}C$ and $\delta^{18}O$ data were generated at the British Geological Survey using an IsoPrime 100 Gas Source Isotope Ratio Mass Spectrometer with Multiprep Device. Average analytical error (2σ) was 0.06‰ for $\delta^{13}C$ and 0.08‰ for $\delta^{18}O$ (n=25) for the standard (KCM) analysed at the same time. Data are reported relative to the Vienna Pee Dee Belemnite (VPDB) scale.

4.4.3 Planktic foraminiferal trace element analysis

Specimens of the planktic foraminifera *D. venezuelana* were also analysed for trace elements, paired with stable isotope analyses, with the primary aim to derive planktic foraminiferal Mg/Ca temperatures (see Section 4.4.3.1). Between 8 and 20 individuals were picked from each sample, then subsequently cracked, homogenised and split, with approximately 1/3 used for the stable isotopes and 2/3 for the trace element analyses. Samples with less than 8 individuals were analysed for stable isotopes only.

Trace element concentrations of 11 elements (Mg, Sr, Li, Ba, Cd, Nd, U, Mn, Fe, Al, Si) were analysed on 87 of the split planktic foraminifera samples. Analyses were conducted at the Open University. Samples were cleaned using a modification of the method outlined in Boyle & Keigwin (1985). Samples were first washed in repeated Milli-Q and methanol rinses, ultrasonicating for ~10 seconds with each rinse, in order to remove any clays. Samples then underwent both a reducing step (ammonia solution and hydrous hydrazine) and an oxidative step (hydrogen peroxide [H_2O_2] and sodium hydroxide [NaOH]) in order to remove Fe-

Mn coatings and organic material respectively (Pena et al., 2005). Finally, samples were polished using a weak (0.001 M) HNO_3 leach and subsequently dissolved in 0.075 M HNO_3.

Samples were analysed using an Agilent Technologies Triple-Quadrupole Inductively Coupled Plasma Mass Spectrometer (QQQ-ICP-MS). An aliquot of sample solution was first used to check [Ca] prior to preparing samples at a fixed [Ca] of 10 ppm for trace element analysis to matrix match with synthetic standards (Rosenthal et al., 1999). Error in analyses were calculated based on a repeat measurement of a synthetic monitor standard during the analytical window (Mg/Ca of 3.32 mmol mol^{-1} with a 2σ of 0.19 mmol mol^{-1} and Mn/Ca of 146.46 µmol mol^{-1} with a 2σ of 5.27 µmol mol^{-1}; n=12). Ratios of Al/Ca and Fe/Ca were monitored and compared with Mg/Ca ratios to assess the efficiency of the cleaning method and any potential contamination (Fig. 7.2; Appendix 8). The ratio of Mn/Ca was used as a proxy for relative oxygenation at the site (Dickens & Owen, 1994).

4.4.3.1 Converting Mg/Ca to temperature

The incorporation of Mg into foraminiferal test calcite is dependent on temperature; the higher the temperature, the greater the ratio of Mg to Ca (Elderfield & Ganssen, 2000). Incorporation of Mg in foraminifera tests has also been shown to be sensitive to both changes in Mg/Ca of seawater (Mg/Ca_{sw}) and pH (Evans et al., 2016a; Gray & Evans, 2019) in various species. To assess the potential impact of Mg/Ca_{sw} and pH, measured planktic Mg/Ca values were corrected using Oligo–Miocene modelled pH values (Zeebe & Tyrrell, 2019) and using the linear regression equation (Eq. 4.2) from Evans et al. (2016a). The average pH value used to correct the data was 8.004 ± ~0.2. A 3-Myr moving average of pH values was also used which acted to lower temperatures by approximately 1ºC compared to values calculated using the average pH; this was smaller than the calculated error, and was therefore not implemented for these analyses.

$$\frac{\mathrm{Mg}}{\mathrm{Ca}} = -0.70 \times \mathrm{pH} + 6.7 \qquad [\mathrm{Eq.}\ 4.2]$$

D. venezuelana is extinct, so no species-specific calibration exists. Thus, temperature (T in °C) was calculated using the multi-species calibration of Anand et al. (2003) (Eq. 4.3) with adjustments of the exponential and pre-exponential constants as per Evans et al. (2016b) (Eqs. 4.4 and 4.5):

$$\frac{\mathrm{Mg}}{\mathrm{Ca}} = \mathrm{B}\exp^{\mathrm{AT}} \qquad [\mathrm{Eq.}\ 4.3]$$

where

$$\mathrm{A} = -0.0029 \times \frac{\mathrm{Mg}}{\mathrm{Ca}_{\mathrm{sw}}^2} + 0.032 \times \frac{\mathrm{Mg}}{\mathrm{Ca}_{\mathrm{sw}}} \qquad [\mathrm{Eq.}\ 4.4]$$

$$\mathrm{B} = 0.019 \times \frac{\mathrm{Mg}}{\mathrm{Ca}_{\mathrm{sw}}^2} - 0.16 \times \frac{\mathrm{Mg}}{\mathrm{Ca}_{\mathrm{sw}}} + 0.804 \qquad [\mathrm{Eq.}\ 4.5]$$

An estimate for Oligocene Mg/Ca_{sw} of 2.15 mol mol^{-1} was taken from Evans et al. (2018) and assumed to be constant throughout the investigated interval as high-resolution data of Mg/Ca_{sw} for this time interval is not available. Mg/Ca_{sw} values from Horita et al. (2002) form an error envelope on the pre-exponential and exponential constants (maximum Mg/Ca_{sw} value of 2.92 mol mol^{-1} and minimum value of 1.67 mol mol^{-1}) due to the uncertainties in the Mg/Ca_{sw} estimations through this interval. The differences between the three calibrations (i.e., Anand et al., 2003 and Evans et al., 2016b with and without pH adjustment) are shown in Figure 7.3 (Appendix 8); the trends remain the same throughout, but with differences in absolute temperatures. The average temperature from the three calibrations is presented in subsequent figures. Calculation of the error propogation of Mg/Ca-temperature estimates is shown in Appendix 7, with the calculated propagated error being 2.93°C.

4.4.3.2 Calculating upper water column $\delta^{18}O$ ($\delta^{18}O_{sw}$)

The geochemical assessment of various size fractions of *D. venezuelana* suggests that it did not host photosymbionts during its life cycle (Stewart et al., 2012). As such, when calculating $\delta^{18}O_{sw}$ it is appropriate to use the low light

calibration from Bemis et al. (1998) to most accurately reflect the relationship between $\delta^{18}O_{sw}$ and foraminiferal test chemistry (Eq. 4.6).

$$T\,(℃) = 16.5 \pm 0.2 - 4.8 \pm 0.16 \times (\delta^{18}O_c - \delta^{18}O_{sw}) \qquad [Eq.\,4.6]$$

This calculation was performed using the various options for temperature reconstructions described above (Fig. 7.3; Appendix 8). The average $\delta^{18}O_{sw}$ from the three calibrations is used in Figure 4.6. Error propagation calculations for the $\delta^{18}O_{sw}$ estimates are shown in Appendix 7, with the calculated propagated error being 1.79‰.

4.4.4 Core scanning X-ray fluorescence (XRF) (data supplied by LG)

Core scanning XRF was undertaken at Woods Hole Oceanographic Institution using a Cox Analytical ITRAX with a Mo X-Ray tube set to 60 kV and 30 mA with a 15 second count time. The XRF spectra were interpreted, and the peak areas were quantified using software Q-Spec. A suite of 13 elements were analysed at 4 mm resolution. Raw counts of Ca are calibrated against values of $CaCO_3$ wt% (this study; see below and Fig. 7.4 in Appendix 8), thus absolute counts detected in XRF have been used quantitatively. Other elements were not calibrated against absolute concentrations of the same sediment samples, therefore only ratios of XRF elemental count data are used. Core scanning XRF-derived elemental ratio of Ti/Ca was used as a proxy for terrigenous input versus biogenic carbonate, Mn/Ti and Mn/Fe were used as proxies for redox conditions (see Rothwell & Croudace, 2015 and references therein).

4.4.5 Inductively coupled plasma optical emission spectroscopy (ICP-OES)

A total of 46 bulk samples were analysed on an ICP-OES Agilent 5110 Series at the University of Exeter Penryn Campus at a resolution of ~1 m. Bulk samples were micro-drilled and weighed at 500–1000 µg using an MSE3.6P-000-DM Sartorius Cubis Micro Balance. The samples were dissolved using 2% HNO_3 and diluted to a nominal Ca concentration of 25 µg g^{-1}. Solutions were run with the limestone standard JLs-1 and synthetic quality control solutions BCQC in order to assess data quality. Ca concentration data were used to calculate percentage

calcium carbonate ($CaCO_3$ wt%) by comparing the theoretical amount of Ca present in the samples based on their weight, versus the measured Ca values in each sample (e.g., Razmjooei et al., 2020). The error, based on the reproducibility of the JLs-1 standard, was measured at 0.6% (2 rsd; n=12), plus the associated weighing error (estimated at ~1%) giving a combined error of 1.2% for $CaCO_3$ wt%.

4.4.6 Scanning electron microscope (SEM)

A scanning electron microscope was used to image representative specimens of *Dentoglobigerina venezuelana* and *Cibicidoides* cf. *mundulus* (Fig. 4.3) in order to assess preservation. Samples were imaged from intervals of both high and low percentage coarse fraction, which in other sites has been related to variable carbonate preservation (e.g., Littler et al., 2014). Analysis was carried out at the University of Exeter, Penryn Campus on a TESCAN VEGA3 GMU SEM. Samples were carbon coated prior to analysis and examined at 20 kV, at a working distance of 2.55–11.88 mm. Images were taken in both back scattered election and secondary electron modes.

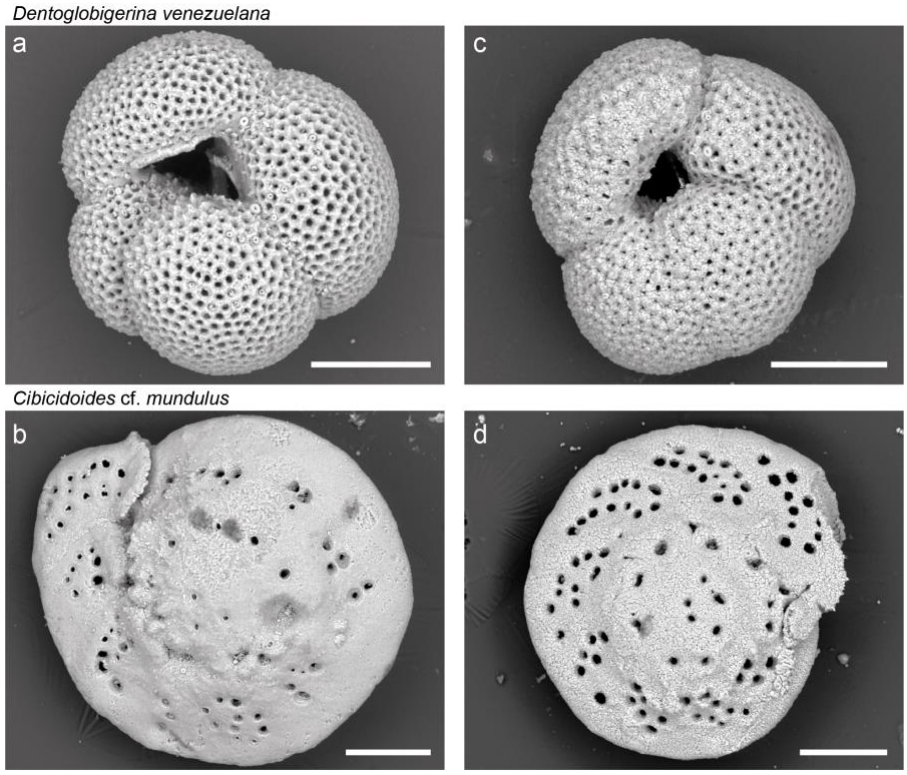

Figure 4.3: *SEM images of foraminiferal species* D. venezuelana *(planktic) and* C. *cf.* mundulus *(benthic) used in stable isotope and trace element analyses. Specimens a (24.4 Ma) and b (21.1 Ma) from intervals with high (5–8%) percentage coarse fraction*

and high (70–80%) $CaCO_3$ wt%. Specimens c (~22.4 Ma) and d (~22.5 Ma) from intervals with low (~0.5%) percentage coarse fraction and lower (~50–60%) $CaCO_3$ wt%. Note more optimal preservation (clear pores and minimal dissolution) in specimens from higher percentage coarse fraction intervals (a and b). Scale bars are 100 µm.

4.4.7 Terrigenous flux (ICP-OES and DBD data supplied by LG)

The rate of terrigenous mass accumulation (MAR) can be used to reveal insights into non-carbonate related sedimentation at a site, assuming minimum contribution from biogenic silica. The terrigenous MAR was calculated using high-resolution $CaCO_3$ (wt%), dry bulk density (DBD), and linear sedimentation rate (LSR) as follows:

$$\mathrm{MAR} = [(100 - \mathrm{CaCO_3}) \times \mathrm{DBD} \times \mathrm{LSR}] \div 100 \qquad [\mathrm{Eq.}\ 4.7]$$

High-resolution $CaCO_3$ (wt%) was calculated (Fig. 7.5 in Appendix 8; R^2 = 0.9558) using Ca counts from core-scanning XRF calibrated to discrete sample measurements of $CaCO_3$ (wt%) performed at WHOI using JY Ultima C ICP-OES following methodology from Bertrand et al. (2012; based on Murray et al., 2000). High-resolution DBD was calculated using discrete sample measurements of DBD correlated to high-resolution multi-sensor core logging density measurements from shipboard data (Fig. 7.5 in Appendix 8; R^2 = 0.4851). The LSR from the biostratigraphic age model were also used.

4.5 Results

4.5.1 Age model

Calcareous nannofossil datums originally identified in Flores et al. (2014) at a relatively low resolution were constrained further in this study to decrease the depth uncertainty associated with each event (blue circles; Fig. 4.4). Two bioevents were not further constrained due to large age uncertainties (orange circles; Fig. 4.4). Sedimentation rates calculated between each age control point (Fig. 4.4) were then used to build an age model by assuming linear sedimentation rates between points. Due to the low resolution of benthic stable isotope data, it was not possible to astronomically tune the record for the age model, and

shipboard magnetostratigraphy was not conducted. Despite this, the biostratigraphic age model appears robust, and is particularly well-constrained around the Oligocene–Miocene boundary. Benthic stable isotope trends are consistent with high-resolution records, which provides support for the implemented age model (Fig. 4.5).

From 262–280 mbsf (lower/middle Oligocene) samples were taken at a resolution of ~50 cm, equating to an approximate temporal resolution of 65 kyr between samples. The sections 243–262 mbsf (late Oligocene) and 214–224 mbsf (early Miocene) were sampled at a ~15 cm resolution, an approximate temporal resolution of 10–40 kyr. The section 224–243 mbsf (Oligocene–Miocene boundary) was sampled at an ~8 cm resolution or a sample every ~13 kyr in the late Oligocene or ~30 kyr in the early Miocene.

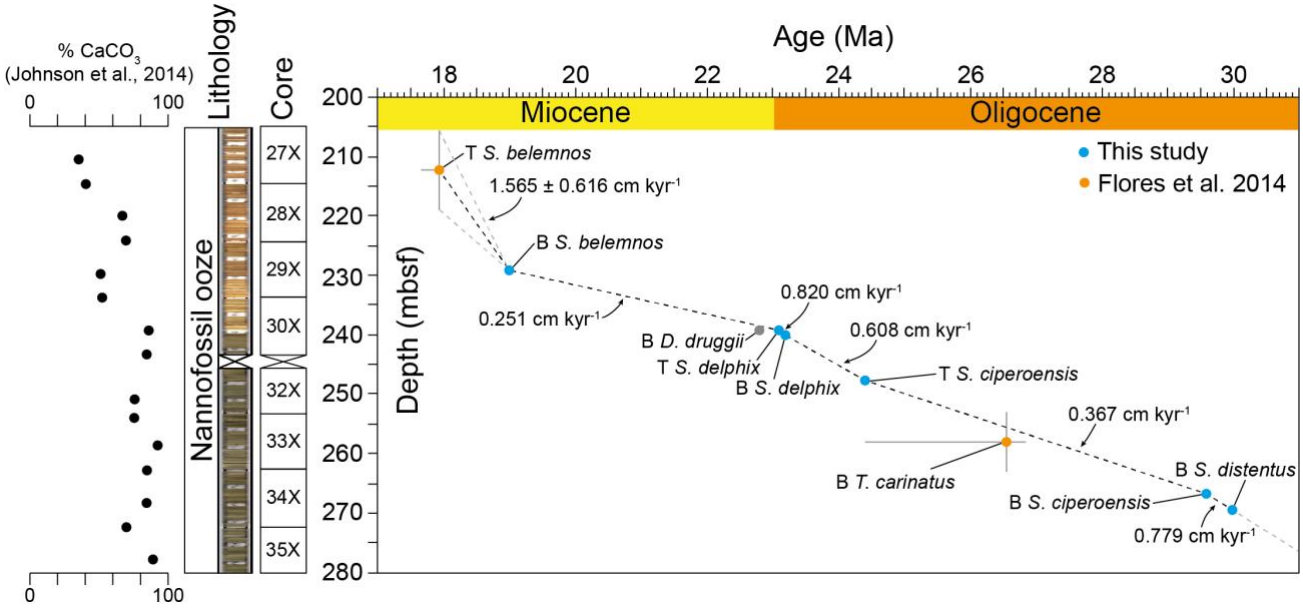

Figure 4.4: *Age-depth plot constructed using the calcareous nannofossil events listed in Tables 7.2 and 7.3 (Appendix 9). B is base of biozone, T is top of biozone. Where no depth error can be seen, error is smaller than data point plotted. Dashed line shows linear interpolated sedimentation rate, with numbers showing calculated sedimentation rates between tie points (in cm kyr^{-1}) used to construct age model (Table 7.3; Appendix 9). Core lithology and core images are shown on the left-hand side. White boxes in the core photos are missing core due to sampling for gas hydrates. Low resolution percentage calcium carbonate data from Johnson et al. (2014) shows decrease approximately coincident with change in core colour ~240 mbsf. Grey data point (*Discoaster druggii *first occurrence) was not used to construct the age model due to poor age constraint on this bioevent, but its approximate position in time is plotted here as an additional qualitative constraint (Young, 1998). Orange data points were not further constrained from Flores et al. (2014) position due to associated age uncertainties: B* T. carinatus *~26.84–24.40 Ma (Young, 1998) and T* S. belemnos *~17.95–17.67 Ma (Bergen et al., 2017; Gradstein et al., 2012).*

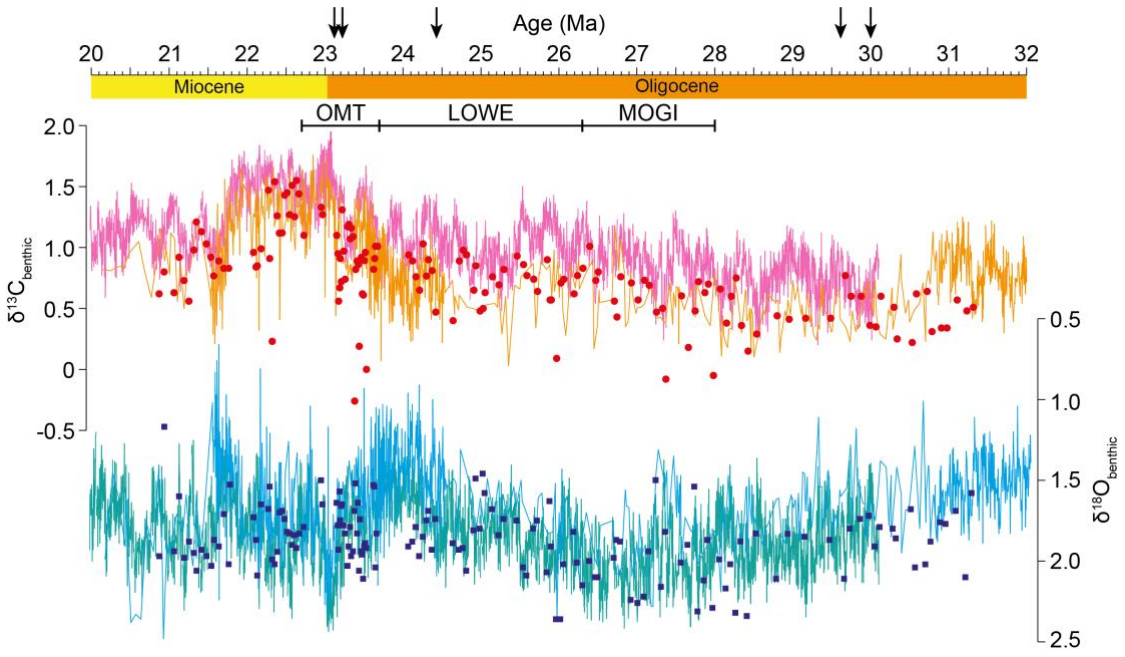

Figure 4.5: *Benthic foraminiferal stable carbon (red circles) and oxygen (blue squares) isotope data from this study (Site NGHP-01-01A; paleodepth ~2250 mbsl) on the new biostratigraphic age model (Fig. 4.4) against other contemporaneous high-resolution data (raw carbon isotope data). ODP Site 1218 (Pälike et al., 2006; paleodepth ~4200 mbsl) in the eastern equatorial Pacific in orange and light blue. ODP Site 1264 (Liebrand et al., 2016; paleodepth ~2500 mbsl) in the equatorial Atlantic in pink and green. Carbon isotopes show good correlation between the records, with offsets in absolute values likely due to different ages of deep-water masses in each ocean basin. Oxygen isotopes show generally similar overall values between sites, with some differences in trends, for example, in the late Oligocene interval where data from the Arabian Sea (this study) remain more positive relative to the Pacific and Atlantic datasets.*

4.5.2 Percentage coarse fraction (%CF) and percentage calcium carbonate

The core is carbonate-rich throughout, with $CaCO_3$ wt% values varying between 45 and 90% (Fig. 4.6a). The highest $CaCO_3$ wt% values are found in the latest Oligocene with distinctly lower values in the Miocene; this is also visible in the cores with an increased brown colouration up section suggesting higher relative clay content (Fig. 4.4). The average percentage coarse fraction (%CF), which is related primarily to foraminiferal content, was 3.85% throughout the whole core, with a maximum value of 11.86% and a minimum of 0.23% (Fig. 4.6c). Two sustained minima (~200 kyr long) of %CF were observed in the core at ~25 Ma (late Oligocene) and ~22.5 Ma (early Miocene). At the 25 Ma %CF minima, values of $CaCO_3$ wt% remain at ~70–80%. At 22.5 Ma the minimum in %CF coincides with lower $CaCO_3$ wt% of 50–60%. Within this interval of low %CF and

low $CaCO_3$ wt% both benthic and planktic foraminifera were less well-preserved, as observed by SEM imaging (Fig. 4.3). Despite this, there is no correlation between %CF and either oxygen isotope values or Mg/Ca-derived temperatures in the whole record (Fig. 7.6; Appendix 8), suggesting that these proxies have not been affected by diagenetic alteration in the core (Edgar et al., 2013). At 23 Ma $CaCO_3$ wt% decreases from ~80% to ~60%; values of $CaCO_3$ wt% remain around 60% until the end of the record at 20 Ma.

Figure 4.6 (next page): *Geochemical and sedimentological analysis of bulk sediment and benthic and planktic foraminifera from Site NGHP-01-01A spanning the middle Oligocene to early Miocene (~31.5–20 Ma). Vertical dashed lines show boundaries between climate intervals of Liebrand et al. (2017); MOGI = mid Oligocene glacial interval; LOWE = late Oligocene warming event; OMT = Oligocene–Miocene transition. Vertical grey line depicts Oligocene–Miocene boundary (~23 Ma). Black arrows show biostratigraphic tie points used to construct age model (Table 7.2; Appendix 9). (a) Weight percent $CaCO_3$ (orange circles); (b) XRF-derived Ca in CPS (grey line); (c) Percentage coarse fraction (%CF; green line); (d) Benthic ($\delta^{18}O_b$) and (e) Planktic ($\delta^{18}O_p$) foraminiferal oxygen isotopes (squares) with 5-point running averages (solid lines); (f) Benthic ($\delta^{13}C_b$) and (g) Planktic ($\delta^{13}C_p$) foraminiferal carbon isotopes (circles) with 5-point running averages (solid lines); (h) Calculated difference between planktic and benthic carbon isotope values ($\Delta\delta^{13}C$); (i) Planktic foraminiferal Mn/Ca (µmol mol^{-1}) with 5-point running average; (j) Temperature and (k) $\delta^{18}O_{sw}$ derived from thermocline dwelling planktic foraminifera* Dentoglobigerina venezuelana*. Modern mean annual sea surface temperature (~28.5°C) depicted by horizontal grey line (from Ocean Data View).*

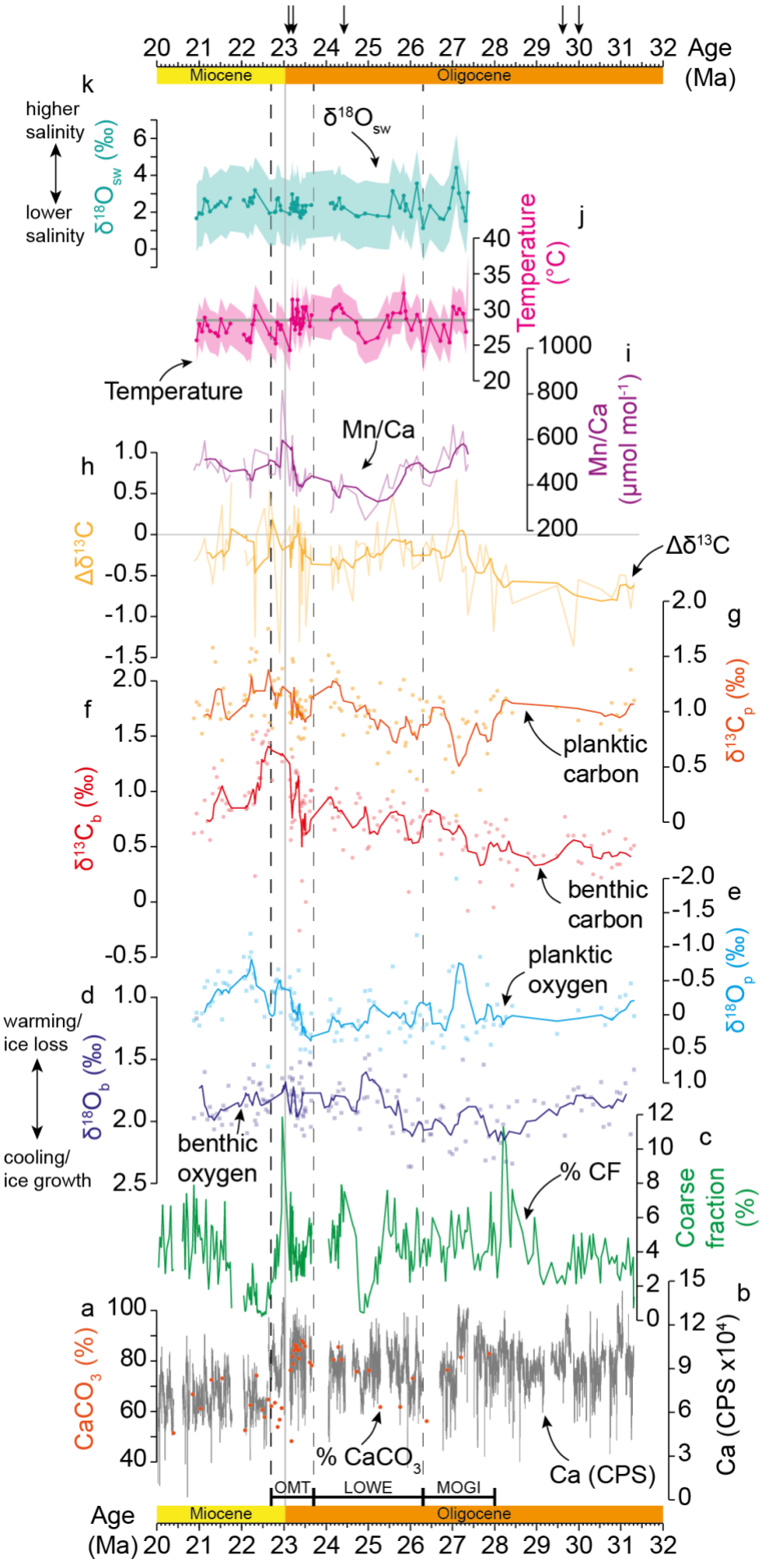
20 21 22 23 24 25 26 27 28 29 30 31 32 Age (Ma)
Miocene
Oligocene
k
higher salinity
lower salinity
δ18Osw (‰)
δ18Osw
j
Temperature (°C)
Temperature
i
Mn/Ca (µmol mol-1)
Mn/Ca
h
ΔδC
ΔδC
g
δ13Cp (‰)
f
δ13Cb (‰)
planktic carbon
benthic carbon
e
δ18Op (‰)
planktic oxygen
d
warming/ ice loss
cooling/ ice growth
δ18Ob (‰)
benthic oxygen
c
% CF
Coarse fraction (%)
a
CaCO3 (%)
% CaCO3
b
Ca (CPS x10⁴)
Ca (CPS)
OMT
LOWE
MOGI
Age (Ma)

4.5.3 Foraminiferal stable isotope analysis

Benthic foraminiferal oxygen isotopes ($\delta^{18}O_b$) have an average value of ~+1.9‰ throughout the record (Fig. 4.6d). In the middle Oligocene, from 31.5–27 Ma, $\delta^{18}O_b$ values increased by approximately 0.6‰ from ~+1.7‰ to ~+2.2‰. Subsequently, there is a decreasing trend (warming/ice loss) from ~+2.1‰ at 26 Ma to ~+1.6‰ at 25 Ma, the approximate time frame of the LOWE. At ~24.9 Ma there is a rapid 0.5‰ increase in $\delta^{18}O_b$ over 0.12 Myr, followed by a subsequent decrease of 0.3‰ over ~1.9 Myr. From 23.1 to ~22.6 Ma (latest Oligocene to early Miocene) $\delta^{18}O_b$ once again increased by ~0.3‰, with values then remaining more stable from 22.6 to 21 Ma at ~+1.7 to +2‰. Planktic foraminifera oxygen isotope ($\delta^{18}O_p$) values are –0.5 to +0.5‰ between ~31.5 and 23.5 Ma (middle to late Oligocene), with a number of spikes to more negative values of up to –2‰ (Fig. 4.6e). From 23.5 Ma to 22 Ma (~OMT) $\delta^{18}O_p$ values have a decreasing trend from +0.5‰ to –1.0‰, with a positive spike within this trend at ~22.6 Ma. From 22 Ma $\delta^{18}O_p$ values once again become more positive, with values ranging from –1‰ to +0.1‰.

Benthic carbon isotopes ($\delta^{13}C_b$) show an overall increasing trend from ~28 Ma, from values of +0.5‰ to a maximum of +1.5‰ at ~22.5 Ma (Fig. 4.6f). From 22 Ma values show a decrease of ~0.8‰. Prior to 28 Ma (middle Oligocene), planktic carbon isotopes ($\delta^{13}C_p$) are ~+1‰ (Fig. 4.6g). From ~28 to 23 Ma (late Oligocene) $\delta^{13}C_p$ values show an overall 1‰ increase, with significant higher frequency variability on the order of ±1‰. After 23 Ma (early Miocene) $\delta^{13}C_p$ values stabilise at between +1‰ and +1.5‰ with variability <±1‰. Benthic carbon and benthic oxygen isotopes show generally similar trends to other equatorial sites in the Pacific and Atlantic through the Oligocene to Miocene interval (Fig. 4.5). Prior to 27 Ma (late Oligocene) $\Delta\delta^{13}C$ (benthic minus planktic carbon isotopes) is –0.5‰; from 27 Ma values trend towards +0‰, with occasional intervals where planktic carbon isotopes are more negative than benthic carbon isotopes (i.e., $\Delta\delta^{13}C$ is positive). This is especially apparent from 23.5–22.3 Ma (latest Oligocene to earliest Miocene). Average $\Delta\delta^{13}C$ values for the investigated interval are –0.29‰, with benthic values being on average more negative than planktic values, as would be expected in normal open marine settings (Fig. 4.6h).

4.5.4 Planktic foraminiferal trace element analysis

We used Mg/Ca ratios to calculate an upper water column paleotemperature record (see Methods), and Al/Ca and Fe/Ca ratios to monitor for contamination by clays (Fig. 7.2; Appendix 8). Both Al/Ca and Fe/Ca show no correlation with Mg/Ca (R^2 values = 0.0084 for Al/Ca, 0.0365 for Fe/Ca), suggesting effective cleaning and a negligible effect of clays on Mg/Ca ratios. From ~27.5 Ma to 26 Ma Mg/Ca values remain around the overall average (3.33 mmol mol^{-1}). At 26 Ma and 24 Ma values peak at ~4 mmol mol^{-1}, with a low between these peaks of ~2.9 mmol mol^{-1}. From 24 Ma onwards Mg/Ca values show an overall decrease of ~1 mmol mol^{-1} from 4 to 3 mmol mol^{-1} over ~3 Myr. Between 21–22 Ma values remain steady at 3 mmol mol^{-1} (Fig. 7.3; Appendix 8).

The overall values of Mn/Ca were high at ~300–800 µmol mol^{-1} (2σ = 5.27 µmol mol^{-1}), however, there is no significant correlation (R^2 = <<0.1) between Mn/Ca or any of the other elemental ratios (Fig. 7.7; Appendix 8) suggesting that that Mn-rich phases have little overall effect on trace element compositions. A reductive step was included in the cleaning of foraminiferal samples prior to trace element analysis, which acts to remove diagenetic Fe-Mn crusts to ensure that only the primary Mn signature is measured. From 27.5–23.5 Ma the Mn/Ca ratio varies between ~400–600 µmol mol^{-1}. From ~23.5–22.9 Ma values peak at up to 800 µmol mol^{-1}, subsequently then decreasing to ~500 µmol mol^{-1} from 22.9–21 Ma.

4.5.4.1 Mg/Ca-temperature calibrations

The average temperature difference between the different Mg/Ca-temperature calibrations is ~7°C (Fig. 7.3; Appendix 8). The multi-species calibration from Anand et al. (2003) resulted in the lowest average temperatures (24°C) and the Evans et al. (2016b) calibration without a pH correction produced the highest average temperatures (31°C). Despite these differences in absolute temperatures, overall trends are very similar (Fig. 7.3; Appendix 8). From 27.4 Ma to ~25 Ma (late Oligocene) there is ~5°C of overall temperature decrease, superimposed with higher resolution orbital-scale variability (Fig. 4.6j). In the latest Oligocene at 25 Ma temperatures increase by approximately 4–7°C

(calibration dependent) over ~0.6 Myr, after which they become more stable until 23.2 Ma where there is a rapid (~60 kyr; 23.20–23.14 Ma) temperature decline of 2–4°C. Two further cycles of gradual warming and rapid cooling then follow from ~23.1–22 Ma with temperature variability of ~5°C. From 22 Ma in the early Miocene values appear to stabilise at 25–30°C. Average values ~23.2–21 Ma are 1.2–2°C cooler than the preceding interval of ~27.5–23.2 Ma.

4.5.4.2 Upper water column $\delta^{18}O$ ($\delta^{18}O_{sw}$)

Calculated $\delta^{18}O_{sw}$ values vary by ~1 to 2‰ due to the different temperature calibrations used, however trends between the different calibrations are similar (Fig. 7.3; Appendix 8). In general, values from 27.5–25.5 Ma (late Oligocene) are highly variable, with maximum values of +5‰ and minimum values +1.5‰ (if using the Evans et al., 2016b calibration). From 25.5–21.0 Ma (late Oligocene to early Miocene) values are more stable, remaining at approximately +3 ± 0.5‰ during this interval (Fig. 4.6k).

4.5.5 XRF core scanning

All XRF-derived elemental ratio records appear to show cyclicity coinciding with short eccentricity pacing (~100 kyr cycles; Fig. 4.7) based on the new biostratigraphic age model, however, cyclostratigraphic analysis of the records was not possible as frequent core gaps were present due to gas hydrate sampling (Fig. 4.4).

The ratio of Ti/Ca can be used to track the changing flux of terrestrially derived Ti against $CaCO_3$ through time. There is clear optical evidence that the $CaCO_3$ in these sediments is dominated by calcareous nannofossils and foraminifera (Collett et al., 2008; Flores et al., 2014; this study), suggesting a dominantly biogenic origin of the $CaCO_3$. The good correlation of XRF-derived Ca counts per second (CPS) against $CaCO_3$ wt% (R^2 = 0.58) and XRF-derived Ca/Ti against $CaCO_3$ wt% (R^2 = 0.70; Fig. 7.4 in Appendix 8) suggests the XRF-derived Ca counts (CPS) can be used as a proxy for changing $CaCO_3$ content in the core (Fig. 4.6a). There is a clear step-change in Ti/Ca ratio at ~23.2 Ma, just prior to the Oligocene–Miocene boundary, where baseline Ti/Ca increases by ~95%

(~0.01 CPS) relative to the Oligocene. Prior to this step increase there are higher-frequency changes in Ti/Ca that appear to occur on ~100 kyr eccentricity timescales (Fig. 4.7).

Raw XRF-derived Ti counts (CPS) increase by 88% at 23.0 Ma. Raw XRF-derived Ca counts (CPS) also show a step-decrease; however, this occurs at ~22.7 Ma (early Miocene). This change also appears to be stratigraphically offset from the decrease in $CaCO_3$ wt% that occurs in the early Miocene at ~23.0 Ma, suggesting that some of the Ca detected in the core scanning XRF data could be derived from clay minerals, rather than exclusively from biogenic $CaCO_3$ (Fig. 4.6a).

Mn/Ti and Mn/Fe also show clear orbital-scale variability throughout the Oligocene interval, with a switch to lower baseline ratios at the Oligocene–Miocene boundary (Fig. 4.7). Prior to this decrease, there is a short interval through the OMT (~23.6–22.9 Ma) where values remain at a higher baseline, with no obvious imprint of short eccentricity as is seen throughout the late Oligocene.

4.5.6 Terrigenous flux

In general, the terrigenous flux (Fig. 4.7a) reflects the sedimentation rate (Fig. 4.7b). Values vary from ~0.1–0.3 g cm^{-2} kyr^{-1} from 30.0–23 Ma, with a very minor reduction in variability to 0.1–0.2 g cm^{-2} kyr^{-1} from 23–20 Ma. Values 30–31.5 Ma are higher than the average for the record, at ~0.3–0.5 g cm^{-2} kyr^{-1}; however, this may be driven by the uncertainty in the age model prior to 30 Ma, and subsequently the LSR, due to a lack of biostratigraphic tie points before 30 Ma.

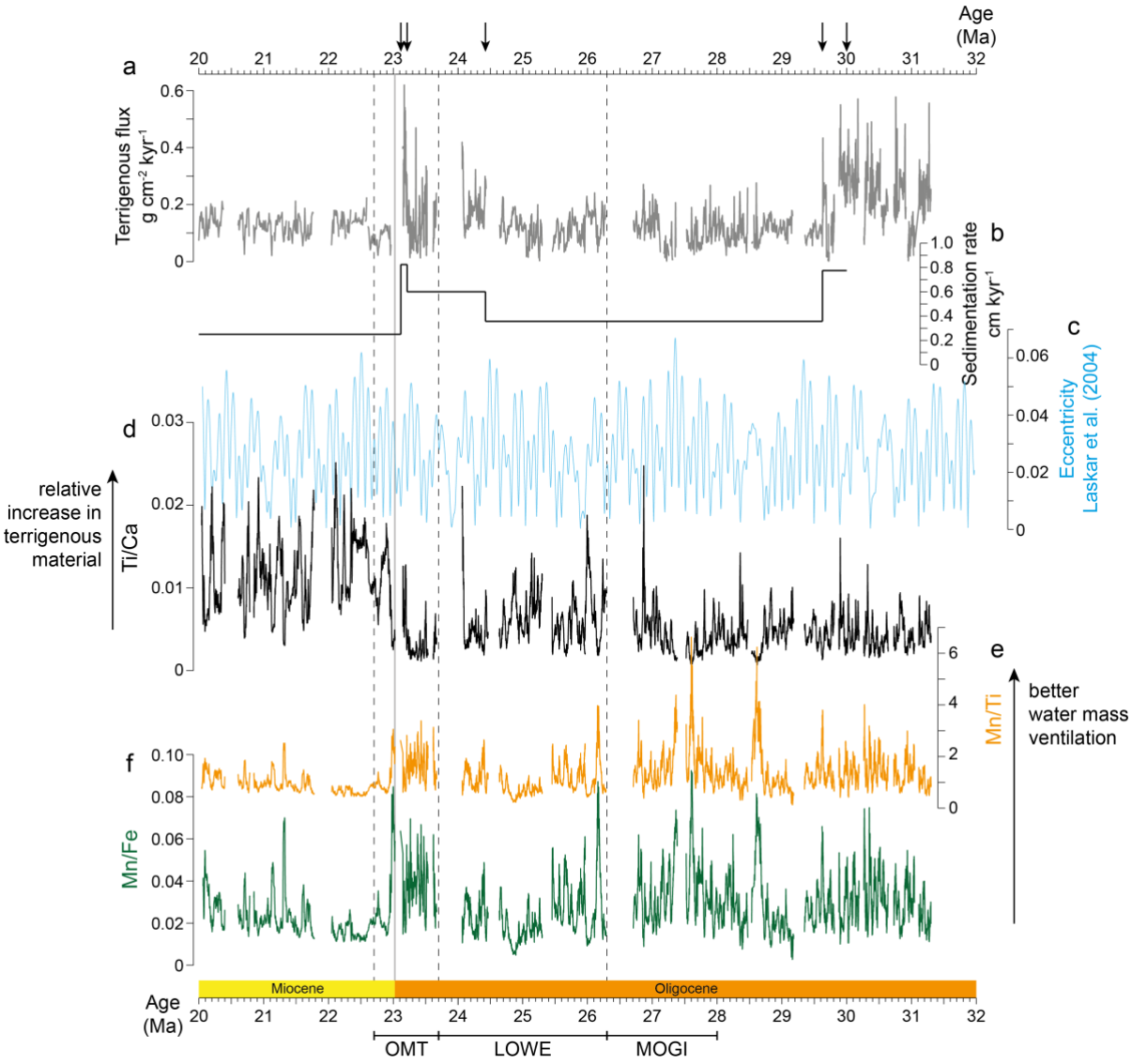

Figure 4.7: *(a) Terrigenous flux (g cm^{-2} kyr^{-1}). (b) Sedimentation rate (cm kyr^{-1}). (c) Laskar et al. (2004) eccentricity solution. Core-scanning XRF-derived elemental ratios (5-point running averages) of Ti/Ca (d), Mn/Ti (e), and Mn/Fe (f). Grey line depicts Oligocene–Miocene boundary. Dashed lines depict boundaries between OMT, LOWE and MOGI (Liebrand et al., 2017), abbreviations as in Figure 4.6. The gaps in the data are due to gas hydrate sampling during the coring expedition; the gap around 26.5 Ma was due to difficulties running core scanning XRF analysis on one section, thus this is not a gap in other data sets.*

4.6 Discussion

4.6.1 Change in Dentoglobigerina venezuelana *depth habitat*

Before drawing broad conclusions about surface water mass changes over time in terms of temperature, salinity, etc., derived from planktic foraminiferal archives, it is important to constrain any changes in the ecological niche that the target

organism may have inhabited. Multi-species stable isotope analyses reveal that the planktic foraminifera species *Dentoglobigerina venezuelana* changed its depth habitat during the late Oligocene, from being a mixed layer dweller (Wade et al., 2007) to a thermocline dweller (Stewart et al., 2012; Matsui et al., 2016). The timing for this change is poorly constrained and appears diachronous across ocean basins, occurring as a two-step change in the eastern equatorial Pacific from 27.4–26.3 Ma (late Oligocene) at IODP Site U1334 (Matsui et al., 2016) and ODP Site 1218 (Wade & Pälike, 2004) and from 24 Ma (latest Oligocene) in the equatorial Atlantic (ODP Site 925; Stewart et al., 2012).

The difference between planktic and benthic carbon isotopes ($\Delta\delta^{13}C$: benthic minus planktic carbon isotopes) can provide insights into the depth habitat of a particular foraminifera species. At Site NGHP-01-01A in the Arabian Sea, at ~27 Ma there is a step shift in $\Delta\delta^{13}C$ towards values approaching 0‰ (Fig. 4.6h) with almost no gradient for the remainder of the record. This convergence of benthic and planktic $\delta^{13}C$ values between ~28–27 Ma in the Arabian Sea, driven by planktic $\delta^{13}C$ becoming ~0.5‰ more negative, is consistent with the migration of *D. venezuelana* to a deeper, thermocline habitat. Other factors that could influence the carbon isotope gradient are a change in surface water primary productivity, or possibly an increase in water mass mixing. There is no concurrent change in other proxies to suggest a change in productivity, for example in the Ca in the core or the %CF (Fig. 4.6b, 4.6c). There is also no concurrent change in proxies for water mass oxygenation (Mn/Fe or Mn/Ti ratios), which may be expected if the water mass became less stratified through increased mixing (Fig. 4.7). We therefore favour the interpretation that the change in $\Delta\delta^{13}C$ at 27 Ma is a result of a deepening in *D. venezuelana* depth habitat to the thermocline, consistent with timing seen in the Pacific Ocean (Wade & Pälike, 2004; Matsui et al., 2016).

There is no concurrent step-change in $\delta^{18}O_p$ data at 27 Ma, merely a long-term increase in values of ~1‰ between ~30.5–23.5 Ma, suggesting this apparent change in depth habitat is not the primary driver of the trend in this parameter. The lack of increase in $\delta^{18}O_p$ (suggestive of a cooler, deeper habitat) could be due to any change being masked by other factors influencing this parameter. For example, a simultaneous increase in freshwater incursion to the site would act to

decrease $\delta^{18}O_p$, masking depth-related changes. Importantly, the Mg/Ca-derived temperature estimates for this record only begin at 27 Ma, by which time the $\Delta\delta^{13}C$ data suggest the depth migration of *D. venezuelana* in the Arabian Sea is complete: hence any subsequent variability in temperature or calculated $\delta^{18}O_{sw}$ across the late Oligocene to early Miocene is independent of additional depth migration issues and can be regarded as representing thermocline conditions. Future additional analyses of multi-species planktic stable isotopes would help to constrain these proposed changes in *D. venezuelana* depth habitat.

4.6.2 Oligocene–Miocene upper water column temperature evolution

The Mg/Ca-derived thermocline temperature recorded at Site NGHP-01-01A is characterised by relatively high variability for a tropical site, which is especially apparent over the period of the LOWE (~26.5–24 Ma; dark green squares in Fig. 4.8). The reconstructed absolute temperatures and trends are broadly in line with other equatorial sites, especially those from equatorial Atlantic ODP Site 926 (light green squares; Stewart et al., 2017), also based on *D. venezuelana* Mg/Ca ratios. All things being equal, the TEX_{86}-derived temperatures would be expected to be warmer than the contemporaneous Arabian Sea temperatures as TEX_{86} is thought to track SSTs rather than thermocline temperatures; this may explain some of the cooler temperatures in the late Oligocene Arabian Sea data compared to the contemporaneous Atlantic data. In general, there is a ~2–4°C temperature decline over the OMT at all sites apart from ODP Site 929 in the equatorial Atlantic (dark grey circles; O'Brien et al., 2020). Temperatures recorded in the latest Oligocene and early Miocene are generally very similar in all the records (~26–30°C), with somewhat higher variability in the range of temperatures in the early–middle Oligocene (temperatures ~25–31°C).

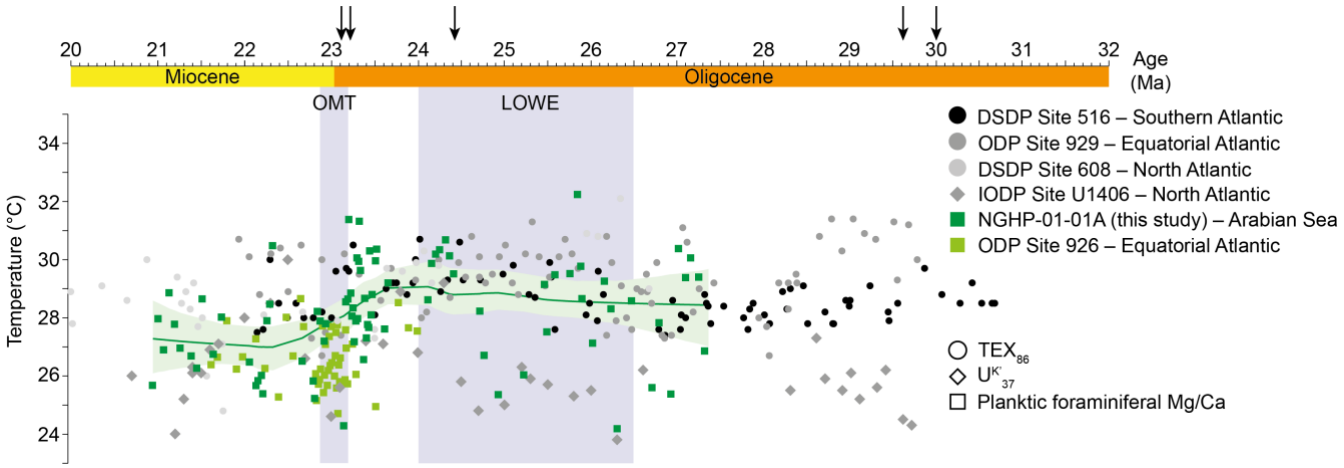

Figure 4.8: *Site NGHP-01-01A (Arabian Sea) compared with other records of upper water column temperature. Planktic foraminiferal (*D. venezuelana*) Mg/Ca records are squares, data from Stewart et al. (2017; ODP Site 926) and this study. TEX_{86} records are circles, data from Super et al. (2018; DSDP Site 608) and O'Brien et al. (2020; ODP Site 929 and DSDP Site 516). $U^{k'}_{37}$ record in diamonds from Guitán et al. (2019; IODP Site U1406). Green data points are those recording thermocline temperatures, grey data points are those recording the surface/mixed layer. The green line is a LOESS curve (smooth = 0.4) and bootstrap confidence interval (shading) of the Arabian Sea data (this study). Arrows show biostratigraphic age model tie points for Site NGHP-01-01A record.*

4.6.3 The early phase of the Oligocene–Miocene transition (23.7–23.0 Ma)

The OMT encompasses a transient glaciation event (~23.7–23.0 Ma), followed by a deglaciation (recovery phase) into the early Miocene (~23.0–22.7 Ma; Liebrand et al., 2017). This event stands out from the background orbitally-driven variability due to the magnitude of the excursion and the two-pulse structure of the positive $\delta^{18}O$ excursion, similar to the Eocene–Oligocene glaciation (~34 Ma; Coxall et al., 2005). It also terminates the long-term warming trend of the LOWE (Liebrand et al., 2017).

From the beginning of the OMT (~23.7 Ma; Liebrand et al., 2017) at Site NGHP-01-01A there is a decrease in the surface-to-deep carbon isotope gradient (decreased $\Delta\delta^{13}C$), an increase in XRF-derived sedimentary Mn/Ti and Mn/Fe ratios, and generally high $CaCO_3$ wt% contents (Fig. 4.9). There is also an increase in foraminiferal Mn/Ca values beginning at ~23.3 Ma (Fig. 4.6i). As it seems likely that *D. venezuelana* has completed its depth migration in this region by this point, the decrease in $\Delta\delta^{13}C$ at the start of the OMT is suggestive of either a decrease in surface water productivity and subsequent decrease in export productivity to deep waters, an increase in vertical water mass mixing stimulating

carbonate productivity, or an incursion of a southern sourced (older) water mass with higher oxygen and carbonate ion content. The concurrent increase in Mn in the core (first bulk, then foraminiferal) suggests increased oxygenation during the early part of the OMT (23.7–23.0 Ma). Increased presence of Mn is generally thought to signal increased ventilation due to Mn becoming less soluble in a more oxygenated water mass (Barras et al., 2018). Importantly, in this study foraminiferal test calcite was cleaned using a reductive cleaning step in order to remove diagenetic Fe-Mn crusts prior to trace element analysis, and so this signal is not related to secondary contamination. While it is possible that some diagenetic crusts persisted after cleaning, there is no correlation between Mn/Ca ratios or any other trace element including Fe/Ca (R^2 = <<0.1; Fig. 7.7 in Appendix 8). In the equatorial Atlantic *D. venezuelana* Mn/Ca ratios were also high (500–1000 µmol mol^{-1}; Stewart et al., 2017), comparable to the values seen in the Arabian Sea. It is thought that Mn can be adsorbed onto foraminiferal test calcite within the water column, during sinking and prior to deposition (Davis & Benitez-Nelson, 2020) with Mn incorporation varying between species (Barras et al., 2018). A decline in Mn abundance in sediments has been used as a proxy for reduced oxygenation and OMZ development in the northern Indian Ocean during the Miocene and Pliocene (Dickens & Owen, 1994; Bialik et al., 2020). All of these factors taken together suggest that during the early part of the OMT, until the Oligocene–Miocene boundary (~23.7–23.0 Ma), there was increased ventilation of thermocline/intermediate waters at Site NGHP-01-01A resulting in high productivity, improved preservation (high $CaCO_3$ wt%, high %CF), and increased Mn incorporation.

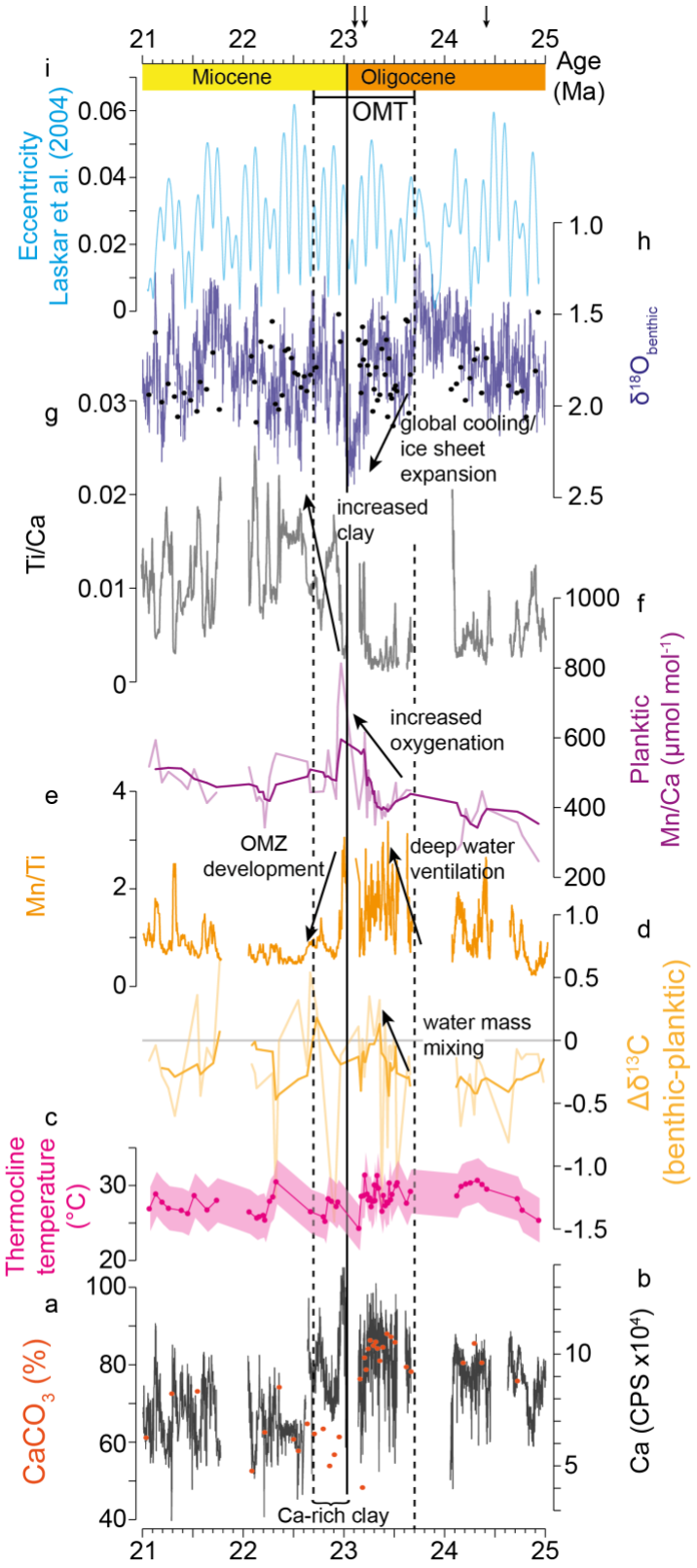

Figure 4.9. *Geochemical data from NGHP-01-01A covering the late Oligocene to early Miocene (25–21 Ma). (a) CaCO3 wt% (circles); (b) XRF-derived Ca abundance (black line); (c) Planktic foraminiferal (thermocline) Mg/Ca-temperature; (d) Surface to deep carbon isotope gradient ($\Delta\delta^{13}C$); (e) XRF-derived Mn/Ti; (f) Planktic foraminiferal Mn/Ca with 5-point running average; (g) XRF-derived Ti/Ca ratio; (h) Benthic oxygen isotopes ($\delta^{18}O_b$) from ODP Site 1264 in the equatorial Atlantic (blue line; Liebrand et al., 2016) and Site NGHP-01-01A (black circles; this study); (i) Eccentricity solution from Laskar et al. (2004).*

This first part of the OMT (23.7–23.0 Ma) is associated with a global increase in benthic $\delta^{18}O$, thought to be due to the expansion of ice sheets in East Antarctica (Zachos et al., 1997; Zachos et al., 2001b), possibly driven by an extended period of low-amplitude orbital cyclicity (Fig. 4.9i; Zachos et al., 2001b; Liebrand et al., 2011). During past global cooling events (Bischoff & Schneider, 2014), Northern Hemisphere cooling (Broccoli et al., 2006), and changes in polar ice cover (Schneider et al., 2014), the ITCZ has been shown to have moved equatorwards, possibly in response to increased net energy input at the low latitudes. With a relative southward shift of the ITCZ over the NGHP-01-01A study site, there would likely be stronger and dominant “winter monsoon” type atmospheric circulation (Dimri et al., 2016; Parvathi et al., 2017), i.e., dry winds would dominantly flow from the Indian landmass in the northeast towards the Indian Ocean (SAWM; Fig. 4.2b).

An average southward shift of the ITCZ during the Oligocene to Miocene glaciation has also been suggested to occur on the basis of data from the equatorial Pacific and Atlantic Oceans: a transient change in surface water flow direction is thought to have allowed the migration of planktic foraminifera *Paragloborotalia kugleri* from the Pacific into the Atlantic via the Central American Seaway (Fraass et al., 2019), and a temporary alteration in wind direction drove dust provenance changes in the equatorial Pacific (Hyeong et al., 2014). Due to the low-resolution nature of both of these datasets, exact timings for these changes are not well-constrained, however both are associated with the early OMT glaciation event (“Mi-1” event; Miller et al., 1991). Hyeong et al. (2014) suggest the southward ITCZ shift is due to an increased Northern Hemisphere cooling rate; this is supported by low-resolution TEX_{86}-derived SST datasets compiled from the Atlantic (Fig. 4.10) which show a relatively warmer South Atlantic during the early phase of the OMT (Super et al., 2018; Guitán et al., 2019; O’Brien et al., 2020).

With a southward shift of the ITCZ causing winter monsoon-like circulation in the Arabian Sea, surface water flows would be predominantly from the south to the north, along the western Indian continental margin (Fig. 4.2b) (Lee et al., 2020a). This would bring relatively warmer, southern sourced surface/thermocline waters to this site during the early OMT (~23.7–23.0 Ma). Relatively warmer thermocline

temperatures are observed in the core over this glaciation interval (Fig. 4.9c), possibly driven by such a change in the source of surface/thermocline waters.

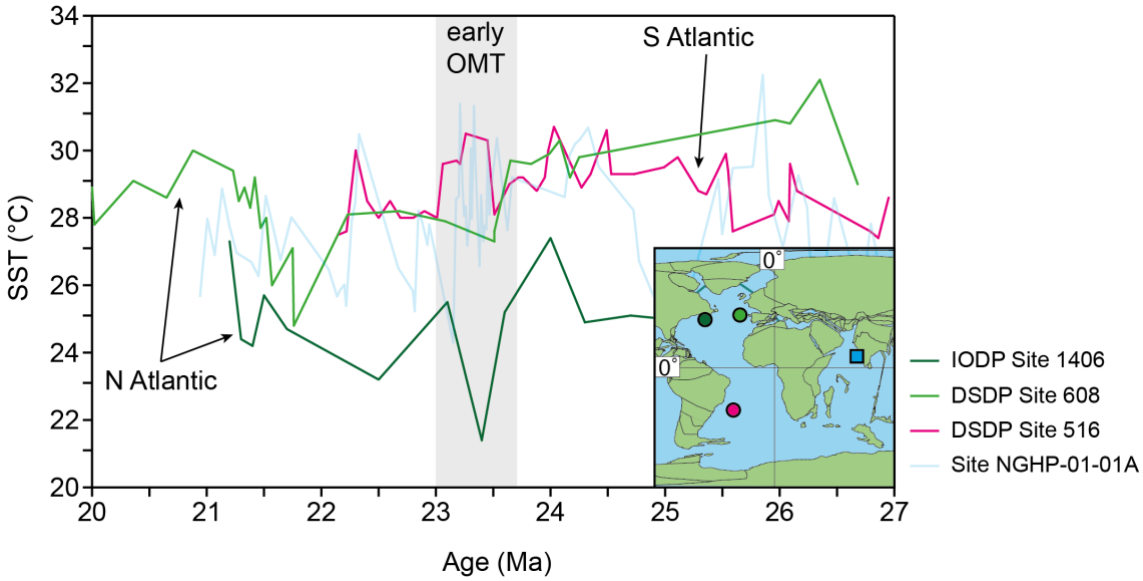

Figure 4.10. Sea surface temperature (SST) records from North Atlantic locations IODP Site 1406 (Guitán et al., 2019) and DSDP Site 608 (Super et al., 2018), and South Atlantic DSDP Site 516 (O'Brien et al., 2020). All Atlantic SST records derived from TEX_{86}, Site NGHP-01-01A thermocline temperature derived from planktic foraminiferal Mg/Ca. Grey box depicts the early phase of the OMT (~23.7–23.0 Ma). Note the relatively cooler North Atlantic and relatively warmer South Atlantic during the early OMT interval. Inset map shows 23 Ma palaeogeography and location of sites discussed.

4.6.3.1 Tectonic changes over the Oligocene to early Miocene

Throughout the Paleogene and early Neogene, Tethyan Indian saline water (TISW) flowed from the Tethys into the northern Indian Ocean as a deep, saline water mass (Wright et al., 1992). This throughflow was dependent on the eastern Tethys gateway between Africa and Eurasia remaining deep and open (Fig. 4.2a). The gateway gradually shallowed from the late Eocene until its eventual closure in the middle Miocene (~14 Ma; Hamon et al., 2013). Modelling studies suggest that even with the gateway being ~250 m deep, effective TISW throughflow may have been compromised (de la Vara et al., 2013; Hamon et al., 2013). Global sea level fall over the OMT is thought to have been on the order of 50–65 m (Wade & Pälike, 2004; Beddow et al., 2016; Miller et al., 2020). As such, as the eastern Tethys gateway continued to shallow, reductions in relative sea level, for example transiently through a glaciation event, may have acted to temporarily change ocean circulation patterns in the Arabian Sea. If the

intermediate TISW mass was temporarily restricted, this could have allowed a northward incursion of the intermediate AAIW-SAMW, transiently affecting ocean circulation and thus foraminiferal geochemistry at Site NGHP-01-01A over the Oligocene–Miocene glaciation. However, at this time more evidence is required to support this hypothesis.

The role of changing tectonics/topography in the initiation of the Indo-Asian monsoon systems has been investigated through increasingly detailed modelling (Chakraborty et al., 2009; Wei & Bordoni, 2016; Acosta & Huber, 2020). Acosta and Huber (2020) show that monsoonal atmospheric circulation is established over the Bay of Bengal and Arabian Sea regions with sufficient SST gradients and subsequent seasonal movement of the ITCZ; however, the flow of moisture onto the continent and summer precipitation above 30°N is weak or absent without topographically forced (e.g., HTP-related) orographic precipitation. For Site NGHP-01-01A, direct precipitation in the models occurs over the locality even in the flat topographic simulation (Acosta & Huber, 2020). The Western Ghats are shown to be important drivers of orographic precipitation in this region, supplying runoff into the eastern Arabian Sea (Xie et al., 2006). A study of $^{40}Ar/^{39}Ar$ ages in the Western Ghats has shown that weathering and denudation has been active since at least the middle Eocene (~44 Ma; Jean et al., 2020). Modelling studies suggest that African and Arabian topography impact the strength and pattern of the Somali Jet but with only small effects on the spatial pattern, strength and seasonality of SAM precipitation (Chakraborty et al., 2009; Wei & Bordoni, 2016). These modelling studies therefore suggest that the tectonic/topographic configuration required for an active monsoon system (in terms of atmospheric circulation) in the Arabian Sea region has been present since at least the middle Eocene. However, it is unclear when the SAM atmospheric circulation and runoff intensified enough to have a strong impact on the Arabian Sea such that it became the dominant control on ocean circulation, salinity and oxygen content in the region.

4.6.4 The late phase of the Oligocene–Miocene transition (23.0–22.7 Ma)

Coincident with the Oligocene–Miocene boundary (~23 Ma) there is a distinctive change in the sediment colour at Site NGHP-01-01A, from a carbonate-rich,

green/grey nannofossil ooze in the Oligocene to a brown, clay-rich ooze in the Miocene (~240 mbsf; Fig. 4.4). Associated with this observed sedimentological change is: 1) a step increase in Ti/Ca counts suggesting a relative increase in the terrigenous fraction (Figs. 4.7, 4.9); 2) a decrease in $CaCO_3$ wt% (Fig. 4.9a); 3) significant decreases in XRF-derived Mn/Fe and Mn/Ti ratios (Fig. 4.7); and 4) a small decrease in planktic Mn/Ca (Fig. 4.9f; Betzler et al., 2016; Bialik et al., 2020). Previous investigations of clay mineralogy at this site are at a much lower resolution but show that between ~228–240 mbsf (~23.0–19.0 Ma) smectite within the core makes up ~80% of the smectite vs. kaolinite fraction, whilst ~250–280 mbsf (prior to 23 Ma) it only made up ~50% (Phillips et al., 2014). Illite also shows a step-increase from 0% to ~50% of the illite vs. chlorite fraction at ~23 Ma (Phillips et al., 2014). Given the low resolution, these changes occurred sometime between ~25 and 23 Ma (Phillips et al., 2014). Within the Arabian Sea, provenance studies from the Holocene to Miocene have shown that smectite and illite are derived from the weathering of the Deccan province in western India and transported to the Arabian Sea via the Indus fan. Hence, these data may suggest a general increase in contribution from the weathering of NW India and/or the Himalayas to the eastern Arabian Sea (Alizai et al., 2012; Limmer et al., 2012; Cai et al., 2018; Chen et al., 2019; Yu et al., 2019; Chen et al., 2020) from the late Oligocene to early Miocene (Phillips et al., 2014). However, high-resolution provenance data for this site are required to support this hypothesis.

Coincident with the relative increase in terrigenous input (i.e., increased Ti/Ca) at the Arabian Sea site, there is a contemporaneous long-term decrease in sedimentation rate from 0.6 cm kyr^{-1} in the late Oligocene to 0.25 cm kyr^{-1} in the early Miocene (Fig. 4.7b). The decrease in sedimentation rate would suggest that the observed sedimentological changes are driven by a relative reduction in $CaCO_3$ deposition (as opposed to, or in addition to, an actual increase in clay input), beginning at the Oligocene–Miocene boundary (~23 Ma) and continuing into the early Miocene. This assertion is supported by the steady rate of terrigenous flux throughout this interval suggesting terrigenous supply to this site remained unbroken into the early Miocene (Fig. 4.7a), although we note that sedimentation at a single site cannot be considered representative of the region as a whole. There is also a transient decrease in $CaCO_3$ preservation shown by the significant fall in average %CF (Fig. 4.6c), as well as the less well-preserved

foraminifera observed under SEM during these low %CF intervals (Fig. 4.3). Benthic foraminifera *C.* cf. *mundulus* shows enlarged pores (Fig. 4.3d) and planktic foraminifera *D. venezuelana* displays encrusted/overgrown pores (Fig. 4.3c), both indicative of minor dissolution/recrystallisation. Enlarged pores of epibenthic foraminifera has also been shown to be a proxy for reduced bottom water oxygen (Rathburn et al., 2018), supporting the inference of reduced oxygenation during this interval. Importantly, although there seems to be some dissolution of foraminifera in the low %CF intervals this has not systematically biased either the isotope or trace element data (e.g., to lower Mg/Ca values; Fig. 7.6 in Appendix 8). An apparent offset between the decline in $CaCO_3$ wt% data and XRF-derived Ca counts specifically in the interval 23.0–22.7 Ma (Fig. 4.6a) is possibly due to the presence of Ca within smectite clays enhancing XRF-derived Ca. This $CaCO_3$–Ca offset therefore supports our interpretation of a decrease in carbonate fraction (biogenic calcite) and concurrent relative increase in (likely smectite dominated) clays at 23.0–22.7 Ma.

The most harmonious explanation for a simultaneous dissolution event (reduced $CaCO_3$ and preservation), decrease in oxygenation (Mn/Ca and sedimentary Mn), and a relative increase in terrigenous material (possibly driven by a change in chemical weathering) in the earliest Miocene (23.0–22.7 Ma; Fig. 4.9) is a strengthening of SASM-like conditions in the Arabian Sea, such that the impacts are observed at Site NGHP-01-01A. The SASM under modern oceanographic conditions induces an intense OMZ in the north, central and eastern Arabian Sea due to strong southwest winds causing upwelling and productivity in the western Arabian Sea (Fig. 4.2c). The Arabian Sea OMZ is present at intermediate depths (between ~150–1250 m depth in the modern; Reichart et al., 2002b; Lachkar et al., 2018). Although the Arabian Sea OMZ is partly driven by seasonal summer upwelling and high productivity, it is present throughout the year (McCreary et al., 2013), however observations suggest a seasonally decreased southward and westward extent during the SAWM (Shenoy et al., 2020). Intriguingly, the zone of high productivity is in the west, but the most intense part of the OMZ is in the north and east of the Arabian Sea; although a number of theories have been put forward to explain this offset between upwelling and deoxygenation zones, it remains enigmatic (Shenoy et al., 2020). *D. venezuelana* was a thermocline dwelling species (Wade & Pälike, 2004; Stewart et al., 2012; Matsui et al., 2016),

therefore likely inhabiting the upper part of our proposed OMZ through the early Miocene. The apparent dissolution of foraminifera at ~23.0–22.0 Ma could either be due to increased CO_2 (acidification) in the water column from high productivity/organic carbon flux and associated biotic respiration in surface waters (Lombard et al., 2010; Mungekar et al., 2020) and/or respiratory dissolution of carbonates on the seafloor due to increased organic carbon burial (Mawbey & Lear, 2013; Stewart et al., 2017).

The main terrigenous input to Site NGHP-01-01A today is via rivers flowing off the Western Ghats. Although many of the rivers originating in the Western Ghats flow to the east into the Bay of Bengal, several small rivers flow west into the Arabian Sea (Yang et al., 2020). As such, we expect terrigenous material derived from our proposed increase in the SASM at the Oligocene–Miocene boundary to have a provenance indicative of the Deccan Traps region (e.g., Phillips et al., 2014; Cai et al., 2018; Chen et al., 2019; Yu et al., 2019; Chen et al., 2020; Clift et al., 2020). Without quantitative provenance data such as neodymium isotopes (to constrain weathering source) we are unable to unequivocally state that the increase in weathering products (e.g., Ti) were sourced from the Deccan Traps. Future work will aim to constrain provenance changes and weathering fluxes from the hinterland through this time interval.

The deglaciation phase of the OMT (~23.0–22.7 Ma; Mawbey & Lear, 2013) is characterised by high-amplitude variability in short (~100-kyr) eccentricity cycles (Liebrand et al., 2017), in contrast to the low variability during the onset of the OMT glaciation period (Miller et al., 1991; Zachos et al., 2001b). This is reflected in the amplitude of benthic oxygen isotope records at this time (Zachos et al., 2001b; Liebrand et al., 2016; 2017). This change in orbital configuration could be the driving mechanism behind this intensification of the SAM (especially the SASM) over this deglaciation interval. An increase in orbital variability may trigger high frequency variability in atmospheric CO_2, perhaps not observed in currently available supra-orbital scale records of pCO_2 over the Oligocene and early Miocene (Fig. 4.1e; Grein et al., 2013; Zhang et al., 2013; Greenop et al., 2017; Liebrand et al., 2017; Tesfamichael et al., 2017; Londoño et al., 2018; Greenop et al., 2019; Steinthorsdottir et al., 2019). General circulation modelling suggests increased pCO_2 is linked to increased SAM precipitation amount and area (Turner

& Annamalai, 2012; Kitoh et al., 2013) as well as stronger atmospheric winds blowing northwards in the Indian sector (Cherchi et al., 2011), thus suggesting increased CO_2 during the Oligocene–Miocene may have driven the observed changes at Site NGHP-01-01A.

Our data record no clear change in $\delta^{18}O_{sw}$ over the OMT, which would be an indicator of an intensification of monsoonal precipitation in the eastern Arabian Sea and/or increased monsoon-driven runoff from peninsular India. Despite this, there is a significant decrease in planktic foraminiferal $\delta^{18}O$ values (Fig. 4.6e). This disparity in oxygen isotope trends suggests there was no change in the evaporation-precipitation balance at this site, despite the development of an intense OMZ suggesting monsoonal atmospheric circulation was active from at least the earliest Miocene. As *D. venezuelana* is a thermocline dwelling species during this interval it is possible that the effects of changes in surface ocean evaporation-precipitation balance was not transmitted to these depths. Our data therefore suggest an intensification of a proto-SAM based upon the influence of the monsoon systems on the thermocline and deep waters in this region, not on the sea surface.

4.6.5 Long-term shift in sedimentology at Site NGHP-01-01A

Several modelling studies have suggested that the SAM has been active since at least the early Eocene (e.g., Huber & Goldner, 2012; Farnsworth et al., 2019; Acosta & Huber, 2020). Based on our data from the eastern Arabian Sea, the Oligocene–Miocene boundary was a key interval of strengthening of this proto-monsoon system. This suggests that perhaps there was a long-term shift in climatic/tectonic/orbital conditions, which triggered the intensification of a proto-SAM wind system over this interval (i.e., a well-developed OMZ in the eastern Arabian Sea), implying a strong Somali/Findlater jet (monsoonal atmospheric circulation). A number of possibilities arise for a long-term strengthening of a proto-SAM through this interval, evidenced from the decrease in biogenic calcite (decreased $CaCO_3$ wt% and XRF-derived Ca), occurrence of a well-developed OMZ (decrease in Mn) and possible increase in chemical weathering products (smectite) from 23 Ma onwards (Fig. 4.9). These possibilities are discussed below.

It has been suggested that as India transitioned northwards to its current position, it moved through the ITCZ during the early Miocene (Beaumont et al., 2001; Clift et al., 2008; Armstrong & Allen, 2011). This movement not only initiated more intense monsoonal rainfall but may have also created a feedback, which initiated elevated Himalayan exhumation rates (due to increased denudation and subsequent lithospheric unloading). This is supported by the existence of a large unconformity in Himalayan sedimentary sequences spanning the Oligocene–early Miocene interval, possibly due to high rates of erosion of the Himalayas (Clift & Vanlaningham, 2010). Modelling of Eocene boundary conditions also showed that this northward movement of India through the ITCZ acted to redistribute moisture convergence in the region (Huber & Goldner, 2012). As India continued to move further north into its current position, a more seasonal, modern monsoon system would have been established (Armstrong & Allen, 2011; Allen & Armstrong, 2012).

Alternatively, the retreat of the Paratethys Sea (a restricted sub-basin of the Tethys Ocean), due to HTP uplift, is thought to have facilitated a shift from a temperate to continental climate in central Eurasia, causing a subsequent drying of this area (Ramstein et al., 1997; Fluteau et al., 1999). This would have provided a source of aeolian dust to be transported to the Arabian Sea and northern Indian Ocean, predominantly by north-easterly winter monsoon winds (Aston et al., 1973; Betzler et al., 2016). However, the flux of aeolian material to the eastern Arabian Sea is thought to be negligible compared to fluvially-derived terrigenous materials (Clemens & Prell, 1990; 1991). Estimates vary for when central Eurasian desertification may have occurred, yet several Central Asian loess and paleobotanical records are dated to the late Oligocene to early Miocene interval (Guo et al., 2002; Sun & Wang, 2005; Qiang et al., 2011; Lu & Guo, 2014; Zheng et al., 2015; Licht et al., 2016).

Finally, changes in orbital configuration drive changes in insolation at the Earth's surface which in turn affects the hydrological cycle. During the Oligocene, periods of global warmth (indicated by benthic oxygen isotope compilations) coincided with times of high insolation in the Northern Hemisphere (i.e., perihelion in Northern Hemisphere summer), whereas global warmth during the Miocene occurred during times of both Northern and Southern Hemisphere high insolation

(De Vleeschouwer et al., 2017). The early Miocene interval was also a time of high amplitude variability in short eccentricity (Liebrand et al., 2017). These changes in orbital forcing are proposed to have driven changes in Antarctic ice volume and atmospheric CO_2 on astronomical timescales (De Vleeschouwer et al., 2017; 2020), with the latter having a potential impact on the global and regional hydrological cycle (Yang et al., 2003; Lu & Guo, 2014; Carmichael et al., 2016) and subsequently the monsoon systems.

Given that tectonic movements are relatively slow, and the apparent increase in proto-monsoon intensity at the Oligocene–Miocene boundary in our records occurs over <500 kyr, it is likely that the sudden step-change we observe in the eastern Arabian Sea at ~23 Ma is primarily due to orbitally-forced climatic factors superimposed on long-term regional tectonic forcing of oceanic gateways and uplift. The strengthening of a proto-SAM system by the earliest Neogene is supported by fossil megaflora in India (Srivastava et al., 2012), dust provenance studies from the Maldives (Betzler et al., 2016), enhanced weathering of the Western Ghats at the Oligocene–Miocene boundary (Jean et al., 2020), a major Oligocene–Miocene unconformity in the Himalayan foreland basin (Clift & Vanlaningham, 2010), increased erosion of the Himalayan foreland basin evidenced from thermochronology data (Clift et al., 2008; Webb et al., 2017), and increased SAM precipitation observed in a recent modelling study (Thomson et al., 2021). Data from the same Site NGHP-01-01A from the middle Miocene show a major strengthening in SAM precipitation and runoff from ~15 Ma (Yang et al., 2020). Our records now also show a strengthening of a proto-SAM system at the Oligocene–Miocene boundary.

4.7 Conclusions

The sedimentary sequence from eastern Arabian Sea site NGHP-01-01A is the first marine record to cover the Oligocene to early Miocene interval in this region, helping to fill a critical gap in our knowledge of this time period. We employ a multi-proxy approach, including core scanning XRF data to investigate bulk sediment elemental composition, as well as foraminiferal geochemistry (stable isotopes and trace elements). According to foraminiferal stable isotope compositions ($\delta^{13}C$, $\delta^{18}O$), the isotopic records from this site are commensurate

with other low latitude sites through this time interval, following broadly the global trends, especially in benthic carbon isotopes. Throughout the Oligocene and early Miocene interval warm subtropical thermocline temperatures persisted (~25–32°C), with climate events such as the LOWE and OMT not being particularly prominent, similar to other records from the low latitudes.

During the earliest part of the OMT (23.7–23.0 Ma) there was an increase in water column mixing and ventilation at this site, possibly driven by an increase in winter monsoon-type atmospheric circulation. This is evidenced by a reduction in $\Delta\delta^{13}C$, increase in bulk sediment Mn/Fe and Mn/Ti and foraminiferal Mn/Ca (signalling increased oxygenation), and good $CaCO_3$ preservation. We suggest this change was driven by a southward shift of the ITCZ over the peak of OMT glaciation due to the occurrence of an extended period of low eccentricity orbits (Zachos et al., 2001b; Liebrand et al., 2017). Coincident with the Oligocene–Miocene boundary in the latter part of the OMT (~23.0 Ma) there was a long-term change in sedimentation at this site. A reduction in $CaCO_3$ and %CF, rise in Ti/Ca, high smectite (possible weathering products of the Deccan Traps), and relative reduction in bulk sediment Mn/Fe and Mn/Ti (reduced oxygenation) all suggest that this step-change was caused by an strengthening of a proto-SAM system and associated development of an intense OMZ. It is evident from middle Miocene age data from this site that there was a major intensification of the SASM coinciding with the middle Miocene climate transition (Yang et al., 2020). Overall, our new data suggests an earlier intensification of a proto-SAM at the Oligocene–Miocene boundary.

Chapter 5: Palaeoceanography of the Tethyan corridor over the Paleocene–Eocene transition

5.1 Abstract

A new record of marine neodymium isotope values was generated from the eastern Tethys (onshore Jordan) in order to investigate the oceanographic configuration in this previously understudied area over the late Paleocene–early Eocene (~58–54 Ma) interval, including the Paleocene–Eocene thermal maximum (PETM). Preliminary results show a long-term change in the neodymium isotope record, from being relatively radiogenic (more positive) in the late Paleocene to less radiogenic (more negative) in the early Eocene. The cause of this long-term decrease could be due to a combination of internal cycling processes bringing radiogenic neodymium to the site during the late Paleocene and a change in water mass contribution to this site during the early Eocene. Additional data are required to ground truth this hypothesis. There does not appear to be a significant change in the neodymium isotope composition, and thus the water mass composition or source, during the PETM itself, although the number of data points across the event is limited. Due to disruption associated with the Covid-19 pandemic, this chapter is not complete and contains preliminary data and discussions. Future analyses required to complete this dataset are discussed in Chapter 6.

Co-author contribution: AD provided sample material. CB disaggregated, processed, cleaned, and ran column chemistry and isotope analysis of first batch of samples. CB disaggregated and processed second batch of samples, AD cleaned and ran isotope analysis (due to Covid-19 pandemic CB was not able to access Royal Holloway labs). CB constructed chapter, with edits from AD and KL.

5.2 Introduction

The PETM (~56 Ma) was a time of rapid, transient global warming superimposed on a multi-million year warming trend that occurred from the late Paleocene to middle Eocene (~59–50 Ma; Westerhold et al., 2020). A detailed introduction to

the causes and consequences of the PETM is given in Chapter 2. Although this event has been extensively studied, especially in the deep sea, there is a lack of detailed geochemical data to reconstruct palaeoceanographic circulation in the Tethyan realm. This was an important area with respect to potential transient changes in oceanic circulation through this time (see Section 5.2.2). The dearth of data is especially apparent in the record of neodymium (Nd) isotopes, where large data gaps exist in the 'global' long-term records (Stille et al., 1996; Thomas et al., 2003; Thomas et al., 2014; Abbott et al., 2016).

5.2.1 Neodymium isotopes as ancient water mass tracers

Radioactive isotope ^{147}Sm occurs in many rock-forming minerals and alpha decays to form radiogenic isotope ^{143}Nd with a half-life of ~106 billion years. This decay system imparts different $^{143}Nd/^{144}Nd$ ratios in rock formations, depending on lithology and age (van de Flierdt et al., 2016). When these rocks are subsequently weathered and the products eroded and transported to the sea, these signatures are imprinted on local oceanic water masses where they behave in a quasi-conservative fashion (Piepgras et al., 1979). Isotopic ratios of Nd are expressed in epsilon notation (ε_{Nd}) relative to the CHUR (chondritic uniform reservoir; Eq. 5.1; Jacobsen & Wasserburg, 1980) at the time of deposition. Traditionally Nd isotopes in palaeoceanography are used to track changes in the sources of water masses through time, as each ocean (sub)basin can have a different Nd isotopic signature, inherited from the weathering and erosion of crustal rocks surrounding the basin. While dust and riverine input are important sources of Nd to the oceans, boundary exchange (i.e., the interaction of seawater with continental margins) is now thought to be a dominant process through which Nd is incorporated into seawater (Lacan & Jeandel, 2005; Jeandel et al., 2007; van de Flierdt et al., 2016). Internal cycling processes, such as adsorption/desorption or dissolution/precipitation in particulate phases (also known as reversible scavenging), can also modify ε_{Nd} values (van de Flierdt et al., 2016). In the modern world the Pacific Ocean has the most radiogenic (i.e., the most positive) ε_{Nd} isotopic signature (~0 to –5), due to the weathering and erosion of young volcanic rocks around this basin, the Atlantic has the least radiogenic (i.e., the most negative; ~–10 to –14) due to the erosion and input of much older (cratonic) rocks, with the Indian Ocean being intermediate between

these values (Piepgras et al., 1979) (Fig. 5.1). These spatial trends have broadly persisted throughout the Cenozoic (Fig. 5.2), albeit with deviations caused by internal cycling processes which modify water mass ε_{Nd}, as well as changes to oceanic circulation and end-member water mass mixing (e.g., Thomas et al., 2014; Batenburg et al., 2018; McKinley et al., 2019). Neodymium has a short residence time in the oceans compared to the oceanic mixing time (600–2000 yrs; Frank, 2002), making Nd isotopes a quasi-conservative tracer of oceanic circulation due to their homogeneity across ocean basins (Piepgras et al., 1979; Arsouze et al., 2007; Tachikawa et al., 2017).

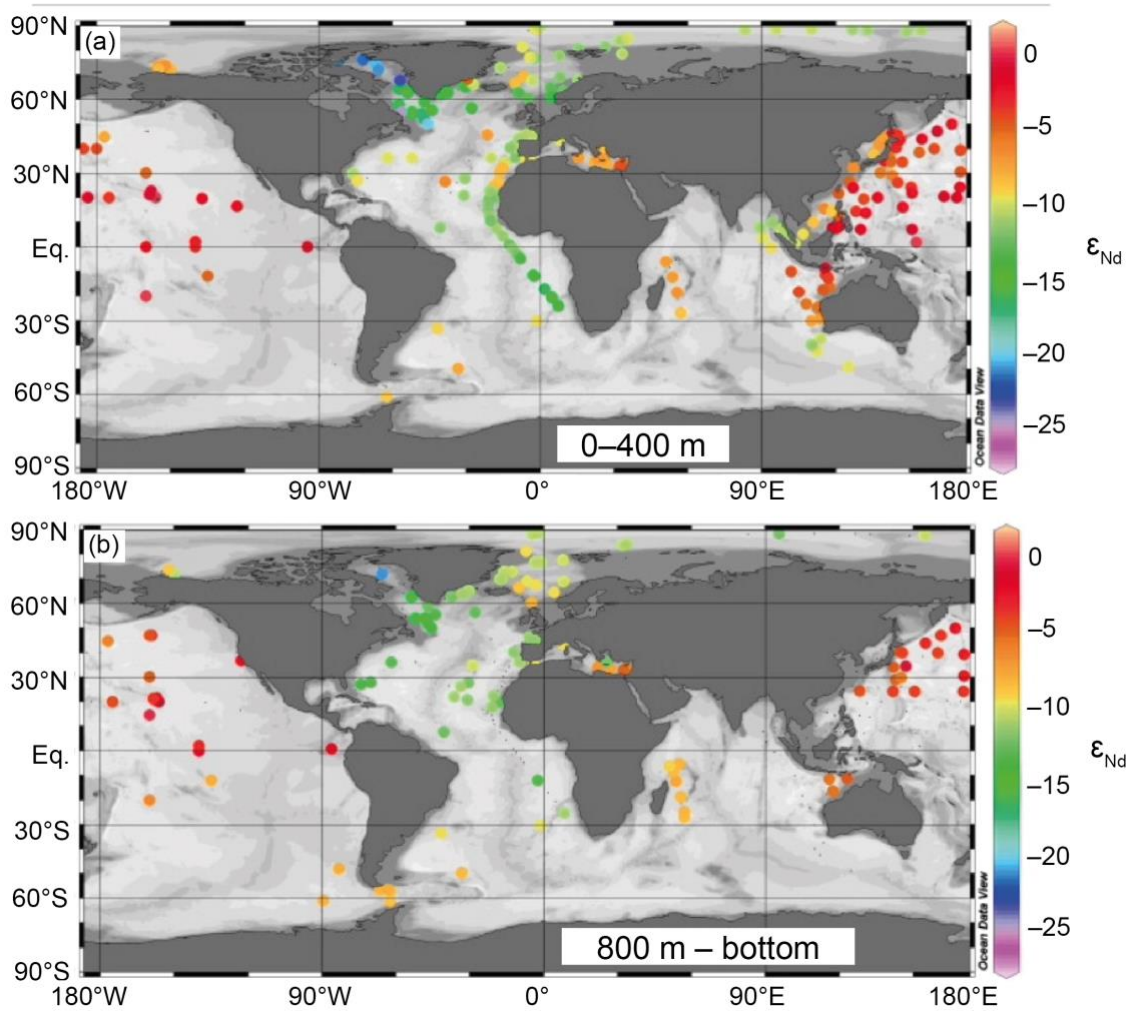

Figure 5.1: *ε_{Nd} averaged between the surface and 400m depth (a) and between 800 m depth and the bottom (b) (Lacan et al., 2012).*

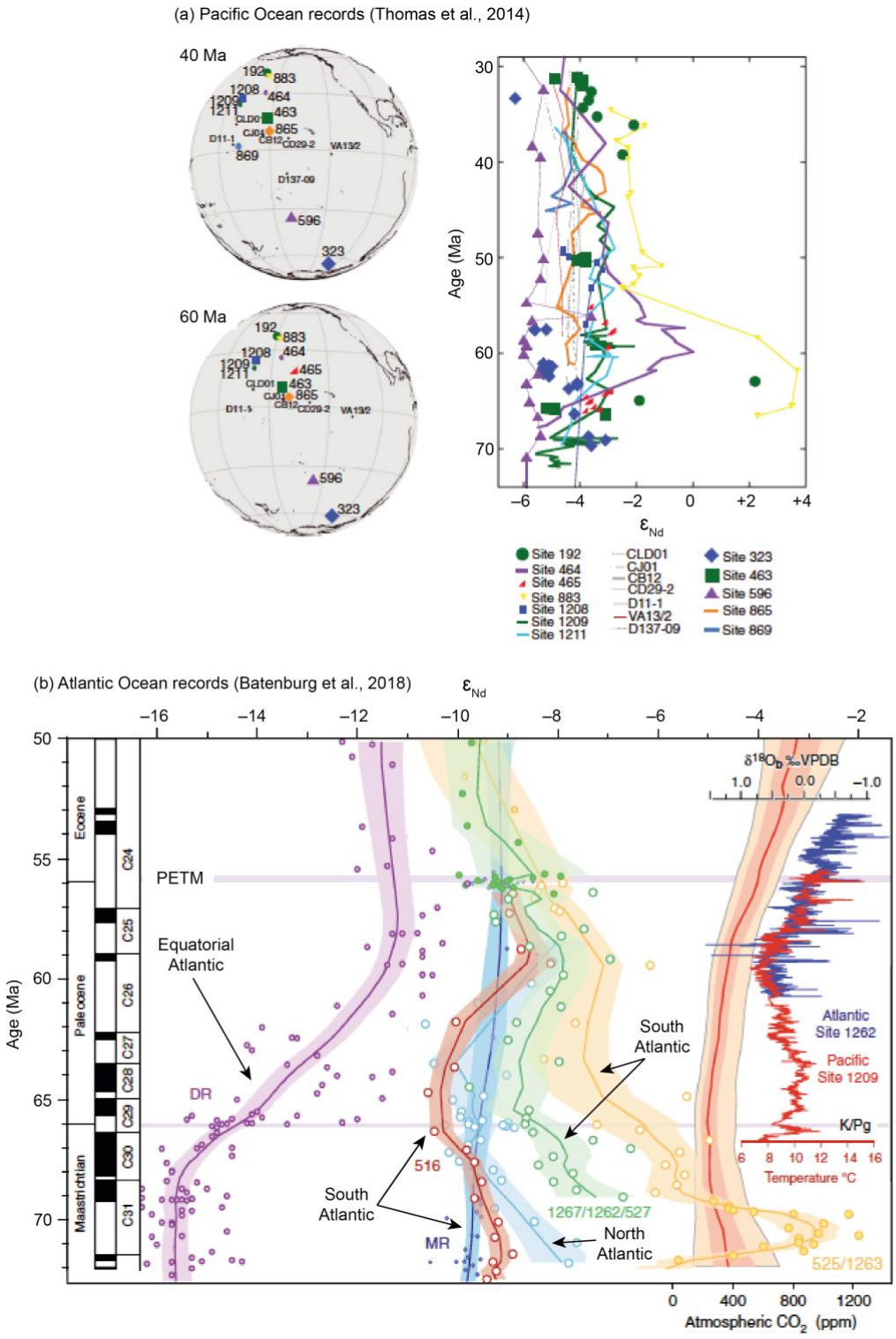

Figure 5.2: *(a) Pacific Ocean records of late Cretaceous to Cenozoic neodymium isotope values (Thomas et al., 2014), and (b) Atlantic Ocean records of late Cretaceous to Cenozoic neodymium isotopes (Batenburg et al., 2018). In general, the Atlantic Ocean is less radiogenic (~–6 to –15) than contemporaneous records from the Pacific Ocean (~–2 to –6) during the Paleogene, although there is a large spread in values between the North and South Atlantic, which begins to converge after ~59 Ma.*

Fish teeth made of apatite are a particularly useful recorder of the contemporaneous bottom-water Nd isotopic composition, due to their ability to

concentrate and retain Nd quickly upon deposition and remain resistant to diagenetic alteration (Martin & Haley, 2000; Martin & Scher, 2004; Huck et al., 2016). Fish teeth are often present at low concentrations in many pelagic and hemipelagic settings, making them well suited to constructing time-series in marine sediment cores. Other geological materials such as foraminifera and bulk sediments can also be used to reconstruct ancient ε_{Nd} profiles, should fish teeth be scarce within the sediments, or should shallower parts of the water column be the target (e.g., Vance et al., 2004; Martin et al., 2010). Due to this large potential analytical reservoir ε_{Nd} time-series from marine cores have been used to reconstruct changes in water mass distribution across many key events in Earth history. This includes the Eocene–Oligocene boundary (e.g., Wright et al., 2018), the last deglaciation (e.g., Gu et al., 2017), the Middle Miocene climate transition (e.g., Kender et al., 2018), and the PETM (Thomas et al., 2003; Abbott et al., 2016).

Carbon isotope data from benthic foraminifera has also been used as a proxy for changes in water masses (Tripati & Elderfield, 2005; Nunes & Norris, 2006); however, interpretation of $\delta^{13}C$ in marine sediments is complicated by both the effects of local productivity and by large-scale changes in the global carbon cycle which must be corrected for or at least considered. Because changes in ε_{Nd} recorded in marine cores are independent of changes in the carbon cycle (Abbott et al., 2016), Nd isotopes are an ideal proxy for observing broad scale ocean circulation changes over transient events such as the PETM, which are characterised by large changes to the climate-carbon cycle. Nd isotopes are also unaffected by carbonate dissolution events, which impact the utility of $\delta^{13}C$ over past hyperthermal events due to significant reductions in the global ocean calcite compensation depth (e.g., Zachos et al., 2005).

5.2.2. Neodymium isotope records across the PETM

From ~80–50 Ma there was a general increase in ε_{Nd} to more radiogenic values in both the Tethys and the Atlantic oceans, from ~–10 to –6 (Stille et al., 1996). This trend is also shown in higher resolution data from the Equatorial Atlantic (Fig. 5.2b; Batenburg et al., 2018), where values become more radiogenic between ~67 and ~58 Ma. However, contemporaneous data from the South

Atlantic either show little change or values become less radiogenic (Batenburg et al., 2018). Both datasets lack data from the Tethys covering over the Paleocene to Eocene interval. This data gap covers the PETM hyperthermal, a time when it has been suggested that rapid warming caused transient changes to deep water formation and ocean circulation patterns (Tripati & Elderfield, 2005; Nunes & Norris, 2006; Lunt et al., 2010; Cope & Winguth, 2011; Abbott et al., 2016). Modelling has suggested that increased freshwater input to the Arctic Ocean over the PETM led to greater stratification in the North Pacific, temporarily shifting dominant deep water formation to the South Pacific and the Northern Tethyan realms (Cope & Winguth, 2011). Alternatively, compilations of carbon and oxygen isotope and Mg/Ca-temperature records suggest a transient change of deep water formation from the Southern Hemisphere before and after the PETM, to the Northern Hemisphere during the PETM (Tripati & Elderfield, 2005; Nunes & Norris, 2006), which is supported by some modelling studies (Bice & Marotzke, 2002; Lunt et al., 2010). This theory remains controversial, with other global data compilations of neodymium isotopes (Thomas et al., 2003) and modelling (Panchuk et al., 2008) providing little support for significant changes in thermohaline circulation over the PETM.

Throughout the Paleogene the Tethys had gateways to both the east and west, allowing the throughflow of an intermediate-water mass known as Tethyan Indian Saline Water (TISW; Fig. 5.3). This current flowed from the Atlantic through to the northern Indian Ocean (Woodruff & Savin, 1989). Due to the lack of ε_{Nd} data from the Tethyan realm during this interval, the impact of proposed transient changes in thermohaline circulation on this region are not well constrained. As the Tethys was an important gateway for the transport of warm, saline waters to the southern high latitudes (Woodruff & Savin, 1989), transient changes in this water mass configuration could have been an important negative feedback mechanism during the PETM hyperthermal.

A new ε_{Nd} isotope record is presented here, paired with existing organic carbon isotope data covering the late Paleocene to early Eocene interval from the Jordan oil shale. This record is from a key geographic location in the eastern Tethys where changes in water mass transport between the Atlantic and Indian oceans may be recorded (Fig. 5.3). Due to the ongoing Covid-19 pandemic, the additional

lab work required to complete this chapter has not been possible. This chapter therefore details the results thus far and conclusions based on these results are preliminary. It is hoped that this study will be completed in the future, through the addition of higher resolution ε_{Nd} data from this core, when the pandemic situation improves.

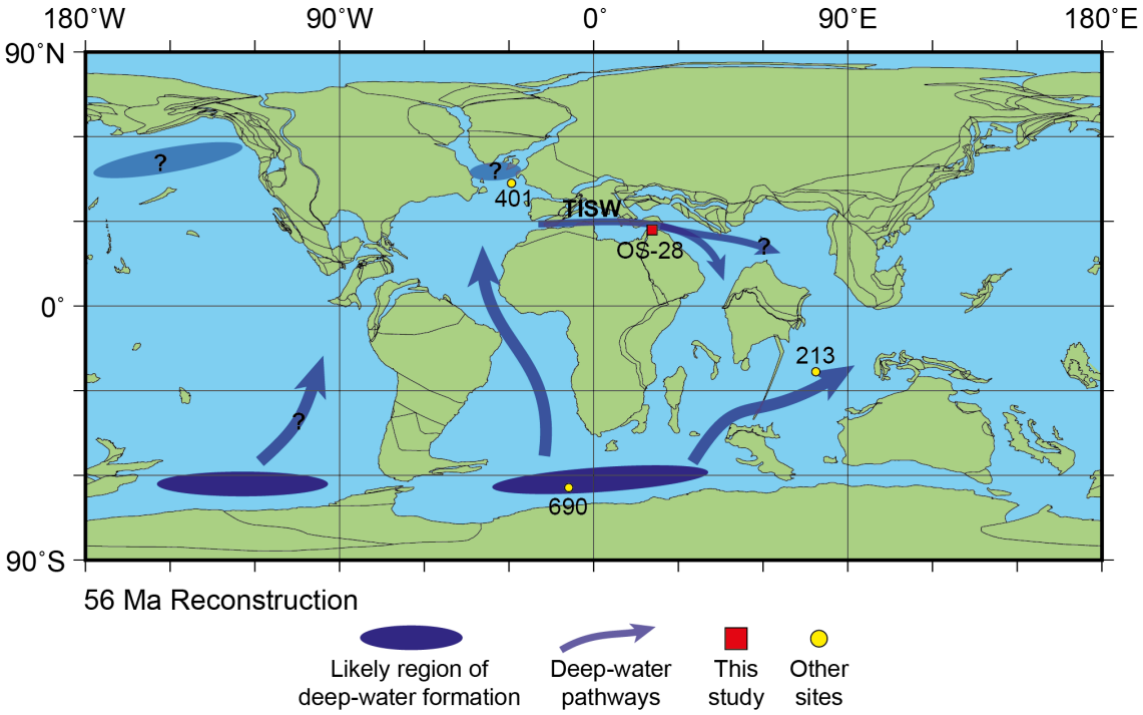

Figure 5.3: *Locality of Site OS-28 in the eastern Tethys Ocean (red square). Paleogeographic reconstruction of the Paleocene–Eocene boundary interval (~56 Ma). Blue areas show likely regions of deep water formation, with blue arrows showing likely pathways of deep water flow (Woodruff & Savin, 1989; Thomas et al., 2003; Tripati & Elderfield, 2005; Nunes & Norris, 2006; Cope & Winguth, 2011; Barnet et al., 2020). Yellow circles show locations of other DSDP/ODP sites mentioned in this study (Thomas et al., 2003; Nunes & Norris, 2006; Abbott et al., 2016). Map generated through Ocean Drilling Stratigraphic Network (ODSN) Paleomap project (https://www.odsn.de/odsn/services/paleomap/paleomap.html).*

5.3 Materials and geological setting

Industry Core OS-28 was drilled by the Jordan Oil Shale Company (JOSCO) in 2010, approximately 100 km east of Amman in central-east Jordan (Fig. 5.4). The core comprises Maastrichtian to Eocene marls and organic-rich shales, with the investigated interval (~44–54 m) covering the Paleocene–Eocene boundary (Fig. 5.5). These sediments were deposited within a sub-basin on the southern margin of the Paleogene Tethys Ocean (Alqudah et al., 2014a). During the Paleocene–Eocene the core was in a distal, outer neritic to upper bathyal shelf setting

(Giraldo Gomez et al., 2018). Detailed calcareous nannofossil and foraminiferal biostratigraphy shows there to be a continuous Paleocene to early Eocene sedimentary sequence at this site (Alqudah et al., 2014b; Giraldo Gómez et al., 2017), with little to no reworking (Alqudah, 2014c). Oil shales (organic-rich shales) are present during the late Paleocene to early Eocene interval, suggesting there was bottom-water anoxia (and possible euxinia) during the PETM at this site (Siedenberg et al., 2018). The early Eocene sees a return to oxic bottom-water conditions in a non-restricted basin (Giraldo Gómez et al., 2018; Siedenberg et al., 2018).

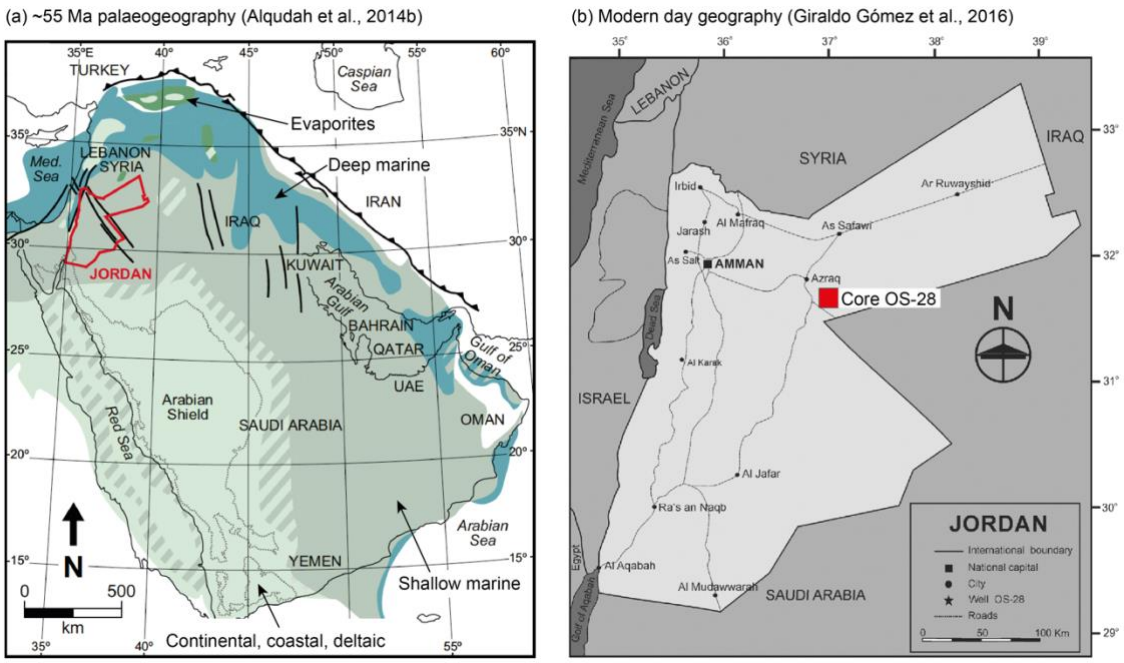

Figure 5.4: *(a) Paleogeography and oceanographic setting of the Arabian Plate during the Paleogene, red outline shows location of Jordan (Alqudah et al., 2014b). (b) Red square shows location of Site OS-28 on modern geography (Giraldo Gómez et al., 2016).*

5.4 Methods

5.4.1 Sample preparation

A total of 45 samples were processed from Core OS-28 from between the depths of ~44 to 54 m within the core. As the Paleocene–Eocene sediments at this site are highly indurated, they required significant processing to liberate the fish teeth needed for geochemical analysis. Samples were disaggregated using the freeze-thaw technique of Kennedy and Coe (2014) whereby samples are covered in

Milli-Q water and repeatedly frozen and rapidly thawed with hot water until the material is sufficiently broken down. Samples requiring further processing were placed in 10% hydrogen peroxide (H_2O_2) for approximately 48 hours. Once samples were broken down, they were washed over a 63 µm sieve with Milli-Q water and dried overnight in an oven at 50°C. Fish teeth were picked from the entirety of the coarse fraction (>63 µm) of each sample using a light microscope. Table 5.1 details the methods used on the samples (n=10) presented in this Chapter. Of the 45 samples processed, 27 samples yielded a sufficient number of fish teeth for ε_{Nd} isotope analysis. Of these, 17 produced data that was not reliable due to issues with machine stability during the run. Subsequently ten samples generated reliable ε_{Nd} isotope data. This data is at a resolution of ~1 m corresponding to a temporal resolution of ~400 kyrs (see Section 5.4.3 below).

Table 5.1: *Details of how each successful sample was disaggregated.*

Depth (m)	Freeze thaw?	Hydrogen peroxide?
44.45	Y	Y
45.40	Y	
45.50	Y	Y
46.60	Y	
47.10	Y	
48.05	Y	
48.55	Y	Y
50.85	Y	
51.85	Y	
53.35	Y	

5.4.2 Neodymium isotope analysis

All fish teeth from each sample were placed into individual 2 ml centrifuge tubes and cleaned first with ultrapure (18.2 MΩ) water to agitate any clays, then samples were washed in methanol, and finally with hydrogen peroxide to remove organic matter (cf. Barker et al., 2003). The teeth were then transferred to 7 ml Teflon vials using ultrapure water; excess water was then evaporated on a hot plate. Once dry, 1 ml of 4M HCl (hydrochloric acid) was added to each sample, vials were sealed, and the acid was refluxed on a hot plate at 90°C overnight. All

samples were centrifuged to remove any remaining particulate matter and 500 µl of concentrated nitric acid (HNO_3) was added and again refluxed on a hot plate for ~1 hour then subsequently evaporated. Samples were re-dissolved in 50 µl 0.25M HCl and refluxed on hot plate for ~30 mins to ensure full mixing.

All samples underwent a chromatographic separation with Ln-spec resin in order to isolate and purify the neodymium (Scher & Delaney, 2010). Purified samples were then evaporated on a hot plate and re-dissolved in 0.5 ml 3% HNO_3. Prior to analysis a concentration check was performed with a 50-fold diluted aliquot of each sample. Isotopic ratios of Nd were analysed using a Thermo Neptune Plus multi-collector inductively coupled plasma mass spectrometer (MC-ICP-MS) in the Department of Earth Sciences at Royal Holloway University of London. The concentration-matched reference standard JNd-i bracketed each three samples, with measured $^{143}Nd/^{144}Nd$ ratios corrected to the accepted standard value $^{143}Nd/^{144}Nd$ of 0.512115 (Tanaka et al., 2000). Samples were corrected for their age (~56 Ma) using an assumed $^{147}Sm/^{144}Nd$ ratio of 0.1286 (Thomas et al., 2003) and then compared to the composition of the CHUR as in Equation 5.1. Values are given in ε_{Nd} units.

$$\varepsilon_{\mathrm{Nd(t)}} = \left(\left[143/144_{\mathrm{Nd_{sample(t)}}} - 143/144_{\mathrm{Nd_{CHUR(t)}}}\right] \div 143/144_{\mathrm{Nd_{CHUR(t)}}}\right) \times 10^4 \quad [\mathrm{Eq.}\,5.1]$$

The external reproducibility (2σ) of JNd-i was ±0.7 epsilon units (Table 7.4; Appendix 10).

5.4.3 Age model construction

The age model for this core is based upon previously conducted organic carbon isotope analysis ($\delta^{13}C_{org}$; Wouters et al., 2014) and calcareous nannofossil biostratigraphy (Giraldo Gómez et al., 2016). The tie points used to construct the age model are shown in Figure 5.5. The first occurrence (FO) of *Discoaster mohleri* (Alqudah et al., 2014a) occurs at 57.57 Ma (Agnini et el., 2014). The NP9a/NP9b boundary is defined by the FO of *Rhomboaster cuspis* and *D. araneus* (Giraldo Gómez et al., 2016) at 55.9 Ma (Agnini et al., 2007), adding confidence to the PETM recovery tie point also at 55.9 Ma. The NP9/NP10 boundary is defined by the FO of *Tribrachiatus bramlettei* (Giraldo Gómez et al.,

2016) at 55.00 Ma (Agnini et al., 2014). The peak PETM has been calibrated to 56.00 Ma (McInerney & Wing, 2011). The average sedimentation rate is 0.25 cm kyr^{-1}.

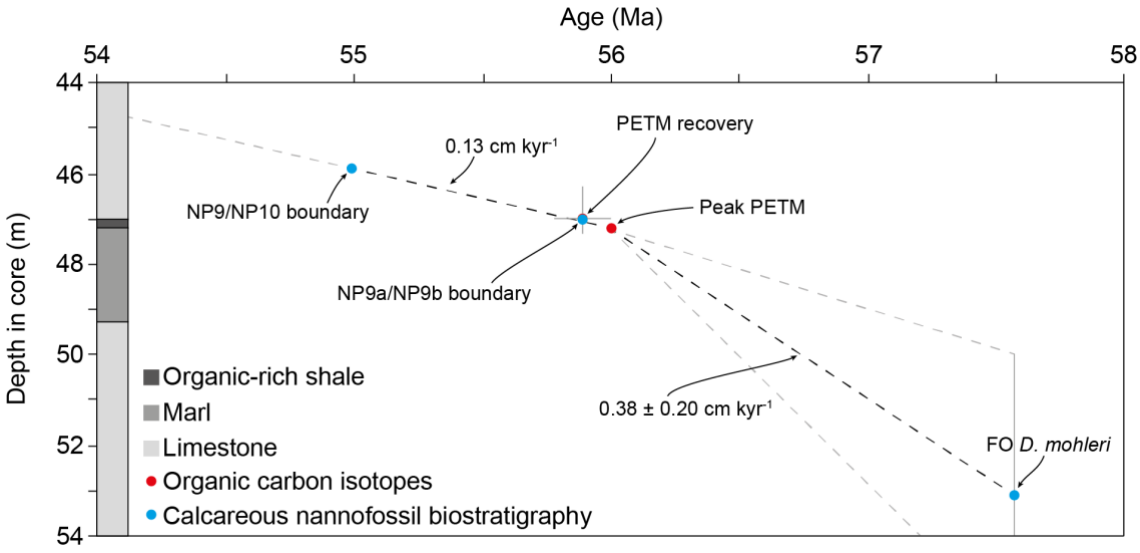

Figure 5.5: *Age-depth plot for Core OS-28. Tie points used are from organic carbon isotope chemostratigraphy (red; Wouters et al., 2014) and calcareous nannofossil biostratigraphy (blue; Alqudah et al., 2014a; Giraldo Gómez et al., 2016). Lithological log after Giraldo Gómez et al. (2016).*

5.5 Results

5.5.1 Neodymium isotopes

The ε_{Nd} values recorded throughout the interval are relatively radiogenic (positive), ranging from –6.5 to –2. In comparison, contemporaneous values from the adjacent Atlantic and Indian Oceans were ~–12 and –8 respectively (Piepgras et al., 1979). In general, there was a decrease to less radiogenic (more negative) values through the studied interval, with ε_{Nd} values of –2 to –4 during the late Paleocene to –3 to –6.5 in the early Eocene (Table 5.2, Fig. 5.6). ε_{Nd} values become most radiogenic (~–2) during the latest Paleocene. Due to delays caused by the Covid-19 pandemic, the rare earth element (REE) profiles for these samples have not yet been analysed.

Table 5.2: *Details of sample Nd isotope ratios, ε_{Nd}, and 2 standard error (2SE), for each of the ten samples in this study.*

Depth (m)	$^{143}Nd/^{144}Nd$	ε_{Nd}	2SE
44.45	0.51209126	-6.75	0.25
45.40	0.51217554	-4.67	0.19
45.50	0.51210090	-6.56	0.22
46.60	0.51221104	-3.68	0.36
47.10	0.51225527	-2.91	0.17
48.05	0.51222394	-4.05	0.26
48.55	0.51234100	-2.03	0.19
50.85	0.51221705	-3.66	0.25
51.85	0.51220321	-3.84	0.22
53.35	0.51227268	-3.09	0.92
		Average	0.29

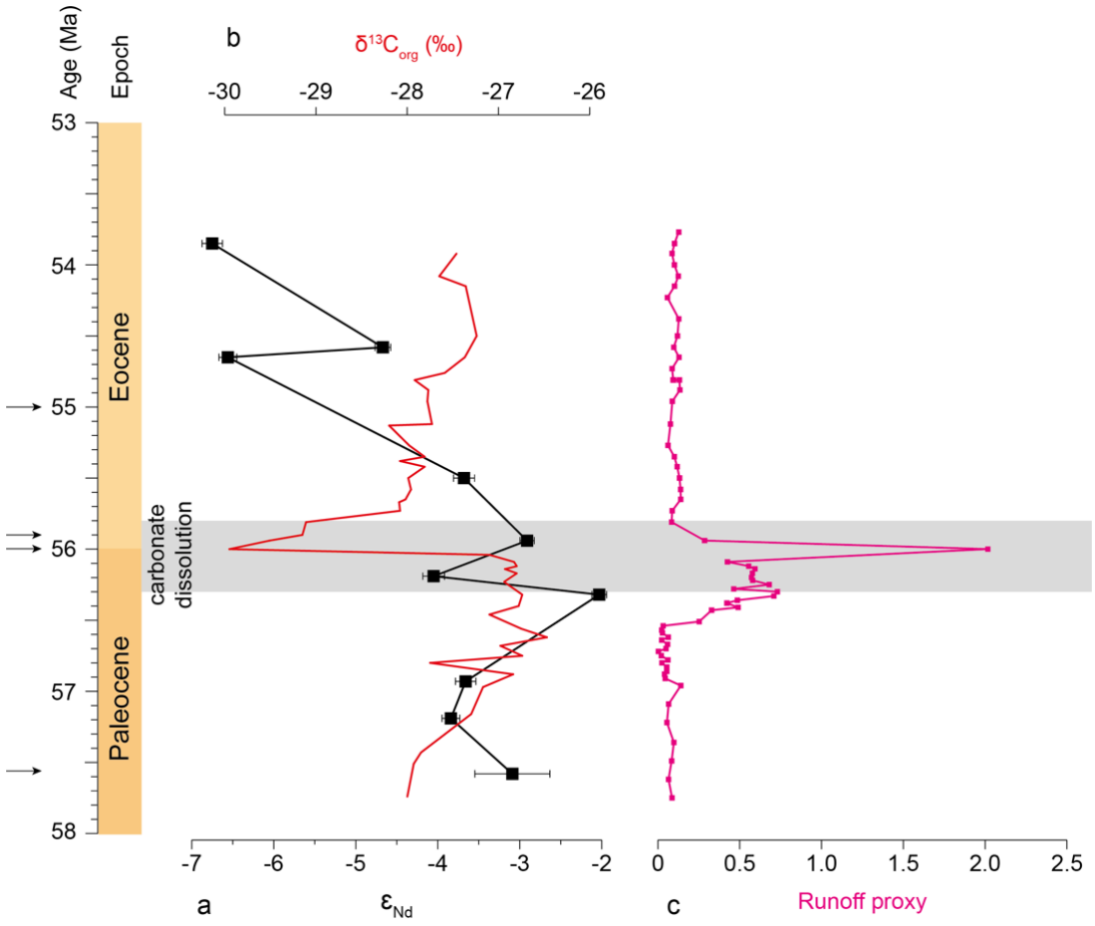

Figure 5.6: *Geochemical tracers from Core OS-28. (a) Neodymium isotopes (ε_{Nd}) in black (error bars are 2SE; Table 5.2); (b) Organic-carbon isotopes in red (Wouters et al., 2014) (c) Runoff proxy in pink from hand-held XRF-derived elemental data, (Ti+Al+Mg+Fe+Zr)/Ca (Wouters et al., 2014). Grey bar depicts carbonate dissolution interval (Giraldo Gómez et al., 2016). Apparent increase in runoff proxy associated with the PETM may be due to carbonate dissolution in the core. Black arrows show age model tie points (this study; Fig. 5.5).*

5.6 Discussion

The investigated interval encompasses the late Paleocene to early Eocene (~58.0–53.8 Ma), defined by calcareous nannofossil biozonation and organic carbon isotopes (Figs. 5.5 and 5.6). There is no evidence for a transient change in ε_{Nd} values within the Tethys during the PETM itself, with broadly similar values in the peak of the CIE to those characteristic of the late Paleocene (–2 to –4). This is consistent with data from other sites that shows no discernible change in ε_{Nd} values associated with the PETM in the Atlantic, Pacific, Indian, or Southern Oceans (Thomas et al., 2003), thus suggesting this event was not associated with large changes in global thermohaline circulation patterns, at least at the resolution of currently available ε_{Nd} records. There is, however, a long-term shift to less radiogenic values of ε_{Nd} recorded in Core OS-28 in the early Eocene (~56–54 Ma). This shift could be indicative of either regional changes in end-member water mass mixing, a change in local environmental processes, or changes in internal cycling processes such as boundary scavenging. Without REE profiles for these samples it is not known if the values observed are truly marine-derived values of ε_{Nd}; REE profiles will be generated in future lab work to ground truth the observed values (Section 6.3.3). Despite this, the possible causes for the radiogenic values observed in the late Paleocene, and the long-term change to less radiogenic values in the early Eocene, will be discussed below.

5.6.1 Neodymium data record regional end-member water mass mixing processes

One hypothesis for the long-term decrease in ε_{Nd} values during the early Eocene would be a change to end-member water mass mixing. As the change in ε_{Nd} to less radiogenic values occurs after the PETM CIE (~55.4 Ma), after the local anoxia (Giraldo Gómez et al., 2016), and during a time with no significant terrigenous input/biological productivity (Fig. 5.6) (Giraldo Gómez et al., 2018) it is possible that the less radiogenic values are representative of a regional signal rather than a local signal. If this is the case, it could suggest an increased contribution to this site from waters sourced from the less radiogenic (more negative) Atlantic or Indian Oceans (Fig. 5.7). During the early Eocene there is a transient increase to more radiogenic values of ε_{Nd} at Indian Ocean DSDP Site

213 from –9 to –7 (Fig. 5.7; Thomas et al., 2003). Concurrently, in the Atlantic and Southern Ocean ε_{Nd} values remain at ~–9 throughout the early Eocene (Fig. 5.7; Thomas et al., 2003). The less radiogenic ε_{Nd} values at the Tethyan site of –5 to –7 during the early Eocene could therefore be a result of an increased contribution of a less radiogenic Atlantic or Indian Ocean water mass during the early Eocene. However, as the Tethyan ε_{Nd} values remain more radiogenic than both the Atlantic and Indian Oceans, it would suggest that the Tethyan water mass affecting Core OS-28 did not obtain its ε_{Nd} signature by end-member water mass mixing alone. The possibility of internal cycling processes affecting the ε_{Nd} values is discussed in Section 5.6.3.

If the ε_{Nd} data are representative of regional/global oceanographic circulation, they do not suggest that there was a transient change in throughflow in the Tethys over the PETM itself. ε_{Nd} values remain at ~–4 during the PETM, similar to values observed during the late Paleocene, therefore indicating little or no change to water mass contribution over this time. This is in agreement with other Nd isotope records through the Paleocene–Eocene interval that suggest a Southern Ocean source of deep water formation that is present throughout this time (Thomas et al., 2003).

5.6.2 Neodymium data record local environmental processes

The relatively radiogenic ε_{Nd} values in the eastern Tethys compared to the adjacent Atlantic and Indian Oceans during the Paleocene (Fig. 5.7) suggest that simple mixing of end-member water masses is an unlikely source of these values. There may therefore have been an additional input of radiogenic material to Core OS-28 during this time. In the modern, radiogenic dust (ε_{Nd} = ~–7 to +3) from East Africa is transported by northwesterly winds to the Arabian Sea and Arabian Peninsula (Jewell et al., 2021). The River Nile is also a source of radiogenic ε_{Nd} values (~–3) to the eastern Mediterranean Sea (Goldstein et al., 1984). However, the source of this radiogenic ε_{Nd} is largely from East African rifting around the Red Sea and associated volcanism which is not thought to have begun until the Oligocene (~31 Ma; Ebinger & Sleep, 1998; Ilani et al., 2001; Stern & Johnson, 2019).

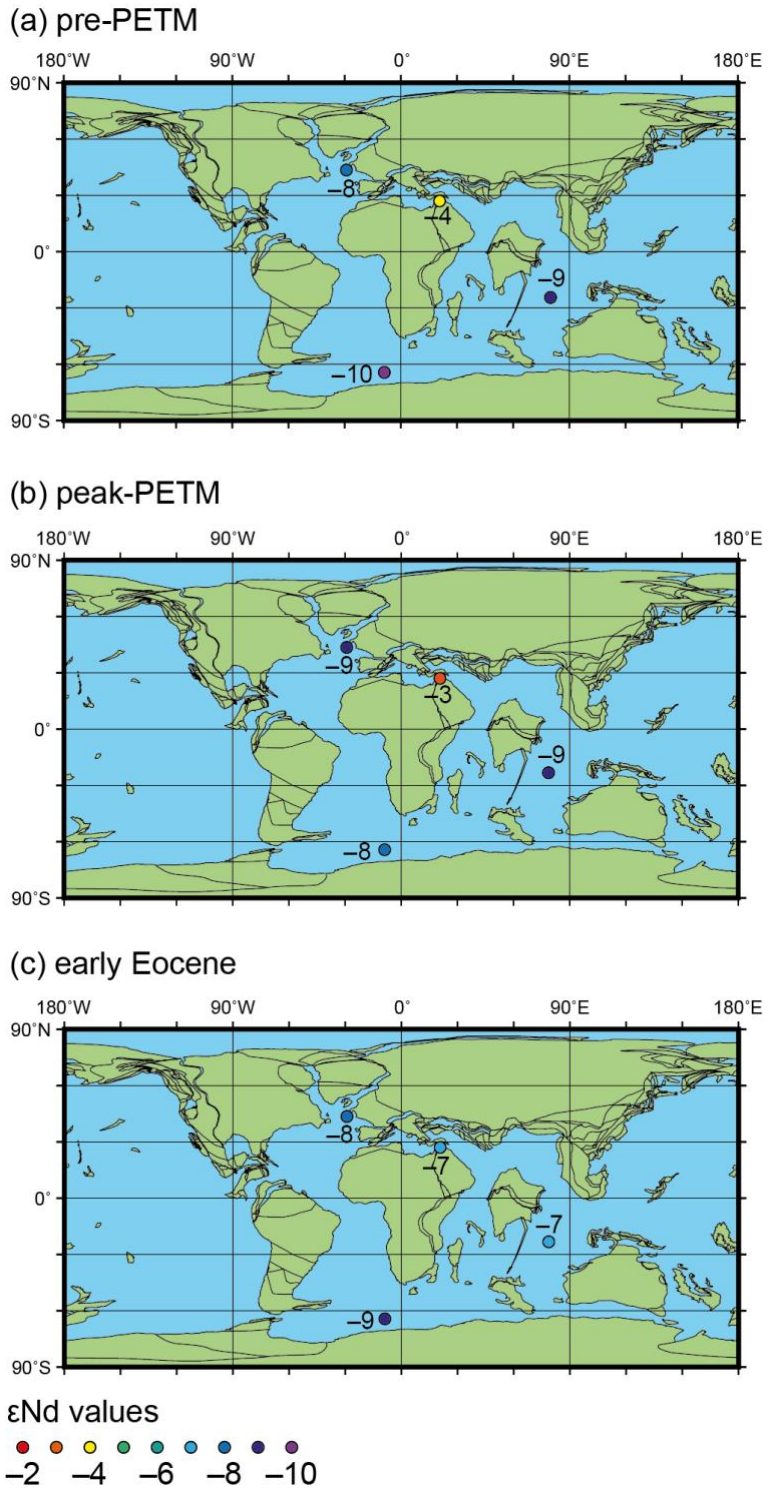

Figure 5.7: *ε_{Nd} data compilation from the Indian Ocean (DSDP Site 213), the North Atlantic (DSDP Site 401), the Southern Ocean (ODP Site 690) (all Thomas et al., 2003) and the eastern Tethys Ocean (OS-28; this study) through three time intervals: (a) pre-PETM, (b) peak-PETM (~56 Ma), and (c) early Eocene.*

Another possible source of radiogenic ε_{Nd} to Core OS-28 during the early Paleogene could be the Deccan Traps (Fig. 5.8), which were being erupted on the Indian subcontinent throughout the late Cretaceous to earliest Paleogene (Renne et al., 2015; Schoene et al., 2015) and have a variable but generally

radiogenic ε_{Nd} signature (~–7 to +4; Vanderkluysen et al., 2011). Predominant deep water flow in the Tethys is thought to have been from the Atlantic through the Tethys into the northern Indian Ocean (TISW; Woodruff & Savin, 1989), however, modelling suggests that surface water flows were in the opposite direction (von der Heydt & Dijkstra, 2006; Hamon et al., 2013). The incorporation of this potentially radiogenic surface water into the deep waters would depend upon ocean mixing times/stratification of the water column (Siddall et al., 2008), which is not well constrained for the Tethys during this interval. The more radiogenic ε_{Nd} values may not be observed at Indian Ocean Site 213 due to it being located in the central Indian Ocean, away from oceanic circulation pathways going via the Deccan Traps region (Fig. 5.8).

5.6.2.1 Neodymium data controlled by internal cycling processes (boundary exchange and reversible scavenging)

If only accounting for riverine/dust inputs of Nd to water masses, there is an imbalance between the sources and sinks of oceanic Nd (the “Nd paradox”; Siddall et al., 2008; Jeandel, 2016). Internal cycling processes (i.e., boundary exchange and reversible scavenging) are therefore key elements of the global oceanic budget of radiogenic isotopes. Boundary exchange is the process by which dissolved particulates exchange Nd with continental margin sediments (Jeandel, 2016; van de Flierdt et al., 2016). Reversible scavenging is the same process occurring within the water column, involving adsorption/desorption onto particles (Arsouze et al., 2007; Siddall et al., 2008). The physical process can occur through adsorption/desorption, isotopic exchange, or dissolution/precipitation and can also be enhanced in biologically productive areas (van de Flierdt et al., 2016).

If surface waters flowing from the Indian Ocean into the Tethys underwent boundary scavenging processes along on the western Indian continental margin Deccan Traps region (Fig. 5.8), this would bring a water mass with a radiogenic ε_{Nd} signature towards Core OS-28. This combination of internal cycling processes and water mass convection (transferring the radiogenic surface waters into deeper waters) may account for the radiogenic ε_{Nd} values observed at Core OS-28 during the late Paleocene. During the early Eocene the ε_{Nd} values became

less radiogenic at Core OS-28. If the dominant process for providing the radiogenic ε_{Nd} to this site was through internal cycling, this change could be representative of either a decrease in the contribution of the water mass sourced from the Deccan Traps region (northern Indian Ocean) or an increase in the contribution of a less radiogenic water mass (e.g., from the Atlantic Ocean).

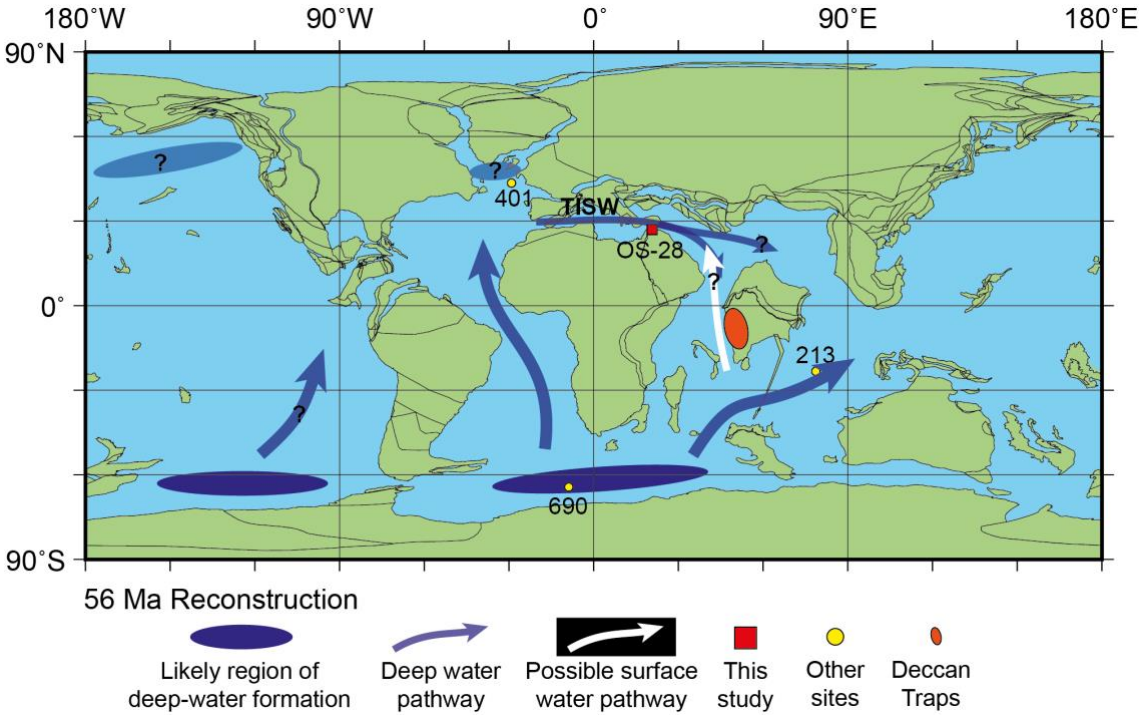

Figure 5.8: *Location of Deccan Traps in relation to Core OS-28 and possible routes of deep water and surface water pathways affecting the site.*

5.7 Preliminary conclusions

New neodymium isotope data from fish teeth are presented alongside existing organic carbon isotope and trace element data from the eastern Tethys (onshore Jordan, Core OS-28). There is no discernible change in ε_{Nd} values across the PETM itself at this site, which is consistent with previously published data from all other major ocean basins (Thomas et al., 2003), although the resolution of the data precludes a definitive analysis. There is, however, a long-term change in ε_{Nd} values from being relatively radiogenic in the late Paleocene (–2 to –4), to less radiogenic in the early Eocene (–5 to –7) at this site, which could be explained by two possible scenarios:

1) The radiogenic values are a result of changes in the balance of end-member water mass mixing between the Atlantic and Indian Oceans. The decrease in ε_{Nd} values at Core OS-28, to less radiogenic values, is due to an increased contribution of the less radiogenic Atlantic or Indian Ocean water masses in the early Eocene.

2) Active boundary scavenging/internal cycling processes incorporate the radiogenic ε_{Nd} signature of the Deccan Traps region and surface water currents (and subsequent water mass mixing) bring this to Core OS-28 bottom waters. During the early Eocene, there is an increased contribution of less radiogenic Atlantic waters and/or a decreased contribution of radiogenic surface waters from the northern Indian Ocean.

As the Core OS-28 Tethyan ε_{Nd} values are more radiogenic than contemporaneous values in both the Atlantic and Indian Oceans, it would suggest that internal cycling processes are the primary driver of the ε_{Nd} trends observed at this site. Further work will aim to constrain the REE profiles of the samples in order to ground truth the observed ε_{Nd} values and ensure that they record a primary seawater signal; this is expanded upon in Section 6.3.3.

Chapter 6: Synthesis and conclusions

6.1 Synthesis of data and conclusions

This thesis aims to reveal new insights into the palaeoceanographic, palaeoclimatic, and palaeobiological development of the tropical low latitudes (Fig. 6.1) through major long-term and transient climate events of the Paleogene and earliest Neogene (Fig. 6.2). A suite of geochemical techniques were applied to a range of sedimentary archives. This included stable oxygen and carbon isotopes ($\delta^{18}O$ and $\delta^{13}C$) of bulk carbonate sediment and foraminiferal calcite and X-ray fluorescence (XRF) derived bulk elemental analysis, in combination with detailed biostratigraphy (of larger benthic foraminifera [LBF] and calcareous nannofossils) and careful determination of the sedimentary environment. These were used to reconstruct palaeoceanographic change through the rise and terminal decline of the Paleogene greenhouse Earth (Fig. 6.2). The increasing temperatures of the late Paleocene to Eocene interval were used as a basis to determine the effects of long-term global warmth on the palaeoecology (Chapter 2) and palaeoceanographic configuration (Chapter 5) of the tropical low latitudes. The subsequent effects of the decline into a global “coolhouse” state (Westerhold et al., 2020) on the same low latitude region were also investigated (Chapter 4). The main conclusions of each chapter are detailed below.

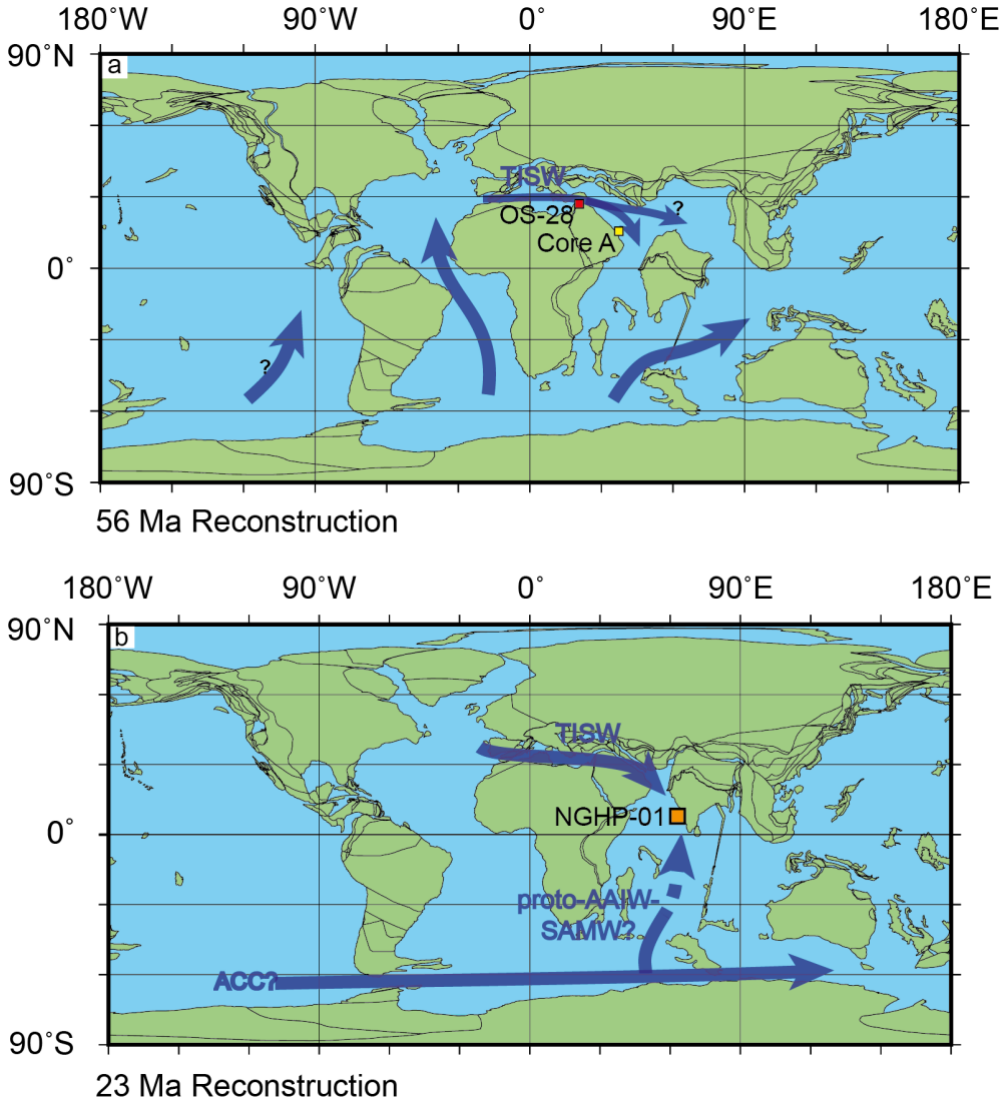

Figure 6.1: *Location of sites investigated in this thesis. (a) Palaoegeographic reconstruction of Paleocene–Eocene boundary (~56 Ma) with sites Core A (yellow; Chapter 2) and OS-28 (red; Chapter 5). (b) Oligocene–Miocene palaeogeography (~23 Ma) with Site NGHP-01-01A (orange; Chapter 4). Dark blue arrows show possible deep water currents affecting the study sites. TISW is Tethyan Indian Saline Water; AAIW-SAMW is Antarctic Intermediate and Subantarctic Mode Water; ACC is Antarctic Circumpolar Current. Maps generated through Ocean Drilling Stratigraphic Network (ODSN) Paleomap project (https://www.odsn.de/odsn/services/paleomap/paleomap.html).*

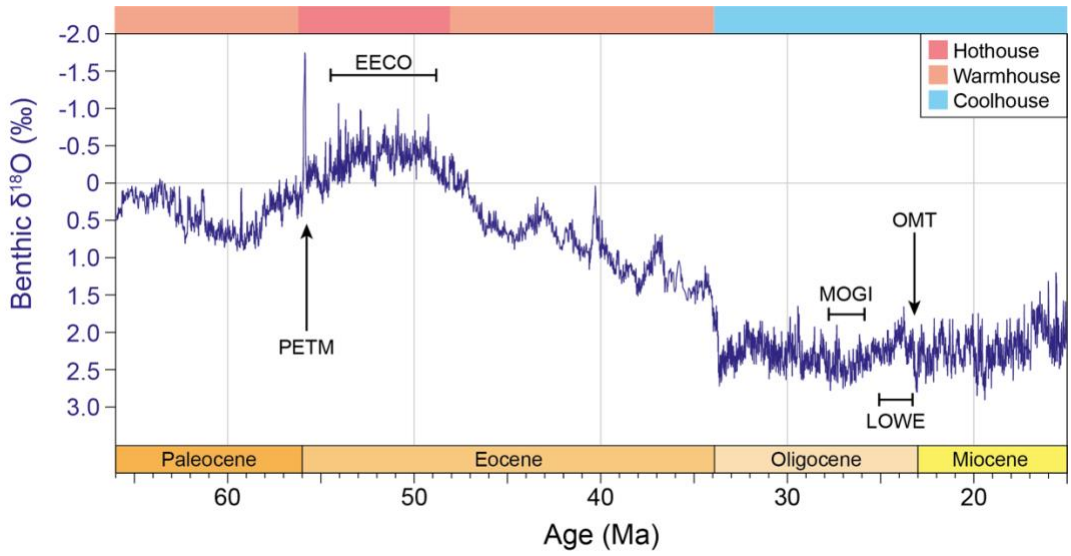

Figure 6.2: *Benthic foraminiferal oxygen isotope ($\delta^{18}O_b$) global compilation (Westerhold et al., 2020) showing short-term, transient events (i.e., the PETM and OMT) and intervals of long-term palaeoclimatic change (i.e., the EECO and LOWE) investigated in this thesis.*

In Chapter 2 an integrated record of LBF and calcareous nannofossil biostratigraphy, combined with carbonate stable isotope chemostratigraphy, was generated from the easternmost Tethys (United Arab Emirates; UAE) over the Paleocene to early Eocene interval. During the Paleocene there was a general period of stability in the shallow water, carbonate-dominated reef setting, with high diversity in the biotic assemblage. Over the Paleocene–Eocene transition there was a gradual loss of the diverse reef assemblage as a response to globally warmer temperatures, with the systematic loss of corals, gastropods, and bivalves. In the early Eocene, the LBF assemblage underwent overturning, involving an overall increase in specific and generic level diversity and the eventual dominance of less specialised genera such as *Rotalia* and *Sakesaria*. Over the onset of the Paleocene–Eocene thermal maximum (PETM) hyperthermal itself there was no significant change in the LBF assemblage, suggesting that it was the crossing of a long-term climatic threshold, rather than the rapid, transient perturbation, that caused the observed changes in the LBF assemblage. This record of LBF and calcareous nannofossil biostratigraphy integrated with chemostratigraphy was one of the first to combine these techniques in the shallow water domain, providing important constraints on low latitude shallow water biostratigraphy for the region.

During the processing of samples for Chapter 2 a number of issues with disaggregating samples were encountered due to the indurated nature of the carbonate samples. To better identify LBF to the genera or species level it is necessary to liberate specimens from surrounding matrix in order to individually thin section each fossil; this was not possible with the currently available disaggregation techniques, therefore a new method was sought to facilitate this in the future. In Chapter 3 electric pulse fragmentation (EPF) was compared to two traditional methods of carbonate disaggregation, showing it to be more effective and efficient at liberating microfossil material (primarily LBF). The method disaggregated samples with calcitic, silicic and clay matrices/cements, primarily liberating microfossils >500 µm in size. Within this chapter suggestions were made for how the methodology could be tailored for smaller microfossils, which is expanded upon in Section 6.3.1 below.

In Chapter 4 the focus shifted to the palaeoclimate and palaeoceanography of the late Paleogene–earliest Neogene, specifically the Oligocene–Miocene transition (OMT) glaciation and its expression in the low latitudes of the Arabian Sea. An Oligocene–early Miocene sedimentary sequence from the eastern Arabian Sea was investigated with the aim to constrain how regional climate and ocean responded to this important global event, and whether the South Asian monsoon (SAM) system was active during this time. A multi-proxy approach of benthic and planktic stable isotope and trace element geochemistry, XRF and ICP-MS-derived elemental analysis, and calcareous nannofossil biostratigraphy was employed to investigate changes in the sedimentary environment and palaeoredox conditions. The OMT was shown to be a key step in the palaeoclimatic evolution of the eastern Arabian Sea. The transient glaciation event during the early OMT (23.7–23.0 Ma) was associated with an increase in winter monsoon-like atmospheric circulation during which there was an increase in water mass mixing and ventilation at the site. The latter part of the OMT (after ~23.0 Ma), the deglaciation phase, was associated with a long-term change in sedimentation at the site. Other notable changes include: 1) a relative increase in clays; 2) a decrease in $CaCO_3$; and 3) a decrease in oxygenation. Evidence suggests the development of an intense oxygen minimum zone (OMZ) in the eastern Arabian Sea, signifying an initiation/intensification of proto-SAM atmospheric circulation. This is the first marine record from the eastern Arabian

Sea area that suggests an Oligocene–Miocene initiation of a proto-SAM; however, proximal terrestrial records of weathering, increased denudation rates of the Western Ghats mountain range on peninsular India, and dust records from the Maldives all support this hypothesis.

In Chapter 5 a sedimentary sequence from the Middle East was investigated through a transient, global climatic perturbation, the PETM. The aim was to reconstruct palaeoceanographic circulation through the eastern Tethys through the use of neodymium isotopes, combined with previously conducted XRF-derived elemental data and organic carbon isotopes ($\delta^{13}C_{org}$). Due to delays caused by the Covid-19 pandemic conclusions for this chapter are preliminary; however, initial datasets show that, associated with the PETM hyperthermal, there is no discernible change in neodymium isotopes measured from fish teeth. This suggests that this transient perturbation to the climate-carbon cycle did not affect the palaeoceanographic setting of this site in the eastern Tethys within the resolution of the study. Over the longer-term, however, there was change to less radiogenic (more negative) neodymium isotope values. It is hypothesised that this could be driven by a change to end-member water mass mixing, either through a decrease in incorporation of a radiogenic water mass (for example sourced from the Deccan Traps region) or from an increase in influence of a less radiogenic water mass (either from the Indian or Atlantic Ocean).

6.2 Addressing research questions

This section aims to recap the research questions originally posed in Chapter 1 and to detail how the subsequent data chapters addressed them.

> 1) Are Paleogene hyperthermals (e.g., the PETM) preserved in the shallow water and/or low latitude sediments in this region? If so, how are the hyperthermals characterised in the investigated sediments and what does this tell us about the effects of hyperthermals on these shallow water/low latitude environments?

In Chapter 2 it was demonstrated that within the shallow water sediments of the low latitude Tethys, Paleocene–Eocene hyperthermals are expressed

chemostratigraphically and biostratigraphically within carbonate sediments. A partial record of the PETM, as well as other early Eocene hyperthermals such as ETM2, were expressed in the bulk carbonate carbon isotope record as a major negative CIE, comparable to those observed in contemporaneous deep water records (e.g., Fig. 2.10; p. 56). Calcareous nannofossil biozonation constrained the age model and enabled the observed hyperthermal events to be tied with increased confidence to deep water ODP Site 1262 stratigraphy (Barnet et al., 2019). There is a dearth of data from the tropical low latitudes, especially from shallow water sites, that incorporate geochemical, sedimentological, and biostratigraphic data. This record from onshore UAE indicated that the shallow water chemostratigraphic record is impacted by rapid, transient global warming events, but the sedimentological and biotic records are impacted differently to the better studied deep water sites. This is expanded upon in research question 2. The potential of shallow water sites to reveal new insights into well-studied events such as the PETM were validated.

In Chapter 5 possible changes in the palaeoceanography and weathering regime of the eastern Tethys across the PETM hyperthermal were investigated using neodymium isotope analysis of fossil fish teeth. The evidence from Nd isotopes suggesting no change in current configuration contrasts with previous investigations, based on carbon isotope data and modelling, that previously suggested a possible transient change in thermohaline circulation over the PETM (Tripati & Elderfield, 2005; Nunes & Norris, 2006; Lunt et al., 2010; Cope & Winguth, 2011; Abbott et al., 2016). This result is also in line with data from other neodymium isotope studies, which did not show evidence for wholesale reorganisation of global ocean circulation associated with the PETM (Fig. 5.7; p. 150) (Thomas et al., 2003). However, the Jordan study was based on a small sample set of neodymium analyses due to Covid disruption, which led to only 3 data points spanning the latest Paleocene to earliest Eocene, and further work is required to corroborate this hypothesis (Section 6.3.3).

2) Are shallow water palaeo-fauna adversely affected by either transient climate perturbations or long-term climate change in the early Paleogene? Specifically, how do the larger benthic foraminifera (LBF) respond to long-term climate warming through this interval?

Intriguingly, despite the PETM hyperthermal onset being resolvable in the shallow water realm of the eastern Tethys (e.g., UAE), the impacts of this event on the biotic environment, and specifically the LBF, were different to those typically observed in foraminifera in the deep sea. In a number of deep water sites benthic foraminiferal communities experienced up to 50% extinction; coincident with the PETM in the eastern Tethys there was little change in the LBF assemblage. Instead, the long-term warming over the early Eocene interval caused an overturning in the LBF assemblage (Fig. 2.4; p. 41). This led to an eventual dominance of generalist genera that were able to rapidly colonise ecological niches, as well as an overall increase in LBF species richness. Prior to this, in the late Paleocene, there were substantial changes in the overall biotic assemblage at this site. A systematic loss of the diverse, shallow water reef assemblage began in the late Paleocene, with corals and gastropods becoming absent and the more rapidly calcifying LBF instead beginning to dominate. This suggests the shallow water LBF were sensitive to long-term warming, but resilient to short-term, transient hyperthermal events.

3) Can we improve the currently available methods for disaggregating heavily indurated carbonate samples to effectively and efficiently retrieve LBF (and possibly other micro- and macrofossils)?

In Chapter 3 it was demonstrated that EPF is an effective and efficient method of liberating LBF from indurated carbonates. This technique significantly improved the processing of samples when compared to the traditional methods of Calgon and acetic acid disaggregation. EPF was also able to liberate the microfossils (predominantly LBF) with little to no damage (Fig. 3.7; p. 83). The progress made in this area will enable more detailed study of shallow water carbonates that are typically well cemented due to diagenetic processes.

4) Are there associated palaeoceanographic changes in the study region through the late Paleocene to early Eocene time interval? It has been suggested that the PETM caused transient palaeoceanographic circulation changes; do we detect this in the study region?

Although there was no change in neodymium isotope values associated with the PETM itself in the eastern Tethys, there was a long-term change from more radiogenic values in the late Paleocene to less radiogenic values in the early Eocene (Chapter 5; Fig. 5.6; p. 147). Results are based on a limited dataset and plans for future work on this study are detailed in Section 6.3.3.

5) What are the impacts of the transient, global cooling events (e.g., the Oligocene–Miocene transition glaciation event) in the same low latitude regions? How does this long-term evolution of climate interact with this region which has active monsoonal circulation? What can this tell us about the proto-South Asian monsoon?

The late Oligocene to early Miocene interval was studied at a high-resolution in the Arabian Sea in order to investigate the effects of long-term warming (the late Oligocene warming event; LOWE) and short-term cooling (the OMT) in a low latitude region (Chapter 4). There is currently a lack of recovered sedimentary archives available from the Arabian Sea covering this interval, thus the impacts of these changes in climate combined with the contemporaneous changes in palaeogeography (e.g., the Himalayan-Tibetan plateau; HTP) and palaeoceanography (closing east Tethys gateway) were previously poorly constrained. This chapter showed that the combination of climatic/tectonic/orbital factors likely created a step-change in the sedimentary sequence from carbonate-dominated to clay-dominated sediments (Fig. 4.8; p. 110). This change occurred coincident with the OMT. During the early OMT, the Southern Hemisphere glaciation caused an increase in oxygenation at this site, possibly orbitally-driven by a southward migration of the intertropical convergence zone (ITCZ). This resulted in winter monsoon-like atmospheric circulation, increasing vertical mixing of the water column and the observed increase in oxygenation. During the latter part of the OMT, the deglaciation caused a decrease in oxygenation and a relative increase in clay at this site. It is hypothesised this is caused by an initiation/intensification of a proto-SAM system in the Arabian Sea, inducing an intense OMZ in the eastern Arabian Sea (Fig. 4.15; p. 124). This crossing of a long-term climatic threshold impacting the low latitudes was also observed in Chapter 2 where long-term Paleocene–Eocene warmth caused an overturning in the LBF assemblage.

6) Can the effects of contemporaneous tectonic and climatic shifts be disentangled through sedimentological and geochemical analyses?

The OMT transient glaciation occurred contemporaneously amid tectonic changes adjacent to Site NGHP-01-01A in the Arabian Sea; namely the continuing uplift of the HTP and the gradual closure of the eastern Tethyan gateway (Chapter 4). It was concluded that the observed sedimentological and geochemical changes at the Oligocene–Miocene boundary were likely caused as a combination of climatic/tectonic factors, however, it was not possible to equivocally say what the main driving influences were. Further work that would aim to disentangle these causation mechanisms is detailed in Section 6.3.2.

6.3 Future work

6.3.1 Tailoring the EPF methodology for smaller microfossils and developing comparison

A new methodology for using EPF to liberate microfossils from indurated carbonates is detailed in Chapter 3. The EPF method predominantly freed microfossils >500 µm in size, therefore future work would aim to adapt the methodology for use on microfossils <500 µm. By using multiple rounds of EPF on each sample, progressively decreasing the size of the sieve aperture, the process would continue breaking down non-disaggregated sediments, whilst allowing progressively smaller microfossils to fall through the sieve. This adaptation to the method described in Chapter 3 requires testing to ensure that the liberated microfossils are not damaged or broken during this more intensive treatment process, as this would render them unusable for biostratigraphic analysis. Further to this, a comparison with the freeze-thaw disaggregation method implemented in the Chapter 5 methods (Section 5.4.1) could increase the utility of the EPF method to a wider range of substrates. Freeze-thaw is commonly used to disaggregate organic-rich sedimentary rocks (Saini-Eidukat & Weiblen, 1996), therefore it’s comparison with EPF is important to gauge which is the more efficient method for liberating microfossils in such substrates.

6.3.2 Constraining weathering fluxes in the Arabian Sea

Within Chapter 4 it was hypothesised that the step-change in weathering patterns over the Oligocene–Miocene transition was triggered by the initiation/intensification of a proto-SAM. The main terrigenous input to Site NGHP-01-01A in the eastern Arabian Sea is from rivers draining the Western Ghats (Yang et al., 2020). Therefore, any increase in input from these areas should have a distinct geochemical and mineralogical signature; this has been documented in Miocene to recent studies from the eastern and northern Arabian Sea (Alizai et al., 2012; Limmer et al., 2012; Phillips et al., 2014; Cai et al., 2018; Yu et al., 2019; Chen et al., 2019, 2020; Clift et al., 2020). Future work would aim to constrain weathering fluxes from the hinterland through the use of clay mineralogy data. Presently available low-resolution data from this site shows both step-changes and long-term changes in clay mineralogy throughout the Oligocene and Miocene epochs. Higher resolution data would build on this data to improve our understanding of what the main sources of terrigenous input to the eastern Arabian Sea were during this time period, and to validate the hypothesis that the OMT was a key transition in the evolution of the proto-SAM system.

6.3.2.1 Constraining palaeoceanographic and tectonic interactions in the Arabian Sea

In Chapter 4 it was hypothesised that a transient sea level fall over the OMT could have temporarily changed oceanographic currents due to a reduction/restriction in TISW throughflow (Fig. 6.1), resulting in the increased oxygenation observed during the early part of the OMT. More evidence is required to corroborate this statement and future work would aim to investigate this further, for example, through the use of neodymium isotopes. As was discussed in Chapter 5, water masses have distinct neodymium isotopic values depending on their source region. If there had been changing influence of intermediate water masses at Site NGHP-01-01A during the early part of the OMT, for example from mainly TISW to mainly southern-sourced AAIW-SAMW (Fig. 6.1), there may be an associated change in neodymium isotopes. At the present day, the eastern Mediterranean has a generally radiogenic signature (ε_{Nd} = ~–5 to –8) and the Southern Ocean

is less radiogenic (ε_{Nd} = ~–8 to –10; van de Flierdt et al., 2016). Data from the late Oligocene to earliest Miocene (~25–22 Ma) suggest similar trends of neodymium isotopic signatures, with the eastern Mediterranean being more radiogenic (ε_{Nd} = ~–4 to –5) and the northern Indian Ocean being less radiogenic (ε_{Nd} = ~–7 to –9) (Bialik et al., 2019).

6.3.3 Constraining Dentoglobigerina venezuelana *depth habitat*

The planktic foraminifera used in Chapter 4 was inferred to be an indicator of thermocline conditions, for reasons detailed in Section 4.6.1. However, the species *D. venezuelana* is known to have changed depth in the water column through time (Wade et al., 2007; Stewart et al., 2012; Matsui et al., 2016) and the genera *Dentoglobigerina* has also been shown to have a complicated life cycle, revealed through detailed multi-species analysis (Woodhouse et al., 2021). Future work would involve multi-species stable isotope analysis of planktic foraminifera samples from both the Oligocene and Miocene to constrain in more detail any changes in *D. venezuelana* depth habitat through time.

6.3.4 Increasing data density of Tethyan neodymium data

Increasing the data density of the neodymium isotope data in Chapter 5 would aid in validating some of the possible hypotheses of mechanisms forcing the change observed in the current low-resolution data. Due to delays caused by Covid-19 related lab closures it was not possible to generate as much data as was originally intended for this chapter, including the rare earth element (REE) profiles of the samples presented. Future work would include these REE profiles as well as increased resolution neodymium isotope data. REE profiles can be used to assess if there has been any diagenetic overprint to the Nd isotopes prior to analysis. With increasing degrees of diagenetic overprint, the REE profile becomes enriched in intermediate REE, giving the profile a bell-shaped pattern (Reynard et al., 1999). A typical seawater derived profile is more enriched in lighter REE. The ratio of La/Sm normalised to the North American Shale Composite can also be used to assess REE substitution. A value of less than 0.3 is indicative of extensive modification of the REE contents through diagenesis (Reynard et al., 1999; Pucéat et al., 2005).

Appendix 1

Newsletters on Stratigraphy
Published online August 2020

Triumph and tribulation for shallow water fauna during the Paleocene–Eocene transition; insights from the United Arab Emirates

Charlotte Beasley[1]*, Laura Cotton[2,3], Aisha Al-Suwaidi[4], Leah LeVay[5], Appy Sluijs[6], Clemens V. Ullmann[1,7], Stephen P. Hesselbo[1,7] and Kate Littler[1,7]

With 9 figures and 1 table

Abstract. The Paleocene–Eocene transition was a time of short-term rapid climatic and biotic change, superimposed on a long-term warming trend. The response of shallow tropical carbonate systems to past rapid warming is important to understand in the context of ongoing and future anthropogenic global warming. Larger benthic foraminifera (LBF) were abundant and important components of shallow water ecosystems throughout the early Paleogene and are sensitive to environmental change, making them ideal organisms to track shallow marine biodiversity. Furthermore, through the use of integrated bio- and chemostratigraphy it is possible to correlate the shallow (<100 m) and deep water realms to create a regional stratigraphic framework for the time period. Here we present a new LBF biostratigraphic and high-resolution carbonate carbon isotopic record spanning the Paleocene–Eocene transition from the onshore sub-surface of the United Arab Emirates (UAE). Results show a turnover event in the LBF assemblage during the early Eocene, wherein there are a number of first and last occurrences of species. However, assemblages remain generally stable coincident with the large negative carbon isotope excursion interpreted to be the onset of the Paleocene–Eocene thermal maximum (PETM). Turnover in the LBF assemblage in the early Eocene likely occurred due to the crossing of a long-term climatic and oceanographic threshold. The impacts of this long-term climatic change on the overall biotic assemblage at this site are significant, with LBF outcompeting a previously diverse community of corals, gastropods, and bivalves to become the dominant carbonate producers through the Paleocene–Eocene transition. Despite this, modern studies suggest that LBF are not immune to impacts of anthropogenic climate change, perhaps due to the significantly higher rates of change in the modern compared to the Paleocene–Eocene transition.

Key words. Paleogene, larger benthic foraminifera, palaeoenvironment, biodiversity, PETM, shallow marine, carbonates

Authors' addresses:
[1] Camborne School of Mines, University of Exeter, Penryn Campus, Penryn, Cornwall, TR10 9FE, UK
[2] School of Earth Sciences, University of Bristol, Wills Memorial Building, Queens Road, Bristol, BS8 1RJ, UK
[3] Present address: School of Environment, Geography and Geosciences, Burnaby Building, Burnaby Road, Portsmouth, PO1 3QL, UK
[4] Earth Science Department, Khalifa University of Science and Technology, PO Box 127788, SAN Campus, Abu Dhabi, United Arab Emirates
[5] International Ocean Discovery Program, Texas A&M University, 1000 Discovery Drive, College Station, TX 77845, USA
[6] Department of Earth Sciences, Faculty of Geosciences, Utrecht University, Marine Palynology and Paleoceanography, Laboratory of Palaeobotany and Palynology, Princetonlaan 8a, 3584CB, Utrecht, The Netherlands
[7] Environment and Sustainability Institute, University of Exeter, Penryn Campus, Penryn, Cornwall, TR10 9FE, UK
* Corresponding author: c.beasley@exeter.ac.uk

DOI: 10.1127/nos/2020/0573 Borntraeger Science Publishers, Stuttgart, www.borntraeger-cramer.com

1. Introduction

The Paleocene and early Eocene (~66–50 Ma) interval is characterised by long-term warming associated with changes in the carbon cycle (e. g., Eldholm and Thomas 1993, Zachos et al. 2008, Komar et al. 2013, Anagnostou et al. 2016). Shorter period Milankovitch cyclicity, changes in Earth's orbital configuration (i. e., eccentricity, obliquity and precession), also drove both variations in climate and perturbations to the carbon cycle during this period (Cramer et al. 2003, Lourens et al. 2005, Westerhold et al. 2011, Littler et al. 2014, Westerhold et al. 2017, Barnet et al. 2019). Against the background of warming during the late Paleocene to early Eocene, several transient global warming phases, so called 'hyperthermal' events of varying severity and duration, occurred that are likely to have been paced by Milankovitch cyclicity (e. g., Cramer et al. 2003, Lourens et al. 2005, Zeebe and Lourens 2019). These hyperthermals are associated with ocean acidification (Zachos et al. 2005, Stap et al. 2009), and negative carbon and oxygen isotope excursions as recorded in carbon bearing phases in both marine and terrestrial archives (Kennett and Stott 1991, Koch et al. 1992, Thomas and Shackleton 1996, Bolle et al. 2000, Lourens et al. 2005, Sluijs et al. 2009), providing strong evidence of rapid and massive injections of carbon into the ocean-atmosphere system (Dickens et al. 1995, 1997). During the largest of these hyperthermal events, the Paleocene Eocene Thermal Maximum (PETM; ~56 Ma), global climate rapidly warmed by ~5 °C, with limited extratropical amplification (Dunkley Jones et al. 2013, Zeebe et al. 2014, Frieling et al. 2017). The PETM is recognised in geochemical records by a sudden negative carbon isotope excursion (CIE), followed by the 'body' of the CIE and relatively more gradual recovery to background levels, all of which is thought to have taken ~170 kyr (Röhl et al. 2007) but possibly more than 200 kyr (Zeebe and Lourens 2019). In many deep sea sites the magnitude of this negative excursion, as recorded in marine carbonates by benthic foraminifera, is ~2–3‰ (Kennett and Stott 1991, Bains et al. 1999, Zachos et al. 2003). However, some bulk marine organic matter records show a negative excursion of up to ~8‰ in magnitude (Sluijs et al. 2006, Cohen et al. 2007, McInerney and Wing 2011). The differences in size and shape of the CIEs measured on specific substrates and regions are thought to relate to changes in the relative abundance of mixed components with different $\delta^{13}C$ values within a measured substrate, changes in isotopic fractionation through physiological changes, changes in the isotope composition of the carbon source, and possibly effects of diagenetic alteration (Sluijs and Dickens 2012).

Following the PETM, the general warming of early Paleogene global climate continued, peaking at the early Eocene climatic optimum (EECO) between ~52–50 Ma (Zachos et al. 2001, 2008, Bijl et al. 2009, Cramwinckel et al. 2018). High-resolution records of benthic foraminifera oxygen isotope values document a number of hyperthermal events within this early Eocene general warming trend (Galeotti et al. 2010, Littler et al. 2014, Lauretano et al. 2015, 2016, Westerhold et al. 2018, Barnet et al. 2019). These events include Eocene Thermal Maximum (ETM) –2 (also referred to as Elmo or H-1; Lourens et al. 2005, Sluijs et al. 2009, Stap et al. 2010) at ~53.7 Ma and ETM-3 (or the "X" event; Agnini et al. 2009, Thomas et al. 2018) at ~52.5 Ma. Many of these early Eocene hyperthermals are thought to be orbitally paced by both the long (~405 kyr) and short (~100 kyr) eccentricity cycles, and the precession (~21 kyr) cycle (Cramer et al. 2003, Lourens et al. 2005, Galeotti et al. 2010, Zachos et al. 2010, Littler et al. 2014, Galeotti et al. 2019, Zeebe and Lourens 2019).

Throughout this early Paleogene interval larger benthic foraminifera (LBF) were abundant in tropical, shallow (<100 m) waters (Hottinger 1998, BouDagher-Fadel 2008). LBF are single-celled organisms which form more complex tests (shells) than smaller foraminifera (BouDagher-Fadel 2008). Many genera of LBF possess algal photosymbionts, similar to corals, restricting them to the marine photic zone (Haynes 1965). LBF are sensitive to environmental change, making them ideal organisms to study the effects of sudden global warming events, such as the PETM (Hallock and Glenn 1986). From the late Paleocene into the early Eocene LBF were increasingly important shallow water calcifiers, becoming the dominant carbonate producers in shallow oligotrophic environments as corals underwent decline (Scheibner and Speijer 2008a, Afzal et al. 2011, Zamagni et al. 2012). Coral reefs declined from the late Paleocene to early Eocene, possibly due to a number of stressors which include increased water temperatures and an increase in sediment load/nutrient supply (Zamagni et al. 2012). Over the Paleocene–Eocene transition, LBF underwent gradual turnover, as expressed in multiple low latitude sites including Spain, Egypt and Tibet (Scheibner et al. 2005, Pujalte et al. 2009, Zhang et al. 2018). LBF also experienced species diversification and increases in adult dimorphism and test size at this

time (Hottinger 1998, Scheibner et al. 2005, Zhang et al. 2018); these changes are termed the larger foraminifera turnover (LFT). It remains uncertain whether this LFT event coincides with, and is therefore likely to be causally related to, the PETM (Pujalte et al. 2009, Scheibner and Speijer 2009), or if it predates this event and is therefore unrelated (Hottinger 1998, Zhang et al. 2013). The correlation of the LFT event to global biostratigraphy and chemostratigraphy would tie together shallow and deep water stratigraphies; however, most sites where the LFT is well expressed lack the additional stratigraphic control to definitively link to the global expression of the PETM (e. g., Pakistan; Afzal et al. 2010). Continued diversification of the LBF through the Paleogene created "hotspots" of high generic and species-level diversity which moved eastwards through this interval, from the Tethys to the current hotspot in the Indo-Pacific (Renema et al. 2008). Absolute timing and location for the beginning of this upturn in diversity is debated, with some suggesting that it started earlier in the late Paleocene to early Eocene in the eastern Tethys (Scheibner et al. 2005, Hottinger 2014), and others proposing a later start during the late middle Eocene in the western Tethys (Renema et al. 2008).

Contrary to this more gradual turnover and diversity increase of LBF in the shallow water domain, smaller benthic foraminifera in the deep water domain experienced a major extinction. Known as the benthic foraminifera extinction event (BEE; Thomas 1989, Thomas and Shackleton 1996, Thomas 1998, Alegret and Ortiz 2006), 30–50 % of known deep sea smaller benthic foraminifera species did not survive into the Eocene (Schmitz et al. 1996, Thomas 1998, 2007). It is suggested that the recorded ~5 °C of bottom water warming could have caused the BEE (Thomas et al. 2000, Winguth et al. 2012), either through warming of surface waters in regions of bottom water formation, or due to a switch of bottom water formation to lower latitudes (Thomas and Shackleton 1996). Additional factors affecting the smaller benthic community were marine waters that were increasingly corrosive to $CaCO_3$, decreased oxygenation, and changes in productivity (Thomas 1998, 2007). It has also been suggested that the rapidity of the climate perturbations at the PETM, rather than the magnitude itself, caused the BEE (Thomas 2007). Across the gradual (~500 kyr) global cooling at the Eocene–Oligocene transition, abyssal and bathyal benthic foraminifera show little change associated with the boundary itself, in contrast to the PETM (Coxall and Pearson 2007). This suggests an ability to adapt to such gradual changes and an inability to cope with the sudden change in palaeoenvironment at the onset of the PETM.

It is increasingly clear that hyperthermal events such as the PETM have a spatially heterogenous expression, where different regions experienced contrasting shifts in temperature (Sluijs et al. 2006, Aze et al. 2014, Sluijs et al. 2014, Frieling et al. 2017) and hydrology (Bolle and Adatte 2001, Bowen et al. 2004, Schmitz and Pujalte 2007, Bowen and Bowen 2008, Carmichael et al. 2017), as well as differing biological responses to these conditions (Speijer et al. 2012). For example, general circulation model (GCM) simulations for the PETM indicate that some regions, such as the eastern US coast and a number of localities around the Tethys, likely experienced increased precipitation, while the western US and the Angola Basin experienced aridification over the same interval (Carmichael et al. 2017). It is therefore important that the proxy record also has broad spatial coverage, both in terms of latitude/longitude and depth in the oceans.

Although there are excellent representative deep sea marine records of the late Paleocene to early Eocene from most of the major ocean basins, more multi-proxy records from the low latitudes and tropics are required in order to test these models. In particular, there is a dearth of data from shallow marine (<100 m), low latitude areas (Fig. 1). Although geochemical, sedimentological, palaeogeographical, and palaeobiological data spanning this interval are available from other east Tethyan sections (Nolan et al. 1990, Keen and Racey 1991, Alsharhan and Nairn 1995, Racey 1995, Schmitz et al. 1996, Charisi and Schmitz 1998, Speijer and Schmitz 2000, Speijer and Wagner 2002, Dupuis et al. 2003, Alegret and Ortiz 2006, Beavington-Penney et al. 2006, Dill et al. 2007, Khozyem et al. 2015, Serra-Kiel et al. 2016a, Giraldo-Gomez et al. 2018) comparable data from the United Arab Emirates (UAE) is of limited spatial and temporal resolution (Dill et al. 2007, Faris et al. 2014, Tomas et al. 2016). Importantly, the UAE is significantly further south (by ~5°) and further east than most of these existing sites (Fig. 1). High-resolution, integrated geochemical and palaeoecological records from low latitude, shallow water sites of this age are important to constrain how these regions responded to both long-term changes in the climate and carbon cycle and geologically rapid events such as the PETM. A multi-proxy, integrated approach is key in order to be able to tie local stratigraphy to a global stratigraphic model, allowing for correlation from the shallow to the deep oceans.

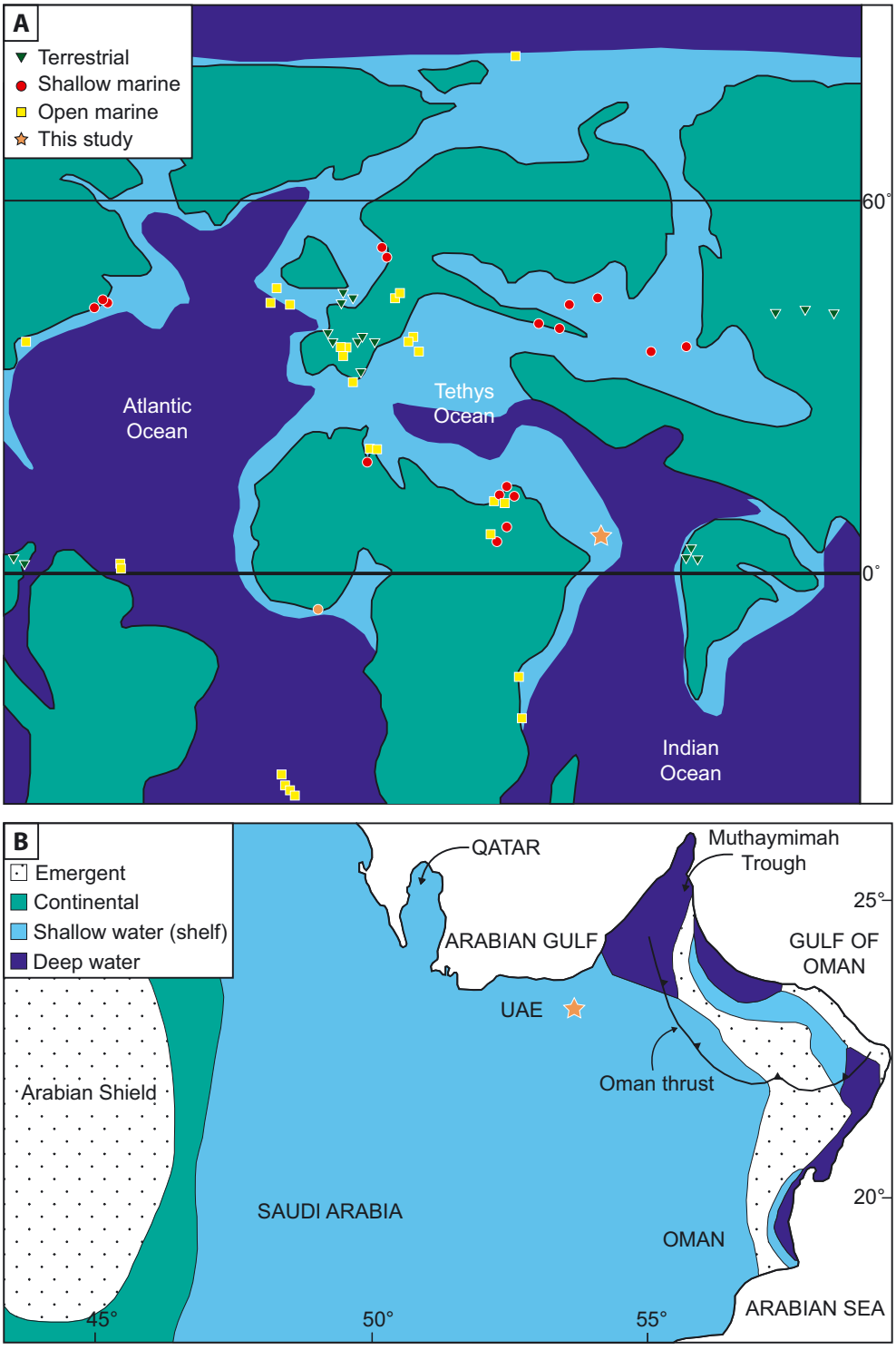

Fig. 1. **A** – Map of late Paleocene (~56 Ma) palaeogeography (adapted from Dickson et al. 2015) displaying locations of PETM records (modified from McInerney and Wing 2011). Shallow marine defined as <200 m water palaeodepth, open marine defined as 200 m to pelagic. Note the lack of sections from the southern and eastern Middle East, and the Arabian Sea. **B** – Palaeogeography of the Arabian Plate during the late Paleocene to early Eocene showing relationships between shallow and deeper water facies (modified from Ziegler 2001, Haq and Al-Qahtani 2005). Orange star indicates Core A location in both figures.

Here we present an integrated, high-resolution LBF record with stable isotope and calcareous nannofossil stratigraphy from the subsurface of onshore United Arab Emirates (UAE) covering the late Paleocene into early Eocene interval. This area previously lacked integrated, high-resolution palaeoclimatic data from this globally important time interval (Fig. 1). The core investigated in this study provides an opportunity to examine a long-ranging interval in which the LBF response to global climate change can be tied to the global isotope and biostratigraphy. The response of the low latitude and shallow water domains to past climate perturbations provides important insight for the future response of these fragile ecosystems to anthropogenic climate change.

2. Geological setting of study area

In order to address the outstanding questions surrounding the response of the shallow marine realm to the climatic changes during the late Paleocene to early Eocene, we produced new geochemical and palaeontological records from "Core A", onshore UAE (Fig. 1). Core A was recovered by Abu Dhabi National Oil Company (ADNOC) and may have economic significance, and as such the specific core name and precise locality cannot be published. Located in the western UAE, Core A is from an area otherwise dominated by sandy desert with no available outcrop. Core A was logged at a high-resolution along the entirety of its length revealing the core consists of ~383 m of dominantly shallow (<100 m) marine carbonate sediments, rich in bioclasts (Fig. 2). The examined core was previously split and slabbed, allowing for sedimentary structures and biota to be observed. The top of the core starts at approximately 985 m depth below surface (mbs), extending to ~1350 mbs at the base of the core. For the purpose of this study 985 mbs was used as the zero level and will be referred to as such for the rest of the text.

3. Methods

3.1. Microfossils

3.1.1. Larger benthic foraminifera

A total of 48 samples were analysed for LBF biostratigraphy through the use of 56 petrological thin sections. Multiple thin sections were made for some samples in order to aid identification of LBF; identification to species level requires the specimen to be orientated with the section passing through the first chamber (proloculus), thus duplicate thin sections were made in key intervals at right angles to one another. Standard petrographic thin sections were used for identification of LBF taxa and ground to a thickness of 50 µm in order to ensure skeletal grains were identifiable. Samples were taken approximately every 20 m for the lower part of the core, increasing to a ~5 m resolution from ~50 m depth to the top of the core (Fig. 2). Taxonomy follows that of Hottinger (2014).

3.1.2. Calcareous nannofossils

Sixteen samples from between 5.8–372.6 m were studied in order to provide a biostratigraphic framework. Samples that contained a higher percentage of marl were chosen for analysis on the basis that preservation was likely to be better in the finer grained sediment. Smear slides were prepared using standard techniques (Bown and Young 1998) and the slides used 24 mm x 40 mm cover slips. Transects across the cover slip were made at x630–1000 magnification using a Zeiss Axioscope A1. The transects were intended to capture the whole cover slip, but some fields of view may have been missed.

Total nannofossil abundance in the slide was visually assessed using the following criteria (Clemens et al. 2016): D = dominant (>90 % of sediment particles in a field of view); A = abundant (50–90 % of sediment particles); C = common (10–50 % of sediment particles); F = few (1–10 % of sediment particles); R = rare (<1 % of sediment particles); B = barren (no specimens present).

The relative abundance of nannofossil species was not collected due to the overall rarity of fossils. In Figure 5, the presence of a species is denoted with an 'X', and questionable species occurrences due to poor preservation are marked with a '?'.

The preservation state of the nannofossils was qualitatively described using the categories (Clemens et al. 2016): VG = very good (no evidence of dissolution and/or recrystallisation, no alteration of primary morphological characteristics, and specimens identifiable to species level); G = good (little evidence of dissolution and/or recrystallisation, primary morphological characteristics only slightly altered, and specimens identifiable to species level); M = moderate (specimens exhibit some etching and/or recrystallisa-

tion, primary morphological characteristics somewhat altered, and most specimens identifiable to species level); P = poor (specimens severely etched or overgrown, primary morphological characteristics largely destroyed, fragmentation has occurred, and specimens could not be identified to species and/or genus level).

The biostratigraphic classification of the study succession is based upon the Martini (1971) NP zonation (Agnini et al. 2007, 2014). Nannofossil taxonomy follows Perch-Nielsen (1985) and the Nannotax database (Young et al. 2019).

3.1.3. Palynomorphs

Three samples were processed for palynology. These samples bordered the Paleocene–Eocene boundary, with slides at 7.4 m, 8.2 m, and 153.3 m from the top of the core. Palynological slides were prepared at the National Oceanography Centre, University of Southampton. Approximately 5 g of roughly crushed rock was treated with 30 % HCl to remove carbonates, followed by decant washing to a neutral pH. Samples were further demineralised in 60 % HF followed by decant washing again to a neutral pH and sieved at 15 µm. Samples were then placed in glass beakers and briefly boiled in 30 % HCl to solubilise neoformed fluorides that were then removed by diluting into a large volume of water and re-sieving. Residues were then vialed, with strew slides made and mounted in Elvacite 2044™. Residues were analysed at Utrecht University, Laboratory of Palaeobotony and Palynology for general palynological content, with emphasis on dinoflagellate cysts (dinocysts) following the taxonomy of Williams et al. (2017).

3.2. Carbon and oxygen isotope analysis

The bulk carbonate fraction from a total of 710 samples was analysed for stable carbon and oxygen isotopes. This consisted of 379 samples from the top 79 m of Core A, at a resolution of 10 cm, and 331 samples from the remaining ~300 m, at a resolution of approximately 1 m. These samples were drilled using a micro-drill, choosing fresh surfaces and avoiding macrofossil material. The bulk rock powder was weighed at 500 ± 50 µg for each sample and subsequently analysed for $\delta^{13}C$ and $\delta^{18}O$ values using a SerCon 20-22 Gas Source Isotope Ratio Mass Spectrometer (GS-IRMS) in the Environment and Sustainability Institute, University of Exeter. Samples were weighed using a MSE3.6P-000-DM Sartorius Cubis® Micro Balance. Standards and samples are reported in δ-notation relative to VPDB (Vienna Pee Dee Belemnite). Each complete run of analysed samples consisted of 80 samples plus 22 aliquots of the in-house standard CAR (Carrara Marble, $\delta^{13}C$ = +2.10‰ VPDB; $\delta^{18}O$ = –2.03‰ VPDB) and 8 aliquots of the in-house standard NCA (Namibia Carbonatite, $\delta^{13}C$ = –5.63‰ VPDB; $\delta^{18}O$ = –21.90‰ VPDB). Standards were also weighed at 500 ± 50 µg.

All samples were flushed with He for 80 seconds before manual injection of ~100 µL of nominally anhydrous phosphoric acid. Samples were measured alternating with a reference gas in continuous flow mode (Spötl and Vennemann 2003). For the results shown in this report the average 2 sd repeatability of CAR was found to be 0.06‰ for $\delta^{13}C$ and 0.14‰ for $\delta^{18}O$ and average 2 sd repeatability of NCA was 0.09‰ for $\delta^{13}C$ and 0.30‰ for $\delta^{18}O$ (Table S1, Supplementary Information).

3.3. Percentage calcium carbonate analysis

Percentage calcium carbonate (%$CaCO_3$) data were determined as a by-product of the carbonate carbon and oxygen isotope analysis detailed in Section 3.2. Bulk sediment samples were weighed before analysis (as above), and this known amount was dissolved using anhydrous phosphoric acid. Once dissolved the samples release CO_2, and through calibration of the size of this CO_2 peak relative to known standards, the % $CaCO_3$ could be determined for each sample, yielding a 2 sd reproducibility of ± 2.3 % for the in-house standard NCA (n = 79) (e. g., Razmjooei et al. 2020).

3.4. Inductively coupled plasma optical emission spectroscopy (ICP-OES)

A total of 34 bulk carbonate samples were analysed using ICP-OES, at a resolution of approximately 10 m, for their trace element signal. Bulk samples were micro-drilled, choosing fresh surfaces and avoiding macrofossil material. Bulk rock powder was weighed at 850 ± 100 µg using a MSE3.6P-000-DM Sartorius Cubis® Micro Balance. The samples were dissolved using 2 % nitric acid and diluted to a nominal Ca concentration of 25 µg/g. These solutions were run on an Agilent 5110 Series machine at the University of Exeter Penryn Campus with three multi-elemental standards consisting of 12 JLS-1, 8 AK and 4 BCQC. Table S2 (Supplementary Information) shows

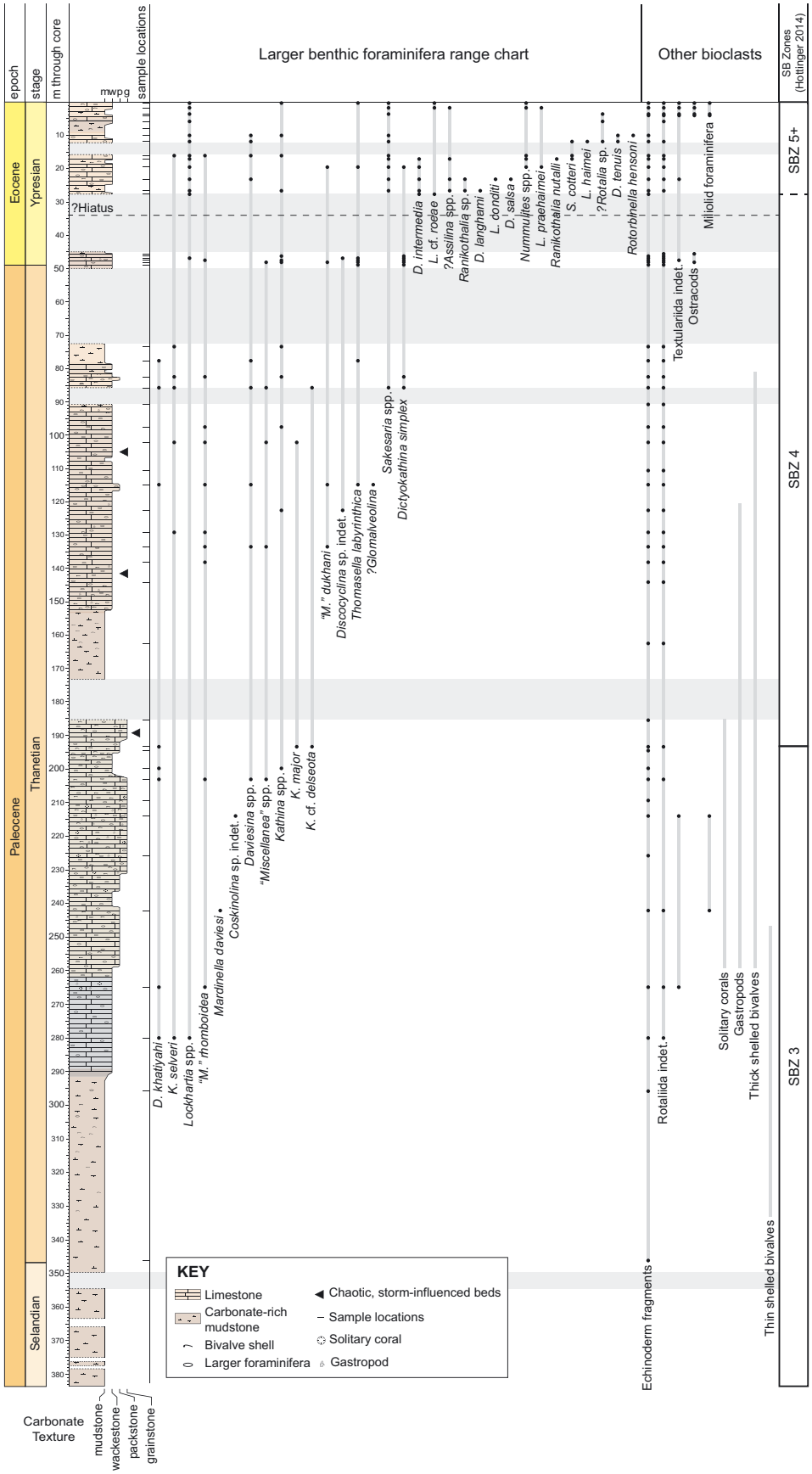

Fig. 2. Log of Core A and range chart of LBF species and genera observed, arranged by first occurrence in the core. Also included are other bioclasts observed in the core. Shallow benthic (SB) zonation scheme from Hottinger (2014). Colours of log directly reflect changes in lithology colour of core. Horizontal grey boxes mark core gaps.

the suite of analysed elements with their 6 sd quantification limits. Data repeatability (2 relative standard deviations) is generally better than the larger value of either the quantification limit (for low element/Ca ratios) or 1 % of the measured element/Ca ratio (for high element/Ca ratios).

3.5. Optical cathodoluminescence microscopy

Three representative thin sections from Core A were observed using a Nikon Eclipse LV100ND with CITL Analytical Instruments MK 5-2 cold cathodoluminescence microscope in order to observe areas of possible diagenetic alteration. Investigated samples were from ~0.2 m, ~16.1 m, and ~85.6 m, within bioclastic facies dominated by LBF. Impurities within the carbonate rocks affect the luminescence of the material, with Mn^{2+} activating luminescence and Fe^{2+} quenching it. The ratio of these elements, therefore, control the intensity of luminescence in a material (Adams and MacKenzie 1998).

3.6. Wireline logging

Wireline logging data, collected during drilling operations, were obtained from ADNOC. The wireline undifferentiated gamma ray data has been used in this study; spectral gamma ray was not available. Measurements were taken approximately every 15 cm downcore.

4. Results

4.1. Sedimentology

Within the core there are three distinct lithofacies (Fig. S1): 1) Marl with few or no bioclasts; 2) LBF-rich bioclastic wackestone/packstone and; 3) Bioclastic grainstone with LBF, gastropods, bivalves, and solitary corals. In the lower part of the core, from 383–285 m, facies type 1 dominates with occasional thin-shelled bivalves and rare or absent photosymbiont bearing organisms, such as corals or LBF. This lower interval transitions up into facies type 3 from ~285–185 m. From ~173 m upwards in the core there are a series of shallowing-up parasequences on the order of 10's of metres (Fig. 2). Marls with thin-shelled bivalves and LBF, suggestive of a low energy environment, grade upwards into more bioclastic facies (facies type 2) with thicker shelled bivalves, occasional gastropods and abundant LBF. Within these parasequences there are intermittent grainstone beds composed of broken up, poorly sorted bioclasts (Fig. 2). The nature of these beds is suggestive of storm-influenced deposits.

Within the observed sedimentary sequence there is no evidence of sub-aerial emergence of the platform indicating that there is an absence of large regression episodes on the platform. However, there are large gaps in the record at the top of the core where no sediments were recovered during drilling.

4.2. Micropalaeontological results

4.2.1. The larger benthic foraminiferal assemblages

The LBF assemblages were examined throughout Core A (Figs. 2 and 3) in order to construct the basis of an age model and determine palaeoecological changes through the Paleocene–Eocene interval. Biostratigraphy of LBF uses regional schemes; within the Tethyan region this is the shallow benthic zonation (SB) scheme (Papazzoni and Pignatti 2019), which is the closest and most widely used in the Arabian Peninsula region. To create the biostratigraphic model, the SB Zonation scheme constructed in the Tethyan region, updated and modified in nearby areas of the Arabian Plate, was utilised (Serra-Kiel et al. 1998, Scheibner and Speijer 2009, Serra-Kiel et al. 2016a, Serra-Kiel et al. 2016b).

The LBF assemblage in Core A consists largely of the genera *Daviesina*, *Kathina*, *Lockhartia*, *Miscellanea*, *Sakesaria*, *Ranikothalia*, and *Nummulites*, all of which are typical for the region. From the bottom of Core A to ~50 m the LBF assemblages are composed

Fig. 3. Selected late Paleocene to early Eocene LBF from Core A. **1**) *Miscellanea "rhomboidea"* Kuss and Leppig 1989, range undefined, 133.5 m. **2**) *Daviesina khatiyahi* Smout 1954, Zone SB 3–4, 194.6 m. **3**) *Kathina selveri* Smout 1954, Zone SB 3–4, 280 m. **4**) *Lockhartia* cf. *conditi* (Nuttall 1926), Zone SB 4–8, 23.1 m. **5**) *Nummulites* sp., Zone SB 5+, 16.1 m. **6**) *Sakesaria cotteri* Davies and Pinfold 1937, Zone SB 5–7, 17.1 m. **7**) *Dictyokathina simplex* Smout 1954, Zone SB 3–4, 194.6 m. **8**) *Mardinella daviesi* (Henson 1950), Zone SB (?–)4, 242.1 m. **9**) *Thomasella labyrinthica* Grimsdale 1952, Zone SB 4(–5?), 115 m. **10**) *Miscellanea dukhani* Smout 1954, Zone SB 4–5, 133.5 m. **11**) *Ranikothalia nuttalli* (Davies 1927), Zone SB 4, 17.1 m.

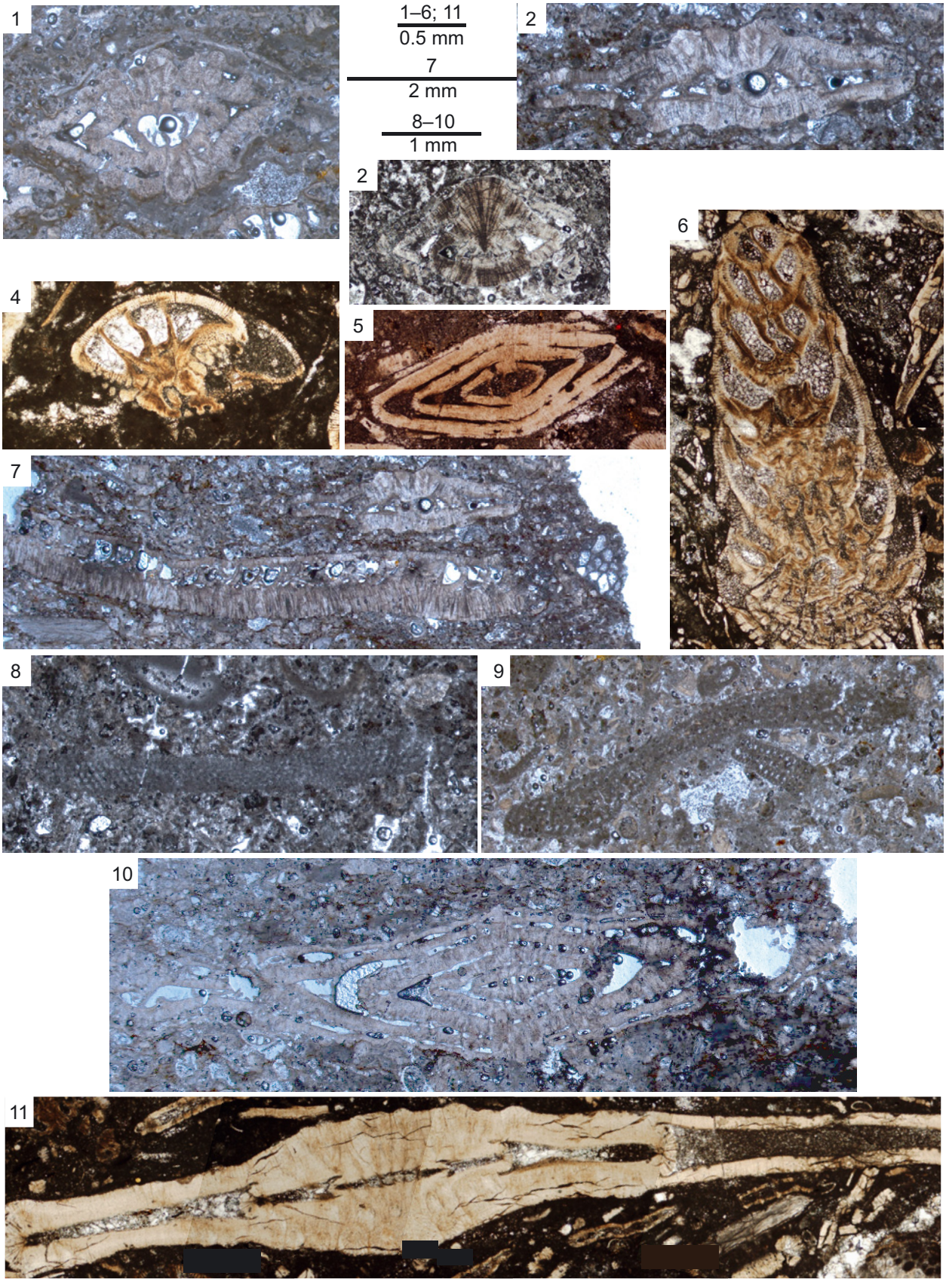
1
1–6; 11
0.5 mm
7
2 mm
8–10
1 mm
2
2
6
4
5
7
8
9
10
11

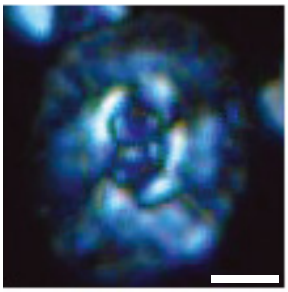
1

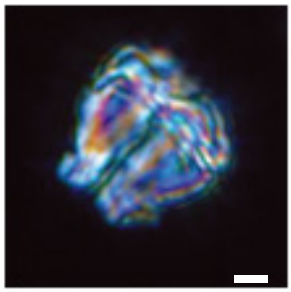
2

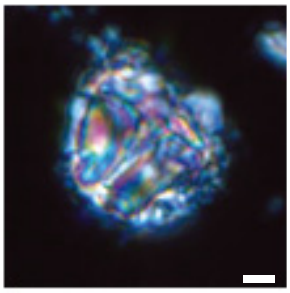
3

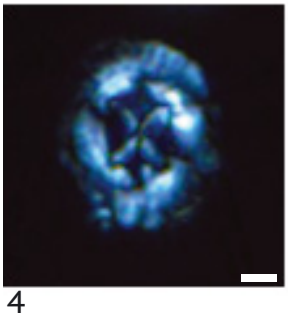
4

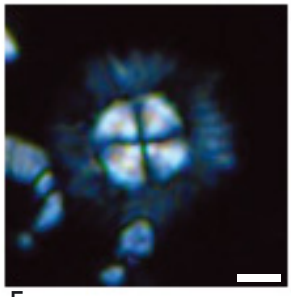
5

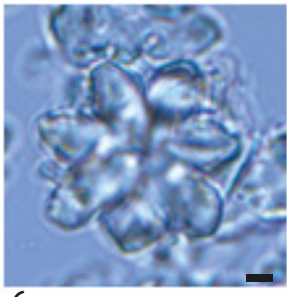
6


7

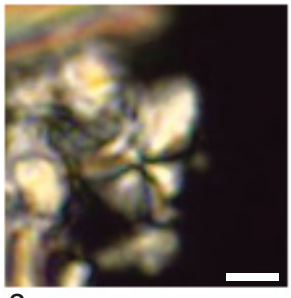
8

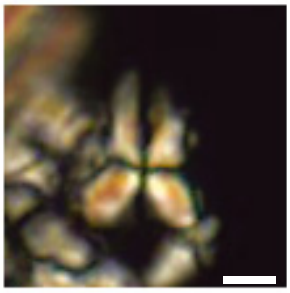
9


10

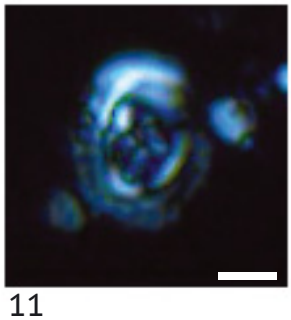
11

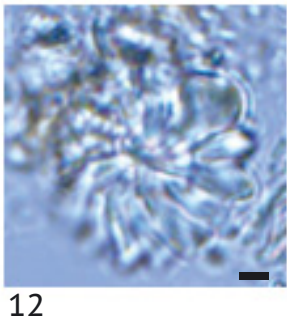
12


13

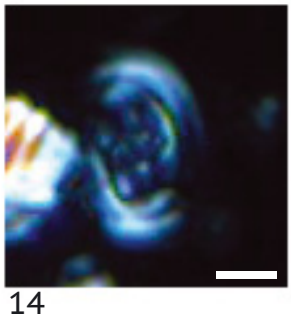
14

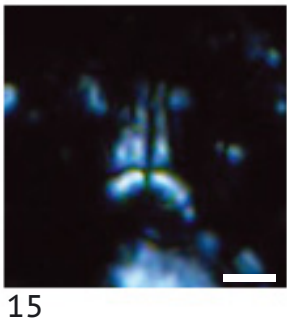
15

Fig. 4. Select nannofossils from Core A. The horizontal scale bar is 2 microns. **1**) *Chiasmolithus nitidus* ? Perch-Nielsen 1971, 372.6 m. **2, 3**) *Lithoptychius janii* Perch-Nielsen 1971, 372.6 m. **4**) *Chiasmolithus consuetus* (Bramlette & Sullivan 1961), Hay & Mohler 1967, 368.6 m. **5**) *Bomolithus megastypus* (Bramlette & Sullivan 1961), Bown 2010, 170.2 m. **6**) *Discoaster nobilis* ? Martini 1961, 170.2 m. **7**) *Discoaster multiradiatus* Bramlette & Riedel 1954, 77.7 m. **8, 9**) *Sphenolithus apoxis* ? Bergen & de Kaenel 2017, 77.7 m. **10**) *Discoaster multiradiatus* Bramlette & Riedel 1954, 27.7 m. **11**) *Campylosphaera eodela* Bukry & Percival 1971, 27.7 m. **12, 13**) *Discoaster barbadiensis* Tan 1927, 16.1 m. **14**) *Campylosphaera eodela* Bukry & Percival 1971, 16.1 m. **15**) *Sphenolithus orphanknollensis* Perch-Nielsen 1971, 11.9 m.

primarily of the genera *Daviesina*, *Miscellanea, Kathina* and *Dictyokathina*, diagnostic of Zones SB 3 and SB 4, which broadly correlate to a mid to late Paleocene age (Serra-Kiel et al. 1998). The first occurrence (FO) of *Kathina major* and *K. delseota* and the FO of *Miscellanea dukhani* occur at ~193 and ~134 metres respectively (Hottinger 2009, 2014), placing the Zone SB 3–4 boundary at approximately 193 m (Fig. 2). Between 134 and 46 m the assemblages remain relatively consistent, with 5 first occurrences and 4 last occurrences recorded. There is then a core gap between ~46–27 m.

Above ~27 m in the core the genera *Sakesaria* and *Nummulites* along with small rotaliids and miliolids dominate the assemblages, indicative of Zone SB 5 and higher, approximately correlating to the early Eocene (Serra-Kiel et al. 1998, Scheibner and Speijer 2009). A more precise SB Zone cannot be determined due to a lack of age diagnostic species in these samples. Following Serra-Kiel et al. (1998), Scheibner et al. (2005) and Scheibner and Speijer (2009) the Zone SB 4–5 boundary is defined by the last occurrence (LO) of *Dictyokathina simplex* and all representatives of the genus *Miscellanea*, along with the FO of *Sakesaria cotteri*, *Ranikothalia nuttalli*, *Rotalia* spp. and *Nummulites* spp. This suggests the boundary between Zone SB 4 and 5 is between 27 and 16 metres, within which *Ranikothalia nuttalli*, *Sakesaria* spp. and *Nummulites* spp. all have first occurrences preceding the last occurrences of *Dictyokathina simplex* and the genus *Miscellanea*.

Within the defined Zone SB 4–5 interval (27–16 m; Fig. 2), LBF species richness increases over approximately 10 m of stratigraphy. The assemblages from the bottom of the core to ~45 m is relatively uniform, with 6 genera and 7 species in Zone SB 3 and 9 genera and 9 species in Zone SB 4. From ~45 m, Zone SB 5 and higher, the number of genera increases to 11 and the number of species increases substantially to 16.

4.2.2. Calcareous nannofossil biostratigraphy

In general, nannofossils are poorly preserved (Fig. 4) and have abundances ranging from rare to few when present (Fig. 5). A total of 29 species plus 7 undifferentiated genera are recognised (Fig. 5). The estimated age assignments are primarily based upon the assemblage and documented ranges of non-marker species, as few marker species are present in the samples. We caution that the presented zones are estimates that provide age constraints and, without the presence of marker taxa, cannot be regarded as precise. The samples range from middle Paleocene (Zone ~NP 4–6) to the early Eocene (~NP 11). Of the 16 samples, approximated biozone ranges are assigned to 9 of them. Where approximate ages are stated, they are calibrated to GTS2012 (Gradstein et al. 2012).

The base of the core (~370 m) contains *Lithoptychius janii*, which constrains the age of these sediments to likely be within the NP 4–6 biozones (Varol 1989, Young et al. 2019) and corresponds to the middle Paleocene. Below the large gaps in the core, at ~78 m, the first appearance of the robust marker species *Discoaster multiradiatus* is present indicating late Paleocene age (marker species for the base of Zone NP 9; Martini 1971). The top of the core (~28 m and above) contains *Campylosphaera eodela*, *D. multiradiatus*, *D. barbadiensis*, *Coccolithus latus* and *Sphenolithus orphanknollensis*. This assemblage suggests this sample likely falls within or near Zone NP 11 (Agnini et al. 2007, Shamrock and Watkins 2012) correlating to the early Eocene. The primary marker for the base of NP 11, *Tribrachiatus contortus*, is absent, which may be due to poor preservation or ecological exclusion. The change in biozones from ~NP 9 to NP 11 that occurs between ~78 m and ~28 m, suggests either a hiatus in sedimentary deposition or that stratigraphic condensation occurred. More detailed descriptions of the calcareous nannofossil assemblages are given in the Supplementary Information.

4.2.3. Palynology

In the three samples analysed for palynology the main component is amorphous organic matter (AOM), most likely of marine origin, with abundant organic linings of benthic foraminifera, sometimes abundant phyto-

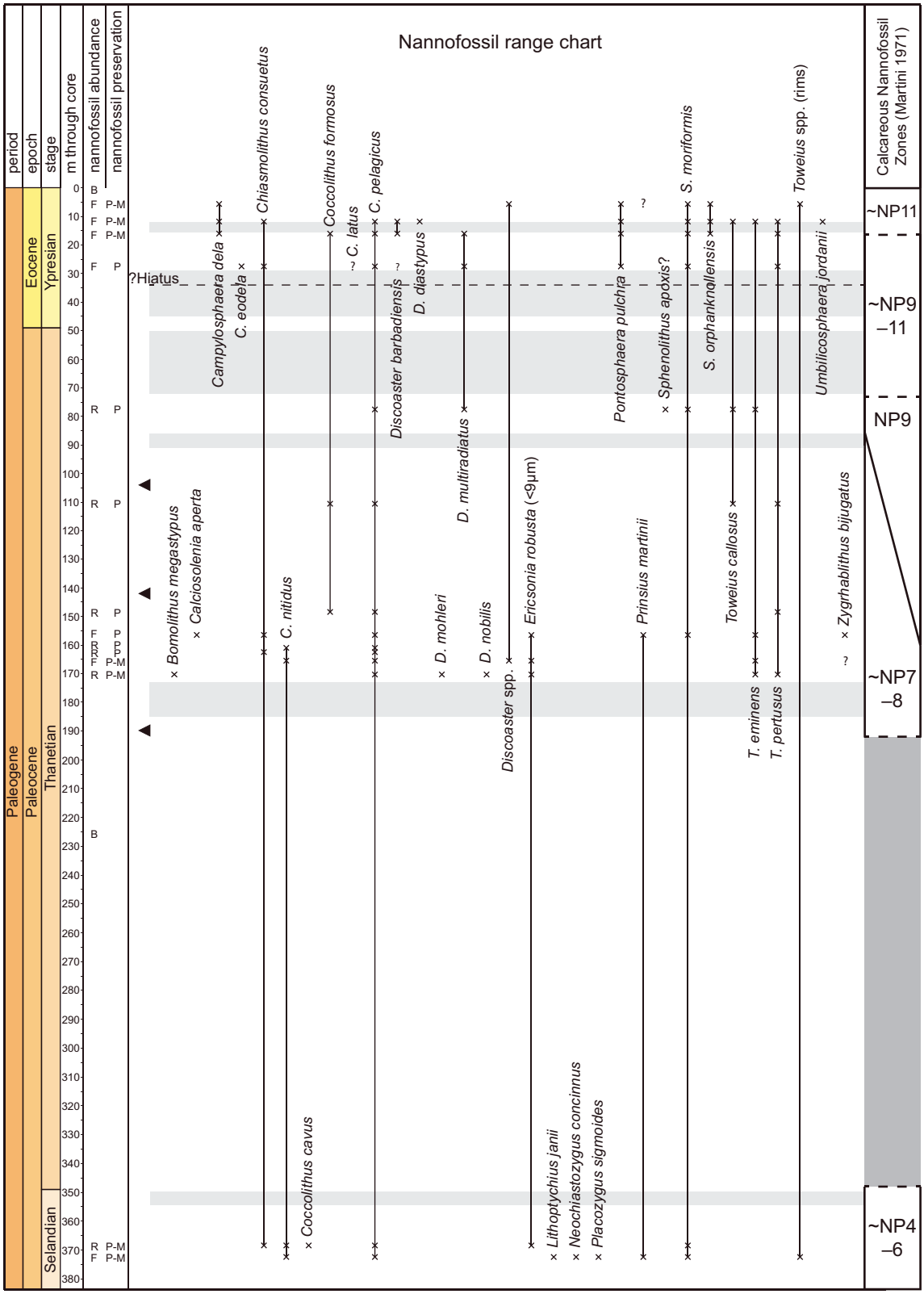

Fig. 5. Calcareous nannofossil range chart with estimated calcareous nannofossil zones (Martini 1971). Other than Zone NP 9, all other calcareous nannofossil zones are approximated as the marker species for these zones are absent; discussion of the assemblages these estimates are based on is provided in the Supplementary Information. Grey boxes mark core gaps. Black triangles indicate location of chaotic, storm-influenced beds.

clasts and only very small contributions of dinoflagellate cysts and pollen. Only one sample, at ~153 m, contains significant numbers of marine palynomorphs; these consist largely of the dinocyst genera *Operculodinium*, *Spiniferites*, *Hafniasphaera*, and *Cordosphaeridium*. The sample at 8.2 m contains mainly AOM, of a presumed dominantly marine origin due to the lack of structures assignable to components of terrestrial plants with high preservation potential, as well as increased amounts of terrestrial phytoclasts relative to the sample at 153 m. The sample at 7.4 m is dominated by AOM, with few terrestrial phytoclasts. Two dinocysts were observed in this sample, both *Polysphaeridium* spp. Detailed palynological assemblages are shown in Supplementary Information Table S3.

4.3. Bulk carbonate carbon and oxygen isotopes

The bulk carbon isotope record (Fig. 6) of Core A can be split into two distinct intervals. Firstly, below 70 m the record is relatively stable, with $\delta^{13}C$ values around +3‰ comparable to the bulk carbonate record of other late Paleogene shallow water (Zhang et al. 2017) and deep water (Barnet et al. 2019) sites. Within this lower part of the record there are two long-term cycles (occurring over 100's of metres) in the carbon isotope record with an amplitude of ~0.5–1‰. The first of these cycles runs from 380 m (the bottom of the core) to 200 m, with values peaking at around +3‰. The second cycle runs from 200 m to ~50 m, with values peaking at +3.5‰ at ~130 m.

Between approximately 50 m and 46 m there is a carbon isotope excursion (CIE), with values dropping rapidly (within 4 m) from +3‰ to +2‰ (Fig. 6). A core gap between 45–27 m cuts off a large section of the recorded carbon isotope record. The initial decrease in carbon isotope values occurs in the upper part of Zone SB 4 and between the Zones NP 9–11, suggesting this is the Paleocene–Eocene transition. Subsequent values from 27 m upwards are significantly more negative, with values from 0‰ to –1‰ recorded. These values occur in Zone NP 11, suggesting this part of the record is early Eocene in age.

The oxygen isotope record of Core A (Fig. 6) is characterised by values of approximately –3.5‰ to

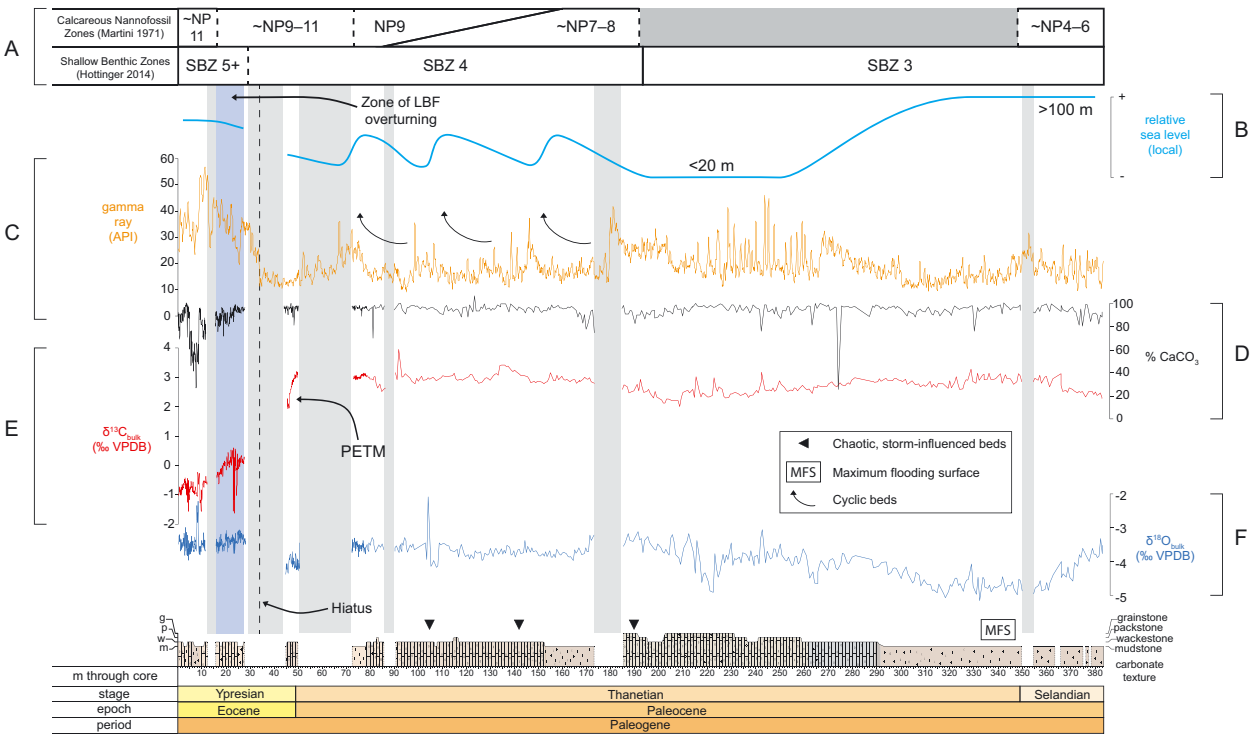

Fig. 6. **A** – SBZ and estimated calcareous nannofossil zonations. **B** – Relative sea level curve derived from sedimentology and palaeoecology of faunal assemblages. **C**– Gamma ray data from wireline log. **D** – %$CaCO_3$. **E** – Bulk carbonate carbon isotopes. **F** – Bulk carbonate oxygen isotopes. Blue box depicts zone of turnover in LBF record. Grey boxes indicate core gaps. Dashed black line indicates possible location of hiatus/condensation, based on rapid increase on the gamma ray record.

–4.5‰. These values do not suggest that the core has been extensively diagenetically altered by interaction with meteoric water, whereby values would be much more negative (e. g., Knauth and Kennedy 2009, Ullmann and Korte 2015, Schobben et al. 2016). The cross-plot of pre-CIE $\delta^{13}C$ vs. $\delta^{18}O$ (Fig. S2) in which the R^2 value of the data is low ($R^2 = 0.0231$), indicates that there is little correspondence between these data sets, further excluding a high degree of meteoric diagenesis. All the data also plot within values expected for a primary marine-derived carbonate (Arthur et al. 1983). In addition, cathodoluminescence analysis (Fig. S2) did not show the foraminifera or surrounding sediment to be luminescent, which would be an indication of possible alteration. Mg/Ca ratios from ICP-OES analysis are slightly higher than average values for a normal marine-derived carbonate (average Core A values of 35.6 mmol/mol); however, this can be explained by the high abundance of echinoid fragments as seen in the LBF biostratigraphic log (Fig. 2) which have a naturally high Mg/Ca ratio (Riechelmann et al. 2018, Ullmann et al. 2018). Shell remains of echinodermata typically rapidly recrystallise to low-Mg calcite, supplying excess Mg to diagenetic fluids which in turn would likely favour the formation of Mg-enriched carbonate cements.

4.4. Percentage calcium carbonate

Percentage calcium carbonate values are generally very high and stable throughout the majority of the core, fluctuating between ~80–100 % (Fig. 6). There does not seem to be a close correspondence between described lithology as displayed in the sedimentary log and % $CaCO_3$, with all lithologies clearly dominated by carbonate phases regardless of texture and fossil content. There is a significant drop in average % $CaCO_3$ between 5–10 m, with values reaching as low as ~30 %, indicating a terrigenous fraction dominates the sedimentology towards the very top of the core.

4.5. Gamma ray

The gamma ray record shows a degree of variability, with values ranging from ~10–55 API, but with most values between ~10–40 API through the majority of the core below 35 m. Average values increase to ~30–50 API at the top of the core between ~0–35 m. There appears to be cyclicity in certain parts of the record, particularly between ~180 and 70 m, where ~3 cycles can be visually identified with a wavelength of ~30–40 m (Fig. 6). A sharp change in gamma ray values at ~35 m suggests this may be the location of a hiatus.

5. Discussion

5.1. An integrated age model for the late Paleocene to early Eocene of the central UAE

LBF biostratigraphy (e. g., the SB Zone scheme) is critically important for providing age models in Paleogene-aged shallow water strata, which form extensive hydrocarbon reservoir rocks in the Middle East. Other marine taxa, such as calcareous nannofossils or planktonic foraminifera, are often absent due to differing environmental preferences. As a result of this mutual environmental exclusion of other taxa, it is often difficult to tie LBF biostratigraphy to global stratigraphy, which is key for correlating the stratigraphy of the deep and shallow water domains and for understanding responses to global climatic events. Exceptionally, in the new Core A section we have records of both LBF and calcareous nannofossil biostratigraphy from the same samples, as well as high resolution chemostratigraphy, which allows for correlation to global stratigraphy (Fig. 7).

In order to tie local and global, shallow and deep water stratigraphies together it is important to analyse variations in species ranges between localities. Improved knowledge of such discrepancies will allow for more precise and robust age models to be constructed based upon biostratigraphic horizons. In general the LBF assemblages in this study are in good agreement with other published literature from the Arabian Plate region (e. g., Pignatti et al. 1998, Serra-Kiel et al. 1998, Hottinger 2014) and are consistent with carbon isotope stratigraphies developed from deep sea records through this interval (Fig. 7 and Barnet et al. 2019). The broad trend, of more positive $\delta^{13}C$ values in the late Paleocene and more negative values in the early Eocene, is coherent between the ODP Site 1262 reference section and the new Core A record, although there are discrepancies in the fine detail. Offsets in absolute values between the deep sea and shallow water bulk carbon isotope records (Fig. 7) may be influenced by the differing composition of biogenic carbonates in the shallow and deep sea (e. g., differing

proportions of carbonate-secreting taxa), or differing isotopic compositions of the (bottom) waters due to the relative age and organic matter content of the water masses (Sluijs and Dickens 2012). Further to this, discrepancies in trends between the two bulk carbonate records could be due to a number of factors; for example the two sites are from different ocean basins (ODP Site 1262 is from the South Atlantic) and coeval carbon isotope records from different regions are rarely exactly the same due to differences in oceanic setting and productivity (e. g., Giusberti et al. 2007, Cramer et al. 2009, Westerhold et al. 2011, Slotnick et al. 2012, Agnini et al. 2016). The composition of the bulk material also differs, with ODP Site 1262 sediments composed of a nannofossil-foraminifera ooze with minimal diagenetic overprint, while Core A sediments are composed of both macro- and microfossil material with significant diagenetic cements in places. Finally, the two sites represent deposition at very different palaeodepths; Paleocene–Eocene-aged sediments at ODP Site 1262 were deposited at ~3000–3500 m water depth, while coeval sediments at Core A were deposited in <100 m water depth. The potential differences in effects of burial and diagenesis in such different settings cannot be discounted. Alternative age models, based on tying the $\delta^{13}C$ data between the sites more closely, yielded unrealistic sedimentation rates and do not agree with the LBF biostratigraphy of Core A, therefore they are not taken as the preferred option here (See Supplementary Information for further discussion and Figure S4).

The late Paleocene Zone SB 3–4 boundary within Core A is no younger than the calcareous nannofossil Zone NP 8 (Fig. 7). This agrees in general with the correlation in previous studies (Serra-Kiel et al. 1998, Scheibner et al. 2005) where the Zone SB 3–4 transition occurs at the end of Zone NP 8. However, results from this study place the Zone SB 3–4 boundary in the middle of Zones NP 7–8 rather than at the end (Fig. 7). Due to the uncertainty in the nannofossil stratigraphy at Core A, we consider this to be consistent with previous studies.

Previous studies from the Arabian Plate region (Serra-Kiel et al. 1998, Scheibner et al. 2005) place the Zone SB 4–5 boundary younger than Zone NP 8–9 boundary; however, in this study the Zone SB 4–5 boundary is located after the first occurrence of *Discoaster multiradiatus* (base of NP 9) and within the Zones NP 9–11. Some difficulties arise when positioning the Zone SB 4–5 boundary primarily due to the occurrence of a hiatus/condensation in the sedimentary sequence (discussed below; Fig. 7). This problem is confounded by the lack of some Arabian Plate Eocene marker species and genera in the assemblage, such as the alveolinids (cf. Serra-Kiel et al. 1998, Scheibner and Speijer 2009). This could be due to Core A recording a relatively deeper shelf environment over this transition, indicated by the presence of *Nummulites* spp. and *Assilina* spp. which are thought to have resided below fair weather wave base (Racey 1995). The precise location of the Zone SB 4–5 transition, and its correlation to the calcareous nannofossil biozones, is important when discussing the PETM and the larger foraminifera turnover (LFT) event. Whether the LFT coincides with the PETM (Pujalte et al. 2009, Scheibner and Speijer 2009) or predates the PETM (Hottinger 1998, Zhang et al. 2013) is important for the applicability of the global stratigraphic horizon that the LFT creates, as well as the mechanisms driving the LFT. If, for example, the LFT denotes the Zone SB 4–5 transition, which in turn correlates to Zone NP 9, this creates a correlative surface across the breadth of Tethyan fauna as well as an easily recognisable change on which to base the biostratigraphy of the region. Results from this study suggest that the LFT event can be utilised to define the Zone SB 4–5 transition, which in turn correlates to calcareous nannofossil Zones NP 9–11 (Fig. 7).

Further to these potential discrepancies in biozone boundary correlations, the biostratigraphic ranges of some species at this site are different to those suggested in published literature (Fig. 8). In Core A the ranges of *Lockhartia praehaimei*, *L. roeae*, *Kathina selveri*, *Dictyokathina simplex*, *Daviesina tenuis*, and *Thomasella labyrinthica* extend to younger ages than previously recorded in literature from the Arabian Plate region (Pignatti et al. 1998, Serra-Kiel et al. 1998, Hottinger 2014). *Miscellanea "rhomboidea"* and *Mardinella daviesi* extend into older strata than currently recorded (Pignatti et al. 1998). Proposed expansions to these species biostratigraphic ranges are shown in Figure 8. These differences in ranges of some species could be due to a number of reasons, for example, variability in local environmental conditions, diachroneity of speciation/extinction, or incomplete outcrop sections. Shallow, reef-associated LBF assemblages today are typically regionally heterogenous, with significant differences in the dominant taxa present (Hallock 1984, Hallock and Glenn 1986). This heterogeneity seems to be largely depth controlled, due to subsequent differences in light and nutrient availability, water energy, and substrate (Hottinger 1983). It is

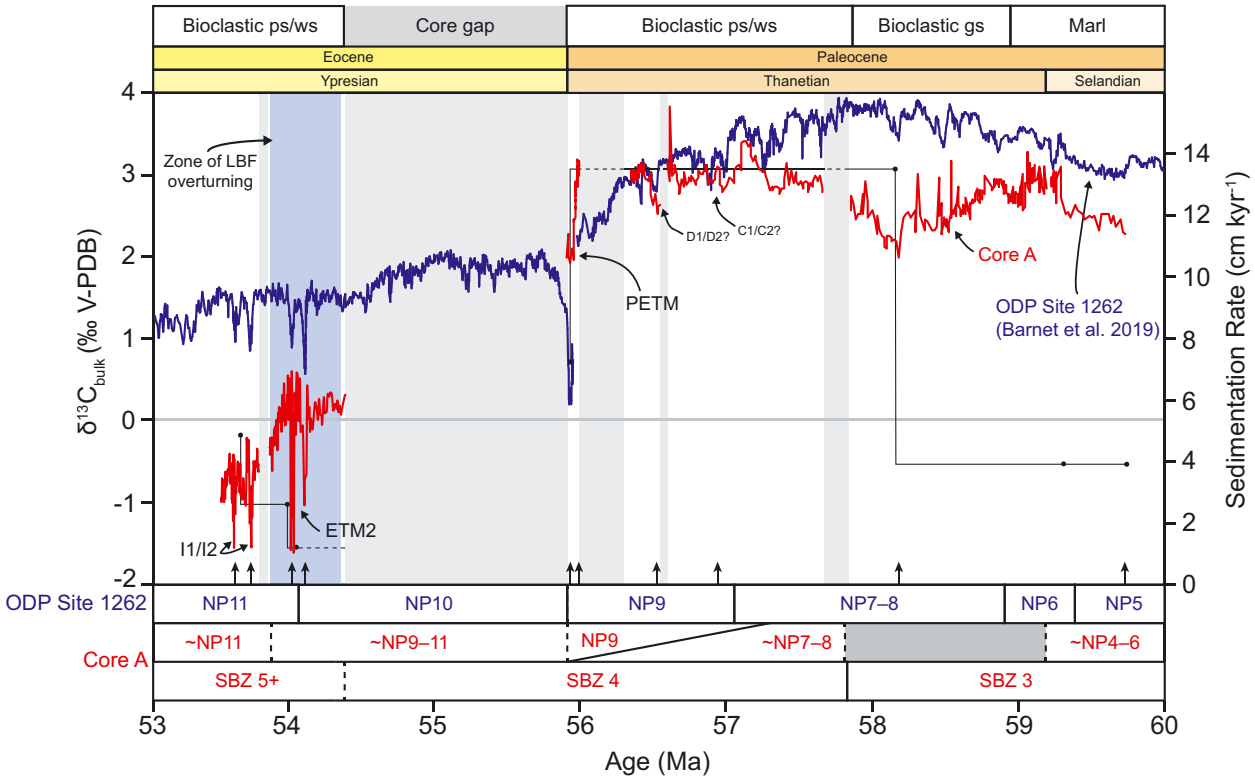

Fig. 7. Carbon isotope data from Core A (red) placed onto the latest orbitally-tuned age model by comparison to bulk carbon isotope data from South Atlantic ODP Site 1262 (blue; Barnet et al. 2019). Constraints from biostratigraphy (primarily calcareous nannofossils) and matching of characteristic shapes in the $\delta^{13}C_{bulk}$ record have been used to tune the Core A record. Sedimentation rates are shown with black circles and solid/dashed black lines. Tie points used to create the age model are shown with vertical black arrows. For further details on tie points and construction of this age model see the Supplementary Information and Figure S4. The calcareous nannofossil zonations of both records are shown in red (Core A) and blue (Barnet et al. 2019), along with the Core A shallow benthic (SB) zonations. Core gaps are shown with grey boxes. Note the gap in data between ~54.4 to ~55.8 Ma (grey shaded area), which is partly the result of a coring gap in the Core A record, and partly the result of an apparently genuine hiatus/sedimentary condensation in this record. Potential hyperthermal events captured in the Core A record are annotated. Facies types are shown at the top of the figure: ps = packstone; ws = wackestone; gs = grainstone.

such spatial variability in LBF records that necessitates the application of integrated stratigraphic techniques and investigation of a range of localities.

All three stratigraphic indicators suggest there is a hiatus or sediment condensation in the core gap between 45–27 m (Fig. 7), as evidenced by missing biozones and the step change in carbon isotopes to significantly more negative values (Fig. 6). The core gap itself results in ~1.4 million years of strata missing, with the possible hiatus/condensation totalling an unknown amount of this time. The precise location of the hiatus within the core gap may be ~34 m, as denoted by the rapid increase in the (continuous) down-hole gamma ray values. Importantly, the initial drop in carbon isotopes ratios between 50–46 m occurs within a core section where there is no sedimentological evidence for a hiatus. This suggests we have captured one of the late Paleocene hyperthermal events, most likely the PETM CIE based upon reasonable estimates of sedimentation rates in such settings (Fig. S3) as well as the sedimentological and LBF biostratigraphic evidence (Fig. S4).

5.2. Paleocene–Eocene palaeoenvironmental and biotic trends

The late Paleocene sedimentary sequence preserved in Core A is indicative of a shallow (<100 m), low-energy, storm-dominated epeiric platform setting (Tucker and Wright 1990, Sharland et al. 2001) within the easternmost Paleogene Tethys Ocean (Fig. 1). Through the late Paleocene at this site there is a broad-scale change in the biotic assemblage, occurring across a number of

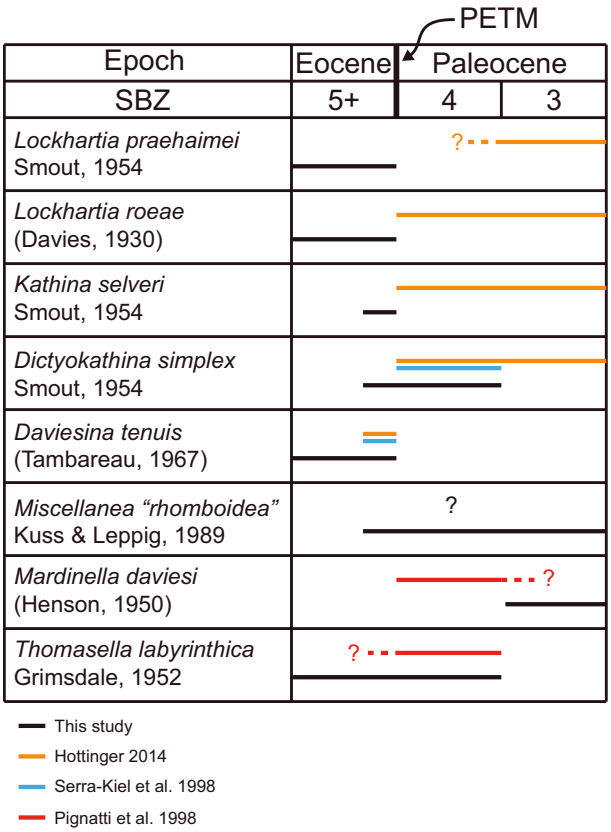

Fig. 8. Differences in biostratigraphic ranges between Core A and published literature.

genera, coupled to changing palaeoenvironmental settings. The lowermost facies (383–285 m) of marl is likely to represent a relatively deeper water (Fig. 6), low energy environment, below storm wave base, as indicated by the presence of thin-shelled bivalves and rare or absent photosynthetic organisms such as corals or LBF. This is interpreted as being locally representative of the regional maximum flooding surface recognised at ~59.5 Ma (re-calibrated to GTS2012; Fig. 6; Sharland et al. 2001, Haq and Al-Qahtani 2005). The Core A record has been correlated to the latest orbitally tuned age model from Ocean Drilling Program (ODP) Site 1262 (Fig. 7 and Supplementary Information; Barnet et al. 2019), using the carbon isotope records and biostratigraphy from both sites. Sedimentation rates at Core A can be estimated (Fig. S3), and through this interval they are among the lowest in the record (~3.9 cm kyr^{-1}), which agrees well with the observed sedimentological sequence.

As the shallower water facies prograded over these deeper water sediments, shallow water fauna including solitary corals, gastropods, bivalves, and LBF became abundant (~260–185 m). This fauna represents a diverse shallow water reef assemblage, a highly productive "carbonate factory" likely deposited at <15 m water depth (cf. Tucker and Wright 1990). Sedimentation rates through this time increase significantly up to ~13.5 cm kyr^{-1} (Figs. 7 and S3). This is interpreted as the Arabian Plate carbonate platform prograding out into the adjacent deeper water Muthaymimah Trough sub-basin to the north-east (Fig. 1B). Progradation occurs due to rapid subsidence in this region during the early Paleogene initiated by the cessation of Semail ophiolite obduction to the east (Ziegler 2001). This rapid tectonic deepening is also enhanced by eustasy (Sharland et al. 2001). As the carbonate platform filled the available accommodation space, with inferred accelerating carbonate production, an overall shallowing-up sequence is observed. From ~173 m upwards a series of cyclic shallowing-up parasequences are observed in both the sedimentology and the gamma ray signal (Fig. 6). Three cycles can be observed in the record with a wavelength of ~30–40 m. The top of each parasequence is marked by a chaotic, storm-influenced bed with broken bioclasts (Figs. 2 and Fig. 6), due to a relative decrease in sea level, bringing Core A to above storm-wave base, suggesting these may be a series of 4^{th} order sea level cycles. From the orbitally tuned age model (Fig. 7) these cycles cover ~57.6 Ma to 56.3 Ma, a period of approximately 1.3 Myr, making these cycles roughly 400 kyr in duration. As such, these cycles could reflect the long eccentricity (405 kyr) cycle. High-resolution orbitally tuned stable isotope records from the late Paleocene of the South Atlantic (Zachos et al. 2010, Littler et al. 2014, Barnet et al. 2019) and Pacific Ocean (Westerhold et al. 2008) show long eccentricity as the dominant frequency expressed in both climate and carbon-cycle records.

From ~152 m upwards in the core there is the systematic loss of corals and gastropods (Fig. 2). This gradual transition through the core, with the loss of the diverse biotic assemblage but increases in LBF diversity, suggests that the environment became more favourable to the rapidly calcifying LBF (Scheibner et al. 2005). This could be forced by a number of factors, such as an increase in nutrient input disturbing the previously stable oligotrophic environment and creating a more meso- to eutrophic environment (Scheibner and Speijer 2008b, Zamagni et al. 2008), or increases in pCO_2 through this interval adversely affecting the growth of calcareous macroorganisms (Shirayama and Thornton 2005). Alternatively, this gradual change could be due to an overall

deepening in the sequence, losing the diverse fauna present on the reef and moving towards an open shelf setting (Hallock and Glenn 1986). This latter hypothesis is supported for the upper part of the core, after the core gap (Fig. 2), by the presence of generally deeper dwelling nummulitids (Racey 1995).

5.2.1. The Paleocene–Eocene transition

The partial record of the PETM onset recovered within Core A spans ~4 m of stratigraphy and is therefore relatively expanded compared to many other PETM records from deeper water sites. Such expanded PETM sections have also been recorded in other marginal marine sites, such as Svalbard (Cui et al. 2010), the New Jersey margin (Zachos et al. 2006, Sluijs et al. 2007, Kopp et al. 2009), the Northern Tethys (Giusberti et al. 2007), and Tibet (Zhang et al. 2017). Unlike deep sea records, this very shallow marine (~<20 m water depth) environment is unaffected by shoaling of the carbonate compensation depth (CCD). Over the expanded section of the PETM onset, high resolution sample intervals (approximately every ~0.8 m; Fig. 2) allow us to assess changes in the LBF assemblage during this interval. Despite a major perturbation to the carbon cycle shown by the rapid decline in carbon isotope values (Fig. 6) the LBF assemblage is stable throughout this 4 m of stratigraphy (Fig. 2), with 9 of the 11 species present in the latest Paleocene also present after the Paleocene–Eocene boundary. The two exceptions are *Discocyclina* sp. and *Miscellanea* sp., with last occurrences at ~47 m; however, as this is the start of the coring gap it could be that the continued record of these genera has not been captured.

Above the hiatus/condensation in sedimentary deposition, occurring in the core gap between 45–27 m (Fig. 6; likely ~34 m), the sediments are likely within Zone NP 11, correlating to the early Eocene. After the core gap, carbon isotope values decrease further from 0‰ to –1‰. These values, therefore, likely represent the decline towards the early Eocene climatic optimum (EECO; ~52–50 Ma), the peak of Paleogene warmth (Zachos et al. 2001, 2008, Cramwinckel et al. 2018). Prior to the EECO there are a number of orbitally paced hyperthermal events observed in the carbon isotope record, on the order of ~-1‰ (Cramer et al. 2003, Zachos et al. 2010, Littler et al. 2014, Barnet et al. 2019). Within the Core A record there are three CIEs stratigraphically above 27 m. These occur at 23 m, 10 m, and 4 m and are –1.5‰, –1‰ and –0.8‰ in magnitude, respectively. Located within Zones NP 9–11, it is likely that these negative excursions are expressions of hyperthermal events, such as Eocene thermal maximum 2 (ETM-2 at ~53.7 Ma; Lourens et al. 2005, Stap et al. 2010). As with the PETM interval at this site, there would be no expected dissolution during these events due to the shallow shelf setting located far above the CCD. Calculated sedimentation rates here fit with this interpretation; approximate average rates of 2.9 cm kyr^{-1} at the top of the core (Figs. 7 and S3) would equate to the top 27 m the core covering a ~925 kyr period from ~54.4 Ma, which is the time period and scale on which these hyperthermals occur (Barnet et al. 2019).

There is no increase in gamma ray values throughout the putative PETM interval (Fig. 6), commensurate with the LBF evidence for a relatively stable local environment during this time. However, there is a significant increase in gamma ray values after the hiatus/sedimentary condensation (~30 m) within the coring gap and into the early Eocene (Fig. 6). As gamma ray values represent the combined abundance of radioactive K, U and Th, an increase is indicative of either an increase in organic matter within the sediments, or of increasing clay content in the core (Bigelow 2002), both of which can contain incorporated radioactive elements. There is no evidence for glauconite in the core, which can also elevate total gamma ray values through elevated K content (e. g., Hesselbo 1996). The $\%CaCO_3$ values through this interval also decrease (Fig. 6), potentially due to dilution from increased terrigenous input (Slotnick et al. 2012). Taken together, these trends suggest that through the early Eocene interval prior to the EECO, there may have been increased humidity and/or rainfall in this part of the Arabian Peninsula. This humidity could have caused either enhanced input of riverine transported clay material derived from the areas of emergence to the east and west of the Core A locality (Fig. 1), and/or elevated organic matter burial through increased nutrient-driven algal productivity potentially coupled with increased anoxia. The former argument is supported by the increase in abundance of terrestrially derived phytoclasts, most likely dominantly river transported, in the sediments during the early Eocene (~8 m; Table S3) relative to the late Paleocene (Hollis et al. 2005, Slotnick et al. 2012). Calculated sedimentation rates through this interval also show an increase from ~1.2 to 5 cm kyr^{-1} (Fig. S3), which is consistent with elevated terrestrial input in this setting. This matches trends seen in open ocean sites, such as ODP Site 1262 in the South Atlantic

(Barnet et al. 2019), and shelf sites, such as Mead Stream in New Zealand (Slotnick et al. 2012), where sedimentation rates also show an increase into the Eocene.

5.3. Response of shallow marine biota to Eocene warmth

Following the PETM CIE there is a gradual turnover in the LBF assemblage at Core A, within a broadly consistent lithology suggesting the depositional environment is largely unchanging. The larger foraminifera turnover (LFT) event is preceded by a major perturbation to the carbon cycle and elevated terrestrial input to the Core A site. Despite these perturbations to the environment, during the PETM onset the LBF assemblage is stable (Fig. 2), with the turnover occurring later in the early Eocene. This suggests long-term warming into the early Eocene may have been the trigger for the LFT, rather than the PETM itself. From ~27 m to ~16 m, above the core gap, there is a step-change in the assemblage, with an increased dominance of less-specialised and smaller fauna that are better able to inhabit/colonise perturbed environments, and/or are more tolerant to a wider range of oceanographic conditions. Examples of such genera include *Rotalia* spp. and *Sakesaria* spp. (Fig. 2). Through the early Eocene interval there is also an increase in the genera and species richness of the LBF assemblage. One way to facilitate increases in species diversity is known in modern ecology as the intermediate disturbance hypothesis (IDH). The IDH theory suggests that when there is increasing ecological disturbance to an environment there may also be increasing species diversity (Townsend et al. 1997). Once an intermediate level of disturbance is reached both rapid opportunistic colonisers and species which are more competitive are able to co-occur (Townsend et al. 1997). The changes observed in the Core A LBF assemblage, from 27–16 m, could therefore be due to an intermediate level of disturbance to the environment having been reached, creating a "sweet spot" for increased biodiversity. This increase in genera and species richness over the Paleocene–Eocene interval is also seen in other areas of the shallow Tethys Ocean (Scheibner and Speijer 2008b). Known as the *Lockhartia* Sea (Hottinger 2014), this was a biogeographic region defined by increased generic diversity in "hot spots" (geographic regions of maximum biodiversity in a given time interval) which migrate around the Paleogene Tethys Ocean (Fig. 9; Renema et al. 2008, Hottinger 2014). Prior to the PETM, the environment was characterised by stable, low-diversity conditions, as demonstrated by the relatively unchanging sediments (Fig. 2), LBF assemblage, and the dominance of *Cibicides* spp. in the smaller benthic foraminiferal assemblage (Boscolo-Galazzo, pers. comm.). The disturbance to the ecosystem precipitated by the PETM, and likely continuing into the early Eocene (section above the core gap) may have triggered the concurrent increase in diversity and dominance of LBF.

A number of studies have measured LBF diversity or species richness on or near the Arabian Plate during the Paleogene; however, estimates of generic and specific level diversity vary across locations (Table 1). In the mid to late Paleocene the number of LBF genera in Oman was shown to be n = 8 (Serra-Kiel et al. 2016a), increasing to n = 18 in the mid-Eocene (Serra-Kiel et al. 2016b). In the nearby offshore India province the number of species/morphotypes in the Eocene was measured at n = 29, with this significantly decreasing to n = 2 in the Oligocene, although few Oligocene samples were available (Cotton et al. 2019). Contrary to these estimates Renema et al. (2008) suggest that the number of genera in the south-eastern Arabian Plate was as low as n = 5–8 in the mid Eocene, increasing to its maximum of n = 9–12 in the Miocene. This study suggests that the modern hotspot in the

Table 1. Summary table of changes in LBF specific- and generic-level diversity changes through time described in the text.

Location	Number of genera/species	Approximate age	Reference
Oman	8 genera	Mid to late Paleocene	Serra-Kiel et al. 2016a
UAE	9 genera, 9 species	Late Paleocene	This study
UAE	11 genera, 16 species	Early Eocene	This study
Oman	18 genera	Mid Eocene	Serra-Kiel et al. 2016b
South east Arabian Plate	5–8 genera	Mid Eocene	Renema et al. 2008
Western India	29 species	Eocene	Cotton et al. 2019
Western India	2 species	Oligocene	Cotton et al. 2019
South east Arabian Plate	9–12 genera	Miocene	Renema et al. 2008

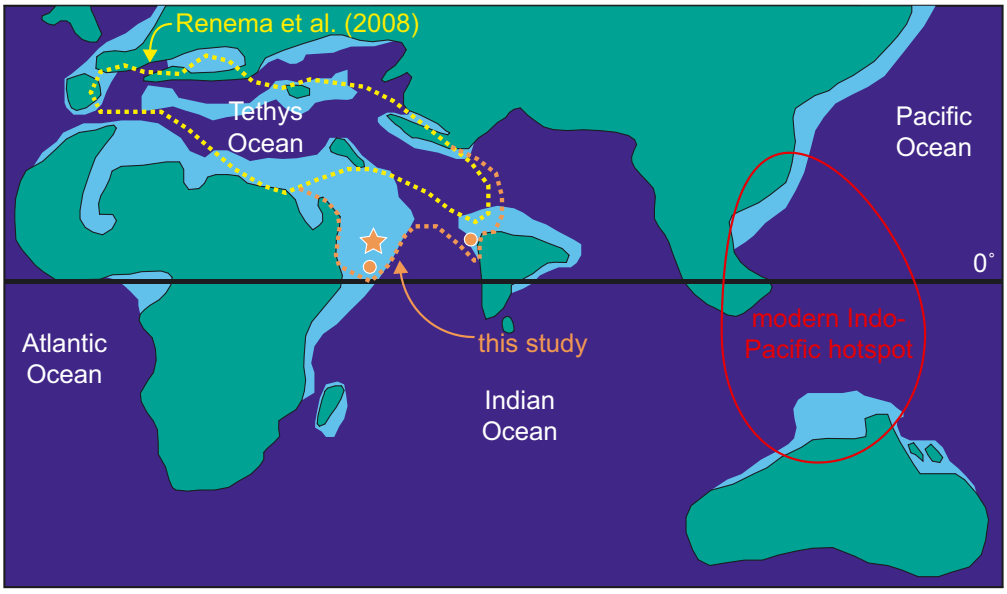

Fig. 9. Figure adapted from Renema et al. (2008) to demonstrate the extensions of the proposed hotspots through the early–middle Eocene. Yellow dashed area denotes the middle Eocene hotspot from Renema et al. (2008), orange dashed area denotes extension of this hotspot in the early Eocene from this study (orange star) and others (orange circles: Serra-Kiel et al. 2016a, Cotton et al. 2019). Red solid line indicates area of modern hotspot in the Indo-Pacific (Renema et al. 2008).

Indo-Pacific region evolved due to the eastward movement of generic level alpha biodiversity (number of genera in a single location) from the Tethys in the middle Eocene (Fig. 9 and Renema et al. 2008). Our data from the UAE suggests that the increase in generic and species richness in this region actually began as early as the early Eocene (Fig. 9), which is in agreement with other more recent studies from the broader region (Serra-Kiel et al. 2016b, Cotton et al. 2019). It has been suggested that changes in tectonic configuration of continents, creating and destroying numerous shallow water habitats, is the main driving force behind these changes in biodiversity (Renema et al. 2008). However, the timing of these biodiversity increases, coincident with or following on from the PETM both in this study and others, suggests that early Eocene climate could have been a contributing factor in the upward trajectory of biodiversity (Orue-Etxebarria et al. 2001, Pujalte et al. 2009, Scheibner and Speijer 2009).

5.4. The early Paleogene vs anthropogenic climate change in the shallow water realm

The results of this study suggest that the shallow water LBF community was able to turnover and subsequently thrive throughout the extreme warming experienced over the early Eocene, becoming the dominant shallow water carbonate producers of the Eocene (Scheibner and Speijer 2008a, Afzal et al. 2011, Zamagni et al. 2012). There are, therefore, implications for the future of shallow water environments with continued anthropogenic climate change and ocean acidification. For example, will there be a shift of the dominant carbonate producers? Will modern coral reefs be replaced by a diverse fauna of LBF? Larger foraminifera at present produce 2.5 % of the total $CaCO_3$ in the oceans (Langer 2008), they are therefore important for the global climate-carbon cycle and constitute a substantial carbon sink in the shallow oceans.

Short-term (maximum 6 weeks) lab experiments suggest that LBF are unaffected by pH decrease (acidification) and temperature increase, in some cases even displaying an increase in growth yields under these conditions (Hikami et al. 2011, Vogel and Uthicke 2012, Prazeres et al. 2015). On the long-term, however, the effects are markedly different. In both lab and field experiments long-term changes to pH or temperature had major negative effects upon the LBF communities, with the highest impact observed in lab experiments when temperature increase and acidification acted in unison (Schmidt et al. 2014). Alternatively, in field studies conducted on shallow benthic communities close to volcanic CO_2 seeps indicate an

inability to tolerate pH < 7.9. At current rates of CO_2 injection into the atmosphere, this suggests that ocean acidification will reach a threshold of major extinctions in the shallow water benthos community by 2100 (Uthicke et al. 2013). Over this long-term, coral reefs also show major disruption as a result of acidification and increased temperatures (Fabricius et al. 2011), similar to the negative effects observed in the Paleocene (Scheibner and Speijer 2008a). Ultimately, this comparison shows us that rate of change is likely key when assessing the ability for shallow water benthos to adapt. However, with anthropogenic climate change being orders of magnitude faster than changes that occurred during the early Eocene or even the PETM, it is problematic to use the two as direct analogues for the near future.

6. Conclusions

Integrated LBF and calcareous nannofossil biostratigraphy and carbonate stable isotope chemostratigraphy from this easternmost Tethyan site show a stepwise shift in palaeoenvironment from the late Paleocene into the early Eocene. The Paleocene strata in this region record a relatively stable time period in terms of climate, oceanography, and palaeoenvironmental setting, allowing a diverse shallow water (<100 m) biotic assemblage to thrive through the late Paleocene. The local response to globally warmer temperatures during the Paleocene to Eocene involved the systematic loss of corals, gastropods, and bivalves. Further to this, the LBF assemblage underwent turnover in the early Eocene, with smaller and less specialised genera such as *Rotalia* spp. and *Sakesaria* spp. outcompeting the previously dominant Paleogene genera (Figs. 2 and 6). It is hypothesised that the perturbations to ocean and atmosphere temperature, the carbon cycle, run-off, and nutrient input through the early Eocene were the trigger for an increase in generic and specific level diversity at this site and others in the eastern Tethys Ocean. This was the beginning of the generic biodiversity hotspot that developed through the Paleogene and Neogene in the Tethys, moving eastwards to its present-day hotspot in the Indo-Pacific (Fig. 9). Despite the success of the larger benthic community through this major palaeoclimatic change, they do not appear to be resilient to anthropogenic climate change. It is likely that the significantly faster rate of change in pH and temperature at the present, compared to the Paleocene–Eocene, is the explanation; however, the vastly different timescale lengths these studies are conducted on does not allow for a more definite conclusion.

With an integrated record of biostratigraphy and chemostratigraphy from this region it is possible to tie a local, shallow water record to global stratigraphy through the early Paleogene interval. This record suggests that the LFT event can be correlated to Zone SB 5. This stratigraphic interval, recorded in the shallow water domain, can be tied to calcareous nannofossil Zones NP 9–11. These integrated records allow for the correlation of the shallow and deep water domains and provide important and easily recognisable stratigraphic horizons which tie directly to a bio- and chemostratigraphic age model.

Acknowledgements. We would like to thank Flavia Boscolo-Galazzo, Johannes Pignatti and Cesare Papazzoni for providing expertise and advice when identifying the smaller benthic and larger benthic foraminifera assemblages and for their further input on the ecological significance of the assemblages. We also thank Steve Pendray for preparing petrological thin sections. We are very appreciative of the two anonymous reviewers who helped to improve the manuscript with detailed comments. We acknowledge Abu Dhabi National Oil Company (ADNOC) for access to core material and permission to publish data based upon interpretations and analysis of this material. The research contained in this publication contains work conducted during a PhD study undertaken as part of the Natural Environment Research Council (NERC) Centre for Doctoral Training in Oil & Gas (grant number NE/M00578X/1) and is fully funded by NERC whose support is gratefully acknowledged. AS thanks the European Research Council for Consolidator Grant 771497.

References

Adams, A. E., MacKenzie, W. S., 1998. Cathodoluminescence. In: Adams, A. E., MacKenzie, W. S. (Eds.), A Colour Atlas of Carbonate Sediments and Rocks Under the Microscope, Manson Publishing, London, 101–156.

Afzal, J., Williams, M., Leng, M. J., Aldridge, R. J., 2011. Dynamic response of the shallow marine benthic ecosystem to regional and pan-Tethyan environmental change at the Paleocene–Eocene boundary. Palaeogeography, Palaeoclimatology, Palaeoecology 309, 141–160.

Afzal, J., Williams, M., Leng, M. J., Aldridge, R. J., Stephenson, M. H., 2010. Evolution of Paleocene to Early Eocene larger benthic foraminifer assemblages of the Indus Basin, Pakistan. Lethaia 44, 299–320.

Agnini, C., Fornaciari, E., Raffi, I., Catanzariti, R., Pälike, H., Backman, J., Rio, D., 2014. Biozonation and biochronology of Paleogene calcareous nannofossils from

low and middle latitudes. Newsletters on Stratigraphy 47 (2), 131–181.

Agnini, C., Fornaciari, E., Raffi, I., Rio, D., Röhl, U., Westerhold, T., 2007. High-resolution nannofossil biochronology of middle Paleocene to early Eocene at ODP Site 1262: Implications for calcareous nannoplankton evolution. Marine Micropalaeontology 64 (3), 215–248.

Agnini, C., Macri, P., Backman, J., Brinkhuis, H., Fornaciari, E., Giusberti, L., Luciani, V., Rio, D., Sluijs, A., Speranza, F., 2009. An early Eocene carbon cycle perturbation at ~52.5 Ma in the Southern Alps: Chronology and biotic response. Paleoceanography 24 (2), 1–14.

Alegret, L., Ortiz, S., 2006. Global extinction event in benthic foraminifera across the Paleocene/Eocene boundary at the Dababiya stratotype section. Micropaleontology 52 (5), 433–447.

Alsharhan, A. S., Nairn, A. E. M., 1995. Tertiary of the Arabian Gulf: sedimentology and hydrocarbon potential. Palaeogeography, Palaeoclimatology, Palaeoecology 114 (2–4), 369–384.

Anagnostou, E., John, E. H., Edgar, K. M., Foster, G. L., Ridgwell, A., Inglis, G. N., Pancost, R. D., Lunt, D. J., Pearson, P. N., 2016. Changing atmospheric CO_2 concentration was the primary driver of early Cenozoic climate. Nature 533 (7603), 380–384.

Arthur, M. A., Anderson, T. F., Kaplan, I. R., Veizer, J., Land, L. S., 1983. Stable isotopes in oxygen and carbon and their application to sedimentologic and paleoenvironmental problems. In: Arthur, M. A. (Ed.), Stable Isotopes in Sedimentary Geology. SEPM Short Course No. 10, Dallas, p.

Aze, T., Pearson, P. N., Dickson, A. J., Badger, M. P. S., Bown, P. R., Pancost, R. D., Gibbs, S. J., Huber, B. T., Leng, M. J., Coe, A. L., Cohen, A. S., Foster, G. L., 2014. Extreme warming of tropical waters during the Paleocene–Eocene thermal maximum. Geology 42 (9), 739–742.

Bains, S., Corfield, R. M., Norris, R. D., 1999. Mechanisms of climate warming at the end of the Paleocene. Science 285, 724–727.

Barnet, J. S. K., Littler, K., Westerhold, T., Kroon, D., Leng, M. J., Bailey, I., Röhl, U., Zachos, J. C., 2019. A High-Fidelity Benthic Stable Isotope Record of Late Cretaceous–Early Eocene Climate Change and Carbon-Cycling. Paleoceanography and Paleoclimatology 34, 1–20.

Beavington-Penney, S. J., Wright, V. P., Racey, A., 2006. The middle Eocene Seeb Formation of Oman: An investigation of acyclicity, stratigraphic completeness, and accumulation rates in shallow marine carbonate settings. Journal of Sedimentary Research 76 (9–10), 1137–1161.

Bigelow, E. L., 2002. Wireline Log Measurements and Supportive Information. In: Bigelow, E. L. (Ed.), Introduction to Wireline Log Analysis. Baker Atlas, Baker Hughes, 43–84.

Bijl, P. K., Schouten, S., Sluijs, A., Reichart, G.-J., Zachos, J. C., Brinkhuis, H., 2009. Early Palaeogene temperature evolution of the southwest Pacific Ocean. Nature Letters 461, 776–779.

Bolle, M. P., Adatte, T., 2001. Palaeocene–early Eocene climatic evolution in the Tethyan realm: clay mineral evidence. Clay Minerals 36 (2), 249–261.

Bolle, M. P., Pardo, A., Hinrichs, K.-U., Adatte, T., Von Salis, K., Burns, S., Keller, G., Muzylev, N., 2000. The Paleocene–Eocene transition in the marginal northeastern Tethys (Kazakhstan and Uzbekistan). International Journal of Earth Sciences 89, 390–414.

BouDagher-Fadel, M. K., 2008. The Cenozoic larger benthic foraminifera: the Palaeogene. In: Wignall, P. B. (Ed.), Evolution and Geological Significance of the Larger Benthic Foraminifera, Elsevier, Amsterdam, 297–419.

Bowen, G. J., Beerling, D. J., Koch, P. L., Zachos, J. C., Quattlebaum, T., 2004. A humid climate state during the Palaeocene/Eocene thermal maximum. Nature 432, 495–499.

Bowen, G. J., Bowen, B. B., 2008. Mechanisms of PETM global change constrained by a new record from central Utah. Geology 36 (5), 379–382.

Bown, P. R., Dunkley-Jones, T., 2012. Calcareous nannofossils from the Paleogene equatorial Pacific (IODP Expedition 320 Sites U1331–U1334). Journal of Nannoplankton Research 32, 3–51.

Bown, P. R., Newsam, C., 2017. Calcareous nannofossils from the Eocene North Atlantic Ocean (IODP Expedition 342 Sites U1403–U1411). Journal of Nannoplankton Research 37, 25–60.

Bown, P. R., Young, J. R., 1998. Techniques. In: Bown, P. R. (Ed.), Calcareous Nannofossil Biostratigraphy. British Micropalaeontological Society Publication Series, Kluwer Academic, London, 16–28.

Carmichael, M. J., Inglis, G. N., Badger, M. P. S., Naafs, B. D. A., Behrooz, L., Remmelzwaal, S., Monteiro, F. M., Rohrssen, M., Farnsworth, A., Buss, H. L., Dickson, A. J., Valdes, P. J., Lunt, D. J., Pancost, R. D., 2017. Hydrological and associated biogeochemical consequences of rapid global warming during the Paleocene–Eocene Thermal Maximum. Global and Planetary Change 157, 114–138.

Charisi, S. D., Schmitz, B., 1998. Paleocene to early Eocene paleoceanography of the Middle East: The $\delta^{13}C$ and $\delta^{18}O$ isotopes from foraminiferal calcite. Paleoceanography 13 (1), 106–118.

Clemens, S. C., Kuhnt, W., LeVay, L. J., Anand, P., Ando, T., Bartol, M., Bolton, C. T., Ding, X., Gariboldi, K., Giosan, L., Hathorne, E. C., Huang, Y., Jaiswal, P., Kim, S., Kirkpatrick, J. B., Littler, K., Marino, G., Martinez, P., Naik, D., Peketi, A., Phillips, S. C., Robinson, M. M., Romero, O. E., Sagar, N., Taladay, K. B., Taylor, S. N., Thirumalai, K., Uramoto, G., Usui, Y., Wang, J., Yamamoto, M., Zhou, L., 2016. Expedition 353 methods. In: Clemens, S. C., Kuhnt, W., LeVay, L. J., the Expedition 353 Scientists (Eds.), Indian Monsoon Rainfall. Proceedings of the International Ocean Discovery Program, 353. College Station, TX (International Ocean Discovery Program).

Cohen, A. S., Coe, A. L., Kemp, D. B., 2007. The Late Palaeocene–Early Eocene and Toarcian (Early Jurassic) carbon isotope excursions: A comparison of their time

scales, associated environmental changes, causes and consequences. Journal of the Geological Society, London 164, 1093–1108.

Cotton, L. J., Wright, V. P., Barnett, A., Renema, W., 2019. Larger benthic foraminifera from the Panna and Mukta fields offshore India: Paleobiogeographic implications. Journal of Foraminiferal Research 49 (3), 243–258.

Coxall, H. K., Pearson, P., 2007. The Eocene–Oligocene Transition. In: Williams, M., Haywood, A. M., Gregory, F. J., Schmidt, D. N. (Eds.), Deep-Time Perspectives on Climate Change: Marrying the Signal from Computer Models and Biological Proxies. . The Micropalaeontological Society, Special Publications. The Geological Society, London, 351–387.

Cramer, B. S., Wright, J. D., Kent, D. V., Aubry, M. P., 2003. Orbital climate forcing of $\delta^{13}C$ excursions in the late Paleocene–early Eocene (chrons C24n–C25n). Paleoceanography 18 (4), 1–25.

Cramwinckel, M. J., Huber, M., Kocken, I. J., Agnini, C., Bijl, P. K., Bohaty, S. M., Frieling, J., Goldner, A., Hilgen, F. J., Kip, E. L., Peterse, F., Ploeg, R. V. D., Röhl, U., Schouten, S., Sluijs, A., 2018. Synchronous tropical and polar temperature evolution in the Eocene. Nature Letters 559, 383–386.

Cui, Y., Kump, L. R., Ridgwell, A. J., Diefendorf, A. F., Junium, C. K., 2010. A high-resolution record from Svalbard of carbon release during the Paleocene–Eocene Thermal Maximum. Journal of Earth Science Special Issue 21, 190.

Cui, Y., Kump, L. R., Ridgwell, A. J., Charles, A. J., Junium, C. K., Diefendorf, A. F., Freeman, K. H., Urban, N. M., Harding, I. C., 2011. Slow release of fossil carbon during the Palaeocene–Eocene Thermal Maximum. Nature Geoscience 4, 481–485.

Dickens, G. R., Castillo, M. M., Walker, J. C. G., 1997. A blast of gas in the latest Paleocene: Simulating first-order effects of massive dissociation of oceanic methane hydrate. Geology 25 (3), 259–262.

Dickens, G. R., Neil, J. R. O., Rea, D. K., Owen, R. M., 1995. Dissociation of oceanic methane hydrate as a cause of the carbon isotope excursion at the end of the Paleocene. Paleoceanography 10 (6), 965–971.

Dickson, A. J., Cohen, A. S., Coe, A. L., Davies, M., Shcherbinina, E. A., Gavrilov, Y. O., 2015. Evidence for weathering and volcanism during the PETM from Arctic Ocean and Peri-Tethys osmium isotope records. Palaeogeography, Palaeoclimatology, Palaeoecology 438, 300–307.

Dill, H. G., Wehner, H., Kus, J., Botz, R., Berner, Z., Stüben, D., Al-Sayigh, A., 2007. The Eocene Rusayl Formation, Oman, carbonaceous rocks in calcareous shelf sediments: Environment of deposition, alteration and hydrocarbon potential. International Journal of Coal Geology 72 (2), 89–123.

Dunkley Jones, T., Lunt, D. J., Schmidt, D. N., Ridgwell, A., Sluijs, A., Valdes, P. J., Maslin, M., 2013. Climate model and proxy data constraints on ocean warming across the Paleocene–Eocene Thermal Maximum. Earth Science Reviews 125, 123–145.

Dupuis, C., Aubry, M., Steurbaut, E., Berggren, W. A., Ouda, K., Magioncalda, R., Cramer, B. S., Kent, D. V., Speijer, R. P., Heilmann-Clausen, C., 2003. The Dababiya Quarry Section: Lithostratigraphy, clay mineralogy, geochemistry and paleontology. Micropaleontology 49 (1), 41–59.

Eldholm, O., Thomas, E., 1993. Environmental impact of volcanic margin formation. Earth and Planetary Science Letters 117 (3–4), 319–329.

Fabricius, K. E., Langdon, C., Humphrey, C., Noonan, S., Muehllehner, N., Fabricius, K. E., De'ath, G., Glas, M. S., Okazaki, R., Uthicke, S., Lough, J. M., 2011. Losers and winners in coral reefs acclimatized to elevated carbon dioxide concentrations. Nature Climate Change 1 (3), 165–169.

Faris, M., Abdelghany, O., Zahran, E., 2014. Upper Maastrichian to Lutetian nannofossil biostratigraphy, United Arab Emirates, west of the Northern Oman Mountains. Journal of African Earth Sciences 93, 42–56.

Frieling, J., Gebhardt, H., Huber, M., Adekeye, O. A., Akande, S. O., Reichart, G., Middelburg, J. J., Schouten, S., Sluijs, A., 2017. Extreme warmth and heat-stressed plankton in the tropics during the Paleocene–Eocene Thermal Maximum. Science Advances 3, 1–9.

Galeotti, S., Krishnan, S., Pagani, M., Lanci, L., Gaudio, A., Zachos, J. C., Monechi, S., Morelli, G., Lourens, L. J., 2010. Orbital chronology of Early Eocene hyperthermals from the Contessa Road section, central Italy. Earth and Planetary Science Letters 290, 192–200.

Giraldo-Gomez, V. M., Mutterlose, J., Podlaha, O. G., Speijer, R. P., Stassen, P., 2018. Benthic foraminifera and geochemistry across the Paleocene–Eocene Thermal Maximum interval in Jordan. Journal of Foraminiferal Research 48 (2), 100–120.

Giusberti, L., Rio, D., Agnini, C., Backman, J., Fornaciari, E., Tateo, F., Oddone, M., 2007. Mode and tempo of the Paleocene–Eocene thermal maximum in an expanded section from the Venetian pre-Alps. GSA Bulletin 119 (3–4), 391–412.

Gradstein, F. M., Ogg, J. G., Schmitz, M. D., Ogg, G. M., 2012. The Geologic Time Scale 2012, Elsevier.

Hallock, P., 1984. Distribution of selected species of living algal symbiont-bearing foraminifera on two Pacific coral reefs. The Journal of Foraminiferal Research 14 (4), 250–261.

Hallock, P., Glenn, E. C., 1986. Larger foraminifera: A tool for paleoenvironmental analysis of Cenozoic carbonate depositional facies. Palaios 1, 55–64.

Haq, B. U., Al-Qahtani, A. M., 2005. Phanerozoic cycles of sea-level change on the Arabian Platform. GeoArabia 10 (2), 127–160.

Haynes, J. R., 1965. Symbiosis, wall structure and habitat in foraminifera. Cushman Foundation, Foraminiferal Research Contribution 16, 40–43.

Hesselbo, S. P., 1996. Spectral gamma-ray logs in relation to clay mineralogy and sequence stratigraphy, Cenozoic of the Atlantic margin, offshore New Jersey. In: Mountain, G. S., Miller, K. G., Blum, P., Twitchell, D. (Eds.), Proceedings of the Ocean Drilling Program, Scientific

Results 150, New Jersey continental slope and rise, 411–422.

Hikami, M., Ushie, H., Irie, T., Fujita, K., Kuroyanagi, A., Sakai, K., Nojiri, Y., Suzuki, A., Kawahata, H., 2011. Contrasting calcification responses to ocean acidification between two reef foraminifers harboring different algal symbionts. Geophysical Research Letters 38 (19), 1–5.

Hollis, C. J., Dickens, G. R., Field, B. D., Jones, C. M., Percy Strong, C., 2005. The Paleocene–Eocene transition at Mead Stream, New Zealand: A southern Pacific record of early Cenozoic global change. Palaeogeography, Palaeoclimatology, Palaeoecology 215, 313–343.

Hottinger, L., 1983. Processes determining the distribution of larger foraminifera in space and time. In: Meulenkamp, J. E. (Ed.), Reconstruction of Marine Paleoenvironments Vol. 30, Utrecht, 239–254.

Hottinger, L., 1998. Shallow benthic foraminifera at the Paleocene–Eocene boundary. Strata 9, 61–64.

Hottinger, L., 2009. The Paleocene and earliest Eocene foraminiferal Family Miscellaneidae: Neither nummulitids nor rotaliids. Notebooks on Geology 6, 1–41.

Hottinger, L., 2014. Paleogene larger Rotaliid Foraminifera from the western and central Neotethys, Springer, Switzerland, 195 p.

Keen, M. C., Racey, A., 1991. Lower Eocene ostracods from the Rusayl Shale Formation of Oman. Journal of Micropalaeontology 10 (2), 227–233.

Kennett, J. P., Stott, L. D., 1991. Abrupt deep-sea warming, paleoceanographic changes and benthic extinctions at the end of the Palaeocene. Nature 353, 225–228.

Khozyem, H., Adatte, T., Spangenberg, J. E., Keller, G., Tantawy, A. A., Ulianov, A., 2015. New geochemical constraints on the Paleocene–Eocene thermal maximum: Dababiya GSSP, Egypt. Palaeogeography, Palaeoclimatology, Palaeoecology 429, 117–135.

Knauth, L. P., Kennedy, M. J., 2009. The late Precambrian greening of the Earth. Nature Letters 460, 728–732.

Koch, P. L., Zachos, J. C., Gingerich, P. D., 1992. Correlation between isotope records in marine and continental reservoirs near the Paleocene/Eocene boundary. Nature 358, 319–322.

Komar, N., Zeebe, R. E., Dickens, G. R., 2013. Understanding long-term carbon cycle trends: The late Paleocene through the early Eocene. Paleoceanography 28, 650–662.

Kopp, R. E., Schumann, D., Raub, T. D., Powars, D. S., Godfrey, L. V., Swanson-Hysell, N. L., Maloof, A. C., Vali, H., 2009. An Appalachian Amazon? Magnetofossil evidence for the development of a tropical river-like system in the mid-Atlantic United States during the Paleocene-Eocene Thermal Maximum. Paleoceanography 24, 1–11.

Kotov, S., Pälike, H., 2018. QAnalyseries – a cross-platform time series tuning and analysis tool. American Geophysical Union, Fall Meeting, Washington D. C., USA.

Langer, M. R., 2008. Assessing the Contribution of Foraminiferan Protists to Global Ocean Carbonate Production. Journal of Eukaryotic Microbiology 55 (3), 163–169.

Lauretano, V., Hilgen, F. J., Zachos, J. C., Lourens, L. J., 2016. Astronomically tuned age model for the early Eocene carbon isotope events: A new high-resolution $\delta^{13}C$ benthic record of ODP Site 1263 between ~49 and ~54 Ma. Newsletters on Stratigraphy 49, 383–400.

Lauretano, V., Littler, K., Polling, M., Zachos, J. C., Lourens, L. J., 2015. Frequency, magnitude and character of hyperthermal events at the onset of the Early Eocene Climatic Optimum. Climate of the Past 11, 1313–1324.

Littler, K., Röhl, U., Westerhold, T., Zachos, J. C., 2014. A high-resolution benthic stable-isotope record for the South Atlantic: Implications for orbital-scale changes in late Paleocene–early Eocene climate and carbon cycling. Earth and Planetary Science Letters 401, 18–30.

Lourens, L. J., Sluijs, A., Kroon, D., Zachos, J. C., Thomas, E., Röhl, U., Bowles, J., Raffi, I., 2005. Astronomical pacing of late Palaeocene to early Eocene global warming events. Nature 435, 1083–1087.

Martini, E., 1971. Standard Tertiary and Quaternary calcareous nannoplankton zonation. In: Farinacci, A. (Ed.), Proceedings of the 2nd International Conference on Planktonic Microfossils Roma, Rome, 739–785.

McInerney, F. A., Wing, S. L., 2011. The Paleocene–Eocene Thermal Maximum: A perturbation of carbon cycle, climate, and biosphere with implications for the future. Annual Review of Earth and Planetary Sciences 39, 489–516.

Miller, K. G., Janecek, T. R., Katz, M. E., Keil, D. J., 1987. Abyssal circulation and benthic foraminiferal changes near the Paleocene/Eocene boundary. Paleoceanography 2 (6), 741–761.

Monechi, S., Reale, V., Bernaola, G., Balestra, B., 2013. The Danian/Selandian boundary at Site 1262 (South Atlantic) and in the Tethyan Region: Biomagnetostratigraphy, evolutionary trends in fasciculiths and environmental effects of the Latest Danian Event. Marine Micropaleontology 98, 28–40.

Nolan, S. C., Skelton, P. W., Clissold, B. P., Smewing, J. D., 1990. Maastrichtian to Early Tertiary stratigraphy and palaeogeography of the Central and Northern Oman mountains. Geological Society, London, Special Publications 49, 495–519.

Orue-Etxebarria, X., Pujalte, V., Bernaola, G., Apellaniz, E., Baceta, J. I., Payros, A., Nuñez-Betelu, K., Serra-Kiel, J., Tosquella, J., 2001. Did the Late Paleocene thermal maximum affect the evolution of larger foraminifers? Evidence from calcareous plankton of the Campo Section (Pyrenees, Spain). Marine Micropaleontology 41, 45–71.

Paillard, D., Labeyrie, L., Yiou, P., 1996. Analyseries 1.0: a Macintosh software for the analysis of geophysical time-series. Eos Transactions, AGU 77, 379 p.

Papazzoni, C. A., Pignatti, J., 2019. The Shallow Benthic Zones: SBZ or SB? 3rd International Congress on Stratigraphy, STRATI 2019, Milan, Italy, 320 p.

Perch-Nielsen, K., 1985. Cenozoic calcareous nannofossils. In: Bolli, H. M., Saunders, J. B., Perch-Nielsen, K. (Eds.), Plankton Stratigraphy, Cambridge University Press, Cambridge, 427–554.

Pignatti, J., Matteucci, R., Parlow, T., Fantozzi, P. L., 1998. Larger foraminiferal biostratigraphy of the Maastrichtian–Ypresian Wadi Mashib succession (South Hadramawt Arch, SE Yemen). Zeitschrift für Geologische Wissenschaften 26 (5–6), 609–635.

Prazeres, M., Uthicke, S., Pandolfi, J. M., 2015. Ocean acidification induces biochemical and morphological changes in the calcification process of large benthic foraminifera. Proceedings of the Royal Society B: Biological Sciences 282, 1–10.

Pujalte, V., Schmitz, B., Baceta, J. I., Orue-Etxebarria, X., Bernaola, G., Dinares-Turell, J., Payros, A., Apellaniz, E., Caballero, F., 2009. Correlation of the Thanetian–Ilerdian turnover of larger foraminifera and the Paleocene–Eocene thermal maximum: confirming evidence from the Campo area (Pyrenees, Spain). Geologica Acta 7 (1–2), 161–175.

Racey, A., 1995. Lithostratigraphy and larger foraminiferal (Nummulitid) biostratigraphy of the Tertiary of northern Oman. Micropaleontology 41, 1–123.

Razmjooei, M. J., Thibault, N., Kani, A., Ullmann, C. V., Jamali, A. M., 2020. Santonian–Maastrichtian carbon-isotope stratigraphy and calcareous nannofossil biostratigraphy of the Zagros Basin: Long-range correlation, similarities and differences of carbon-isotope trends at global scale. Global and Planetary Change 184 (103075), 1–14.

Renema, W., Bellwood, D. R., Braga, J. C., Bromfield, K., Hall, R., Johnson, K. G., Lunt, P., Meyer, C. P., McMonagle, L. B., Morley, R. J., O'Dea, A., Todd, J. A., Wesselingh, F. P., Wilson, M. E. J., Pandolfi, J. M., 2008. Hopping Hotspots: Global shifts in marine biodiversity. Science 321, 654–657.

Riechelmann, S., Mavromatis, V., Buhl, D., Dietzel, M., Hoffmann, R., Jöns, N., Kell-Duivestein, I., Immenhauser, A., 2018. Echinoid skeletal carbonate as archive of past seawater magnesium isotope signatures – Potential and limitations. Geochimica et Cosmochimica Acta 235, 333–359.

Röhl, U., Westerhold, T., Bralower, T. J., Zachos, J. C., 2007. On the duration of the Paleocene–Eocene thermal maximum (PETM). Geochemistry, Geophysics, Geosystems 8 (12), 1–13.

Scheibner, C., Speijer, R. P., 2008a. Decline of coral reefs during late Paleocene to early Eocene global warming. eEarth 3, 19–26.

Scheibner, C., Speijer, R. P., 2008b. Late Paleocene–early Eocene Tethyan carbonate platform evolution – A response to long- and short-term paleoclimatic change. Earth-Science Reviews 90 (3–4), 71–102.

Scheibner, C., Speijer, R. P., 2009. Recalibration of the Tethyan shallow-benthic zonation across the Paleocene–Eocene boundary: the Egyptian record. Geologica Acta 7 (1–2), 195–214.

Scheibner, C., Speijer, R. P., Marzouk, A. M., 2005. Turnover of larger foraminifera during the Paleocene–Eocene Thermal Maximum and paleoclimatic control on the evolution of platform ecosystems. Geology 33 (6), 493–496.

Schmidt, C., Kucera, M., Uthicke, S., 2014. Combined effects of warming and ocean acidification on coral reef Foraminifera *Marginopora vertebralis* and *Heterostegina depressa*. Coral Reefs 33, 805–818.

Schmitz, B., Pujalte, V., 2007. Abrupt increase in seasonal extreme precipitation at the Paleocene–Eocene boundary. Geology 35 (3), 215–218.

Schmitz, B., Speijer, R. P., Aubry, M.-P., 1996. Latest Paleocene benthic extinction event on the southern Tethyan shelf (Egypt): Foraminiferal stable isotopic ($\delta^{13}C$, $\delta^{18}O$) records. Geology 24 (4), 347.

Schobben, M., Ullmann, C. V., Leda, L., Korn, D., Struck, U., Reimold, W. U., Ghaderi, A., Algeo, T. J., Korte, C., 2016. Discerning primary versus diagenetic signals in carbonate carbon and oxygen isotope records: An example from the Permian–Triassic boundary of Iran. Chemical Geology 422, 94–107.

Serra-Kiel, J., Gallardo-Garcia, A., Razin, P., Robinet, J., Roger, J., Grelaud, C., Leroy, S., Robin, C., 2016b. Middle Eocene–Early Miocene larger foraminifera from Dhofar (Oman) and Socotra Island (Yemen). Arabian Journal of Geosciences 9 (5), 1–95.

Serra-Kiel, J., Hottinger, L., Caus, E., Drobne, K., Ferrandez, C., Jauhri, A. K., Less, G., Pavlovec, R., Pignatti, J., Samso, J. M., Schaub, H., Sirel, E., Strougo, A., Tambareau, Y., Tosquella, J., Zakrevskaya, E., 1998. Larger foraminiferal biostratigraphy of the Tethyan Paleocene and Eocene. Bulletin de la Societe Geologique de France 169 (2), 281–299.

Serra-Kiel, J., Vicedo, V., Razin, P., Grelaud, C., 2016a. Selandian–Thanetian larger foraminifera from the lower Jafnayn Formation in the Sayq area (eastern Oman Mountains). Geologica Acta 14 (3), 315–333.

Shamrock, J. L., Watkins, D. K., 2012. Eocene calcareous nannofossil biostratigraphy and community structure from Exmouth Plateau, Eastern Indian Ocean (ODP Site 762). Stratigraphy 9 (1), 1–11.

Sharland, P. R., Archer, R., Casey, D. M., Davies, R. B., Hall, S. H., Heward, A., Horbury, A. D., Simmons, M. D., 2001. Chapter 4: Maximum Flooding Surfaces. In: Aplin, A., Archer, S., Bacon, M., Beck, I., Belopolsky, A., Biteau, J. J., Bjørlykke, K., Buck, S., Burley, S., Christie, M., Craig, J., Deming, D., Doré, A. G., Dromgoole, P. W., Flint, S. S., Geiger, S., Geluk, M., Goulty, N., Green, P. F., Harper, T., Henriquez, A., Hill, D., Japsen, P., Jolley, D. W., Kaldi, J., Larue, D., Lentini, M., Lovell, M., MacDonald, A., Mascle, A., Muggeridge, A., Nadeau, P., Prigmore, J., Ringrose, P., Schollnberger, W. E., Scotchman, I. C., Spitzer, R., Trudgill, B., Turner, J., Vejbæk, O., Whidden, K., Wood, R. (Eds.), Arabian Plate Sequence Stratigraphy. Gulf Petrolink, 127–301.

Shirayama, Y., Thornton, H., 2005. Effect of increased atmospheric CO_2 on shallow water marine benthos. Journal of Geophysical Research C: Oceans 110 (9), 1–7.

Slotnick, B. S., Dickens, G. R., Nicolo, M. J., Hollis, C. J., Crampton, J. S., Zachos, J. C., Sluijs, A., 2012. Large-amplitude variations in carbon cycling and terrestrial weathering during the latest Paleocene and earliest Eocene: The record at Mead Stream, New Zealand. The Journal of Geology 120, 487–505.

Sluijs, A., Brinkhuis, H., Schouten, S., Bohaty, S. M., John, C. M., Zachos, J. C., Reichart, G.-J., Sinninghe Damste, J. S., Crouch, E. M., Dickens, G. R., 2007. Environmental precursors to rapid light carbon injection at the Palaeocene/Eocene boundary. Nature Letters 450, 1218–1221.

Sluijs, A., Brinkhuis, H., Stickley, C. E., Warnaar, J., Williams, G. L., Fuller, M., 2003. Dinoflagellate cysts from the Eocene–Oligocene transition in the Southern Ocean: Results from ODP Leg 189. In: Exon, N. F., Kennett, J. P., Malone, M. J. (Eds.), Proceedings of the Ocean Drilling Program, Scientific Results Vol. 189.

Sluijs, A., Dickens, G. R., 2012. Assessing offsets between the $\delta^{13}C$ of sedimentary components and the global exogenic carbon pool across early Paleogene carbon cycle perturbations. Global Biogeochemical Cycles 26, 1–14.

Sluijs, A., Schouten, S., Donders, T. H., Schoon, P. L., Röhl, U., Reichart, G.-J., Sangiorgi, F., Kim, J.-H., Sinninghe Damsté, J. S., Brinkhuis, H., 2009. Warm and wet conditions in the Arctic region during Eocene Thermal Maximum 2. Nature Geoscience 2, 777–780.

Sluijs, A., Schouten, S., Pagani, M., Woltering, M., Brinkhuis, H., Sinninghe Damsté, J. S., Dickens, G. R., Huber, M., Reichart, G., Stein, R., Matthiessen, J., Lourens, L. J., Pedentchouk, N., Backman, J., Moran, K., 2006. Subtropical Arctic Ocean temperatures during the Palaeocene/Eocene thermal maximum. Nature 441, 610–613.

Sluijs, A., Van Roij, L., Harrington, G. J., Schouten, S., Sessa, J. A., Levay, L. J., Reichart, G. J., Slomp, C. P., 2014. Warming, euxinia and sea level rise during the Paleocene–Eocene thermal maximum on the gulf coastal plain: Implications for ocean oxygenation and nutrient cycling. Climate of the Past 10 (4), 1421–1439.

Speijer, R. P., Scheibner, C., Stassen, P., Morsi, A. M. M., 2012. Response of marine ecosystems to deep-time global warming: A synthesis of biotic patterns across the Paleocene–Eocene thermal maximum (PETM). Austrian Journal of Earth Sciences 105 (1), 6–16.

Speijer, R. P., Schmitz, B., 2000. A synthesis of biotic and stratigraphic data from the Middle East on late Paleocene global change. GFF 122 (1), 152–153.

Speijer, R. P., Wagner, T., 2002. Sea-level changes and black shales associated with the late Paleocene thermal maximum: Organic-geochemical and micropaleontologic evidence from the southern Tethyan margin (Egypt-Israel). Geological Society of America Special Paper 356, 533–549.

Spötl, C., Vennemann, T. W., 2003. Continuous flow isotope ratio mass spectrometric analysis of carbonate minerals. Rapid Communications in Mass Spectrometry 17, 1004–1006.

Stap, L., Lourens, L. J., van Dijk, A., Schouten, S., Thomas, E., 2010. Coherent pattern and timing of the carbon isotope excursion and warming during Eocene Thermal Maximum 2 as recorded in planktic and benthic foraminifera. Geochemistry, Geophysics, Geosystems 11, 1–10.

Stap, L., Sluijs, A., Thomas, E., Lourens, L. J., 2009. Patterns and magnitude of deep sea carbonate dissolution during Eocene Thermal Maximum 2 and H2, Walvis Ridge, southeastern Atlantic Ocean. Paleoceanography 24, 1–13.

Thomas, E., 1989. Development of Cenozoic deep-sea benthic foraminiferal faunas in Antarctic waters. Geological Society Special Publication 47, 283–296.

Thomas, E., 1998. Biogeography of the late Paleocene benthic foraminiferal extinction. In: Aubry, M. P., Lucas, S., Berggren, W. A. (Eds.), Late Paleocene–Early Eocene Climatic and Biotic Events in the Marine and Terrestrial Records, Columbia University Press, New York, 214–243.

Thomas, E., 2007. Cenozoic mass extinctions in the deep sea: What perturbs the largest habitat on Earth? The Geological Society of America Special Paper 424, 1–23.

Thomas, E., Boscolo-Galazzo, F., Balestra, B., Monechi, S., Donner, B., Röhl, U., 2018. Early Eocene Thermal Maximum 3: Biotic response at Walvis Ridge (SE Atlantic Ocean). Paleoceanography and Paleoclimatology 33, 1–22.

Thomas, E., Shackleton, N. J., 1996. The Paleocene–Eocene benthic foraminiferal extinction and stable isotope anomalies. In: Knox, R. W. O., Corfield, R. M., Dunay, R. E. (Eds.), Correlation of the Early Paleogene in Northwest Europe. Geological Society Special Publication 101, 401–441.

Thomas, E., Zachos, J. C., Bralower, T. J., 2000. Deep-sea environments on a warm earth: latest Paleocene–early Eocene. In: Huber, B. T., MacLeod, K. G., Wing, S. L. (Eds.), Warm Climates in Earth History, Cambridge University Press, Cambridge, UK, 132–160.

Tomas, S., Frijia, G., Bomelburg, E., Zamagni, J., Perrin, C., Mutti, M., 2016. Evidence for seagrass meadows and their response to paleoenvironmental changes in the early Eocene (Jafnayn Formation, Wadi Bani Khalid, N Oman). Sedimentary Geology 341, 189–202.

Townsend, C. R., Scarsbrook, M. R., Doledec, S., 1997. The intermediate disturbance hypothesis, refugia, and biodiversity in streams. Limnology and Oceanography 42 (5), 938–949.

Tucker, M. E., Wright, V. P., 1990. Carbonate Sedimentology. Blackwell Science Publications, 482 p.

Ullmann, C. V., Gale, A. S., Huggett, J., Wray, D., Frei, R., Korte, C., Broom-Fendley, S., Littler, K., Hesselbo, S. P., 2018. The geochemistry of modern calcareous barnacle shells and applications for palaeoenvironmental studies. Geochimica et Cosmochimica Acta 243, 149–168.

Ullmann, C. V., Korte, C., 2015. Diagenetic alteration in low-Mg calcite from macrofossils: a review. Geological Quaterly 59 (1), 3–20.

Uthicke, S., Momigliano, P., Fabricius, K. E., 2013. High risk of extinction of benthic foraminifera in this century due to ocean acidification. Scientific Reports 3, 1–5.

Varol, O., 1989. Paleocene calcareous nannofossil biostratigraphy. In: Crux, J. A., Heck, S. E. (Eds.), Nannofossils and their applications. Ellis Horwood Limited, 267–310.

Vogel, N., Uthicke, S., 2012. Calcification and photobiology in symbiont-bearing benthic foraminifera and responses to a high CO_2 environment. Journal of Experimental Marine Biology and Ecology 424–425, 15–24.

Westerhold, T., Röhl, U., Donner, B., McCarren, H. K., Zachos, J. C., 2011. A complete high-resolution Paleocene benthic stable isotope record for the central Pacific (ODP Site 1209). Paleoceanography 26 (2), 1–13.

Westerhold, T., Röhl, U., Donner, B., Zachos, J. C., 2018. Global extent of early Eocene hyperthermal events: A new Pacific benthic foraminiferal isotope record from Shatsky Rise (ODP Site 1209). Paleoceanography and Paleoclimatology 33, 626–642.

Westerhold, T., Röhl, U., Frederichs, T., Agnini, C., Raffi, I., Zachos, J. C., Wilkens, R. H., 2017. Astronomical calibration of the Ypresian timescale: Implications for seafloor spreading rates and the chaotic behavior of the solar system? Climate of the Past 13, 1129–1152.

Westerhold, T., Röhl, U., Raffi, I., Fornaciari, E., Monechi, S., Reale, V., Bowles, J., Evans, H. F., 2008. Astronomical calibration of the Paleocene time. Palaeogeography, Palaeoclimatology, Palaeoecology 257, 377–403.

Williams, G. L., Fensome, R. A., MacRae, R. A., 2017. The Lentin and Williams Index of Fossil Dinoflagellates, 2017 Edition. American Association of Stratigraphic Palynologists Foundation, AASP Contributions Series Number 48, 1–1097.

Winguth, A. M. E., Thomas, E., Winguth, C., 2012. Global decline in ocean ventilation, oxygenation, and productivity during the Paleocene–Eocene Thermal Maximum: Implications for the benthic extinction. Geology 40 (3), 263–266.

Young, J. R., Bown, P. R., Lees, J. A., 2019. Nannotax3. International Nannoplankton Association, Accessed: <http://www.mikrotax.org/Nannotax3, >.

Zachos, J. C., Dickens, G. R., Zeebe, R. E., 2008. An early Cenozoic perspective on greenhouse warming and carbon-cycle dynamics. Nature 451, 279–283.

Zachos, J. C., Mccarren, H., Murphy, B., Röhl, U., Westerhold, T., 2010. Tempo and scale of late Paleocene and early Eocene carbon isotope cycles: Implications for the origin of hyperthermals. Earth and Planetary Science Letters 299, 242–249.

Zachos, J. C., Pagani, M., Sloan, L., Thomas, E., Billups, K., 2001. Trends, rhythms, and aberrations in global climate 65 Ma to present. Science 292, 686–693.

Zachos, J. C., Röhl, U., Schellenberg, S. A., Sluijs, A., Hodell, D. A., Kelly, D. C., Thomas, E., Nicolo, M., Raffi, I., Lourens, L. J., McCarren, H., Kroon, D., 2005. Rapid acidification of the ocean during the Paleocene–Eocene Thermal Maximum. Science 308, 1611–1615.

Zachos, J. C., Schouten, S., Bohaty, S., Quattlebaum, T., Sluijs, A., Brinkhuis, H., Gibbs, S. J., Bralower, T. J., 2006. Extreme warming of mid-latitude coastal ocean during the Paleocene–Eocene Thermal Maximum: Inferences from TEX_{86} and isotope data. Geology 34 (9), 737–740.

Zachos, J. C., Wara, M. W., Bohaty, S., Delaney, M. L., Petrizzo, M. R., Brill, A., Bralower, T. J., Premoli-Silva, I., 2003. A transient rise in tropical sea surface temperature during the Paleocene–Eocene Thermal Maximum. Science 302, 1551–1554.

Zamagni, J., Mutti, M., Košir, A., 2008. Evolution of shallow benthic communities during the Late Paleocene–earliest Eocene transition in the Northern Tethys (SW Slovenia). Facies 54 (1), 25–43.

Zamagni, J., Mutti, M., Kosir, A., 2012. The evolution of mid Paleocene–early Eocene coral communities: How to survive during rapid global warming. Palaeogeography, Palaeoclimatology, Palaeoecology 317–318, 48–65.

Zeebe, R. E., Dickens, G. R., Ridgwell, A., Sluijs, A., Thomas, E., 2014. Onset of carbon isotope excursion at the Paleocene–Eocene thermal maximum took millennia, not 13 years. Proceedings of the National Academy of Sciences 111 (12), 1062–1063.

Zeebe, R. E., Lourens, L. J., 2019. Solar system chaos and the Paleocene–Eocene boundary age constrained by geology and astronomy. Science 365 (6456), 926–929.

Zeebe, R. E., Ridgwell, A., Zachos, J. C., 2016. Anthropogenic carbon release rate unprecedented during the past 66 million years. Nature Geoscience 9 (4), 325–329.

Zhang, Q., Wendler, I., Xu, X., Willems, H., Ding, L., 2017. Structure and magnitude of the carbon isotope excursion during the Paleocene–Eocene thermal maximum. Gondwana Research 46, 114–123.

Zhang, Q., Willems, H., Ding, L., 2013. Evolution of the Paleocene–Early Eocene larger benthic foraminifera in the Tethyan Himalaya of Tibet, China. International Journal of Earth Sciences (Geologische Rundschau) 102, 1427–1445.

Zhang, Q., Willems, H., Ding, L., Xu, X., 2018. Response of larger benthic foraminifera to the Paleocene–Eocene thermal maximum and the position of the Paleocene/Eocene boundary in the Tethyan shallow benthic zones: Evidence from south Tibet. The Geological Society of America Bulletin 131 (1–2), 84–98.

Ziegler, M. A., 2001. Late Permian to Holocene paleofacies evolution of the Arabian Plate and its hydrocarbon occurrences. GeoArabia 6 (3), 445–504.

Manuscript received: September 26, 2019
Revisions required: March 25, 2020
Revised version received: May 26, 2020
Manuscript accepted: May 27, 2020

Appendix 2

J. Micropalaeontology, 39, 169–181, 2020
https://doi.org/10.5194/jm-39-169-2020

Journal of Micropalaeontology
Open Access

Liberating microfossils from indurated carbonates: comparison of three disaggregation methods

Charlotte Beasley[1], Daniel B. Parvaz[2,3], Laura Cotton[4], and Kate Littler[1,5]

[1]Camborne School of Mines, University of Exeter, Penryn Campus, Penryn, Cornwall, TR10 9FE, UK
[2]Lightning Machines, 2nd Floor, Grove House, 774–780 Wilmslow Road, Didsbury, Greater Manchester, M20 2DR, UK
[3]SELFRAG AG, Biberenzelgi 18, 3210 Kerzers, Switzerland
[4]School of Environment, Geography and Geosciences, University of Portsmouth, Burnaby Building, Burnaby Road, Portsmouth, Hampshire, PO1 3QL, UK
[5]Environment and Sustainability Institute, University of Exeter, Penryn Campus, Penryn, Cornwall, TR10 9FE, UK

Correspondence: Charlotte Beasley (c.beasley@exeter.ac.uk)

Received: 11 June 2020 – Revised: 7 August 2020 – Accepted: 20 August 2020 – Published: 9 October 2020

Abstract. Three disaggregation methods, i.e. Calgon, acetic acid and electric pulse fragmentation (EPF), have been applied to a range of heavily lithified, carbonate-rich sedimentary rock samples of Paleogene age. Samples are predominantly from the carbonate-rich, shallow water domain (< 250 m palaeo-water depth) of Tanzania, Malta and the United Arab Emirates (Paleogene Tethys Ocean). The effectiveness and efficiency of each method has been compared, in addition to the preservation of the resultant liberated microfossil material (primarily larger foraminifera; LF). Of the three methods, the most efficient and effective was EPF, which liberated the largest number of LF in a very short processing time and resulted in the best preservation. Samples with calcitic, silicic, and clay matrices and cements were successfully disaggregated using EPF. In this study, recovered microfossils were largely > 500 µm, suggesting this technique may be more appropriate for liberating larger microfossils (e.g. LFs); however, we discuss nuances to the method that would allow for more effective recovery of smaller microfossil specimens. The more traditional acetic acid method was also able to disaggregate a number of the samples; however, preservation of the LF was compromised. We suggest a best-practice methodology for implementing EPF in micropalaeontological studies.

1 Introduction

Indurated carbonate-rich sedimentary rocks (e.g. limestones) are notoriously difficult to disaggregate, something that is essential when liberated microfossils are required for taxonomic or geochemical analyses. "Traditional" methods (i.e. those well documented within current literature) used for disaggregation of deep-sea sediments, such as Calgon, cannot break apart the well-cemented matrix, and methods utilising stronger acids risk damaging microfossils that are themselves often composed of calcium carbonate. Alternative techniques are therefore required to successfully liberate microfossils in such indurated carbonates. The biostratigraphic study of larger foraminifera (LF) in these rocks is more commonly achieved through the use of thin sections or acetate peels; however, the resultant "cut" through the rock may not allow for successful identification to a specific or generic level. In order to identify LF to species level, the specimen must be orientated either on its axial or equatorial axis (Fig. 1). As such, liberated specimens from which individual thin sections can be made are preferred. Similarly, it is extremely difficult to identify smaller foraminifera accurately from thin sections, as various aspects of their external morphology (e.g. the surface of their tests) need to be assessed for specific level identification.

The difficulty in liberating microfossils from indurated carbonates is a widespread problem which is especially ubiquitous when studying outcrop samples which have of-

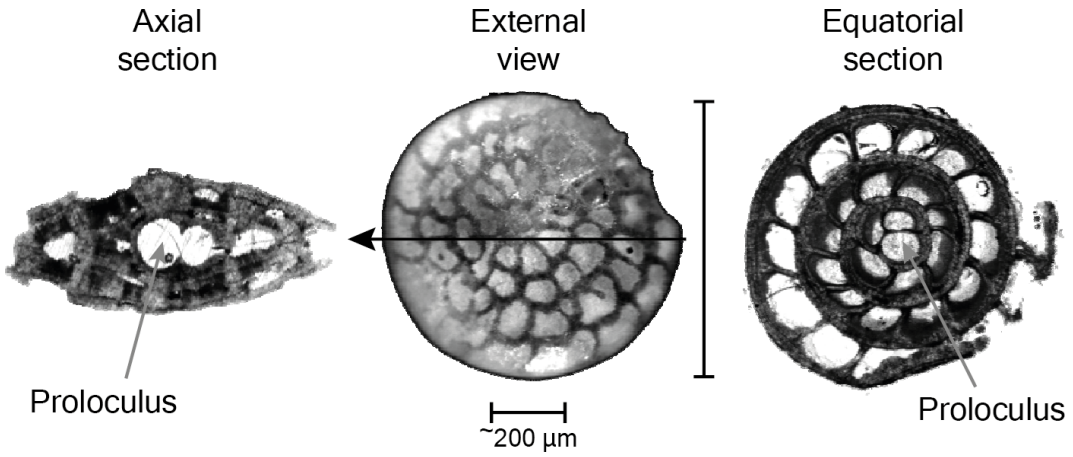

Figure 1. The equatorial and axial orientation of larger foraminifera thin section samples (foraminifera images from Cotton, 2012).

ten been subjected to weathering and enhanced cementation. However, there is a wealth of information to be gained from detailed study of ancient shallow water carbonate settings, which are often exposed as outcrops rather than cores. As such, we have investigated whether electric pulse fragmentation (EPF) is a possible improvement over traditional rock disaggregation techniques to aid microfossil recovery in these lithologies. Commonly used for liberation of coarse zircon grains for geochronological studies, EPF as a tool for microfossil liberation was proposed by Saini-Eidukat and Weiblen (1996); their study successfully liberated a range of microfossil (conodonts, foraminifera, juvenile ammonites, ostracods) and macrofossil (belemnite tip, fossil moulds, fish teeth) material from shales and sandstones. Liberated material was composed of moulds. Despite further industrialisation and more commercially available EPF systems, this technique has not yet been investigated further. More specifically, this method has not previously been applied to any carbonate sediments, within which microfossil and macrofossil material can be abundant.

In an initial pilot study, we successfully liberated LF from surrounding carbonate cement in one sample from the United Arab Emirates (UAE) shallow-water Umm Err Radhuma formation: an indurated, bioclastic Paleogene carbonate (Parvaz et al., 2018). To further test the effectiveness of EPF in LF liberation, we compare it against two traditional methods: Calgon and acetic acid. These two methods were chosen as they represent use of an acid (acetic acid) and a surfactant (Calgon) to disaggregate samples; these are categories into which most other disaggregation techniques fall into (Hodgkinson, 1991). We therefore feel these are representative for comparison across a wide range of techniques. We assess the effectiveness and efficiency of each of these methods in liberating LF from carbonate-rich lithologies by comparing disaggregation time, percentage fossiliferous fraction and number of liberated specimens.

2 Materials and methods

A total of nine field samples from strata of Paleogene age were investigated; each was subjected to disaggregation using three different techniques. Samples were collected on field campaigns in Tanzania, Malta and the UAE; they consisted dominantly of carbonate-rich, bioclastic grainstones with extensive diagenetic cements of varying composition (Table 1). All samples were deposited in a dominantly shallow-water environment (< 250 m) with a diverse assemblage of shallow-water biota present (LF, ostracods, bryozoans, red and green algae). Samples have undergone various stages of diagenesis and are therefore highly lithified with diagenetic cements. The details of the field samples are shown in Table 1. Hand specimen and thin section images are shown in Figs. 2 and 3, respectively.

Two traditional methods (Calgon and acetic acid) used in disaggregating carbonates were employed in order to compare against the new technique (EPF). Each of the nine bulk samples were first imaged (Fig. 2), and one thin section of each sample was made (Fig. 3). Then, three equal-sized amounts of the rocks were broken off from each sample. The resultant amount was dependent upon the initial size of the sample, but each was at least 20 g.

Once the samples were disaggregated using each of the three methods below a selection of liberated microfossil material from each method was imaged using a scanning electron microscope.

2.1 Method 1: Calgon (modification of Riding and Kyffin-Hughes, 2004)

Immersion in cold Calgon is a technique often used to disaggregate less well-indurated calcium carbonate samples (e.g. deep sea oozes, chalks) for the study of smaller microfossils (e.g. Barnet et al., 2019; their Supplement). Within these lithologies this technique can be extremely effective

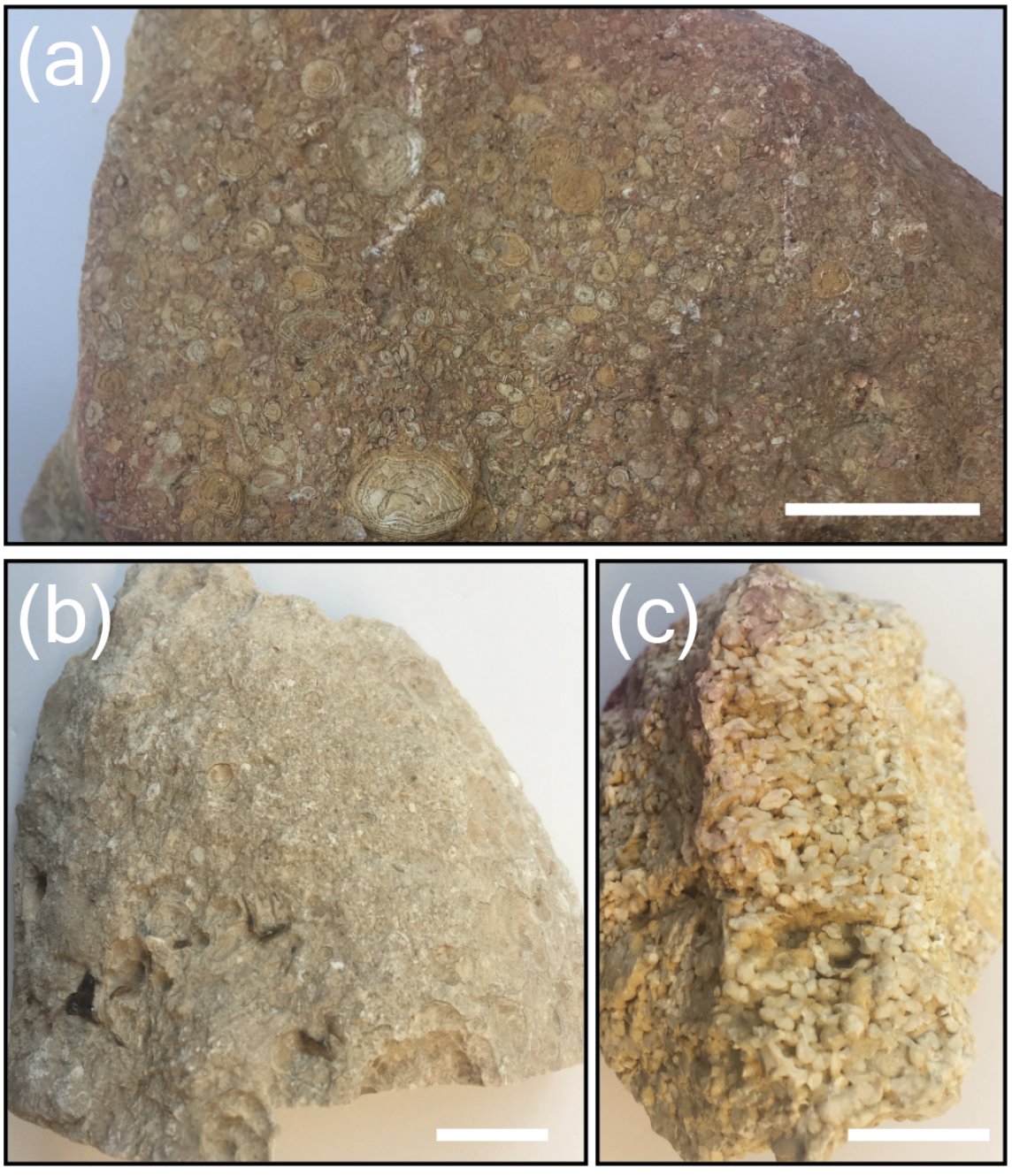

Figure 2. Hand specimen images of three samples. These show the range of fossiliferous carbonate sediments that were tested with the three disaggregation methods: **(a)** LF packstone–grainstone (sample K16), **(b)** bioclastic wackestone (sample JB1) and **(c)** LF packstone (sample L05). Scale bars are 2 cm.

at disaggregating the microfossiliferous content from the carbonate–clay matrix. Although extensively used, this modified technique for use on calcareous foraminifera has rarely been described in full (Riding and Kyffin-Hughes, 2004); as such it is described in full below. The technique requires a buffered (pH-controlled) solution of sodium hexametaphosphate ($[NaPO_3]_6$) to limit the damage that a stronger acid can have on dissolution susceptible calcium carbonate tests (Hodgkinson, 1991). This is achieved by adding sodium carbonate (Na_2CO_3) to the solution in the following proportion: 10 L deionised H_2O, 20 g $(NaPO_3)_6$ and 1.4 g Na_2CO_3. The cold Calgon solution method works due to the deflocculating nature of the phosphate ions present. They reduce the coherence of clay particles by adsorbing strongly to the particle surface, breaking apart the clays due to the high ionic charges (Riding and Kyffin-Hughes, 2004).

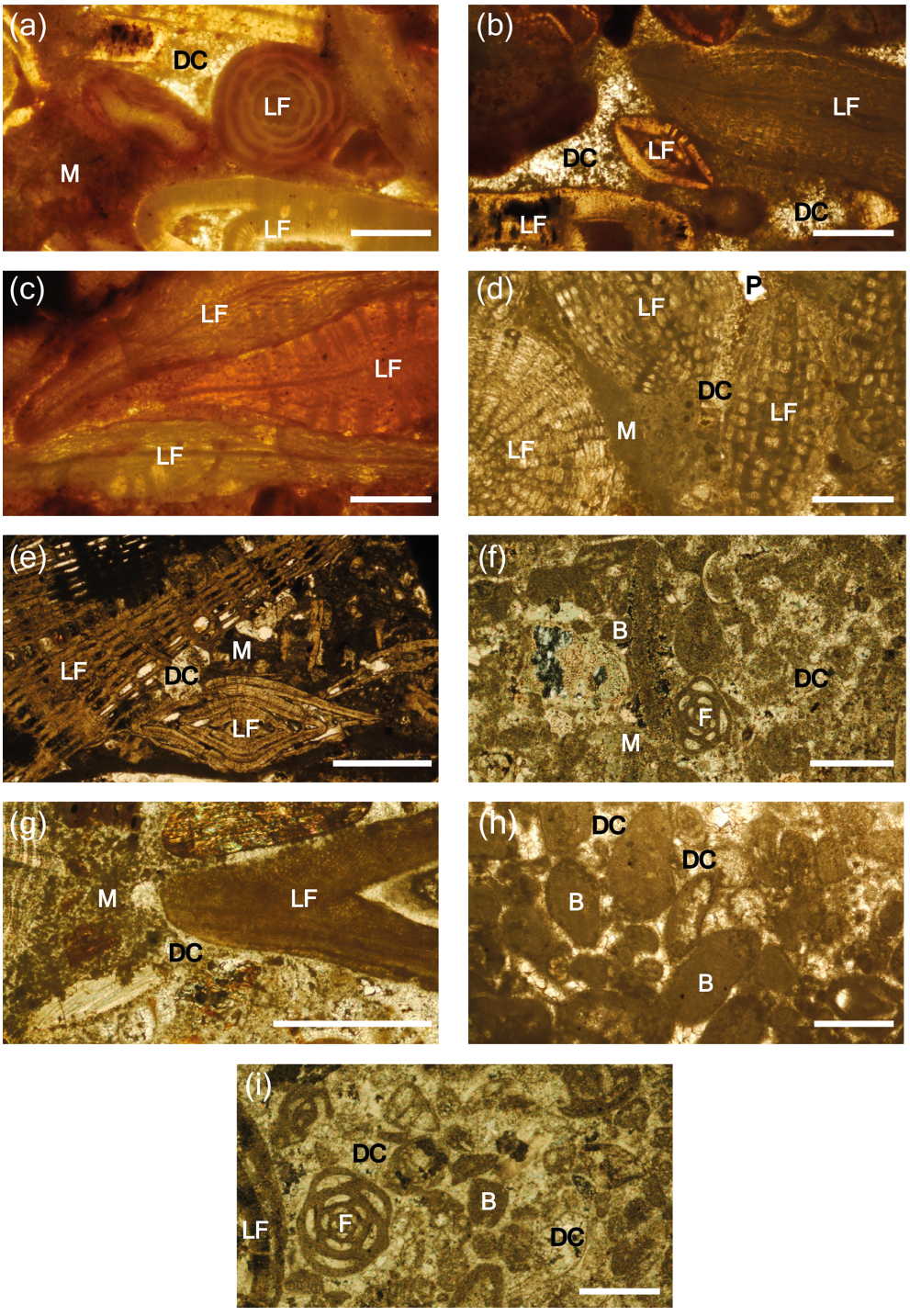

Figure 3. Example thin section images of the bulk samples showing the range of biota and amount and type of cement. Images taken with transmitted light microscope; XPL stands for crossed polarised light, and PPL stands for plane polarised light. White scale bars are 500 µm in each image. **(a)** LF packstone (?*Alveolina* and nummulitids) with quartz grains within a clay matrix (sample K05 in XPL). **(b)** LF packstone (nummulitid and orthophragmine) with quartz grains within a clay matrix (sample K09 in PPL). **(c)** LF packstone–grainstone (orthophragmine) with quartz grains within a clay matrix (sample K16 in PPL). **(d)** LF packstone (miogypsinids and *Sphaerogypsina*) with thin calcitic meniscus cement (sample L05 in PPL). **(e)** LF packstone (*Lepidocyclina* and nummulitid) with calcite cement, clay matrix and quartz grains (sample LCL in PPL). **(f)** Bioclastic wackestone with secondary calcite cement (sample JB1 in XPL). **(g)** Bioclastic wackestone with secondary calcite cement (sample JB3 in XPL). **(h)** Bioclastic grainstone with secondary calcite cement (sample JF2 in PPL). **(i)** Foraminifera wackestone with secondary calcite cement (sample JH1 in XPL). LF stands for larger foraminifera, DC stands for diagenetic cement, M stands for matrix sediment, P stands for porosity, F stands for foraminifera and B stands for other bioclast. Further sample descriptions can be found in Table 1.

Table 1. Details of the different samples used in this study. The details of the biota were identified in thin sections and are shown in Fig. 2.

Sample name	Locality (latitude, longitude)	Bioclasts	Type of cement or matrix	Facies type; approximate age	References and formation names
K05	Kilwa, Tanzania (08°55′ S, 039°30′ E)	LF (*Discocyclina* spp., *Nummulites* spp., *Assilina* spp.), complex miliolids, green algae.	Coarse-grained quartz grains within clay matrix infilling porosity.	LF packstone; Eocene	Kilwa group, Masoko Formation (e.g. Nicholas et al., 2006)
K09	Kilwa, Tanzania (08°55′ S, 039°30′ E)	LF (*Nummulites* spp., *Discocyclina* spp., other orthophragmines).	Fine-grained quartz grains within clay matrix infilling porosity.	LF packstone; Eocene	Kilwa group, Masoko Formation (e.g. Nicholas et al., 2006)
K16	Kilwa, Tanzania (09°16′ S, 039°31′ E)	LF (*Nummulites* spp., *Assilina* spp., *Discocyclina* spp., other orthophragmines).	Fine-grained quartz grains and sporadic clay matrix infilling porosity.	LF packstone-grainstone; Eocene	Kilwa group, Masoko Formation (e.g. Nicholas et al., 2006)
L05	Near Mbanja, Tanzania (09°52′ S, 039°44′ E)	LF (miogypsinids, lepidocyclinids, *Sphaerogypsina* spp.), red algae.	Thin calcitic meniscus cement between bioclasts. Clay lining pores.	LF packstone; Miocene	Miocene; not formally described in literature (Nicholas et al., 2006)
LCL	Il Mara, Malta (35°48′ N, 14°31′ E)	LF (lepidocyclinids, nummulitids).	Fine-grained secondary calcite cement. Quartz grains within clay matrix.	LF packstone; Oligocene	Lower Coralline limestone Formation (e.g. Pedley, 1975)
JB1	Jebel Buhays, UAE (25°01′ N, 55°47′ E)	Smaller benthic foraminifera, complex miliolids.	Coarse-grained secondary calcite cement.	Bioclastic wackestone; Paleocene/Eocene	Muthaymimah/Rus Formation (e.g. Abdelghany and Abu Saima, 2013)
JB3	Jebel Buhays, UAE (25°01′ N, 55°47′ E)	LF (nummulitids, orthophragmines), red algae.	Primary isopachous crust, secondary fine-grained calcite cement.	Bioclastic wackestone; Paleocene/Eocene	Muthaymimah/Rus Formation (e.g. Abdelghany and Abu Saima, 2013)
JF2	Jebel Faiyah, UAE (25°05′ N, 55°49′ E)	Smaller benthic foraminifera, algae.	Coarse-grained secondary calcite cement.	Bioclastic grainstone; Paleocene/Eocene	Muthaymimah Formation (e.g. Nolan et al., 1990)
JH1	Jebel Hafeet, UAE (24°03′ N, 55°45′ E)	LF (*Nummulites* spp., alveolinids), complex miliolids, smaller benthic foraminifera.	Fine-grained secondary calcite cement.	Foraminifera wackestone; early Eocene	Dammam Formation (e.g. Abdelghany, 2002)

The precise method used in this study is as follows: the samples were first broken up with a hammer into small (maximum 2 cm) chunks. Due to the heavily indurated nature of samples JB1, JF2 and JH1 it was not possible to break them down to this smaller size without fracturing the fossiliferous content. These chunks were then placed into a beaker and covered with cold Calgon (buffered sodium hexametaphosphate, i.e., $(NaPO_3)_6$; as described above) and left for 24 h. Samples were then washed over a 63 µm sieve with deionised water, put back into the beaker, covered again with Calgon and left for 48 h. The beakers were then placed on a shaker table for 2 h, washed again over a 63 µm sieve and subsequently covered again in Calgon. After 24 h, the samples were placed on a shaker table for 2 h, washed over a 63 µm sieve and dried in an oven overnight at 50 °C.

2.2 Method 2: acetic acid (after Lirer, 2000)

The cold acetic acid method proposed by Lirer (2000) has been widely used to extract microfossiliferous material from indurated rocks (e.g. Jovane et al., 2007; Falzoni et al., 2016; D'Onofrio and Luciani, 2020). The free hydrogen ions in the acid work to attack the matrix of the rock, dissolving it and breaking it apart (Hodgkinson, 1991; Costa de Moura et al., 1999). Costa de Moura et al. (1999) suggest the impurities present in the matrix of carbonate rocks provide boundaries

for the acid to work on more effectively, whereas the pure biogenic carbonate of a fossil test can be considered more impermeable to the acid. However, assemblage diversity losses have been reported in planktic foraminifera after sample processing with acetic acid, showing that the acid can also attack the calcium carbonate of foraminifera tests (D'Onofrio and Luciani, 2020).

As with method 1, samples were broken into small (maximum 2 cm) chunks, except in samples JB1, JF2 and JH1 where it was not possible to break them down to this smaller size without fracturing the fossiliferous content. Samples were placed into 250 mL beakers, covered with an 80 % acetic acid and 20 % deionised water solution, and left in a fume cupboard for 24 h. After this time, samples were washed with deionised water over a 63 µm sieve and the residue dried overnight in an oven at 50 °C. Due to there being very little organic material in the samples it was not necessary to use the "Desogen" (or neosteramina; D'Onofrio and Luciani, 2020) step in the Lirer (2000) method.

2.3 Method 3: electric pulse fragmentation (EPF; Saini-Eidukat and Weiblen, 1996; Parvaz et al., 2018)

The electric pulse fragmentation (EPF) method utilises highly energetic (150–750 J per pulse), pulsed electrical discharges with a very fast voltage ramp-up time (< 500 ns) to break apart composite materials submerged in a process medium along internal compositional or mechanical boundaries. Dielectric process mediums such as water are more resistive than solids when the pulse rise time is kept below 500 ns, resulting in discharges preferentially grounding on the solid material (Bluhm et al., 2000). In each discharge a movement of electrons, as plasma, occurs from the working electrode to the ground electrode (Andres et al., 1999; van der Wielen, 2013). This plasma channel causes explosive expansion along the discharge pathway (electrodynamic fragmentation; Andres et al., 1999; Bluhm et al., 2000), producing a shockwave that propagates through the material.

The selectivity of the process arises from the interaction of the plasma channel and shockwaves with physico-chemical properties of the material. Discontinuities in electrical permittivity and conductivity at phase boundaries locally enhance the electric field, forcing the discharge channels to these boundaries. The interaction of the shock wave with elastic and acoustic discontinuities concentrates tensile stress at phase interfaces, causing local shearing and thus focussing fragmentation at these boundaries (Andres et al., 1999) and allowing full liberation of discrete components from the feed material. Applicable to a range of disciplines, EPF treatment of various mineral ores has previously shown very high liberation rates (Andres et al., 1999, 2001; Dal Martello et al., 2012; Wang et al., 2012; Bru et al., 2017, 2020), advocating for its potential use in micropalaeontology.

Table 2. Variable parameters of the SELFRAG Lab system.

Parameter	Range
Electrode gap	10–40 mm
Pulse retention rate	1–5 Hz
Voltage	90–200 kV
Number of pulses	1–1000
Sieve aperture	0.12–10 mm

For this study, EPF treatment was performed using a SELFRAG "Lab" (Fig. 4), a laboratory-scale device for the batch processing of material that is manufactured by SELFRAG AG of Switzerland. The equipment is designed to process samples of up to approximately 1 kg with a top particle size of 40–45 mm in a 4 L vessel filled with demineralised water process medium. The working electrode is immersed in the upper part of the vessel, while the bottom of the vessel constitutes the counter electrode (ground). The apparatus produces high-voltage electric discharges between the two electrodes. Operating parameters are presented in Table 2. The lab system can be operated with both a "closed" vessel for when a fixed amount of energy is to be applied to a fixed mass of material and an "open" vessel where the solid lower plate is replaced with a sieve that allows material reaching the target size during crushing to fall through and be protected from further discharge events.

Samples were manually crushed to 40–45 mm to fit into the process vessel. Measurement of the LF to be recovered guided selection of an appropriate aperture sieve for the SELFRAG open-process vessel. Normally the aperture diameter is $\sim 1.5\times$ the target particle diameter. Due to the unknown breakage behaviour of these samples, a larger diameter aperture was used in the first round of crushing and a stepwise crushing process was implemented. A series of 10 pulses were applied to the sample, followed by visual inspection of the remaining sample; if > 10 % of the sample remained above the sieve another 5–10 pulses were administered. When > 90 % of sample material had passed through the sieve, treatment was stopped, and the sample was recovered from the process vessel collection cup (SELFRAG AG, 2012) before drying at 50 °C. Process conditions and total pulses applied to each sample are found in Table 3.

After samples were dried, liberated LF were manually picked from the sample and the remaining material, comprising both particles of LF with attached matrix and only matrix, was returned to the process vessel and reprocessed (Table 3). A lower voltage of 160 kV was used in the second round to minimise the electrical crushing energy per pulse. Accordingly, the electrode gap was reduced to maintain the concentration of the electrical field and increase probability of successful discharges (van der Wielen, 2013).

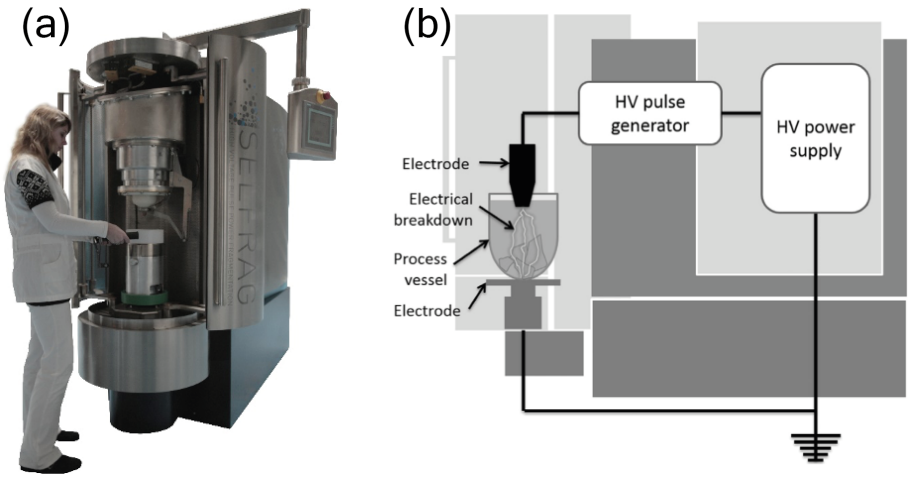

Figure 4. Photograph **(a)** and schematic **(b)** of the SELFRAG Lab system (after Bru et al., 2018).

Table 3. First- and second-round process conditions for EPF-treated samples. Sieve aperture was selected based on measurement of visible LF. The electrode gap is smaller for K05 due to much smaller sample mass. Sample JH1 was not reprocessed as all material was processed successfully in the first processing round.

Sample ID	Processing round	Sieve aperture (mm)	Electrode gap (mm)	Pulse repetition rate (Hz)	Voltage (kV)	Total pulse count	Processing time (s)
K05	1	6	20	2	150	20	10
	2	4	20	2	160	40	20
K09	1	6	40	2	175	20	10
	2	4	20	2	160	40	20
K16	1	6	40	2	175	20	10
	2	4	20	2	160	40	20
L05	1	6	40	2	175	10	5
	2	4	20	2	160	20	10
LCL	1	6	40	2	175	20	10
	2	4	20	2	160	40	20
JB1	1	6	40	2	175	40	20
	2	4	20	2	160	40	20
JB3	1	6	40	2	175	20	10
	2	4	20	2	160	40	20
JF2	1	6	40	2	175	30	15
	2	4	20	2	160	60	30
JH1	1	10	40	2	175	30	15
	n/a	–	–	–	–	–	–

n/a – not applicable.

2.4 Normalising number of liberated microfossils

2.4.1 Larger foraminifera per gram

Number of larger foraminifera picked in each sample was normalised per gram of original sample, due to varying size of the original sample. The entirety of each sample was picked. For the purposes of comparison, we consider a "good disaggregation" to be where more than two larger foraminifera per gram of sediment were liberated.

2.4.2 Percentage fossiliferous fraction (% FF)

Percentage fossiliferous fraction data (% FF) were obtained by first weighing the bulk disaggregated sediment ($bulk_w$), composed of chunks of non-disaggregated carbonate sediment and liberated fossils. The bulk sediment was dried in an oven at 50 °C after each of the disaggregation methods were applied to ensure measured weights were accurate. The > 63 µm fossiliferous fraction was then weighed once picked (FF_w). The entirety of each disaggregated sample was picked for all fossiliferous material. This mainly consisted of LF; however, a number of ostracods were also picked. In order to normalise the data to the original bulk weight of the material, the % FF was calculated using the following equation.

$$\%\,FF = (FF_w/bulk_w) \times 100 \quad (1)$$

By normalising the data in this way, it removes the issues of each sample being of a different starting mass. As such, good disaggregation of samples is shown by a larger % FF.

2.5 Scanning electron microscope (SEM) and energy dispersive spectroscopy (EDS)

Scanning electron microscope and energy dispersive spectroscopy (SEM-EDS) work was carried out at the University of Exeter, Penryn Campus, on a TESCAN VEGA3 GMU SEM with an Oxford XMax 80 mm EDS linked to AZtec analysis software. Samples were carbon coated prior to analysis and examined at 20 kV at a working distance of ~ 11 mm for imaging and ~ 17 mm for EDS analysis. The EDS data were assessed in semi-quantitative mode with an acquisition time of 10 s. Data were used to confirm the mineralogy of diagenetic cements and matrix materials in samples (Table 1).

3 Results

3.1 Calgon

Despite leaving all samples in Calgon for approximately 112 h in total, this method was not effective at disaggregating any of the samples. This is illustrated in Figs. 5 and 6, where extremely few ($< 2\,g^{-1}$) or no LF were liberated, and the percentage fossiliferous fraction was low throughout all processed samples. Where LF were liberated, the residual matrix and cement remained attached to the outside of the test (Fig. 7e and f). It seems unlikely that leaving the samples to sit in the Calgon for a more extended period of time would have led to a significantly improved disaggregation.

3.2 Acetic acid

Three samples, a LF packstones (sample K05 and LCL) and a foraminifera wackestone (sample JH1), disaggregated well with the acetic acid method in terms of numbers of foraminifera liberated per gram (Fig. 5). The highest fossiliferous fraction, of 19.65 %, was recorded using this method with sample K05 (Fig. 6); this sample is an LF packstone of Eocene age with a clay matrix containing quartz grains. All other samples had poor recoveries of LF using the acetic acid method (< 2 LF per gram and low % FF). In all cases, liberated LF were not well preserved following the acetic acid method, with test surfaces having been etched by the strong acid (Fig. 7), likely due to any disaggregation requiring at least 24 h of immersion.

3.3 Electric pulse fragmentation

Four samples disaggregated well with the EPF method both in terms of overall numbers of LF liberated per gram (Fig. 5) and percentage fossiliferous fraction (Fig. 6); these were LF packstones with clay matrices containing quartz grains (samples K05 and K09), a LF packstone with thin calcitic meniscus cement (sample L05), and a LF packstone with a calcite and clay matrix and small patches of quartz grains (sample LCL). All of these samples had bioclasts of 500 µm or larger (Table 1). Within these samples, an average of 182 % more LF per gram were liberated using EPF when compared to Calgon, and 57 % more when compared to acetic acid.

Only two samples yielded more liberated LF per gram when using the acetic acid method (Fig. 5): K05, a LF packstone, yielded 35 % more LF, and JH1, a foraminifera wackestone, yielded 72 % more LF. For all samples, preservation of liberated LF using the EPF technique was good; there was minimal fragmentation, no dissolution of the test surface, and little or no matrix or cement that remained attached to the test surfaces (Fig. 7). EPF liberation gave some of the highest overall recoveries of LF.

3.4 Poor disaggregation

Four samples did not disaggregate well with any of the three methods (Figs. 5 and 6); samples remained in large lithified chunks with little or no microfossil material liberated. These were bioclastic wackestones (samples JB1, JB3) and grainstones (sample JF2) with secondary calcite cements and a LF packstone–grainstone with abundant bioclasts and a clay matrix containing quartz grains (sample K16).

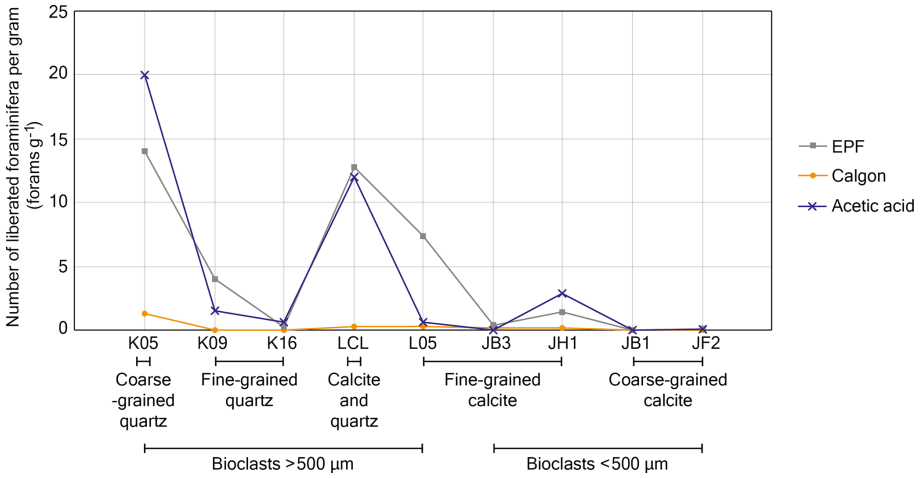

Figure 5. Number of liberated larger foraminifera per gram of each sample for each of the three methods. Samples are organised into types of infilling cements and sizes of bioclasts; further details can be found in Tables 1 and 4.

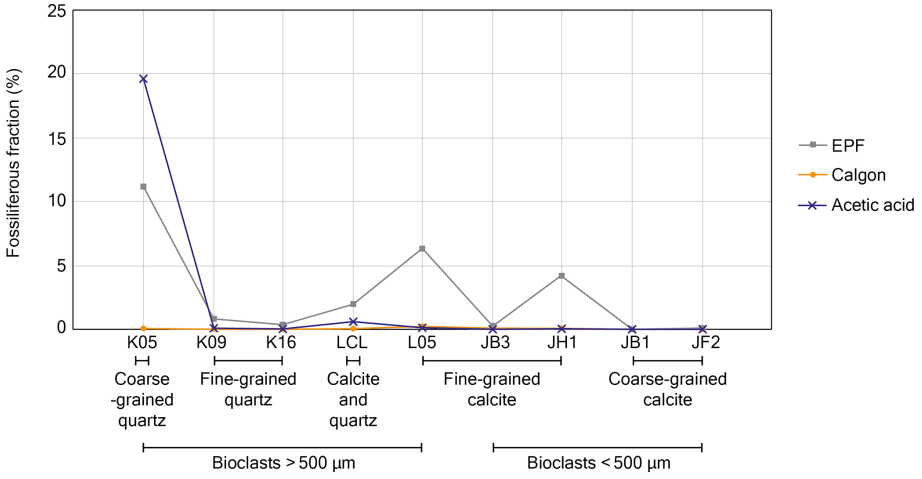

Figure 6. Percentage fossiliferous fraction (> 63 µm) for each sample from the three different methods. Samples are organised into types of infilling cements and sizes of bioclasts; further details can be found in Tables 1 and 4.

4 Discussion

The development of this new methodology, and comparison to other disaggregation techniques, aims to enable higher resolution study of the ancient low-latitude shallow water domain, which is often dominated by indurated calcium carbonate-rich sediments. Whilst there are numerous existing high-resolution palaeoclimate and micropalaeontological records from deep-water settings of Paleogene age, similar resolution records in shallow-water environments are comparatively rare, impeding comparisons of shallow and deep lithologies and the understanding of how these important palaeoenvironments and ecosystems, such as reefs, have evolved. The ability to break apart lithified carbonates into their constituent components enables the study of a wide variety of microfossil material, such as LF, algae (e.g. Rhodoliths), bryozoans, fish teeth, conodonts and more. Expansion of existing studies of evolutionary trends in individual taxa, ecophenotypic variation, species-level biodiversity trends, carbonate platform dynamics and much more thus becomes possible. Whilst other non-destructive techniques such as CT scanning are also possible (e.g. Renema and Cotton, 2015) this cannot be routinely undertaken as bioclasts need to be unfilled (e.g. the chambers must be free of cement) for optimal results and the technique is expensive and time-consuming; therefore, this technique is not suitable for many samples.

There are also other techniques available utilising different strong acids and surfactants in order to break apart fossiliferous lithologies. One such example is Rewoquat (e.g. Jarachowska et al., 2013), the trade name for a tenside (organic detergent; Kennedy and Coe, 2014) that has been used to disaggregate both organic-rich (Jarachowska et al.,

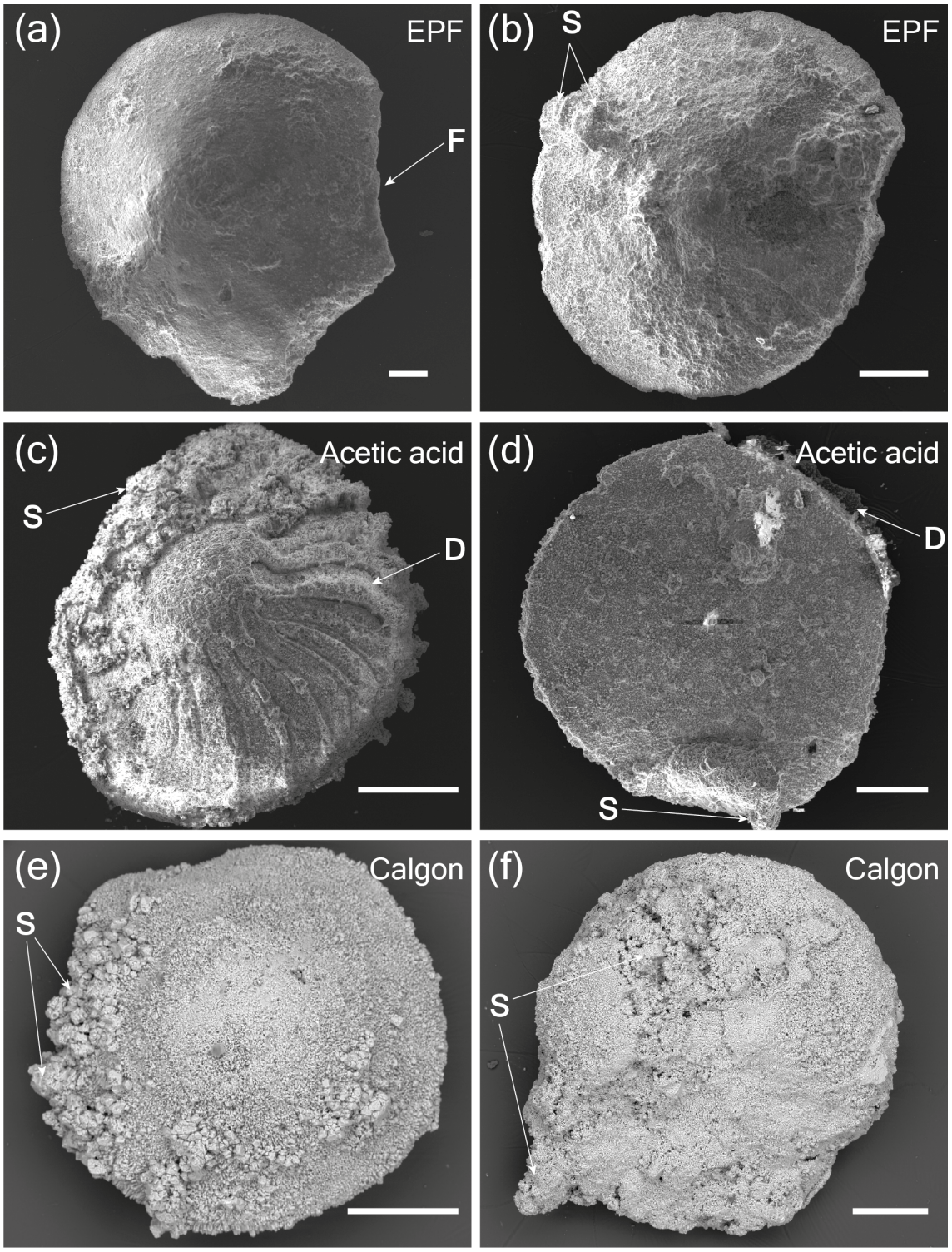

Figure 7. SEM and reflected light microscope images of select larger foraminifera from samples to show differential preservation from each technique. SE means that the image was taken in secondary electron mode. BSE means that the image was taken in backscattered electron mode. **(a)** K05 processed using EPF (SE) where some fragmentation (breakage) of specimen has occurred. **(b)** LCL processed using EPF (SE) where small amounts of sediment remain attached to the test surface. **(c)** K05 processed using acetic acid (SE) where dissolution has caused exposure of the internal chamber walls. **(d)** LCL processed using acetic acid (SE) where dissolution degraded the periphery of the test. **(e)** K05 processed using Calgon (BSE) where clumps of sediment remain attached to the test surface. **(f)** LCL processed using Calgon (BSE) where the test surface is obscured by large amounts of sediment remaining attached to the surface. Scale bars are 200 µm. S signifies sediment remaining attached to test surface, D signifies dissolution of the test surface and F signifies fragmentation of the specimen.

Table 4. Comparison of sample properties and relative success with different disaggregation techniques.

Sample name	Cement or infilling	Average size of clasts	Which disaggregation method was effective?		
			EPF	Acetic acid	Calgon
K05	Quartz grains and clays	> 500 µm	✓	✓	×
K09	Clays and small amount of quartz grains	> 500 µm	✓	✓	×
K16	Clays and quartz grains	1–2 mm	×	×	×
L05	Calcite and thin clays around pores	> 1000 µm	✓	×	×
LCL	Quartz grains and clays, calcitic crusts	> 1000 µm	✓	✓	×
JB1	Coarse-grained calcite	< 400 µm	×	×	×
JB3	Fine-grained calcite	< 500 µm	×	×	×
JF2	Coarse-grained calcite	∼ 50–300 µm	×	×	×
JH1	Fine-grained calcite	200–500 µm	✓	×	×

2013; Kennedy and Coe, 2014) and carbonate lithologies (Wolfgring and Wagreich, 2016). As with the Calgon and acetic acid techniques analysed in this paper, the Rewoquat method requires repeated rounds of processing (multiple days) for more indurated samples, with additional soaking and/or washing with hydrogen peroxide (Kennedy and Coe, 2014). The extended periods of exposure to acids and/or surfactants required with many of these techniques risks dissolution or poor preservation of recovered fossil material.

Results of this study show that, in general, the EPF method disaggregated most samples the most effectively and efficiently; this method overall gave the highest LF recoveries compared to the acetic acid and Calgon methods (Figs. 5 and 6), whilst also liberating the best-preserved specimens (Fig. 7). Only samples K05 and JH1 yielded higher LF recoveries with the acetic acid method (Fig. 5); however, these samples were also successfully disaggregated using EPF with significantly less damage to the fossils. The EPF treatment time varied between 10 and 30 s per sample (Table 3); however, the stepwise processing method, including inspection between cycles and cleaning, resulted in an overall processing time of around 20 min per sample disaggregation, compared to Calgon and acetic acid that both required multiple days.

Samples that disaggregated well with EPF contained larger (> 500 µm) bioclasts (e.g. K05, K09, LCL, L05; Figs. 5 and 6). This method was effective regardless of the cement or matrix material, as samples containing calcitic, silicic, and clay matrix or diagenetic cements were disaggregated using EPF. Furthermore, Saini-Eidukat and Weiblen (1996) previously disaggregated sandstone and shale lithologies using EPF, obtaining a diverse assemblage of well-preserved microfossil moulds such as conodonts, foraminifera, fish teeth and ammonitella. This suggests EPF is a very broadly applicable method of disaggregation in micropalaeontology.

The only sample which did not fit with the above parameters is sample K16 (LF packstone-grainstone), which contained large bioclasts (∼ 1–2 mm) and a clay matrix containing quartz grains but was not disaggregated using any method (Table 4). We hypothesise that the bioclastic material was packed too closely together (Figs. 2a and 3c), therefore there was less cement or matrix for the disaggregation techniques to be effective on. More specifically, the EPF method was not effective on this sample, as a lack of matrix–LF boundaries reduces the contrast in electrical permittivity and conductivity between bioclasts, limiting internal boundaries upon which local shearing and thus fragmentation can be focussed.

Where these larger bioclasts (> 500 µm) were surrounded by a mixture of a quartz grains and clay matrix, acetic acid was also effective in disaggregating the samples (Table 4). We suggest that acetic acid was able to work in these cases due to the higher surface area that the fine-grained clays enabled the acid to work on. However, when acetic acid disaggregation was effective, the preservation of liberated material was compromised, which reduces the utility of the microfossils for further study (Fig. 7).

None of the tested methods were effective at liberating fossiliferous material from samples that contained small (< 500 µm) bioclasts such as planktic foraminifera or smaller benthic foraminifera (Table 4). We propose that future work to tailor the EPF method for use with smaller bioclasts could include the use of smaller sieve apertures and a greater number of processing rounds in which progressively smaller microfossil material could be collected. This would require the picking of already liberated microfossils between each processing round, increasing the time spent (and thus decreasing efficiency) but could ultimately improve the recoveries

of smaller bioclasts. The EPF method could also be used as a pre-treatment step for other disaggregation techniques, such as acetic acid, where fractures generated from the process enhance permeability and thus acid penetration, which may reduce the amount of time that the samples need to be immersed in the corrosive liquid and hence improve preservation. In comparison to manually breaking up bulk material, the EPF method is far less likely to fragment microfossils prior to liberation due to it acting discriminately upon phase boundaries.

In terms of a best-practice methodology for implementing EPF on indurated microfossiliferous carbonates, we suggest the following: microfossils should be 500 µm or larger; individual microfossils should not be touching, i.e. separated by matrix or cement; the composition of the matrix or cement is unimportant and can be fine or coarse grained and made up of calcareous, siliceous, or clay components. We propose that this technique can be used on a range of microfossil material with high specimen yields, good preservation and a short processing time. For the recovery of smaller microfossils (< 500 µm), repeated rounds of EPF processing with a gradually decreasing sieve aperture and picking of liberated material between rounds could improve recoveries, with the sacrifice of a less efficient methodology, although this remains to be experimentally tested.

5 Conclusions

The EPF method is highly efficient and effective as a disaggregation technique for liberating larger microfossils (> 500 µm) from indurated carbonate-rich sedimentary rocks. This method indiscriminately disaggregated indurated carbonates with a mixture of calcitic, silicic, and clay matrices and cements; it has also previously been shown to liberate microfossils from sandstones and shales (Saini-Eidukat and Weiblen, 1996), showing it to be a broadly applicable method to micropalaeontology. We further suggest that the EPF method could be tailored to effectively liberate smaller (< 500 µm) microfossils by using repeated rounds of processing and progressively smaller sieve aperture sizes, although further investigation is required.

Compared to the traditional methods of disaggregation, soaking in Calgon and acetic acid, the time required is significantly reduced and the preservation of liberated material is excellent. Acetic acid proved effective in some highly lithified samples; however, the time taken to process the samples is significantly longer and LF preservation was compromised. Calgon was unable to disaggregate any of the carbonate samples successfully (i.e. few or no LF were liberated) and thus is unsuitable for processing these highly lithified sedimentary rocks.

Data availability. Data will be available from PANGAEA in the future but remain unavailable at time of publishing.

Author contributions. CB conducted acetic acid and Calgon treatments, and DBP performed EPF treatment. CB picked and analysed all samples using thin sections and EDS-SEM. LC and CB provided sample material. CB constructed the manuscript with contributions from DBP, KL and LC.

Competing interests. Author Daniel B. Parvaz previously worked for SELFRAG AG, who donated staff time (Daniel B. Parvaz) and machine access to perform the EPF treatment for this article.

Acknowledgements. We would like to thank SELFRAG for the processing of the samples. We also thank Steve Pendray for preparing petrological thin sections and Calum Beeson for assistance with SEM-EDS analysis. Antonino Briguglio and another anonymous reviewer are thanked for their constructive reviews, which helped to significantly improve the manuscript. The research contained in this publication contains work conducted during CB's PhD programme undertaken as part of the Natural Environment Research Council (NERC) Centre for Doctoral Training in Oil and Gas and is fully funded by NERC, whose support is gratefully acknowledged.

Financial support. This research has been supported by the Natural Environment Research Council Centre for Doctoral Training in Oil and Gas (grant no. NE/M00578X/1).

Review statement. This paper was edited by Kirsty Edgar and reviewed by Antonino Briguglio and one anonymous referee.

References

Abdelghany, O.: Biostratigraphy (*Turborotalia cunialensis/Cribrohantkenina inflata* Concurrent-Range Zone, P16) of the Late Eocene Dammam Formation, west of the Northern Oman Mountains, Micropaleontology, 48, 209–221, 2002.

Abdelghany, O. and Abu Saima, M. M.: Stratigraphy of the Early Paleogene Muthaymimah Formation exposed on the western flank of the Northern Oman Mountains, Hist. Biol., 25, 629–642, https://doi.org/10.1080/08912963.2012.729830, 2013.

Andres, U., Jirestig, J., and Timoshkin, I.: Liberation of minerals by high-voltage electrical pulses, Powder Technol., 104, 37–49, https://doi.org/10.1016/S0032-5910(99)00024-8, 1999.

Andres, U., Timoshkin, I., Jirestig, J., and Stallknecht, H.: Liberation of valuable inclusions in ores and slags by electrical pulses, Powder Technol., 114, 40–50, https://doi.org/10.1016/S0032-5910(00)00260-6, 2001.

Barnet, J. S. K., Littler, K., Westerhold, T., Kroon, D., Leng, M. J., Bailey, I., Röhl, U., and Zachos, J. C.: A high-fidelity benthic stable isotope record of late Cretaceous–early Eocene climate change and carbon-cycling, Paleoceanogr. Paleocl., 34, 1–20, https://doi.org/10.1029/2019PA003556, 2019.

Bluhm, H., Frey, W., Giese, H., Hoppé, P., Schulteiss, C., and Strässner, R.: Application of pulses HV discharges to material

fragmentation and recycling, IEEE Trans. Dieletr. Electr. Insul., 7, 625–636, 2000.

Bru, K., Touzé, S., and Parvaz, D. B.: Development of an innovative process for the upcycling of concrete waste, abstract no. 12, HISER conference, Delft, The Netherlands, 21–23 June 2017, ISBN/EAN: 978-94-6186-826-8, TU Delft Library, 2017.

Bru, K., Touzé, S., Auger, P., Dobrusky, S., Tierrie, J., and Parvaz, D. B.: Investigation of lab and pilot scale electric-pulse fragmentation systems for the recycling of ultra-high performance fibre-reinforced concrete, Miner. Eng., 128, 187–194, https://doi.org/10.1016/j.mineng.2018.08.040, 2018.

Bru, K., Sousa, R., Machado Leite, M., Broadbent, C., Stuart, G., Pashkevich, D., Martin, M., Kern, M., and Parvaz, D. B.: Pilot-scale investigation of two Electric Pulse Fragmentation (EPF) approaches for the mineral processing of a low-grade cassiterite schist ore, Miner. Eng., 150, 106270, https://doi.org/10.1016/j.mineng.2020.106270, 2020.

Costa de Moura, J., de Moraes Rios-Netto, A., Wanderley, M. D., and Pereira de Sousa, F.: Using acids to extract calcareous microfossils from carbonate rocks, Micropalaeontology, 45, 429–436, 1999.

Cotton, L. J.: Paleogene larger benthic foraminifera of Tanzania and the Eocene–Oligocene transition, PhD thesis, Cardiff University, UK, 162 pp., 2012.

Dal Martello, E., Bernardis, S., Larsen, R. B., Tranell, G., Di Sabatino, M., and Arnberg, L.: Electrical fragmentation as a novel route for the refinement of quartz raw materials for trace mineral impurities, Powder Technol., 224, 209–216, 2012.

D'Onofrio, R. and Luciani, V.: Do different extraction techniques impact planktic foraminiferal assemblages? An early Eocene case study, Mar. Micropalaeontol., 155, 101795, https://doi.org/10.1016/j.marmicro.2019.101795, 2020.

Falzoni, F., Petrizzo, M. R., Jenkyns, H. C., Gale, A. S., and Tsikos, H.: Planktic foraminiferal biostratigraphy and assemblage composition across the Cenomanian–Turonian boundary interval at Clot Chevalier (Vocontian Basin, SE France), Cretaceous Res., 59, 69–97, https://doi.org/10.1016/j.cretres.2015.10.028, 2016.

Hodgkinson, R. L.: Microfossil processing: A damage report, Micropalaeontology, 37, 320–326, 1991.

Jarachowska, E., Tonarová, P., Minnecke, A., Ferrová, L., Sklenář, J., and Vodrážková, S.: An acid-free method of microfossil extraction from clay-rich lithologies using the surfactant Rewoquat, Palaeontol. Electron., 16, 1–16, 2013.

Jovane, L., Florindo, F., Coccioni, R., Dinarès-Turell, J., Marsili, A., Monechi, S., Roberts, A. P., and Sprovieri, M.: The middle Eocene climatic optimum event in the Contessa Highway section, Umbrian Apennines, Italy, Geol. Soc. Am. Bull., 119, 413–427, https://doi.org/10.1130/B25917.1, 2007.

Kennedy, A. E. and Coe, A. L.: Development of the freeze-thaw processing technique for disaggregation of indurated mudrocks and enhanced recovery of calcareous microfossils, J. Micropalaeontol., 33, 193–203, https://doi.org/10.1144/jmpaleo2013-020, 2014.

Lirer, F.: A new technique for retrieving calcareous microfossils from lithified lime deposits, Micropaleontology, 46, 365–369, 2000.

Nicholas, C. J., Pearson, P. N., Bown, P. R., Dunkley Jones, T., Huber, B. T., Karega, A., Lees, J. A., McMillan, I. K., O'Halloran, A., Singano, J. M., and Wade, B. S.: Stratigraphy and sedimentology of the Upper Cretaceous to Paleogene Kilwa Group, southern coastal Tanzania, J. Afr. Earth Sci., 45, 431–466, 2006.

Nolan, S. C., Skelton, P. W., Clissold, B. P., and Smewing, J. D.: Maastrichtian to early Tertiary stratigraphy and palaeogeography of the Central and Northern Oman Mountains, in: The Geology and Tectonics of the Oman Region, edited by: Searle, A. H. F. and Ries, M. P., Geol. Soc. Sp., 49, 495–519, 1990.

Parvaz, D. B., Beasley, C., and Littler, K.: Recovery of intact foraminifera from indurated host rock by electric pulse fragmentation, Sample Preparation Using High Voltage Electrical Pulses, Poster, https://doi.org/10.13140/RG.2.2.24194.17602, 2018.

Pedley, H. M.: The Oligo–Miocene sediments of the Maltese islands, PhD thesis, University of Hull, UK, 205 pp., 1975.

Renema, W. and Cotton, L.: Three dimensional reconstructions of *Nummulites* tests reveal complex chamber shapes, PeerJ, 3, e1072, https://doi.org/10.7717/peerj.1072, 2015.

Riding, J. B. and Kyffin-Hughes, J. E.: A review of the laboratory preparation of palynomorphs with a description of an effective non-acid technique, Rev. Bras. Paleontolog., 7, 13–44, 2004.

Saini-Eidukat, B. and Weiblen, P. W.: A new method of fossil preparation, using high-voltage electric pulses, Curator, 39, 139–144, 1996.

SELFRAG AG: Lab v. 2.0 User Manual, Document SELFRAG Lab, SELFRAG AG, Kerzers, Switzerland, 2012.

van der Wielen, K. P.: Application of high voltage breakage to a range of rock types of varying physical properties, PhD thesis, Camborne School of Mines, University of Exeter, UK, 2013.

Wang, E., Shi, F., and Manlapig, E.: Mineral liberation by high voltage pulses and conventional comminution with same specific energy levels, Miner. Eng., 27, 28–36, 2012.

Wolfgring, E. and Wagreich, M.: A quantitative look on northwestern Tethyan foraminiferal assemblages, Campanian Nierental Formation, Austria, PeerJ, 4, e1757, https://doi.org/10.7717/peerj.1757, 2016.

Appendix 3

Core A age model construction

The age model for the Core A record was constructed using QAnalyseries (Paillard et al., 1996; Kotov & Pälike, 2018), on the basis of the LBF and calcareous nannofossil biostratigraphy (black arrows in Figures 2.2 and 2.10) and informed by comparison to an orbitally tuned record from the South Atlantic with a robust biostratigraphic and magnetostratigraphic age model (ODP Site 1262). Distinctive changes in the $\delta^{13}C$ record of Site 1262 were identified in the Core A $\delta^{13}C$ record, which were then tentatively correlated together within the constraints of the biostratigraphic age model. The tie points used in the chosen age model (Option 1) were the PETM onset, ETM-2 and ETM-3, lows in the carbon isotope record at ~58.2 and ~59.8 Ma, and the possible C1/C2 and D1/D2 events (shown in Fig. 2.10). However, given the apparent discrepancies in the $\delta^{13}C$ trends between the two records alternative age models were also created, which aimed to align the two carbon isotope records together more closely. In the first alternative age model (Option 2; Fig. 2.2), a low in the carbon isotope record in Core A at ~210 m depth (Fig. 2.8) was tied to a low at 59.2 Ma at ODP Site 1262. Other tie points are indicated in the figure using black arrows. Despite the $\delta^{13}C$ trends apparently matching more closely in this interpretation, the biostratigraphy and sedimentology are both less parsimonious. The sedimentation rate at the base of the core (~210–380 m), characterised by marls with few bioclasts, increases to ~35 cm kyr^{-1}, which does not fit with the interpretation of this being a relatively deeper depositional environment with slower sedimentation rates (Hallock, 1981; Milliman, 1993). The sedimentation rate between ~59–56 Ma (~50–210 m), characterised by bioclastic-rich carbonates, then decreases to 5 cm kyr^{-1}, which is not consistent with the higher sedimentation rates expected within this highly productive shallow water facies (Hallock, 1981; Tucker, 1985; Tucker & Wright, 1990; Milliman, 1993; Schlager, 2000).

Following this exercise, the rapid decline in carbon isotopes in the Core A record at ~50 m was tied to other minor hyperthermal events in the late Paleocene (Option 3 to D1/D2 and Option 4 to C1/C2; Cramer et al., 2003; Zachos et al., 2010; Littler et al., 2014; Barnet et al., 2019); this is plausible within the

constraints of the calcareous nannofossil and LBF biostratigraphy, however the magnitude of the excursion in Core A (~1‰) is larger than has previously been recorded in these late Paleocene hyperthermal events (~0.5‰; Cramer et al., 2003; Barnet et al., 2019). The age models for these interpretations are shown in Options 3 and 4 (Fig. 2.2). As stated above, although these age models visually improve the correlation in trends between the two records, they do not fit with the observed sedimentological changes, with the new age models suggesting a higher sedimentation rate at the base of the core, characterised by marl, and lower sedimentation rate within the bioclastic facies. It is not possible to shift the base of Core A to be any older than is shown in Options 1–4 as LBF ranges of species such as *Daviesina khatiyahi* and *Kathina selveri* (Fig. 2.4) would extend into Zone SB 2, from which they are not presently known (Afzal et al., 2010; Hottinger, 2014; Serra-Kiel et al., 2016a). We therefore conclude that the age model presented in Figure 2.10 (Option 1) is the most appropriate to account for the carbon isotope, biostratigraphy, and sedimentology data presented herein.

While individual Paleocene–Eocene carbon isotope records from different ocean basins often replicate the global trend in $\delta^{13}C$, albeit with an offset in absolute values, many of these records are from relatively invariant sedimentology with time and are often based on analysis of either a consistent bulk lithology or of individual foraminifera. By contrast, Core A contains sediments that were deposited in a dynamic shallow water setting where lithology changed between marls and variably bioclastic carbonates, and thus the composition of the carbonates (and diagenetic cements) is likely to have varied. While there is no clear relationship between observed lithology and bulk $\delta^{13}C$ within Core A (Fig. 2.8), this temporal change in composition of the carbonate fraction of the sediment would likely have affected the overall profile of the bulk $\delta^{13}C$ curve to some degree and can therefore account for the apparent mismatch between Core A and ODP Site 1262 profiles during the Paleocene.

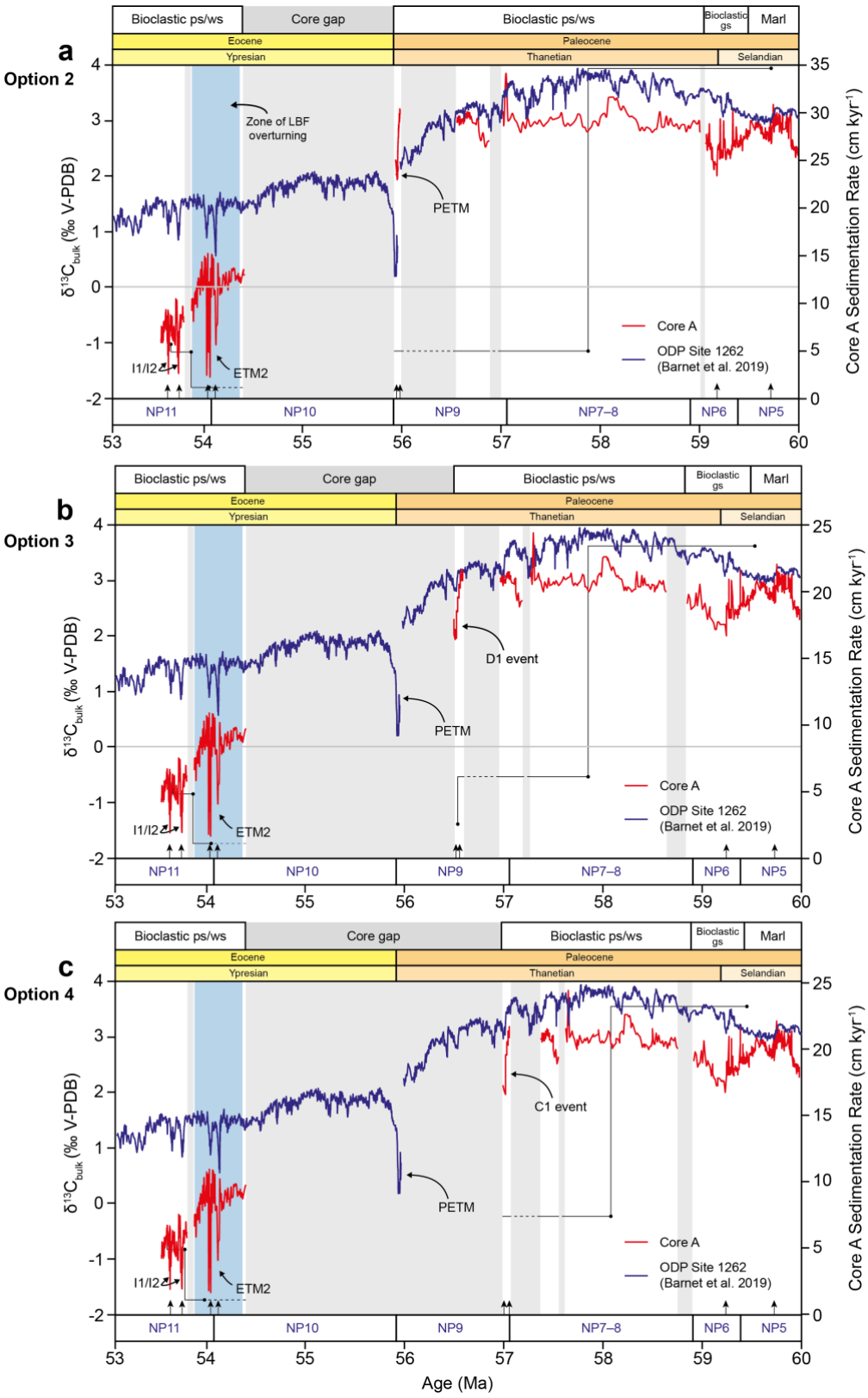

Figure 7.1: *Alternative Core A and ODP Site 1262 correlations constructed in QAnalyseries (Paillard et al., 1996; Kotov & Pälike, 2018). Black circles and solid/dashed black lines indicate sedimentation rates, grey boxes indicate core gaps, and vertical black arrows show tie points used to create the alternative age models. Facies types are shown at the top of the figure: ps = packstone; ws = wackestone; gs = grainstone. Explanations about these alternative age models and the Figure 2.9 age model are provided in above Appendix 7.3 text.*

Appendix 4

Core A calcareous nannofossil biostratigraphy

Calcareous nannofossils were present in 14 of the 16 smear slides analysed. The zonation for the sample at 372.6 m (Fig. 2.6) was based upon the presence of *Lithoptychius janii*, which was assigned a range of top Zone NP 4 to middle Zone NP 6 (Varol, 1989). The presence of the genera *Toweius*, *Chiasmolithus*, and *Prinsius* were consistent with a Paleocene age. The presence of *Sphenolithus* confirmed that the sediment was no older than Zone NP 4 (Monechi et al., 2013).

At 368.6 m *C. consuetus* was present, suggesting an oldest age of Zone NP 5 (Perch-Nielsen, 1985). However, a youngest age could not be determined due to the lack of age diagnostic species in this sample.

Discoaster mohleri (base NP 7; Martini, 1971) was present at 170.2 m. The first occurrence of *D. mohleri* has been calibrated to 58.97 Ma (Gradstein et al., 2012) and 57.57 Ma (Agnini et al., 2014). *D. nobilis*, with a range of NP 8–9 at Site 1262 (South Atlantic, Agnini et al., 2007), and *Bomolithus megastypus*, with a range of NP 7–9 (Perch-Nielsen, 1985), were also present in this sample. This assemblage of species provides a likely zonal range of NP 7–9, correlating to the late Paleocene. The markers for the base of NP 8 and 9, *Heliolithus riedelii* and *D. multiradiatus* respectively, were not present, preventing a more constrained and accurate zonal estimate. Further, the lowest occurrence of *H. riedelii* is deemed an unreliable biomarker and its absence could therefore be the result of biogeographic controls (Agnini et al., 2007).

Despite the absence of nannofossil markers *H. riedelii* and *D. multiradiatus* at 156.6 m, the assemblage in this sample suggested that it was late Paleocene in age. *D. mohleri* and *D. nobilis* were not present in this sample but based on their presence at 170.2 m it can be assumed that this sample was no older than Zone NP 7. This sample contained larger (~9 micron) specimens of *Ericsonia robusta*. Specimens larger than 9-microns have a documented range within NP 8–9 (Agnini et al., 2007).

At 77.7 m *D. multiradiatus* (base of Zone NP 9) was present. The first occurrence of *D. multiradiatus* has been calibrated at 57.32 Ma (Perch-Nielsen, 1985) or 56.01 Ma (Agnini et al., 2014), and its first common occurrence (FCO) to 57.21 Ma (Perch-Nielsen, 1985). No other datum species were present.

At 27.7 m *Campylosphaera eodela* was identified. This species had a first occurrence of 56.66 Ma and a FCO at 55.81 Ma, near the Paleocene–Eocene boundary (Gradstein et al., 2012). Based upon its presence, this sample was no older than Zone NP 9 (Perch-Nielsen, 1985; Agnini et al., 2007). *D. multiradiatus* was also present and had a range of NP 9 to ~NP 11 (Perch-Nielsen, 1985; Agnini et al., 2007). We interpret this sample to be younger than the FCO of *C. eodela* and this places this sample between NP 9–11 in the early Eocene.

S. orphanknollensis (first occurrence near the base of NP 11; Agnini et al., 2007) and *C. eodela* (last occurrence within NP 11; Shamrock & Watkins, 2012) were both present at 16.1 m, likely placing this sample within Zone NP 11, correlating to the early Eocene. At 11.9 m *S. orphanknollensis* was present along with *D. diastypus*, which had a last occurrence within NP 12 (Shamrock & Watkins, 2012). These species narrowed the age range to between NP 11–12. However, the marker species for NP 11 and NP 12 (*Tribrachiatus contortus* and *D. lodoensis*) were not present, leaving uncertainty in the age. The age of the very top of the core, at 5.8 m, was difficult to assess based on the species present. This sample must be at least as old as NP 11, based on the previous two samples. The genus *Toweius* was present; however, all the specimens were lacking central area structures with only the rims preserved. This precluded identification to the species level. The genus *Toweius* likely had a last occurrence within Zone NP 15 (Perch-Nielsen, 1985; Bown & Dunkley-Jones, 2012; Bown & Newsam, 2017), placing the sample in the early (to middle?) Eocene.

Appendix 5

Core A bulk ICP-OES derived Mg/Ca values

Bulk Mg/Ca values of carbonates from Core A. Methodology can be found in Section 2.4.4. Data was used to analyse potential diagenetic alteration in the core.

Table 7.1: *Bulk carbonate ICP-OES derived Mg/Ca values (mmol mol^{-1}).*

Depth (m)	Mg/Ca (mmol mol^{-1})	Depth (m)	Mg/Ca (mmol mol^{-1})	Depth (m)	Mg/Ca (mmol mol^{-1})
1.79	38.88	73.39	23.96	194.58	20.76
3.64	33.94	102.17	22.95	203.14	20.07
4.00	38.56	129.22	88.84	213.96	20.88
17.06	26.04	133.54	37.13	242.07	22.15
19.88	17.50	138.06	27.06	264.88	31.08
23.10	19.89	148.35	35.14	280.00	22.83
26.89	21.17	152.44	35.95	295.82	26.90
45.50	24.90	156.65	43.18	346.16	34.74
46.88	25.13	161.00	24.35	368.62	17.34
48.17	39.38	165.57	28.69	372.58	33.58
49.67	22.92	170.19	20.87	**Average**	**29.60**

Appendix 6

Site NGHP-01-01A paleodepth calculation

In order to calculate a paleodepth for this site, the relationship between sea floor subsidence rates and depth through time from Parsons & Sclater (1977) was used (Eq. S1), with the adjustment for sediment loading (Eq. S2) from Sclater et al. (1985).

$$\mathrm{d(t)} = 2500 + 350(\mathrm{t})^{\frac{1}{2}}\mathrm{m} \qquad [\mathrm{Eq.\,7.1}]$$

$$\mathrm{dw1} = \mathrm{dw2} + \mathrm{x}\frac{(\rho\mathrm{s} - \rho\mathrm{m})}{(\rho\mathrm{w} - \rho\mathrm{m})} \qquad [\mathrm{Eq.\,7.2}]$$

where

d(t) = depth of sea floor in metres at time t

dw1 = un-sedimented water depth

dw2 = sedimented water depth

x = sediment thickness

ρs = sediment density

ρm = mantle density

ρw = water density

Sediment, mantle and water density were obtained from the drilling report (Collett et al., 2008). The sediment thickness was estimated from the global sediment database (Straume et al., 2020) and nearby IODP Site U1457 shipboard report (Routledge et al., 2020). Values were as follows:

x = 750 m

ρs = 1.9 g cm^{-3}

ρm = 3.33 g cm^{-3}

ρw = 1.03 g cm^{-3}

Appendix 7

Mg/Ca-temperature and $\delta^{18}O_{sw}$ estimates error propagation

Error propagation of the Mg/Ca-temperature and $\delta^{18}O_{sw}$ estimates were calculated using the equations from Bevington and Robinson (2003). The standard deviation for Mg/Ca is 0.095 mmol mol^{-1} and for $\delta^{18}O_c$ is 0.385‰ based on repeated analysis of internal standards. For error propagation associated with Mg/Ca-temperature:

$$\sigma_T^2 = \left(\frac{T}{a}\,\sigma_a\right)^2 + \left(\frac{T}{b}\,\sigma_b\right)^2 + \left(\frac{T}{\frac{Mg}{Ca}}\,\sigma_{\frac{Mg}{Ca}}\right)^2 \qquad [\text{Eq. } 7.3]$$

where

a = 0.342 ± 0.02

b = 0.09 ± 0.003 (Anand et al., 2003)

$$\frac{T}{a} = -\frac{1}{a^2}\ln\left(\frac{\frac{Mg}{Ca}}{b}\right) \quad [Eq.\ 7.4]$$

$$\frac{T}{b} = -\frac{1}{ab} \quad [Eq.\ 7.5]$$

$$\frac{T}{\frac{Mg}{Ca}} = \frac{1}{a} \times \frac{1}{\frac{Mg}{Ca}} \quad [Eq.\ 7.6]$$

For calculation of errors associated with the estimation of $\delta^{18}O_{sw}$:

$$\sigma^2_{\delta^{18}O_{sw}} = \left(\frac{\delta^{18}O_{sw}}{T}\ \sigma_T\right)^2 + \left(\frac{\delta^{18}O_{sw}}{a}\ \sigma_a\right)^2 + \left(\frac{\delta^{18}O_{sw}}{b}\ \sigma_b\right)^2 + \left(\frac{\delta^{18}O_{sw}}{\delta^{18}O_c}\ \sigma_{\delta^{18}O_c}\right)^2 \quad [Eq.\ 7.7]$$

where

a = 16.5 ± 0.2

b = –4.8 ± 0.16 (Bemis et al., 1998)

$$\frac{\delta^{18}O_{sw}}{T} = -\frac{1}{b} \quad [Eq.\ 7.8]$$

$$\frac{\delta^{18}O_{sw}}{a} = \frac{1}{b} \quad [Eq.\ 7.9]$$

$$\frac{\delta^{18}O_{sw}}{b} = \frac{T}{b^2} - \frac{a}{b^2} \quad [Eq.\ 7.10]$$

$$\frac{\delta^{18}O_{sw}}{\delta^{18}O_c} = 1 \qquad [Eq.\,7.11]$$

Appendix 8

Site NGHP-01-01A supplementary figures

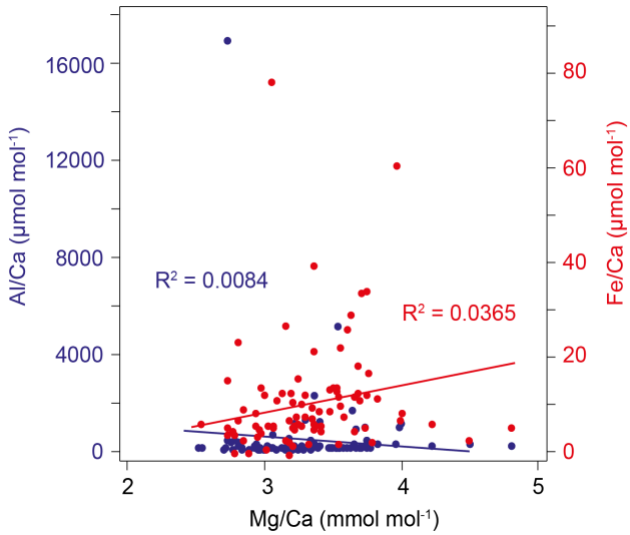

Figure 7.2 D. venezuelana *contaminant indicators. Mg/Ca values plotted versus Fe/Ca (red) and Al/Ca (blue) values to ensure no bias due to clay contamination in the carbonate bound foraminifera Mg.*

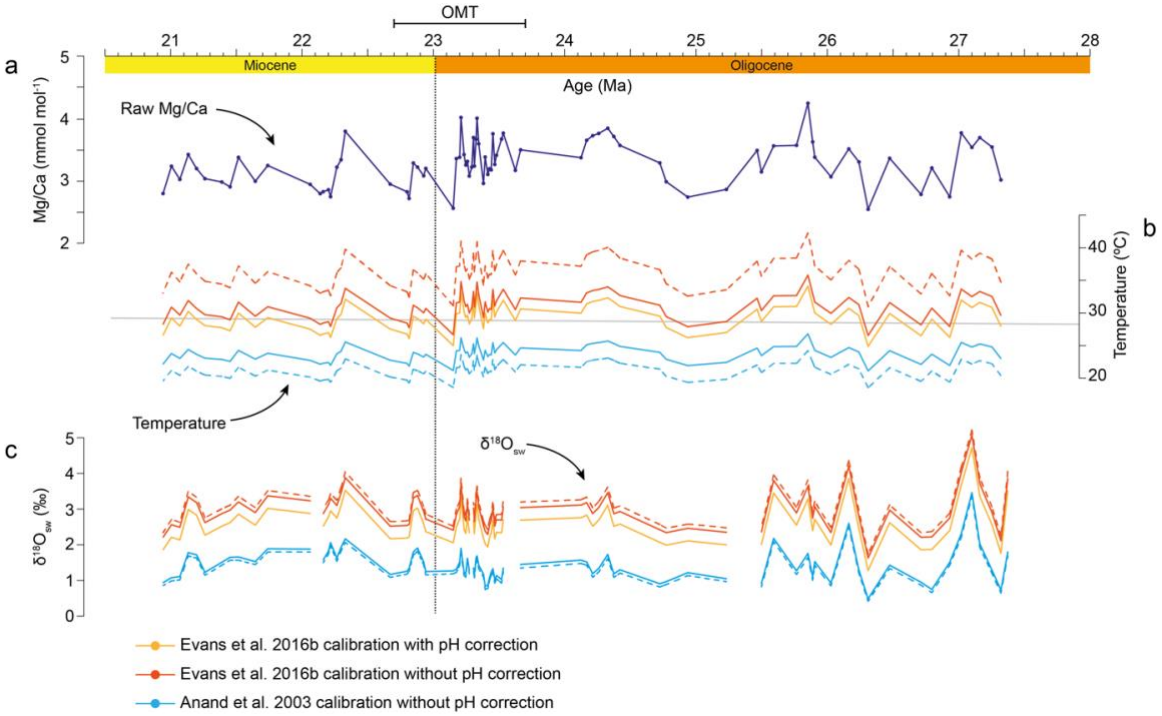

Figure 7.3 *(a) Absolute Mg/Ca (mmol mol^{-1}) values. (b) Mg/Ca temperature (in °C) calculated using the different calibrations described in the text (Section 4.4.3.1). (c) Calculated $\delta^{18}O_{sw}$ (‰) values, with the different methods of calculating Mg/Ca-*

temperature propagated through. Solid lines show absolute values of each calibration, dashed lines are positive and negative error windows. Black dotted line depicts Oligocene–Miocene boundary. Horizontal grey line depicts average temperature for all calibrations combined.

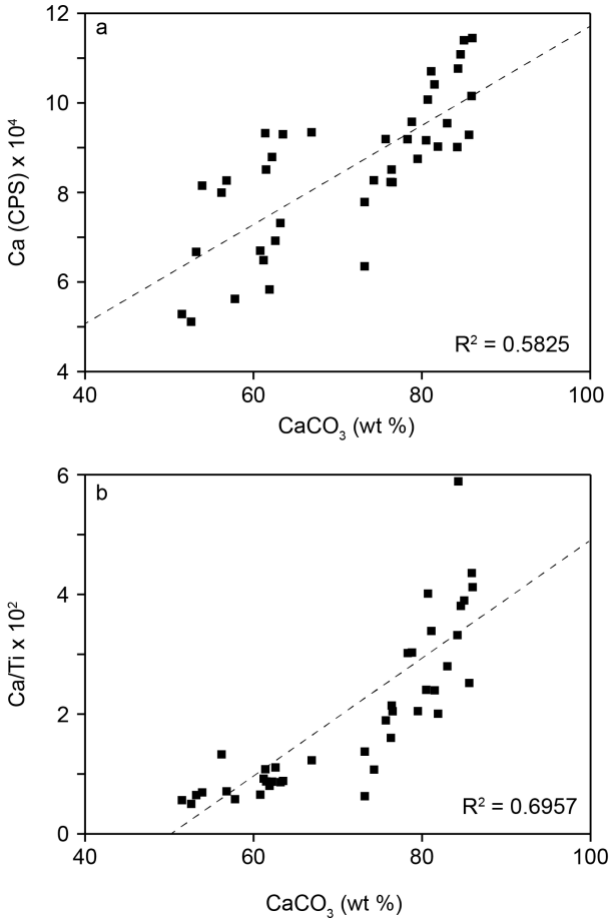

Figure 7.4 *(a) Cross plot of XRF-derived Ca in counts per second (CPS) and calcium carbonate derived from ICP-OES measurements in weight percent ($CaCO_3$ wt%). Data show reasonable correlation (R^2 = 0.58), which suggests that most of the Ca detected in the core is likely from a biogenic origin. (b) Cross plot of XRF-derived Ca/Ti against $CaCO_3$ wt%, R^2 = 0.70. The better correlation between these two variables suggests that an amount of the Ca contained in the core is not contained within $CaCO_3$, perhaps instead having a clay origin (e.g., in smectite).*

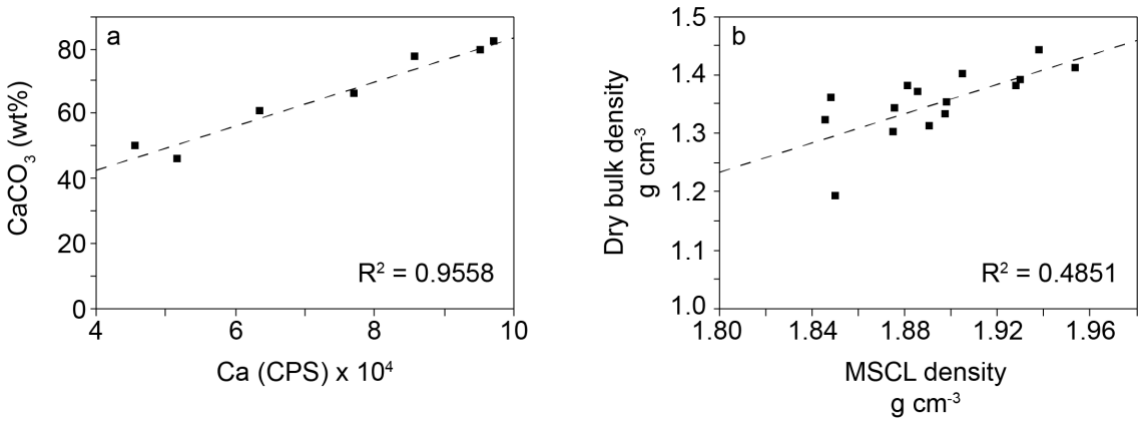

Figure 7.5 *(a) Calibration between $CaCO_3$ (wt%) from ICP-OES measurements and Ca in counts per second from core-scanning XRF analysis, used to make high-resolution $CaCO_3$ (wt%) curve. (b) Calibration of multi-sensor core logging (MSCL) density against dry bulk density (DBD), used to make high-resolution DBD curve.*

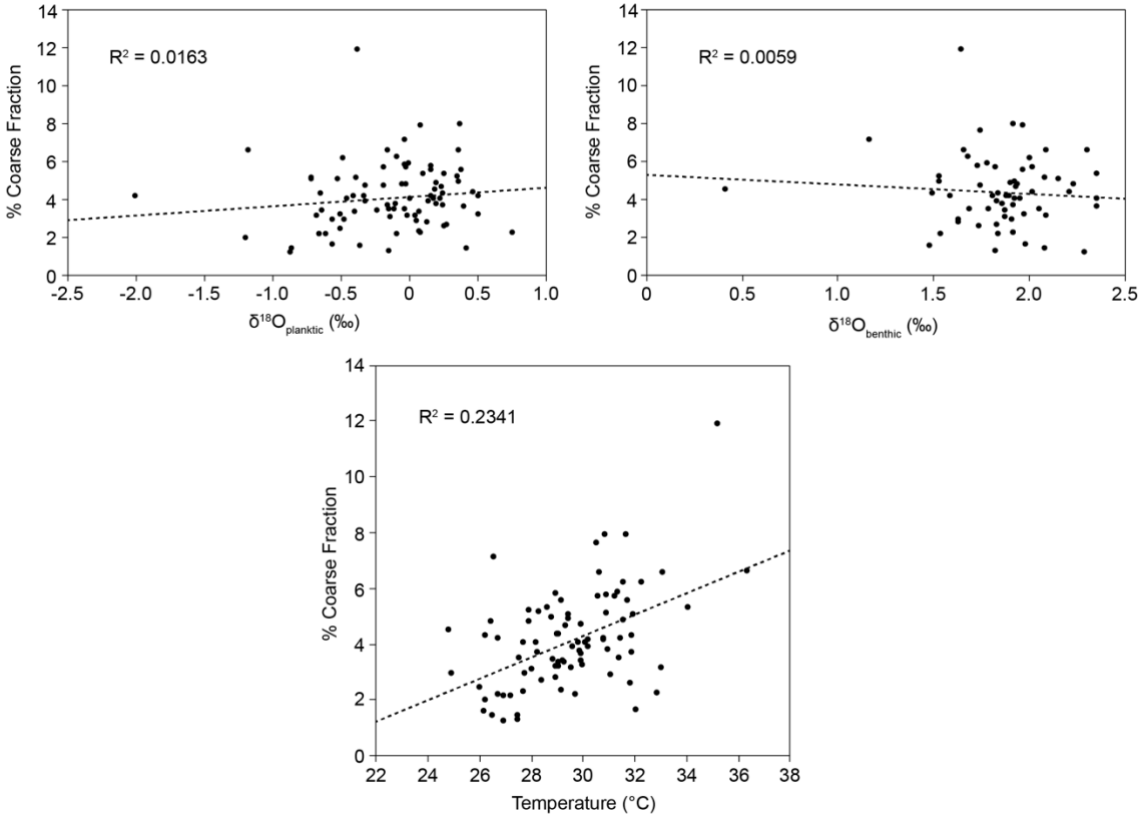

Figure 7.6 *No significant correlation between percentage coarse fraction (%CF) and oxygen isotopes in either planktic or benthic foraminifera or Mg/Ca-derived temperature observed in the core. This suggests there is a lack of diagenetic overprint on the foraminifera during the low %CF intervals acting to bias isotopic ratios or temperatures, despite the impacts on the preservation observed by SEM (Fig. 4.3).*

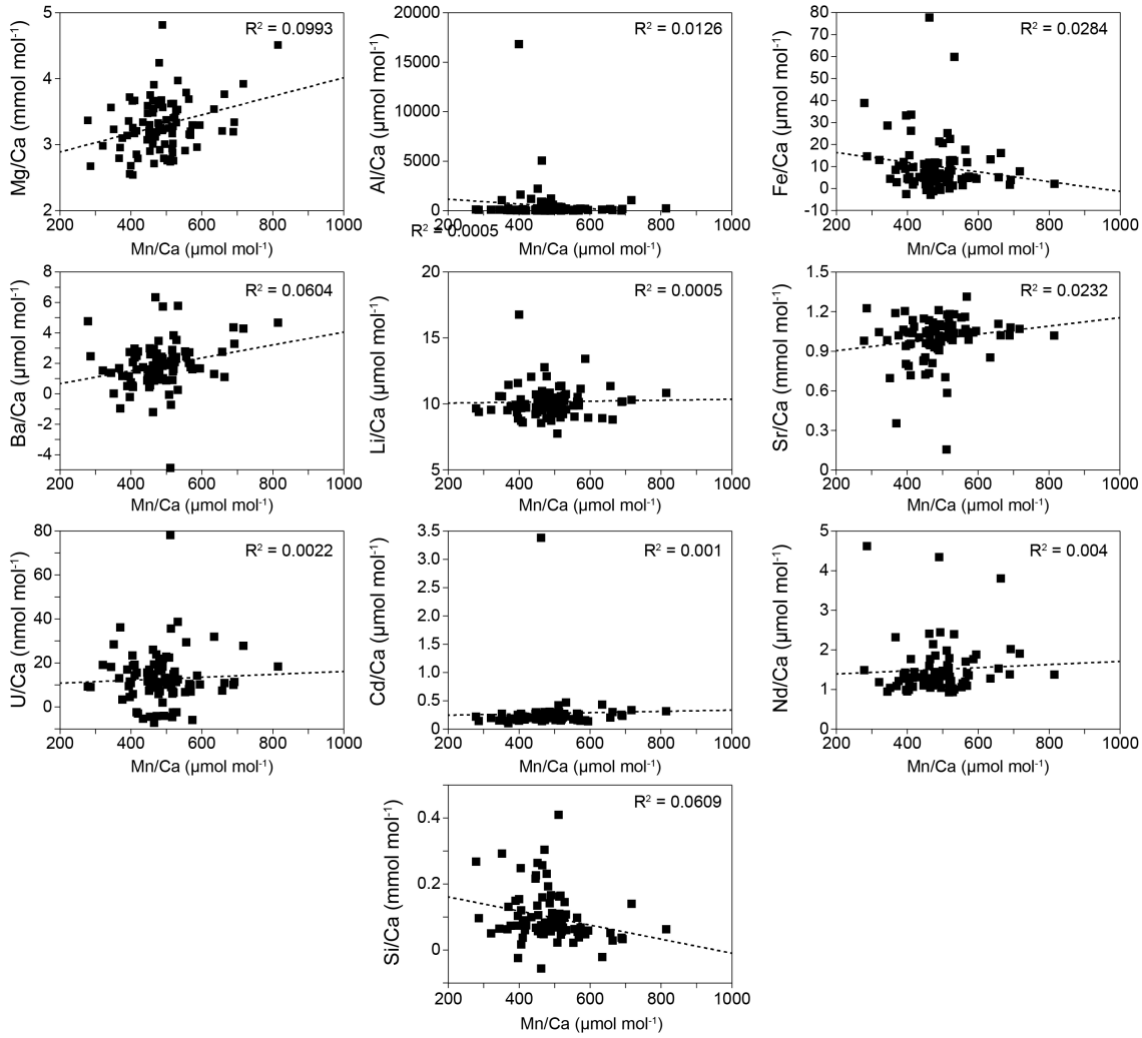

Figure 7.7 *Cross-plots of foraminiferal Mn/Ca against other measured foraminiferal trace element ratios. There is no significant correlation (R^2 = <<0.1) between Mn/Ca and any other elemental ratios.*

Appendix 9

Site NGHP-01-01A supplementary tables

Table 7.2 *List of all identified calcareous nannofossil events throughout sampled section (~210–280 mbsf) in this study and Flores et al. (2014); also shown in Figure 4.4. Events used to construct age model in Table 7.3. B = base of biozone, first occurrence; T = top of biozone, last occurrence. Ages calibrated to GTS2012 (Gradstein et al., 2012).*

Event	Study	Age (Ma)	Top depth (m)	Bottom depth (m)	Depth used (m)	Error +/- (m)
T *Sphenolithus belemnos*	Flores et al., 2014	17.97	205.80	219.10	212.45	6.65
B *Sphenolithus belemnos*	This study	19.03	228.99	229.71	229.35	0.36
B *Discoaster druggii*	This study	22.82	239.25	239.93	239.59	0.34
T *Sphenolithus delphix*	This study	23.11	239.29	239.93	239.61	0.32
B *Sphenolithus delphix*	This study	23.21	240.41	240.45	240.43	0.02
T *Sphenolithus ciperoensis*	This study	24.43	247.07	248.63	247.85	0.78
B *Triquetrorhabdulus carinatus*	Flores et al., 2014	26.57	Unknown	Unknown	258.38	5.00
B *Sphenolithus ciperoensis*	This study	29.62	266.41	267.43	266.92	0.51
B *Sphenolithus distentus*	This study	30.00	269.41	270.35	269.88	0.47

Table 7.3 *Age tie points used for site age model, based upon identified calcareous nannofossil events and known ages.*

Event	Depth (mbsf)	Age (Ma)	Sedimentation rate (cm kyr^{-1})
T *S. belemnos*	212.45	17.97	
			1.56 ± 0.62
B *S. belemnos*	229.25	19.03	
			0.251
T *S. delphix*	239.61	23.11	
			0.820
B *S. delphix*	240.43	23.21	
			0.608
T *S. ciperoensis*	247.85	24.43	
			0.367
B *S. ciperoensis*	266.92	29.62	
			0.779
B *S. distentus*	269.88	30.00	

Appendix 10

Core OS-28 ICP-MS standard results

Table 7.4 *ICP-MS results for the JNd-i standard used in Core OS-28 analysis.*

Repeat No.	$^{143}Nd/^{144}Nd$
1	0.51191
2	0.51191
3	0.51190
4	0.51192
5	0.51195
6	0.51193
7	0.51194
8	0.51192
9	0.51194
2σ	$3.7x10^{-5}$
2σ epsilon units	0.715

Biblography

Abbott, A. N., Haley, B. A., Tripati, A. K., Frank, M., 2016. Constraints on ocean circulation at the Paleocene–Eocene Thermal Maximum from neodymium isotopes. Climate of the Past 12, 837–847, doi:10.5194/cp-12-837-2016.

Abdelghany, O., 2002. Biostratigraphy (*Turborotalia cunialensis/Cribrohantkenina inflata* Concurrent-Range Zone, P16) of the Late Eocene Dammam Formation, west of the Northern Oman Mountains. Micropaleontology 48(3), 209–221.

Abdelghany, O., Abu Saima, M. M., 2013. Stratigraphy of the Early Paleogene Muthaymimah Formation exposed on the western flank of the Northern Oman Mountains. Historical Biology 25(5–6), 629–642, https://doi.org/10.1080/08912963.2012.729830.

Acharya, S. S., Panigrahi, M. K., 2016. Eastward shift and maintenance of Arabian Sea oxygen minimum zone: Understanding the paradox. Deep-Sea Research Part I: Oceanographic Research Papers 115, 240–252, https://doi.org/10.1016/j.dsr.2016.07.004.

Acosta, R. P., Huber, M., 2020. Competing Topographic Mechanisms for the Summer Indo-Asian Monsoon. Geophysical Research Letters 47, 1–11, https://doi.org/10.1029/2019GL085112.

Adams, A. E., MacKenzie, W. S., 1998. Cathodoluminescence. In: Adams, A. E., MacKenzie, W. S. (Eds.), A Colour Atlas of Carbonate Sediments and Rocks Under the Microscope. Manson Publishing, London, p. 101–156.

Afzal, J., Williams, M., Leng, M. J., Aldridge, R. J., Stephenson, M. H., 2010. Evolution of Paleocene to Early Eocene larger benthic foraminifer assemblages of the Indus Basin, Pakistan. Lethaia 44, 299–320.

Afzal, J., Williams, M., Leng, M. J., Aldridge, R. J., 2011. Dynamic response of the shallow marine benthic ecosystem to regional and pan-Tethyan environmental change at the Paleocene–Eocene boundary. Palaeogeography, Palaeoclimatology, Palaeoecology 309, 141–160, doi:10.1016/j.palaeo.2011.04.005.

Agnini, C., Fornaciari, E., Raffi, I., Rio, D., Röhl, U., Westerhold, T., 2007. High-resolution nannofossil biochronology of middle Paleocene to early Eocene at ODP Site 1262: Implications for calcareous nannoplankton evolution. Marine Micropalaeontology 64(3), 215–248,

doi:10.1016/j.marmicro.2007.05.003.

Agnini, C., Macri, P., Backman, J., Brinkhuis, H., Fornaciari, E., Giusberti, L., Luciani, V., Rio, D., Sluijs, A., Speranza, F., 2009. An early Eocene carbon cycle perturbation at ~52.5 Ma in the Southern Alps: Chronology and biotic response. Paleoceanography 24(2), 1–14, doi:10.1029/2008PA001649.

Agnini, C., Fornaciari, E., Raffi, I., Catanzariti, R., Pälike, H., Backman, J., Rio, D., 2014. Biozonation and biochronology of Paleogene calcareous nannofossils from low and middle latitudes. Newsletters on Stratigraphy 47(2), 131–181, doi:10.1127/0078-0421/2014/0042.

Alegret, L., Ortiz, S., 2006. Global extinction event in benthic foraminifera across the Paleocene/Eocene boundary at the Dababiya stratotype section. Micropaleontology 52(5), 433–447.

Alizai, A., Hillier, S., Clift, P. D., Giosan, L., Hurst, A., VanLaningham, S., Macklin, M., 2012. Clay mineral variations in Holocene terrestrial sediments from the Indus Basin. Quaternary Research 77, 368–381, https://doi.org/10.1016/j.yqres.2012.01.008.

Allen, M. B., Armstrong, H. A., 2012. Reconciling the Intertropical Convergence Zone, Himalayan/Tibetan tectonics, and the onset of the Asian monsoon system. Journal of Asian Earth Sciences 44, 36–47, https://doi.org/10.1016/j.jseaes.2011.04.018.

Alqudah, M., Hussein, M. A., van den Boorn, S., Podlaha, O. G., Mutterlose, J., 2014a. Biostratigraphy and depositional setting of Maastrichtian–Eocene oil shales from Jordan. Marine and Petroleum Geology 60, 87–104, http://dx.doi.org/10.1016/j.marpetgeo.2014.07.025.

Alqudah, M., Hussein, M. A., Podlaha, O. G., van den Boorn, S., Mutterlose, J., 2014b. Calcareous nannofossil biostratigraphy of Eocene oil shales from central Jordan. GeoArabia 19(1), 117–140.

Alqudah, M., 2014c. Calcareous nannofossils from Late Cretaceous–Paleogene oil shales of Jordan – implications for age and paleoenvironment (Ph.D. thesis). Ruhr-Universtät Bochum, Germany, 158 pp.

Alsharhan, A. S., Nairn, A. E. M., 1995. Tertiary of the Arabian Gulf: sedimentology and hydrocarbon potential. Palaeogeography, Palaeoclimatology, Palaeoecology 114(2–4), 369–384.

Anagnostou, E., John, E. H., Edgar, K. M., Foster, G. L., Ridgwell, A., Inglis, G. N., Pancost, R. D., Lunt, D. J., Pearson, P. N., 2016. Changing atmospheric

CO_2 concentration was the primary driver of early Cenozoic climate. Nature 533(7603), 380–384, doi:10.1038/nature17423.

Anand, P., Elderfield, H., Conte, M. H., 2003. Calibration of Mg/Ca thermometry in planktonic foraminifera from a sediment trap time series. Paleoceanography 18(2), 1–15, https://doi.org/10.1029/2002pa000846.

Anderson, D. M., Prell, W. L., 1993. A 300 kyr record of upwelling off Oman during the Late Quaternary: Evidence of the Asian southwest monsoon. Paleoceanography 8(2), 193–208.

Andres, U., Jirestig, J., Timoshkin, I., 1999. Liberation of minerals by high-voltage electrical pulses. Powder Technology 104, 37–49, https://doi.org/10.1016/S0032-5910(99)00024-8.

Andres, U., Timoshkin, I., Jirestig, J., Stallknecht, H., 2001. Liberation of valuable inclusions in ores and slags by electrical pulses. Powder Technology 114, 40–50, https://doi.org/10.1016/S0032-5910(00)00260-6.

Armstrong, H. A., Allen, M. B., 2011. Shifts in the intertropical convergence zone, Himalayan exhumation, and late Cenozoic climate. Geology 39(1), 11–14, https://doi.org/10.1130/G31005.1.

Arsouze, T., Dutay, J. -C., Lacan, F., Jeandel, C., 2007. Modelling the neodymium isotopic composition with a global ocean circulation model. Chemical Geology 239, 165–177, doi:10.1016/j.chemgeo.2006.12.006.

Arthur, M. A., Anderson, T. F., Kaplan, I. R., Veizer, J., Land, L. S., 1983. Stable isotopes in oxygen and carbon and their application to sedimentologic and paleoenvironmental problems. In: Arthur M. A. (Ed.), Stable Isotopes in Sedimentary Geology. SEPM Short Course No. 10, Dallas, p. 105.

Aston, S. R., Chester, R., Johnson, L. R., Padgham, R. C., 1973. Eolian dust from the lower atmosphere of the eastern Atlantic and Indian Oceans, China Sea and Sea of Japan. Marine Geology 14, 15–28.

Aze, T., Pearson, P. N., Dickson, A. J., Badger, M. P. S., Bown, P. R., Pancost, R. D., Gibbs, S. J., Huber, B. T., Leng, M. J., Coe, A. L., Cohen, A. S., Foster, G. L., 2014. Extreme warming of tropical waters during the Paleocene–Eocene thermal maximum. Geology 42(9), 739–742, doi:10.1130/G35637.1.

Bains, S., Corfield, R. M., Norris, R. D., 1999. Mechanisms of climate warming at the end of the Paleocene. Science 285, 724–727.

Barker, S., Greaves, M., Elderfield, H., 2003. A study of cleaning procedures used for foraminiferal Mg/Ca paleothermometry. Geochemistry, Geophysics, Geosystems 4(9), 1–20, doi:10.1029/2003GC000559.

Barnet, J. S. K., Littler, K., Westerhold, T., Kroon, D., Leng, M. J., Bailey, I., Röhl, U., Zachos, J. C., 2019. A High-Fidelity Benthic Stable Isotope Record of Late Cretaceous–Early Eocene Climate Change and Carbon-Cycling. Paleoceanography and Paleoclimatology 34, 1–20, https://doi.org/10.1029/2019PA003556.

Barnet, J. S. K., Harper, D. T., LeVay, L. J., Edgar, K. M., Henehan, M. J., Babila, T. L., Ullmann, C. V., Leng, M. J., Kroon, D., Zachos, J. C., Littler, K., 2020. Coupled evolution of temperature and carbonate chemistry during the Paleocene–Eocene; new trace element records from the low latitude Indian Ocean. Earth and Planetary Science Letters 545, 1–15, https://doi.org/10.1016/j.epsl.2020.116414.

Barras, C., Mouret, A., Nardelli, M. P., Metzger, E., Petersen, J., La, C., Filipsson, H. L., Jorissen, F., 2018. Experimental calibration of manganese incorporation in foraminiferal calcite. Geochimica et Cosmochimica Acta 237, 49–64, https://doi.org/10.1016/j.gca.2018.06.009.

Batenburg, S. J., Voigt, S., Friedrich, O., Osborne, A. H., Bornemann, A., Klein, T., Pérez-Díaz, L., Frank, M., 2018. Major intensification of Atlantic overturning circulation at the onset of Paleogene greenhouse warmth. Nature Communications 9(4954, 1–8, doi:10.1038/s41467-018-07457-7.

Beaumont, C., Jamieson, R. A., Nguyen, M. H., Lee, B., 2001. Himalayan tectonics explained by extrusion of a low-viscosity crustal channel coupled to focused surface denudation. Nature 414, 738–742, https://doi.org/10.1038/414738a.

Beddow, H. M., Liebrand, D., Sluijs, A., Wade, B. S., Lourens, L. J., 2016. Global change across the Oligocene–Miocene transition: High-resolution stable isotope records from IODP Site U1334 (equatorial Pacific Ocean). Paleoceanography 31, 81–97, https://doi.org/10.1002/2015PA002820.

Beddow, H. M., Liebrand, D., Wilson, D. S., Hilgen, F. J., Sluijs, A., Wade, B. S., Lourens, L. J., 2018. Astronomical tunings of the Oligocene–Miocene transition from Pacific Ocean Site U1334 and implications for the carbon cycle. Climate of the Past 14(3), 255–270, https://doi.org/10.5194/cp-14-255-2018.

Bemis, B. E., Spero, H. J., Bijma, J., Lea, D. W., 1998. Reevaluation of the oxygen isotopic composition of planktonic foraminifera: Experimental results and revised paleotemperature equations. Paleoceanography 13(2), 150–160, https://doi.org/10.1029/98PA00070.

Bergen, J., de Kaenel, E., Blair, S., Boesiger, T., Browning, E., 2017. Oligocene–Pliocene taxonomy and stratigraphy of the genus Sphenolithus in the circum North Atlantic Basin: Gulf of Mexico and ODP Leg 154. Journal of Nannoplankton Research 37(2–3), 77–112.

Bertrand, S., Hughen, K. A., Sepúlveda, J., Pantoja, S., 2012. Geochemistry of surface sediments from the fjords of Northern Chilean Patagonia (44–47°S): spatial variability and implications for paleoclimate reconstructions. Geochimica et Cosmochimica Acta 76, 125–146, https://doi.org/10.1016/j.gca.2011.10.028.

Betzler, C., Eberli, G. P., Kroon, D., Wright, J. D., Swart, P. K., Nath, B. N., Alvarez-Zarikian, C. A., Alonso-García, M., Bialik, O. M., Blättler, C. L., Guo, J. A., Haffen, S., Horozal, S., Inoue, M., Jovane, L., Lanci, L., Laya, J. C., Mee, A. L. H., Lüdmann, T., Nakakuni, M., Niino, K., Petruny, L. M., Pratiwi, S. D., Reijmer, J. J. G., Reolid, J., Stagle, A. L., Sloss, C. R., Su, X., Yao, Z., Young, J. R., 2016. The abrupt onset of the modern South Asian Monsoon winds. Scientific Reports 6, 1–10, https://doi.org/10.1038/srep29838.

Beavington-Penney, S. J., Wright, V. P., Racey, A., 2006. The middle Eocene Seeb Formation of Oman: An investigation of acyclicity, stratigraphic completeness, and accumulation rates in shallow marine carbonate settings. Journal of Sedimentary Research 76(9–10), 1137–1161, doi:10.2110/jsr.2006.109.

Bevington, P. R., Robinson, K. D., 2003. Data reduction and Error Analysis for the Physical Sciences, 3rd edition. McGraw-Hill, New York.

Bialik, O. M., Frank, M., Betzler, C., Zammit, R., Waldmann, N. D., 2019. Two-step closure of the Miocene Indian Ocean Gateway to the Mediterranean. Scientific Reports 9(8842), 1–10, https://doi.org/10.1038/s41598-019-45308-7.

Bialik, O. M., Auer, G., Ogawa, N. O., Kroon, D., Waldmann, N. D., Ohkouchi, N., 2020. Monsoons, Upwelling, and the Deoxygenation of the Northwestern Indian Ocean in Response to Middle to Late Miocene Global Climatic Shifts. Paleoceanography and Paleoclimatology 35(2), 1–17,

https://doi.org/10.1029/2019pa003762.

Bice, K. L., Marotzke, J., 2002. Could changing ocean circulation have destabilized methane hydrate at the Paleocene/Eocene boundary? Paleoceanography 17(2), 1–12, doi:10.1029/2001PA000678.

Bigelow, E. L., 2002. Wireline Log Measurements and Supportive Information. In: Bigelow, E. L. (Ed.) Introduction to Wireline Log Analysis. Baker Atlas, Baker Hughes, p. 43–84.

Bijl, P. K., Schouten, S., Sluijs, A., Reichart, G. -J., Zachos, J. C., Brinkhuis, H., 2009. Early Palaeogene temperature evolution of the southwest Pacific Ocean. Nature Letters 461, 776–779, doi:10.1038/nature08399.

Bischoff, T., Schneider, T., 2014. Energetic Constraints on the Position of the Intertropical Convergence Zone. Journal of Climate 27, 4937–4951, https://doi.org/10.1175/JCLI-D-13-00650.1.

Bluhm, H., Frey, W., Giese, H., Hoppé, P., Schulteiss, C., Strässner, R., 2000. Application of pulses HV discharges to material fragmentation and recycling. IEEE Transactions on Dielectrics and Electrical Insulation 7, 625–636.

Bolle, M. P., Pardo, A., Hinrichs, K.-U., Adatte, T., Von Salis, K., Burns, S., Keller, G., Muzylev, N., 2000. The Paleocene–Eocene transition in the marginal northeastern Tethys (Kazakhstan and Uzbekistan). International Journal of Earth Sciences 89, 390–414.

Bolle, M. P., Adatte, T., 2001. Palaeocene–early Eocene climatic evolution in the Tethyan realm: clay mineral evidence. Clay Minerals 36(2), 249–261.

Böning, P., Bard, E., 2009. Millennial/centennial-scale thermocline ventilation changes in the Indian Ocean as reflected by aragonite preservation and geochemical variations in Arabian Sea sediments. Geochimica et Cosmochimica Acta 73, 6771–6788, https://doi.org/10.1016/j.gca.2009.08.028.

Boos, W. R., Kuang, Z., 2010. Dominant control of the South Asian monsoon by orographic insulation versus plateau heating. Nature Letters 463, 218–222. https://doi.org/10.1038/nature08707.

Boos, W. R., Kuang, Z., 2013. Sensitivity of the South Asian monsoon to elevated and non-elevated heating. Scientific Reports 3(1192), 1–4, https://doi.org/10.1038/srep01192.

Bordoni, S., Schneider, T., 2008. Monsoon as eddy-mediated regime transitions of the tropical overturning circulation. Nature Geoscience 1, 515–519, doi:

10.1038/ngeo248.

BouDagher-Fadel, M. K., 2008. The Cenozoic larger benthic foraminifera: the Palaeogene. In: Wignall, P. B. (Ed.), Evolution and Geological Significance of the Larger Benthic Foraminifera. Elsevier, Amsterdam, p. 297–419.

Bowen, G. J., Beerling, D. J., Koch, P. L., Zachos, J. C., Quattlebaum, T., 2004. A humid climate state during the Palaeocene/Eocene thermal maximum. Nature 432, 495–499.

Bowen, G. J., Bowen, B. B., 2008. Mechanisms of PETM global change constrained by a new record from central Utah. Geology 36(5), 379–382.

Bown, P. R., Young, J. R., 1998. Techniques. In: Bown, P. R. (Ed.), Calcareous Nannofossil Biostratigraphy. British Micropalaeontological Society Publication Series, Kluwer Academic, London, p. 16–28.

Bown, P. R., Dunkley-Jones, T., 2012. Calcareous nannofossils from the Paleogene equatorial Pacific (IODP Expedition 320 Sites U1331–U1334). Journal of Nannoplankton Research 32, 3–51.

Bown, P. R., Newsam, C., 2017. Calcareous nannofossils from the Eocene North Atlantic Ocean (IODP Expedition 342 Sites U1403–U1411). Journal of Nannoplankton Research 37, 25–60.

Boyle, E. A., Keigwin, L. D., 1985. Comparison of Atlantic and Pacific paleochemical records for the last 215,000 years: changes in deep ocean circulation and chemical inventories. Earth and Planetary Science Letters 76, 135–150, https://doi.org/10.1016/0012-821X(85)90154-2.

Broccoli, A. J., Dahl, K. A., Stouffer, R. J., 2006. Response of the ITCZ to Northern Hemisphere cooling. Geophysical Research Letters 33, 1–4, https://doi.org/10.1029/2005GL024546.

Bru, K., Touzé, S., Parvaz, D. B., 2017. Development of an innovative process for the upcycling of concrete waste. Abstract no. 12, HISER conference, Delft, The Netherlands, 21–23 June 2017, ISBN/EAN: 978-94-6186-826-8, TU Delft Library.

Bru, K., Touzé, S., Auger, P., Dobrusky, S., Tierrie, J., Parvaz, D. B., 2018. Investigation of lab and pilot scale electric-pulse fragmentation systems for the recycling of ultra-high performance fibre-reinforced concrete. Minerals Engineering 128, 187–194, https://doi.org/10.1016/j.mineng.2018.08.040.

Bru, K., Sousa, R., Machado Leite, M., Broadbent, C., Stuart, G., Pashkevich, D., Martin, M., Kern, M., Parvaz, D. B., 2020. Pilot-scale investigation of two

Electric Pulse Fragmentation (EPF) approaches for the mineral processing of a low-grade cassiterite schist ore. Minerals Engineering 150(106270), https://doi.org/10.1016/j.mineng.2020.106270.

Cai, M., Xu, Z., Clift, P. D., Khim, B. K., Lim, D., Yu, Z., Kulhanek, D. K., Li, T., 2018. Long-term history of sediment inputs to the eastern Arabian Sea and its implications for the evolution of the Indian summer monsoon since 3.7 Ma. Geological Magazine, 1–12, https://doi.org/10.1017/S0016756818000857.

Campbell, S. M., Moucha, R., Derry, L. A., Raymo, M. E., 2018. Effects of Dynamic Topography on the Cenozoic Carbonate Compensation Depth. Geochemistry, Geophysics, Geosystems 19, 1025–1034, https://doi.org/10.1002/2017GC007386.

Carmichael, M. J., Lunt, D. J., Huber, M., Heinemann, M., Kiehl, J., LeGrande, A., Loptson, C. A., Roberts, C. D., Sagoo, N., Shields, C., Valdes, P. J., Winguth, A., Winguth, C., Pancost, R. D., 2016. A model-model and data-model comparison for the early Eocene hydrological cycle. Climate of the Past 12(2), 455–481, https://doi.org/10.5194/cp-12-455-2016.

Carmichael, M. J., Inglis, G. N., Badger, M. P. S., Naafs, B. D. A., Behrooz, L., Remmelzwaal, S., Monteiro, F. M., Rohrssen, M., Farnsworth, A., Buss, H. L., Dickson, A. J., Valdes, P. J., Lunt, D. J., Pancost, R. D., 2017. Hydrological and associated biogeochemical consequences of rapid global warming during the Paleocene–Eocene Thermal Maximum. Global and Planetary Change 157, 114–138, http://dx.doi.org/10.1016/j.gloplacha.2017.07.014.

Chakraborty, A., Nanjundiah, R. S., Srinivasan, J., 2009. Impact of African orography and the Indian summer monsoon on the low-level Somali jet. International Journal of Climatology 29, 983–992, https://doi.org/10.1002/joc.

Charisi, S. D., Schmitz, B., 1998. Paleocene to early Eocene paleoceanography of the Middle East: The $\delta^{13}C$ and $\delta^{18}O$ isotopes from foraminiferal calcite. Paleoceanography 13(1), 106–118.

Chen, H., Xu, Z., Clift, P. D., Lim, D., Khim, B. K., Yu, Z., 2019. Orbital-scale evolution of the Indian summer monsoon since 1.2 Ma: Evidence from clay mineral records at IODP Expedition 355 Site U1456 in the eastern Arabian Sea. Journal of Asian Earth Sciences 174, 11–22,

https://doi.org/10.1016/j.jseaes.2018.10.012.

Chen, H., Xu, Z., Lim, D., Clift, P. D., Chang, F., Li, T., Cai, M., Wang, W., Yu, Z., Sun, R., 2020. Geochemical Records of the Provenance and Silicate Weathering/Erosion From the Eastern Arabian Sea and Their Responses to the Indian Summer Monsoon Since the Mid-Pleistocene. Paleoceanography and Paleoclimatology 35, 1–18, https://doi.org/10.1029/2019PA003732.

Cherchi, A., Allesandri, A., Masina, S., Navarra, A., 2011. Effects of increased CO_2 levels on monsoons. Climate Dynamics 37, 83–101, https://doi.org/10.1007/s00382-010-0801-7.

Clemens, S. C., Prell, W. L., 1990. Late Pleistocene variability of Arabian Sea summer monsoon winds and continental aridity: Eolian records from the lithogenic component of deep-sea sediments. Paleoceanography 5(2), 109–145.

Clemens, S. C., Prell, W. L., 1991. One million year record of summer monsoon winds and continental aridity from the Owen Ridge (Site 722), Northwest Arabian Sea. Proceedings of the Ocean Drilling Program, Scientific Results 117, 365–388.

Clemens, S. C., Kuhnt, W., LeVay, L. J., Anand, P., Ando, T., Bartol, M., Bolton, C. T., Ding, X., Gariboldi, K., Giosan, L., Hathorne, E. C., Huang, Y., Jaiswal, P., Kim, S., Kirkpatrick, J. B., Littler, K., Marino, G., Martinez, P., Naik, D., Peketi, A., Phillips, S. C., Robinson, M. M., Romero, O. E., Sagar, N., Taladay, K. B., Taylor, S. N., Thirumalai, K., Uramoto, G., Usui, Y., Wang, J., Yamamoto, M., Zhou, L., 2016. Expedition 353 methods. In: Clemens, S. C., Kuhnt, W., LeVay, L. J., and the Expedition 353 Scientists (Eds.), Indian Monsoon Rainfall. Proceedings of the International Ocean Discovery Program, 353. College Station, TX (International Ocean Discovery Program).

Clift, P. D., Kroon, D., Gaedicke, C., Craig, J., 2002. Tectonic and climatic evolution of the Arabian Sea region: An introduction. Geological Society Special Publications 195, 1–5, https://doi.org/10.1144/GSL.SP.2002.195.01.01.

Clift, P. D., Hodges, K. V., Heslop, D., Hannigan, R., Van Long, H., Calves, G., 2008. Correlation of Himalayan exhumation rates and Asian monsoon intensity. Nature Geoscience 1, 875–880, https://doi.org/10.1038/ngeo351.

Clift, P. D., Vanlaningham, S., 2010. A climatic trigger for a major Oligo–Miocene unconformity in the Himalayan foreland basin. Tectonics 29, 1–18,

https://doi.org/10.1029/2010TC002711.

Clift, P. D., Webb, A. G., 2019. A history of the Asian monsoon and its interactions with solid Earth tectonics in Cenozoic South Asia. In: Treloar, P. J., Searle, M. P. (Eds.), Himalayan Tectonics: A Modern Synthesis, Geological Society, London, Special Publications 483, p. 631–652.

Clift, P. D., Kulhanek, D. K., Zhou, P., Bowen, M. G., Vincent, S. M., Lyle, M., Hahn, A., 2020. Chemical weathering and erosion responses to changing monsoon climate in the Late Miocene of Southwest Asia. Geological Magazine 157, 939–955, https://doi.org/10.1017/S0016756819000608.

Cohen, A. S., Coe, A. L., Kemp, D. B., 2007. The Late Palaeocene–Early Eocene and Toarcian (Early Jurassic) carbon isotope excursions: A comparison of their time scales, associated environmental changes, causes and consequences. Journal of the Geological Society, London 164, 1093–1108.

Collett, T. S., Riedel, M., Cochran, J. R., Boswell, R., Presley, J., Kumar, P., Sathe, A., Sethi, A., Lall, M., Sibal, V., and the NGHP Expedition 01 Scientists, 2008. National Gas Hydrate Program Expedition 01 Initial Reports. Directorate General of Hydrocarbons, New Delhi, p. 1–68.

Cope, J. T., Winguth, A., 2011. On the sensitivity of ocean circulation to arctic freshwater input during the Paleocene/Eocene Thermal Maximum. Palaeogeography, Palaeoclimatology, Palaeoecology 306, 82–94, doi:10.1016/j.palaeo.2011.03.032.

Corfield, R. M., 1994. Palaeocene oceans and climate: An isotopic perspective. Earth-Science Reviews 37, 225–252.

Costa de Moura, J., de Moraes Rios-Netto, A., Wanderley, M. D., Pereira de Sousa, F., 1999. Using acids to extract calcareous microfossils from carbonate rocks. Micropalaeontology 45(4), 429–436.

Cotton, L. J., 2012. Paleogene larger benthic foraminifera of Tanzania and the Eocene–Oligocene transition. PhD thesis, Cardiff University, UK, 162 pp.

Cotton, L. J., Wright, V. P., Barnett, A., Renema, W., 2019. Larger benthic foraminifera from the Panna and Mukta fields offshore India: Paleobiogeographic implications. Journal of Foraminiferal Research 49(3), 243–258.

Coxall, H. K., Wilson, P. A., Pälike, H., Lear, C. H., Backman, J., 2005. Rapid stepwise onset of Antarctic glaciation and deeper calcite compensation in the Pacific Ocean. Nature 433, 53–57, doi:10.1038/nature03135.

Coxall, H. K., Pearson, P., 2007. The Eocene–Oligocene Transition. In: Williams, M., Haywood, A. M., Gregory, F. J., Schmidt, D. N. (Eds.), Deep-Time Perspectives on Climate Change: Marrying the Signal from Computer Models and Biological Proxies. The Micropalaeontological Society, Special Publications. The Geological Society, London, p. 351–387.

Cramer, B. S., Wright, J. D., Kent, D. V., Aubry, M. P., 2003. Orbital climate forcing of $\delta^{13}C$ excursions in the late Paleocene–early Eocene (chrons C24n–C25n). Paleoceanography 18(4), 1–25, doi:10.1029/2003PA000909.

Cramwinckel, M. J., Huber, M., Kocken, I. J., Agnini, C., Bijl, P. K., Bohaty, S. M., Frieling, J., Goldner, A., Hilgen, F. J., Kip, E. L., Peterse, F., Ploeg, R. V. D., Röhl, U., Schouten, S., Sluijs, A., 2018. Synchronous tropical and polar temperature evolution in the Eocene. Nature Letters 559, 383–386, https://doi.org/10.1038/s41586-018-0272-2.

Cui, Y., Kump, L. R., Ridgwell, A. J., Diefendorf, A. F., Junium, C. K., 2010. A high-resolution record from Svalbard of carbon release during the Paleocene–Eocene Thermal Maximum. Journal of Earth Science Special Issue 21, 190.

Cui, Y., Kump, L. R., Ridgwell, A. J., Charles, A. J., Junium, C. K., Diefendorf, A. F., Freeman, K. H., Urban, N. M., Harding, I. C., 2011. Slow release of fossil carbon during the Palaeocene–Eocene Thermal Maximum. Nature Geoscience 4, 481–485, doi:10.1038/NGEO1179.

Dal Martello, E., Bernardis, S., Larsen, R. B., Tranell, G., Di Sabatino, M., Arnberg, L., 2012. Electrical fragmentation as a novel route for the refinement of quartz raw materials for trace mineral impurities. Powder Technology 224, 209–216.

Davis, C. V., Benitez-Nelson, C. R., 2020. Evidence for rapid trace element alteration of planktic foraminiferal shells from the Panama Basin: Manganese adsorption during vertical transport. Marine Micropaleontology 157, 101872, https://doi.org/10.1016/j.marmicro.2020.101872.

DeConto, R. M., Pollard, D., 2003. Rapid Cenozoic glaciation of Antarctica induced by declining atmospheric CO_2. Nature 421, 245–249.

DeConto, R. M., Galeotti, S., Pagani, M., Tracy, D., Schaefer, K., Zhang, T., Pollard, D., Beerling, D. J., 2012. Past extreme warming events linked to massive carbon release from thawing permafrost. Nature 484, 87–92, doi:10.1038/nature10929.

de la Vara, A., Meijer, P. T., Wortel, M. J. R., 2013. Model study of the circulation of the Miocene Mediterranean Sea and Paratethys: closure of the Indian Gateway. Climate of the Past Discussions 9, 4385–4424, https://doi.org/10.5194/cpd-9-4385-2013.

De Vleeschouwer, D., Vahlenkamp, M., Crucifix, M., Pälike, H., 2017. Alternating Southern and Northern Hemisphere climate response to astronomical forcing during the past 35 m.y. Geology 45(4), 375–378, https://doi.org/10.1130/G38663.1.

de Vleeschouwer, D., Drury, A. J., Vahlenkamp, M., Rochholz, F., Liebrand, D., Pälike, H., 2020. High-latitude biomes and rock weathering mediate climate-carbon cycle feedbacks on eccentricity timescales. Nature Communications 11(5013), 1–10, https://doi.org/10.1038/s41467-020-18733-w.

Dickens, G. R., Owen, R. M., 1994. Late Miocene–early Pliocene manganese redirection in the central Indian Ocean: Expansion of the intermediate water oxygen minimum zone. Paleoceanography 9(1), 169–181, https://doi.org/10.1029/93PA02699.

Dickens, G. R., Neil, J. R. O., Rea, D. K., Owen, R. M., 1995. Dissociation of oceanic methane hydrate as a cause of the carbon isotope excursion at the end of the Paleocene. Paleoceanography 10(6), 965–971.

Dickens, G. R., Castillo, M. M., Walker, J. C. G., 1997. A blast of gas in the latest Paleocene: Simulating first-order effects of massive dissociation of oceanic methane hydrate. Geology 25(3), 259–262.

Dickens, G. R., 2011. Down the Rabbit Hole: toward appropriate discussion of methane release from gas hydrate systems during the Paleocene–Eocene thermal maximum and other past hyperthermal events. Climate of the Past 7, 831–846, doi:10.5194/cp-7-831-2011.

Dickson, A. J., Cohen, A. S., Coe, A. L., Davies, M., Shcherbinina, E. A., Gavrilov, Y. O., 2015. Evidence for weathering and volcanism during the PETM from Arctic Ocean and Peri-Tethys osmium isotope records. Palaeogeography, Palaeoclimatology, Palaeoecology 438, 300–307, http://dx.doi.org/10.1016/j.palaeo.2015.08.019.

Dill, H. G., Wehner, H., Kus, J., Botz, R., Berner, Z., Stüben, D., Al-Sayigh, A., 2007. The Eocene Rusayl Formation, Oman, carbonaceous rocks in calcareous shelf sediments: Environment of deposition, alteration and hydrocarbon potential. International Journal of Coal Geology 72(2), 89–123,

doi:10.1016/j.coal.2006.12.012.

Dimri, A. P., Yasunari, T., Kotlia, B. S., Mohanty, U. C., & Sikka, D. R. (2016). Indian winter monsoon: Present and past. Earth-Science Reviews 163, 297–322, http://dx.doi.org/10.1016/j.earscirev.2016.10.008.

Ding, L., Spicer, R. A., Yang, J., Xu, Q., Cai, F., Li, S., Lai, Q., Wang, H., Spicer, T. E. V., Yue, Y., Shukla, A., Srivastava, G., Ali Khan, M., Bera, S., Mehrotra, R., 2017. Quantifying the rise of the Himalaya orogen and implications for the South Asian monsoon. Geology 45(3), 215–218, https://doi.org/10.1130/G38583.1.

D'Onofrio, R., Luciani, V., 2020. Do different extraction techniques impact planktic foraminiferal assemblages? An early Eocene case study. Marine Micropalaeontology 155, https://doi.org/10.1016/j.marmicro.2019.101795.

Dunkley Jones, T., Lunt, D. J., Schmidt, D. N., Ridgwell, A., Sluijs, A., Valdes, P. J., Maslin, M., 2013. Climate model and proxy data constraints on ocean warming across the Paleocene–Eocene Thermal Maximum. Earth Science Reviews 125, 123–145, http://dx.doi.org/10.1016/j.earscirev.2013.07.004.

Drury, A. J., Liebrand, D., Westerhold, T., Beddow, H. M., Hodell, D. A., Wilkens, R. H., Lyle, M., Bell, D. B., Kroon, D., Pälike, H., Lourens, L. J., 2020. Climate, cryosphere and carbon cycle controls on Southeast Atlantic orbital-scale carbonate deposition since the Oligocene (30–0 Ma). Climate of the Past Discussions [preprint], in review, 1–35, https://doi.org/doi.org/10.5194/cp-2020-108.

Dupuis, C., Aubry, M., Steurbaut, E., Berggren, W. A., Ouda, K., Magioncalda, R., Cramer, B. S., Kent, D. V., Speijer, R. P., Heilmann-Clausen, C., 2003. The Dababiya Quarry Section: Lithostratigraphy, clay mineralogy, geochemistry and paleontology. Micropaleontology 49(1), 41–59.

Ebinger, C. J., Sleep, N. H., 1998. Cenozoic magmatism throughout east Africa resulting from impact of a single plume. Nature 395, 788–791.

Edgar, K. M., Pälike, H., Wilson, P. A., 2013. Testing the impact of diagenesis on the $\delta^{18}O$ and $\delta^{13}C$ of benthic foraminiferal calcite from a sediment burial depth transect in the equatorial Pacific. Paleoceanography 28, 468–480, https://doi.org/10.1002/palo.20045.

Egger, L. M., Bahr, A., Friedrich, O., Wilson, P. A., Norris, R. D., van Peer, T. E., Lippert, P. C., Liebrand, D., Pross, J., 2018. Sea-level and surface-water change in the western North Atlantic across the Oligocene–Miocene

Transition: A palynological perspective from IODP Site U1406 (Newfoundland margin). Marine Micropaleontology 139, 57–71, https://doi.org/10.1016/j.marmicro.2017.11.003.

Elderfield, H., Ganssen, G., 2000. Past temperature and $\delta^{18}O$ of surface ocean waters inferred from foraminiferal Mg/Ca ratios. Nature 405, 442–445, https://doi.org/10.1038/35013033.

Eldholm, O., Thomas, E., 1993. Environmental impact of volcanic margin formation. Earth and Planetary Science Letters 117(3–4), 319–329.

Evans, D., Wade, B. S., Henehan, M., Erez, J., Müller, W., 2016a. Revisiting carbonate chemistry controls on planktic foraminifera Mg/Ca: implications for sea surface temperature and hydrology shifts over the Paleocene–Eocene Thermal Maximum and Eocene–Oligocene transition. Climate of the Past 12, 819–835, https://doi.org/10.5194/cp-12-819-2016.

Evans, D., Brierley, C., Raymo, M. E., Erez, J., Müller, W., 2016b. Planktic foraminifera shell chemistry response to seawater chemistry: Pliocene–Pleistocene seawater Mg/Ca, temperature and sea level change. Earth and Planetary Science Letters 438, 139–148, https://doi.org/10.1016/j.epsl.2016.01.013.

Evans, D., Sagoo, N., Renema, W., Cotton, L. J., Müller, W., Todd, J. A., Saraswati, P. K., Stassen, P., Ziegler, M., Pearson, P. N., Valdes, P. J., Affek, H. P., 2018. Eocene greenhouse climate revealed by coupled clumped isotope-Mg/Ca thermometry. Proceedings of the National Academy of Sciences of the United States of America 115(6), 1174–1179, https://doi.org/10.1073/pnas.1714744115.

Fabricius, K. E., Langdon, C., Humphrey, C., Noonan, S., Muehllehner, N., Fabricius, K. E., De'ath, G., Glas, M. S., Okazaki, R., Uthicke, S., Lough, J. M., 2011. Losers and winners in coral reefs acclimatized to elevated carbon dioxide concentrations. Nature Climate Change 1(3), 165–169.

Falzoni, F., Petrizzo, M. R., Jenkyns, H. C., Gale, A. S., Tsikos, H., 2016. Planktic foraminiferal biostratigraphy and assemblage composition across the Cenomanian–Turonian boundary interval at Clot Chevalier (Vocontian Basin, SE France). Cretaceous Research 59, 69–97, https://doi.org/10.1016/j.cretres.2015.10.028.

Faris, M., Abdelghany, O., Zahran, E., 2014. Upper Maastrichian to Lutetian nannofossil biostratigraphy, United Arab Emirates, west of the Northern

Oman Mountains. Journal of African Earth Sciences 93, 42–56.

Farnsworth, A., Lunt, D. J., Robinson, S. A., Valdes, P. J., Roberts, W. H. G., Clift, P. D., Markwick, P., Su, T., Wrobel, N., Bragg, F., Kelland, S. -J., Pancost, R. D., 2019. Past East Asian monsoon evolution controlled by paleogeography, not CO_2. Science Advances 5(10), 1–14, https://doi.org/10.1126/sciadv.aax1697.

Findlater, J., 1969. A major low-level air current near the Indian Ocean during the northern summer. Quarterly Journal of the Royal Meteorological Society 95, 362–380.

Flores, J. A., Johnson, J. E., Mejía-Molina, A. E., Álvarez, M. C., Sierro, F. J., Singh, S. D., Mahanti, S., Giosan, L., 2014. Sedimentation rates from calcareous nannofossil and planktonic foraminifera biostratigraphy in the Andaman Sea, northern Bay of Bengal, and eastern Arabian Sea. Marine and Petroleum Geology 58, 425–437, https://doi.org/10.1016/j.marpetgeo.2014.08.011.

Fluteau, F., Ramstein, G., Besse, J., 1999. Simulating the evolution of the Asian and African monsoons during the past 30 Myr using an atmospheric general circulation model. Journal of Geophysical Research 104(10), 11995–12018.

Fraass, A. J., Leckie, M. R., Lowery, C. M., Deconto, R., 2019. Precision in biostratigraphy: Evidence for a temporary flow reversal in the Central American Seaway during or after the Oligocene–Miocene transition. Journal of Foraminiferal Research 49(4), 357–366, https://doi.org/10.2113/gsjfr.49.4.357.

Frank, M., 2002. Radiogenic isotopes: Tracers of past ocean circulation and erosional input. Reviews of Geophysics 40(1), 1–38, doi:10.1029/2000RG000094.

Frieling, J., Svenson, H. H., Planke, S., Cramwinckel, M. J., Selnes, H., Sluijs, A., 2016. Thermogenic methane release as a cause for the long duration of the PETM. Proceedings of the National Academy of Sciences 113(43), 12059–12064, doi:10.1073/pnas.1603348113.

Frieling, J., Gebhardt, H., Huber, M., Adekeye, O. A., Akande, S. O., Reichart, G., Middelburg, J. J., Schouten, S., Sluijs, A., 2017. Extreme warmth and heat-stressed plankton in the tropics during the Paleocene–Eocene Thermal Maximum. Science Advances 3(e1600891), 1–9.

Frieling, J., Peterse, F., Lunt, D. J., Bohaty, S. M., Sinninghe Damsté, J. S., Reichart, G. -J., Sluijs, A., 2019. Widespread warming before and elevated barium during the Paleocene–Eocene thermal maximum: Evidence for methane hydrate release? Paleoceanography and Paleoclimatology 34, 546–566, https://doi.org/10.1029/2018PA003425.

Galeotti, S., Krishnan, S., Pagani, M., Lanci, L., Gaudio, A., Zachos, J. C., Monechi, S., Morelli, G., Lourens, L. J., 2010. Orbital chronology of Early Eocene hyperthermals from the Contessa Road section, central Italy. Earth and Planetary Science Letters 290, 192–200, doi:10.1016/j.epsl.2009.12.021.

Giraldo Gómez, V. M., Linnert, C., Podlaha, O. G., Mutterlose, J., 2016. Response of calcareous nannofossils to the Paleocene–Eocene thermal maximum from a shelf section in Jordan. Marine Micropaleontology 127, 11–25, http://dx.doi.org/10.1016/j.marmicro.2016.07.003.

Giraldo Gómez, V. M., Beik, I., Podlaha, O. G., Mutterlose, J., 2017. The micropaleontological record of marine early Eocene oil shales from Jordan. Palaeogeography, Palaeoclimatology, Palaeoecology 485, 723–739, http://dx.doi.org/10.1016/j.palaeo.2017.07.030.

Giraldo-Gomez, V. M., Mutterlose, J., Podlaha, O. G., Speijer, R. P., Stassen, P., 2018. Benthic foraminifera and geochemistry across the Paleocene–Eocene Thermal Maximum interval in Jordan. Journal of Foraminiferal Research 48(2), 100–120.

Giusberti, L., Rio, D., Agnini, C., Backman, J., Fornaciari, E., Tateo, F., Oddone, M., 2007. Mode and tempo of the Paleocene–Eocene thermal maximum in an expanded section from the Venetian pre-Alps. GSA Bulletin 119(3–4), 391–412, doi:10.1130/B25994.1.

Goldstein, S. L., O'Nions, R. K., Hamilton, P. J., 1984. A Sm-Nd isotopic study of atmospheric dusts and particulates from major river systems. Earth and Planetary Science Letters 70, 221–236.

Gradstein, F. M., Ogg, J. G., Hilgen, F. J., 2012. On the geologic time scale. Newsletters on Stratigraphy 45(2), 171–188, https://doi.org/10.1127/0078-0421/2012/0020.

Gray, W. R., Evans, D., 2019. Nonthermal Influences on Mg/Ca in Planktonic Foraminifera: A Review of Culture Studies and Application to the Last Glacial Maximum. Paleoceanography and Paleoclimatology 34, 306–315,

https://doi.org/10.1029/2018PA003517.

Greenop, R., Hain, M. P., Sosdian, S. M., Oliver, K. I. C., Goodwin, P., Chalk, T. B., Lear, C. H., Wilson, P. A., Foster, G. L., 2017. A record of Neogene seawater $\delta^{11}B$ reconstructed from paired $\delta^{11}B$ analyses on benthic and planktic foraminifera. Climate of the Past 13, 149–170, https://doi.org/10.5194/cp-13-149-2017.

Greenop, R., Sosdian, S. M., Henehan, M. J., Wilson, P. A., Lear, C. H., Foster, G. L., 2019. Orbital forcing, ice volume, and CO_2 across the Oligocene–Miocene transition. Paleoceanography and Paleoclimatology 34, 316–328, https://doi.org/10.1029/2018PA003420.

Grein, M., Oehm, C., Konrad, W., Utescher, T., Kunzmann, L., Roth-Nebelsick, A., 2013. Atmospheric CO_2 from the late Oligocene to early Miocene based on photosynthesis data and fossil leaf characteristics. Palaoegeography, Palaeoclimatology, Palaeoecology 374, 41–51, http://dx.doi.org/10.1016/j.palaeo.2012.12.025.

Gu, S., Liu, Z., Zhang, J., Rempfer, J., Joos, F., Oppo, D. W., 2017. Coherent response of Antarctic Intermediate Water and Atlantic Meridional Overturning Circulation during the last deglaciation: reconciling contrasting neodymium isotope reconstructions from the tropical Atlantic. Paleoceanography 32, 1036–1053, https://doi.org/10.1002/2017PA003092.

Guitián, J., Phelps, S., Polissar, P. J., Ausín, B., Eglinton, T. I., Stoll, H. M., 2019. Midlatitude temperature variations in the Oligocene to early Miocene. Paleoceanography and Paleoclimatology 34, 1328–1343, https://doi.org/10.1029/2019PA003638.

Guo, Z. T., Ruddiman, W. F., Hao, Q. Z., Wu, H. B., Qiao, Y. S., Zhu, R. X., Peng, S. Z., Wei, J. J., Yuan, B. Y., Liu, T. S., 2002. Onset of Asian desertification by 22 Myr ago inferred from loess deposits in China. Nature 416, 159–163, https://doi.org/10.1038/416159a.

Guo, Z. T., Sun, B., Zhang, Z. S., Peng, S. Z., Xiao, G. Q., Ge, J. Y., Hao, Q. Z., Liang, M. Y., Liu, J. F., Yin, Q. Z., Wei, J. J., 2008. A major reorganization of Asian climate by the early Miocene. Climate of the Past 4, 153–174, https://doi.org/10.5194/cp-4-153-2008.

Gupta, A. K., Yuvaraja, A., Prakasam, M., Clemens, S. C., Velu, A., 2015. Evolution of the South Asian monsoon wind system since the late Middle Miocene. Palaeogeography, Palaeoclimatology, Palaeoecology 438, 160–

167, https://doi.org/10.1016/j.palaeo.2015.08.006.

Gupta, A. K., Prakasam, M., Dutt, S., Clift, P. D., Yadav, R. R., 2020. Evolution and Development of the Indian Monsoon. In: Gupta, N., Tandon, S. K. (Eds.), Geodynamics of the Indian Plate, p. 499–535, https://doi.org/10.1007/978-3-030-15989-4_14.

Gutjahr, M., Ridgwell, A., Sexton, P. F., Anagnostou, E., Pearson, P. N., Pälike, H., Norris, R. D., Thomas, E., Foster, G. L., 2017. Very large release of mostly volcanic carbon during the Paleocene–Eocene Thermal Maximum. Nature 548(7669), 573–577, doi:10.1038/nature23646.

Hallock, P., 1984. Distribution of selected species of living algal symbiont-bearing foraminifera on two Pacific coral reefs. The Journal of Foraminiferal Research 14(4), 250–261.

Hallock, P., Glenn, E. C., 1986. Larger foraminifera: A tool for paleoenvironmental analysis of Cenozoic carbonate depositional facies. Palaios 1, 55–64.

Hamon, N., Sepulchre, P., Lefebvre, V., Ramstein, G., 2013. The role of eastern Tethys seaway closure in the Middle Miocene Climatic Transition (ca. 14 Ma). Climate of the Past 9, 2687–2702, https://doi.org/10.5194/cp-9-2687-2013.

Haq, B. U., Al-Qahtani, A. M., 2005. Phanerozoic cycles of sea-level change on the Arabian Platform. GeoArabia 10(2), 127–160.

Hauptvogel, D. W., Pekar, S. F., Pincay, V., 2017. Evidence for a heavily glaciated Antarctica during the late Oligocene “warming” (27.8–24.5 Ma): Stable isotope records from ODP Site 690. Paleoceanography 32, 384–396, doi:10.1002/2016PA002972.

Haynes, J. R., 1965. Symbiosis, wall structure and habitat in foraminifera. Cushman Foundation, Foraminiferal Research Contribution 16, 40–43.

Hesselbo, S. P., 1996. Spectral gamma-ray logs in relation to clay mineralogy and sequence stratigraphy, Cenozoic of the Atlantic margin, offshore New Jersey. In: Mountain, G. S., Miller, K. G., Blum, P., Twitchell, D. (Eds.), Proceedings of the Ocean Drilling Program, Scientific Results, 150, New Jersey continental slope and rise, p. 411–422.

Hikami, M., Ushie, H., Irie, T., Fujita, K., Kuroyanagi, A., Sakai, K., Nojiri, Y., Suzuki, A., Kawahata, H., 2011. Contrasting calcification responses to ocean acidification between two reef foraminifers harboring different algal symbionts. Geophysical Research Letters 38(19), 1–5,

doi:10.1029/2011GL048501.

Hinnov, L. A., 2004. Earth's orbital parameters and cycle stratigraphy. In: Gradstein, F. M., Ogg, J. G., Smith, A. G. (Eds), A Geologic Timescale 2004. Cambridge University Press, Cambridge, p. 55–62.

Hodgkinson, R. L., 1991. Microfossil processing: A damage report. Micropalaeontology 37(3), 320–326.

Hollis, C. J., Dickens, G. R., Field, B. D., Jones, C. M., Percy Strong, C., 2005. The Paleocene–Eocene transition at Mead Stream, New Zealand: A southern Pacific record of early Cenozoic global change. Palaeogeography, Palaeoclimatology, Palaeoecology 215, 313–343, doi:10.1016/j.palaeo.2004.09.011.

Horita, J., Zimmermann, H., Holland, H. D., 2002. Chemical evolution of seawater during the Phanerozoic: Implications from the record of marine evaporites. Geochimica et Cosmochimica Acta 66(21), 3733–3756, https://doi.org/10.1016/S0016-7037(01)00884-5.

Hottinger, L., 1983. Processes determining the distribution of larger foraminifera in space and time. In: Meulenkamp, J. E. (Ed.), Reconstruction of Marine Paleoenvironments (Vol. 30), Utrecht, p. 239–254.

Hottinger, L., 1998. Shallow benthic foraminifera at the Paleocene–Eocene boundary. Strata 9, 61–64.

Hottinger, L., 2009. The Paleocene and earliest Eocene foraminiferal Family Miscellaneidae: Neither nummulitids nor rotaliids. Notebooks on Geology 6, 1–41.

Hottinger, L., 2014. Paleogene larger Rotaliid Foraminifera from the western and central Neotethys. Springer, Switzerland, 195 p, doi:10.1007/978-3-319-02853-8.

Huber, M., & Goldner, A. (2012). Eocene monsoons. Journal of Asian Earth Sciences 44, 3–23, doi: 10.1016/j.jseaes.2011.09.014.

Huck, C. E., van de Flierdt, T., Jiménez-Espejo, F. J., Bohaty, S. M., Röhl, U., Hammond, S. J., 2016. Robustness of fossil fish teeth for seawater neodymium isotope reconstructions under variable redox conditions in an ancient shallow marine setting. Geochemistry, Geophysics, Geosystems 17, 679–698, doi:10.1002/2015GC006218.

Hutchinson, D. K., Coxall, H. K., Lunt, D. J., Steinthorsdottir, M., de Boer, A. M., Baatsen, M., von der Heydt, A., Huber, M., Kennedy-Asser, A. T.,

Kunzmann, L., Ladant, J. -B., Lear, C. H., Moraweck, K., Pearson, P. N., Piga, E., Pound, M. J., Salzmann, U., Scher, H. D., Sijp, W. P., Śliwińska, K. K., Wilson, P. A., Zhang, Z., 2021. The Eocene–Oligocene transition: a review of marine and terrestrial proxy data, models and model-data comparisons. Climate of the Past 17, 269–315, https://doi.org/10.5194/cp-17-269-2021.

Hyeong, K., Lee, J., Seo, I., Lee, M. J., Yoo, C. M., Khim, B. K., 2014. Southward shift of the Intertropical Convergence Zone due to Northern Hemisphere cooling at the Oligocene–Miocene boundary. Geology 42(8), 667–670, https://doi.org/10.1130/G35664.1.

Ilani, S., Harlavan, Y., Tarawneh, K., Rabba, I., Weinberger, R., Ibrahim, K., Peltz, S., Steinitz, G., 2001. New K-Ar ages of basalts from the Harrat Ash Shaam volcanic field in Jordan: Implications for the span and duration of the upper-mantle upwelling beneath the western Arabian plate. Geology 29(2), 171–174.

Jacobsen, S. B., Wasserburg, G. J., 1980. Sm-Nd isotopic evolution of chondrites. Earth and Planetary Science Letters 50, 139–155.

Jarachowska, E., Tonarová, P., Minnecke, A., Ferrová, L., Sklenář, J., Vodrážková, S., 2013. An acid-free method of microfossil extraction from clay-rich lithologies using the surfactant Rewoquat. Palaeontologica Electronica 16(3), 1–16.

Jean, A., Beauvais, A., Chardon, D., Arnaud, N., Jayananda, M., Mathe, P. E., 2020. Weathering history and landscape evolution of Western Ghats (India) from $^{40}Ar/^{39}Ar$ dating of supergene K–Mn oxides. Journal of the Geological Society, London 177, 523–536, https://doi.org/10.1144/jgs2019-048.

Jeandel, C., Arsouze, T., Lacan, F., Techine, P., Dutay, J. C., 2007. Isotopic Nd compositions and concentrations of the lithogenic inputs into the ocean: a compilation, with an emphasis on the margins. Chemical Geology 239, 156–164, doi:10.1016/j.chemgeo.2006.11.013.

Jeandel, C., 2016. Overview of the mechanisms that could explain the ‘Boundary Exchange’ at the land-ocean contact. Philosophical Transaction of the Royal Society A 374, 1–13, http://dx.doi.org/10.1098/rsta.2015.0287.

Jewell, A. M., Drake, N., Crocker, A. J., Bakker, N. L., Kunkelova, T., Bristow, C. S., Cooper, M. J., Milton, J. A., Breeze, P. S., Wilson, P. A., 2021. Three North African dust source areas and their geochemical fingerprint. Earth and

Planetary Science Letters 554, 1–12, https://doi.org/10.1016/j.epsl.2020.116645.

Jiang, D., Ding, Z., Drange, H., Gao, Y., 2008. Sensitivity of East Asian climate to the progressive uplift and expansion of the Tibetan Plateau under the mid-Pliocene boundary conditions. Advances in Atmospheric Sciences 25(5), 709–722, https://doi.org/10.1007/s00376-008-0709-x.

Johnson, J. E., Phillips, S. C., Torres, M. E., Piñero, E., Rose, K. K., Giosan, L., 2014. Influence of total organic carbon deposition on the inventory of gas hydrate in the Indian continental margins. Marine and Petroleum Geology 58, 406–424, https://doi.org/10.1016/j.marpetgeo.2014.08.021.

Jovane, L., Florindo, F., Coccioni, R., Dinarès-Turell, J., Marsili, A., Monechi, S., Roberts, A. P., Sprovieri, M., 2007. The middle Eocene climatic optimum event in the Contessa Highway section, Umbrian Apennines, Italy. GSA Bulletin 119(3–4), 413–427, https://doi.org/10.1130/B25917.1.

Jung, S. J. A., Kroon, D., Ganssen, G., Peeters, F., Ganeshram, R., 2009. Enhanced Arabian Sea intermediate water flow during glacial North Atlantic cold phases. Earth and Planetary Science Letters 280, 220–228, https://doi.org/10.1016/j.epsl.2009.01.037.

Keen, M. C., Racey, A., 1991. Lower Eocene ostracods from the Rusayl Shale Formation of Oman. Journal of Micropalaeontology 10(2), 227–233.

Keigwin, L. D., Corliss, B. H., 1986. Stable isotopes in late middle Eocene to Oligocene foraminifera. Geological Society of America Bulletin 97, 335–345, https://doi.org/10.1130/0016-7606(1986)97<335:SIILME>2.0.CO;2.

Kender, S., Bogus, K. A., Cobb, T. D., Thomas, D. J., 2018. Neodymium evidence for increased circumpolar deep water flow to the North Pacific during the Middle Miocene Climate Transition. Paleoceanography and Paleoclimatology 33, 672–682, https://doi.org/10.1029/2017PA003309.

Kennedy, A. E., Coe, A. L., 2014. Development of the freeze-thaw processing technique for disaggregation of indurated mudrocks and enhanced recovery of calcareous microfossils. Journal of Micropalaeontology 33, 193–203, http://dx.doi.org/10.1144/jmpaleo2013-020.

Kennett, J. P., Stott, L. D., 1991. Abrupt deep-sea warming, paleoceanographic changes and benthic extinctions at the end of the Palaeocene. Nature 353, 225–228.

Khozyem, H., Adatte, T., Spangenberg, J. E., Keller, G., Tantawy, A. A., Ulianov,

A., 2015. New geochemical constraints on the Paleocene–Eocene thermal maximum: Dababiya GSSP, Egypt. Palaeogeography, Palaeoclimatology, Palaeoecology 429, 117–135, http://dx.doi.org/10.1016/j.palaeo.2015.04.003.

Kim, J. E., Khim, B. K., Ikehara, M., Lee, J., 2018. Orbital-scale denitrification changes in the Eastern Arabian Sea during the last 800 kyrs. Scientific Reports 8, 1–8, https://doi.org/10.1038/s41598-018-25415-7.

Kitoh, A., Endo, H., Kumar, K. K., Cavalcanti, I. F. A., Goswami, P., Zhou, T., 2013. Monsoons in a changing world: A regional perspective in a global context. Journal of Geophysical Research: Atmospheres 118, 3053–3065, https://doi.org/10.1002/jgrd.50258.

Knauth, L. P., Kennedy, M. J., 2009. The late Precambrian greening of the Earth. Nature Letters 460, 728–732, doi:10.1038/nature08213.

Koch, P. L., Zachos, J. C., Gingerich, P. D., 1992. Correlation between isotope records in marine and continental reservoirs near the Paleocene/Eocene boundary. Nature 358, 319–322.

Komar, N., Zeebe, R. E., Dickens, G. R., 2013. Understanding long-term carbon cycle trends: The late Paleocene through the early Eocene. Paleoceanography 28, 650–662, doi:10.1002/palo.20060.

Komar, N., Zeebe, R. E., 2021. Reconciling atmospheric CO_2, weathering, and calcite compensation depth across the Cenozoic. Science Advances 7, 1–7, doi:10.1126/sciadv.abd4876.

Kopp, R. E., Schumann, D., Raub, T. D., Powars, D. S., Godfrey, L. V., Swanson-Hysell, N. L., Maloof, A. C., Vali, H., 2009. An Appalachian Amazon? Magnetofossil evidence for the development of a tropical river-like system in the mid-Atlantic United States during the Paleocene-Eocene Thermal Maximum. Paleoceanography 24, 1–11, doi:10.1029/2009PA001783.

Kotov, S., Pälike, H., 2018. QAnalyseries – a cross-platform time series tuning and analysis tool. American Geophysical Union, Fall Meeting, Washington D.C., USA.

Kutzbach, J. E., Prell, W. L., Ruddiman, W. F., 1993. Sensitivity of Eurasian climate to surface uplift of the Tibetan Plateau. The Journal of Geology 101(2), 177–190.

Lacan, F., Jeandel, C., 2005. Neodymium isotopes as a new tool for quantifying exchange fluxes at the continent–ocean interface. Earth and Planetary Science Letters 232, 245–257, doi:10.1016/j.epsl.2005.01.004.

Lacan, F., Tachikawa, K., Jeandel, C., 2012. Neodymium isotopic composition of the oceans: A compilation of seawater data. Chemical Geology 300–301, 177–184, https://doi.org/10.1016/j.chemgeo.2012.01.019.

Lachkar, Z., Lévy, M., Smith, S., 2018. Intensification and deepening of the Arabian Sea oxygen minimum zone in response to increase in Indian monsoon wind intensity. Biogeosciences 15, 159–186, https://doi.org/10.5194/bg-15-159-2018.

Langer, M. R., 2008. Assessing the Contribution of Foraminiferan Protists to Global Ocean Carbonate Production. Journal of Eukaryotic Microbiology 55(3), 163–169, doi:10.1111/j.1550-7408.2008.00321.x.

Laskar, J., Joutel, F., Boudin, F., 1993. Orbital, precessional, and insolation quantities for the Earth from -20 Myr to +10 Myr. Astronomy and Astrophysics 270, 522–533.

Laskar, J., Robutel, P., Joutel, F., Gastineau, M., Correia, A. C. M., Levrard, B., 2004. A long-term numerical solution for the insolation quantities of the Earth. Astronomy and Astrophysics 428, 261–285, doi: 10.1051/0004-6361:20041335.

Laskar, J., Fienga, A., Gastineau, M., Manche, H., 2011. La2010: a new orbital solution for the long-term motion of the Earth. Astronomy and Astrophysics 532, 1–15, doi:10.1051/0004-6361/201116836.

Lauretano, V., Littler, K., Polling, M., Zachos, J. C., Lourens, L. J., 2015. Frequency, magnitude and character of hyperthermal events at the onset of the Early Eocene Climatic Optimum. Climate of the Past 11, 1313–1324, doi:10.5194/cp-11-1313-2015.

Lauretano, V., Hilgen, F. J., Zachos, J. C., Lourens, L. J., 2016. Astronomically tuned age model for the early Eocene carbon isotope events: A new high-resolution $\delta^{13}C$ benthic record of ODP Site 1263 between ~49 and ~54 Ma. Newsletters on Stratigraphy 49, 383–400, doi:10.1127/nos/2016/0077.

Lear, C. H., Elderfield, H., Wilson, P. A., 2000. Cenozoic deep-sea temperatures and global ice volumes from Mg/Ca in benthic foraminiferal calcite. Science 287, 269–272, https://doi.org/10.1126/science.287.5451.269.

Lear, C. H., Rosenthal, Y., Coxall, H. K., Wilson, P. A., 2004. Late Eocene to early Miocene ice sheet dynamics and the global carbon cycle. Paleoceanography 19(PA4015), doi:10.1029/2004PA01039.

Lear, C. H., Bailey, T. R., Pearson, P. N., Coxall, H. K., Rosenthal, Y., 2008. Cooling and ice growth across the Eocene–Oligocene transition. Geology 36(3), 251–254, https://doi.org/10.1130/G24584A.1.

Lee, J., Kim, S., Khim, B. K., 2020a. A paleoproductivity shift in the northwestern Bay of Bengal (IODP Site U1445) across the Mid-Pleistocene transition in response to weakening of the Indian summer monsoon. Palaeogeography, Palaeoclimatology, Palaeoecology 560, 110018, https://doi.org/10.1016/j.palaeo.2020.110018.

Lee, H., Jo, K. -n., Hyun, S., 2020b. Opposite response modes of NADW dynamics to obliquity forcing during the late Paleogene. Scientific Reports 10, 1–8, https://doi.org/10.1038/s41598-020-70020-2.

Licht, A., Dupont-Nivet, G., Pullen, A., Kapp, P., Abels, H. A., Lai, Z., Guo, Z., Abell, J., Giesler, D., 2016. Resilience of the Asian atmospheric circulation shown by Paleogene dust provenance. Nature Communications 7(12390), 1–6, https://doi.org/10.1038/ncomms12390.

Licht, A., Van Cappelle, M., Abels, H. A., Ladant, J. B., Trabucho-Alexandre, J., France-Lanord, C., Donnadieu, Y., Vandenberghe, J., Rigaudier, T., Lécuyer, C., Terry Jr, D., Adriaens, R., Boura, A., Guo, Z., Soe, A. N., Quade, J., Dupont-Nivet, G., Jaeger, J. -J., 2014. Asian monsoons in a late Eocene greenhouse world. Nature 513, 501–506, https://doi.org/10.1038/nature13704.

Liebrand, D., Lourens, L. J., Hodell, D. A., de Boer, B., van de Wal, R. S. W., Pälike, H., 2011. Antarctic ice sheet and oceanographic response to eccentricity forcing during the early Miocene. Climate of the Past 7, 869–880, doi:10.5194/cp-7-869-2011.

Liebrand, D., Beddow, H. M., Lourens, L. J., Pälike, H., Raffi, I., Bohaty, S. M., Hilgen, F. J., Saes, M. J. M., Wilson, P. A., van Dijk, A. E., Hodell, D. A., Kroon, D., Huck, C. E., Batenburg, S. J., 2016. Cyclostratigraphy and eccentricity tuning of the early Oligocene through early Miocene (30.1–17.1 Ma): *Cibicides mundulus* stable oxygen and carbon isotope records from Walvis Ridge Site 1264. Earth and Planetary Science Letters 450, 392–405, https://doi.org/10.1016/j.epsl.2016.06.007.

Liebrand, D., de Bakker, A. T. M., Beddow, H. M., Wilson, P. A., Bohaty, S. M., Ruessink, G., Pälike, H., Batenburg, S. J., Hilgen, F. J., Hodell, D. A., Huck, C. E., Kroon, D., Raffi, I., Saes, M. J. M., van Dijk, A. E., Lourens, L. J., 2017. Evolution of the early Antarctic ice ages. Proceedings of the National Academy of Sciences 114(15), 3867–3872, doi/10.1073/pnas.1615440114.

Limmer, D. R., Köhler, C. M., Hillier, S., Moreton, S. G., Tabrez, A. R., Clift, P. D., 2012. Chemical weathering and provenance evolution of Holocene–Recent sediments from the Western Indus Shelf, Northern Arabian Sea inferred from physical and mineralogical properties. Marine Geology 326–328, 101–115, https://doi.org/10.1016/j.margeo.2012.07.009.

Lirer, F., 2000. A new technique for retrieving calcareous microfossils from lithified lime deposits. Micropaleontology 46(4), 365–369.

Littler, K., Röhl, U., Westerhold, T., Zachos, J. C., 2014. A high-resolution benthic stable-isotope record for the South Atlantic: Implications for orbital-scale changes in late Paleocene–early Eocene climate and carbon cycling. Earth and Planetary Science Letters 401, 18–30, http://dx.doi.org/10.1016/j.epsl.2014.05.054.

Liu, Z., He, Y., Jiang, Y., Wang, H., Liu, W., Bohaty, S. M., Wilson, P. A., 2018. Transient temperature asymmetry between hemispheres in the Palaeogene Atlantic Ocean. Nature Geoscience 11, 656–660, https://doi.org/10.1038/s41561-018-0182-9.

Lombard, F., da Rocha, R. E., Bijma, J., Gattuso, J. -P., 2010. Effect of carbonate ion concentration and irradiance on calcification in planktonic foraminifera. Biogeosciences 7, 247–255, https://doi.org/10.5194/bg-7-247-2010.

Londoño, L., Royer, D. L., Jaramillo, C., Escobar, J., Foster, D. A., Cárdenas-Rozo, A. L., Wood, A., 2018. Early Miocene CO_2 estimates from a Neotropical fossil leaf assemblage exceed 400 ppm. American Journal of Botany 105(11), 1929–1937, https://doi.org/10.1002/ajb2.1187.

Lourens, L. J., Sluijs, A., Kroon, D., Zachos, J. C., Thomas, E., Röhl, U., Bowles, J., Raffi, I., 2005. Astronomical pacing of late Palaeocene to early Eocene global warming events. Nature 435, 1083–1087, doi:10.1038/nature03814.

Lu, H. Y., Guo, Z. T., 2014. Evolution of the monsoon and dry climate in East Asia during late Cenozoic: A review. Science China Earth Sciences 57(1), 70–79, https://doi.org/10.1007/s11430-013-4790-3.

Lunt, D. J., Valdes, P. A., Dunkley Jones, T., Ridgwell, A., Haywood, A. M., Schmidt, D. N., Marsh, R., Maslin, M., 2010. CO_2-driven ocean circulation changes as an amplifier of Paleocene–Eocene thermal maximum hydrate destabilization. Geology 38(10), 875–878, doi:10.1130/G31184.1.

Martin, E. E., Haley, B. A., 2000. Fossil fish teeth as proxies for seawater Sr and Nd isotopes. Geochimica et Cosmochimica Acta 64(5), 835–847.

Martin, E. E., Scher, H. D., 2004. Preservation of seawater Sr and Nd isotopes in fossil fish teeth: bad news and good news. Earth and Planetary Science Letters 220, 25–39, doi:10.1016/S0012-821X(04)00030-5.

Martin, E. E., Blair, S. W., Kamenov, G. D., Scher, H. D., Bourbon, E., Basak, C., Newkirk, D. N., 2010. Extraction of Nd isotopes from bulk deep sea sediments for paleoceanographic studies on Cenozoic time scales. Chemical Geology 269, 414–431, doi:10.1016/j.chemgeo.2009.10.016.

Martini, E., 1971. Standard Tertiary and Quaternary calcareous nannoplankton zonation. In: Farinacci, A. (Ed.), Proceedings of the 2nd International Conference on Planktonic Microfossils Roma, Rome, p. 739–785.

Matsui, H., Nishi, H., Takashima, R., Kuroyanagi, A., Ikehara, M., Takayanagi, H., Iryu, Y., 2016. Changes in the depth habitat of the Oligocene planktic foraminifera (*Dentoglobigerina venezuelana*) induced by thermocline deepening in the eastern equatorial Pacific. Paleoceanography 31, 715–731, https://doi.org/10.1002/2016PA002950.

Mawbey, E. M., Lear, C. H., 2013. Carbon cycle feedbacks during the Oligocene–Miocene transient glaciation. Geology 41(9), 963–966, doi:10.1130/G34422.1.

McCreary, J. P., Yu, Z., Hood, R. R., Vinaychandran, P. N., Furue, R., Ishida, A., Richards, K. J., 2013. Dynamics of the Indian-Ocean oxygen minimum zones. Progress in Oceanography 112–113, 15–37, https://doi.org/10.1016/j.pocean.2013.03.002.

McInerney, F. A., Wing, S. L., 2011. The Paleocene–Eocene Thermal Maximum: A perturbation of carbon cycle, climate, and biosphere with implications for the future. Annual Review of Earth and Planetary Sciences 39, 489–516, doi:10.1146/annurev-earth-040610-133431.

McKinley, C. C., Thomas, D. J., LeVay, L. J., Rolewicz, Z., 2019. Nd isotopic structure of the Pacific Ocean 40–10 Ma, and evidence for the reorganisation of deep North Pacific Ocean circulation between 36 and 25 Ma. Earth and

Planetary Science Letters 521, 139–149, https://doi.org/10.1015.j.epsl.2019.06.009.

Miller, K. G., Janecek, T. R., Katz, M. E., Keil, D. J., 1987. Abyssal circulation and benthic foraminiferal changes near the Paleocene/Eocene boundary. Paleoceanography 2(6), 741–761.

Miller, K. G., Wright, J. D., Fairbanks, R. G., 1991. Unlocking the ice house: Oligocene–Miocene oxygen isotopes, eustasy, and margin erosion. Journal of Geophysical Research 96(B4), 6829–6848.

Miller, K. G., Browning, J. V., Schmelz, W. J., Kopp, R. E., Mountain, G. S., Wright, J. D., 2020. Cenozoic sea-level and cryospheric evolution from deep-sea geochemical and continental margin records. Science Advances 6, 1–15, https://doi.org/10.1126/sciadv.aaz1346.

Monechi, S., Reale, V., Bernaola, G., Balestra, B., 2013. The Danian/Selandian boundary at Site 1262 (South Atlantic) and in the Tethyan Region: Biomagnetostratigraphy, evolutionary trends in fasciculiths and environmental effects of the Latest Danian Event. Marine Micropaleontology 98, 28–40.

Mudelsee, M., Raymo, M. E., 2005. Slow dynamics of the Northern Hemisphere glaciation. Paleoceanography 20(PA4022), 1–14, https://doi.org/10.1029/2005PA001153.

Mungekar, T. V., Naik, S. S., Nath, B. N., Pandey, D. K., 2020. Shell weights of foraminifera trace atmospheric CO_2 from the Miocene to Pleistocene in the central Equatorial Indian Ocean. Journal of Earth System Science 129, 1–9, https://doi.org/10.1007/s12040-020-1348-6.

Murray, R. W., Miller, D. J., Kryc, K. A., 2000. Analysis of major and trace elements in rocks, sediments, and interstitial waters by inductively couple plasma-atomic emission spectrometry. Technical Note #29, Ocean Drilling Program, 27 pp.

Naafs, B. D. A., Rohrssen, M., Inglis, G. N., Lähteenoja, O., Feakins, S. J., Collinson, M. E., Kennedy, E. M., Singh, P. K., Singh, M. P., Lunt, D. J., Pancost, R. D., 2018. High temperatures in the terrestrial mid-latitudes during the early Palaeogene. Nature Geoscience 11, 766–771, doi:10.1038/s41561-018-0199-0.

Naidu, P. D., Singh, A. D., Ganeshram, R., Bharti, S. K., 2014. Abrupt climate-induced changes in carbonate burial in the Arabian Sea: Causes and

consequences. Geochemistry, Geophysics, Geosystems 15, 1398–1406, https://doi.org/10.1002/2015GC005824.

Nicholas, C. J., Pearson, P. N., Bown, P. R., Dunkley Jones, T., Huber, B. T., Karega, A., Lees, J. A., McMillan, I. K., O'Halloran, A., Singano, J.M., Wade, B. S., 2006. Stratigraphy and sedimentology of the Upper Cretaceous to Paleogene Kilwa Group, southern coastal Tanzania. Journal of African Earth Sciences 45, 431–466.

Nolan, S. C., Skelton, P. W., Clissold, B. P., Smewing, J. D., 1990. Maastrichtian to early Tertiary stratigraphy and palaeogeography of the Central and Northern Oman Mountains. In: Searle, A. H. F., Ries, M. P. (Eds), The Geology and Tectonics of the Oman Region. Geological Society Special Publication No. 49, p. 495–519.

Nunes, F., Norris, R. D., 2006. Abrupt reversal in ocean overturning during the Paleocene/Eocene warm period. Nature 439, 60–63, doi:10.1038/nature04386.

O'Brien, C. L., Huber, M., Thomas, E., Pagani, M., Super, J. R., Elder, L. E., & Hull, P. M., 2020. The enigma of Oligocene climate and global surface temperature evolution. Proceedings of the National Academy of Sciences of the United States of America 117(41), 25302–25309, https://doi.org/10.1073/pnas.2003914117.

Orue-Etxebarria, X., Pujalte, V., Bernaola, G., Apellaniz, E., Baceta, J. I., Payros, A., Nuñez-Betelu, K., Serra-Kiel, J., Tosquella, J., 2001. Did the Late Paleocene thermal maximum affect the evolution of larger foraminifers? Evidence from calcareous plankton of the Campo Section (Pyrenees, Spain). Marine Micropaleontology 41, 45–71.

Paillard, D., Labeyrie, L., Yiou, P., 1996. Analyseries 1.0: a Macintosh software for the analysis of geophysical time-series. Eos Transactions, AGU 77, p. 379.

Pälike, H., Norris, R. D., Herrle, J. O., Wilson, P. A., Coxall, H. K., Lear, C. H., Shackleton, N. J., Tripati, A. K., Wade, B. S., 2006. The heartbeat of the Oligocene climate system. Science 314, 1894–1898, doi:10.1126/science.1133822.

Panchuk, K., Ridgwell, A., Kump, L. R., 2008. Sedimentary response to Paleocene–Eocene Thermal Maximum carbon release: A model-data comparison. Geology 36(4), 315–318, doi:10.1130/G24474A.

Pandey, D. K., Clift, P. D., Kulhanek, D. K., Andò, S., Bendle, J. A. P., Bratenkov, S., Griffith, E. M., Gurumurthy, G. P., Hahn, A., Iwai, M., Khim, B. -K., Kumar, A., Kumar, A. G., Liddy, H. M., Lu, H., Lyle, M. W., Mishra, R., Radhakrishna, T., Routledge, C. M., Saraswat, R., Saxena, R., Scardia, G., Sharma, G. K., Singh, A. D., Steinke, S., Suzuki, K., Tauxe, L., Tiwari, M., Xu, Z., Yu, Z., 2016. Expedition 355 summary. Proceedings of the International Ocean Discovery Program 355, 1–32, https://doi.org/10.14379/iodp.proc.355.101.2016.

Papazzoni, C. A., Pignatti, J., 2019. The Shallow Benthic Zones: SBZ or SB? 3rd International Congress on Stratigraphy, STRATI 2019, Milan, Italy, p. 320.

Parsons, B., Sclater, J. G., 1977. An analysis of the variation of ocean floor bathymetry and heat flow with age. Journal of Geophysical Research 82(5), 803–827.

Parvathi, V., Suresh, I., Lengaigne, M., Izumo, T., Vialard, J., 2017. Robust projected weakening of winter monsoon winds over the Arabian Sea under climate change. Geophysical Research Letters 44, 9833–9843, https://doi.org/10.1002/2017GL075098.

Parvaz, D. B., Beasley, C., Littler, K., 2018. Recovery of intact foraminifera from indurated host rock by electric pulse fragmentation. Poster, https://doi.org/10.13140/RG.2.2.24194.17602.

Paul, H. A., Zachos, J. C., Flower, B. P., Tripati, A. K., 2000. Orbitally induced climate and geochemical variability across the Oligocene/Miocene boundary. Paleoceanography 14(5), 471–485.

Pedley, H. M., 1975. The Oligo–Miocene sediments of the Maltese islands (Ph.D. thesis). University of Hull, UK, 205 pp.

Pekar, S. F., DeConto, R. M., 2006. High-resolution ice-volume estimates for the early Miocene: Evidence for a dynamic ice sheet in Antarctica. Palaoegeography, Palaeoclimatology, Palaeoecology 231, 101–109, doi:10.1016/j.palaeo.2005.07.027.

Pena, L. D., Calvo, E., Cacho, I., Eggins, S., Pelejero, C., 2005. Identification and removal of Mn-Mg-rich contaminant phases on foraminiferal tests: Implications for Mg/Ca past temperature reconstructions. Geochemistry, Geophysics, Geosystems 6(9), 1–25, https://doi.org/10.1029/2005GC000930.

Penman, D. E., Hönisch, B., Zeebe, R. E., Thomas, E., Zachos, J. C., 2014. Rapid and sustained surface ocean acidification during the Paleocene–Eocene Thermal Maximum. Paleoceanography 29, 357–369, doi:10.1002/2014PA002621.

Perch-Nielsen, K., 1985. Cenozoic calcareous nannofossils. In: Bolli, H. M., Saunders, J. B., Perch-Nielsen, K. (Eds.), Plankton Stratigraphy. Cambridge University Press, Cambridge, p. 427–554.

Peterson, L. C., Backman, J., 1990. Late Cenozoic carbonate accumulation and the history of the carbonate compensation depth in the western equatorial Indian Ocean. Proceedings of the Ocean Drilling Program, Scientific Results 115, 467–507.

Phillips, S. C., Johnson, J. E., Underwood, M. B., Guo, J., Giosan, L., Rose, K., 2014. Long-timescale variation in bulk and clay mineral composition of Indian continental margin sediments in the Bay of Bengal, Arabian Sea, and Andaman Sea. Marine and Petroleum Geology 58, 117–138, https://doi.org/10.1016/j.marpetgeo.2014.06.018.

Piepgras, D. J., Wasserburg, G. J., Dasch, E. J., 1979. The isotopic composition of Nd in different ocean masses. Earth and Planetary Science Letters 45, 223–236.

Pignatti, J., Matteucci, R., Parlow, T., Fantozzi, P. L., 1998. Larger foraminiferal biostratigraphy of the Maastrichtian–Ypresian Wadi Mashib succession (South Hadramawt Arch, SE Yemen). Zeitschrift für Geologische Wissenschaften 26(5–6), 609–635.

Prasanna Kumar, S., Narvekar, J., Kumar, A., Shaji, C., Anand, P., Sabu, P., Rijomon, G., Josia, J., Jayaraj, K. A., Radhika, A., Nair, K. K. C., 2004. Intrusion of the Bay of Bengal water into the Arabian Sea during winter monsoon and associated chemical and biological response. Geophysical Research Letters 31, 1–4, https://doi.org/10.1029/2004GL020247.

Prazeres, M., Uthicke, S., Pandolfi, J. M., 2015. Ocean acidification induces biochemical and morphological changes in the calcification process of large benthic foraminifera. Proceedings of the Royal Society B: Biological Sciences 282, 1–10, http://dx.doi.org/10.1098/rspb.2014.2782.

Privé, N. C., Plumb, R. A., 2007. Monsoon Dynamics with Interactive Forcing. Part 2: Impact of eddies and asymmetric geometries. Journal of the Atmospheric Sciences 64, 1431–1442, doi: 10.1175/JAS3917.1.

Pucéat, E., Lécuyer, C., Reisberg, L., 2005. Neodymium isotope evolution of NW Tethyan upper ocean waters throughout the Cretaceous. Earth and Planetary Science Letters 236, 705–720, doi:10.1016/j.epsl.2005.03.015.

Pujalte, V., Schmitz, B., Baceta, J. I., Orue-Etxebarria, X., Bernaola, G., Dinares-Turell, J., Payros, A., Apellaniz, E., Caballero, F., 2009. Correlation of the Thanetian–Ilerdian turnover of larger foraminifera and the Paleocene–Eocene thermal maximum: confirming evidence from the Campo area (Pyrenees, Spain). Geologica Acta 7(1–2), 161–175, doi:10.1344/105.000000276.

Qiang, X. K., An, Z. S., Song, Y. G., Chang, H., Sun, Y. B., Liu, W. G., Ao, H., Dong, J. B., Fu, C., Wu., F., Lu, F., Cai, Y., Zhou, W., Cao, J., Xu, X., Ai, L., 2011. New eolian red clay sequence on the western Chinese Loess Plateau linked to onset of Asian desertification about 25 Ma ago. Science China Earth Sciences 54(1), 136–144, https://doi.org/10.1007/s11430-010-4126-5.

Racey, A., 1995. Lithostratigraphy and larger foraminiferal (Nummulitid) biostratigraphy of the Tertiary of northern Oman. Micropaleontology 41, 1–123.

Ramstein, G., Fluteau, F., Besse, J., Joussaume, S., 1997. Effect of orogeny, plate motion and land-sea distribution on Eurasian climate change over the past 30 million years. Nature 386, 788–795, https://doi.org/10.1038/386788a0.

Rathburn, A. E., Willingham, J., Ziebis, W., Burkett, A. M., Corliss, B. H., 2018. A new biological proxy for deep-sea paleo-oxygen: Pores of epifaunal benthic foraminifera. Scientific Reports 8(9456), doi:10.1038/s41598-018-27793-4.

Raymo, M. E., Ruddiman, W. F., 1992. Tectonic forcing of late Cenozoic climate. Nature 359(6391), 117–122, https://doi.org/10.1038/359117a0.

Razmjooei, M. J., Thibault, N., Kani, A., Ullmann, C. V., Jamali, A. M., 2020. Santonian–Maastrichtian carbon-isotope stratigraphy and calcareous nannofossil biostratigraphy of the Zagros Basin: Long-range correlation, similarities and differences of carbon-isotope trends at global scale. Global and Planetary Change 184(103075), 1–14, https://doi.org/10.1016/j.gloplacha.2019.103075.

Reichart, G. J., Schenau, S. J., De Lange, G. J., Zachariasse, W. J., 2002a. Synchroneity of oxygen minimum zone intensity on the Oman and Pakistan Margins at sub-Milankovitch time scales. Marine Geology 185, 403–415,

https://doi.org/10.1016/S0025-3227(02)00563-7.

Reichart, G. J., Nortier, J., Versteegh, G., Zachariasse, W. J., 2002b. Periodical breakdown of the Arabian Sea oxygen minimum zone caused by deep convective mixing. In: Clift, P. D., Kroon, D., Gaedicke, C., Craig, J. (Eds.), The Tectonic and Climatic Evolution of the Arabian Sea Region. Geological Society, London, Special Publications 195, p. 407–419, https://doi.org/10.1144/GSL.SP.2002.195.01.22.

Renema, W., Bellwood, D. R., Braga, J. C., Bromfield, K., Hall, R., Johnson, K. G., Lunt, P., Meyer, C. P., McMonagle, L. B., Morley, R. J., O'Dea, A., Todd, J. A., Wesselingh, F. P., Wilson, M. E. J., Pandolfi, J. M., 2008. Hopping Hotspots: Global shifts in marine biodiversity. Science 321, 654–657, doi: 10.1126/science.1155674.

Renema, W., Cotton, L., 2015. Three dimensional reconstructions of *Nummulites* tests reveal complex chamber shapes. PeerJ 3:e1072, https://doi.org/10.7717/peerj.1072.

Renne, P. R., Sprain, C. J., Richards, M. A., Self, S., Vanderkluysen, L., Pande, K., 2015. State shift in Deccan volcanism at the Cretaceous–Paleogene boundary, possibly induced by impact. Science 350(6256), 76–78, doi:10.1126/science.aac7549.

Reuter, M., Piller, W. E., Harzhauser, M., Kroh, A., 2013. Cyclone trends constrain monsoon variability during late Oligocene sea level highstands (Kachchh Basin, NW India). Climate of the Past 9, 2101–2115, https://doi.org/10.5194/cp-9-2101-2013.

Reynard, B., Lécuyer, C., Grandjean, P., 1999. Crystal-chemical controls on rare-earth element concentrations in fossil biogenic apatites and implications for paleoenvironmental reconstructions. Chemical Geology 155, 233–241.

Reynolds, P., Planke, S., Millett, J. M., Jerram, D. A., Trulsvik, M., Schofield, N., Myklebust, R., 2017. Hydrothermal vent complexes offshore Northeast Greenland: A potential role in driving the PETM. Earth and Planetary Science Letters 467, 72–78, http://dx.doi.org/10.1016/j.epsl.2017.03.031.

Rickaby, R. E. M., Elderfield, H., 2005. Evidence from the high-latitude North Atlantic for variations in Antarctic Intermediate water flow during the last deglaciation. Geochemistry, Geophysics, Geosystems 6(5), 1–12, https://doi.org/10.1029/2004GC000858.

Riding, J. B., Kyffin-Hughes, J. E., 2004. A review of the laboratory preparation of palynomorphs with a description of an effective non-acid technique. Revista Brasileira de Paleontologia 7(1), 13–44.

Riechelmann, S., Mavromatis, V., Buhl, D., Dietzel, M., Hoffmann, R., Jöns, N., Kell-Duivestein, I., Immenhauser, A., 2018. Echinoid skeletal carbonate as archive of past seawater magnesium isotope signatures – Potential and limitations. Geochimica et Cosmochimica Acta 235, 333–359.

Röhl, U., Westerhold, T., Bralower, T. J., Zachos, J. C., 2007. On the duration of the Paleocene–Eocene thermal maximum (PETM). Geochemistry, Geophysics, Geosystems 8(12), 1–13, doi:10.1029/2007GC001784.

Rosenthal, Y., Field, M. P., Sherrell, R. M., 1999. Precise determination of element/calcium ratios in calcareous samples using sector field inductively coupled plasma mass spectrometry. Analytical Chemistry 71(15), 3248–3253, https://doi.org/10.1021/ac981410x.

Roth-Nebelsick, A., Oehm, C., Grein, M., Utescher, T., Kunzmann, L., Friedrich, J. P., Konrad, W., 2014. Stomatal density and index data of *Platanus neptuni* leaf fossils and their evaluation as a CO_2 proxy for the Oligocene. Review of Palaeobotony and Palynology 206, 1–9, http://dx.doi.org/10.1016/j.revpalbo.2014.03.001.

Rothwell, R. G., Croudace, I. W., 2015. Twenty Years of XRF Core Scanning Marine Sediments: What Do Geochemical Proxies Tell Us? In: Croudace, I. W., Rothwell, R. G. (Eds.), Micro-XRF Studies of Sediment Cores: Applications of a non-destructive tool for the environmental sciences. Springer Nature, Switzerland, p. 25–102, https://doi.org/10.1007/978-94-017-9849-5_2.

Routledge, C. M., Kulhanek, D. K., Tauxe, L., Scardia, G., Singh, A. D., Steinke, S., Griffith, E. M., Saraswat, R., 2020. A revised chronostratigraphic framework for International Ocean Discovery Program Expedition 355 sites in Laxmi Basin, eastern Arabian Sea. Geological Magazine 157, 961–978.

Saini-Eidukat, B., Weiblen, P. W., 1996. A new method of fossil preparation, using high-voltage electric pulses. Curator: The Museum Journal 39, 139–144.

Salabarnada, A., Escutia, C., Röhl, U., Nelson, C. H., McKay, R., Jiménez-Espejo, F. J., Bijl, P. K., Hartman, J. D., Strother, S. L., Salzmann, U., Evangelinos, D., López-Quirós, A., Flores, J. A., Sangiori, F., Ikehara, M., Brinkhuis, H., 2018. Paleoceanography and ice sheet variability offshore

Wilkes Land, Antarctica – Part 1: Insights from late Oligocene astronomically paced contourite sedimentation. Climate of the Past 14(7), 991–1014, https://doi.org/10.5194/cp-14-991-2018.

Scheibner, C., Speijer, R. P., Marzouk, A. M., 2005. Turnover of larger foraminifera during the Paleocene–Eocene Thermal Maximum and paleoclimatic control on the evolution of platform ecosystems. Geology 33(6), 493–496, doi:10.1130/G21237.1.

Scheibner, C., Speijer, R. P., 2008a. Decline of coral reefs during late Paleocene to early Eocene global warming. eEarth 3, 19–26.

Scheibner, C., Speijer, R. P., 2008b. Late Paleocene–early Eocene Tethyan carbonate platform evolution – A response to long- and short-term paleoclimatic change. Earth-Science Reviews 90(3–4), 71–102, doi:10.1016/j.earscirev.2008.07.002.

Scheibner, C., Speijer, R. P., 2009. Recalibration of the Tethyan shallow-benthic zonation across the Paleocene–Eocene boundary: the Egyptian record. Geologica Acta 7(1–2), 195–214, doi:10.1344/105.000000267.

Scher, H. D., Delaney, M. L., 2010. Breaking the glass ceiling for high resolution Nd isotope records in early Cenozoic paleoceanography. Chemical Geology 269, 329–338, doi:10.1016/j.chemgeo.2009.10.007.

Scher, H. D., Bohaty, S. M., Zachos, J. C., Delaney, M. L., 2011. Two-stepping into the icehouse: East Antarctic weathering during progressive ice-sheet expansion at the Eocene–Oligocene transition. Geology 39(4), 383–386, https://doi.org/10.1130/G31726.1.

Schmidt, C., Kucera, M., Uthicke, S., 2014. Combined effects of warming and ocean acidification on coral reef Foraminifera *Marginopora vertebralis* and *Heterostegina depressa*. Coral Reefs 33, 805–818, doi:10.1007/s00338-014-1151-4.

Schmitz, B., Speijer, R. P., Aubry, M.-P., 1996. Latest Paleocene benthic extinction event on the southern Tethyan shelf (Egypt): Foraminiferal stable isotopic ($\delta^{13}C$, $\delta^{18}O$) records. Geology 24(4), 347.

Schmitz, B., Pujalte, V., 2007. Abrupt increase in seasonal extreme precipitation at the Paleocene–Eocene boundary. Geology 35(3), 215–218., doi:10.1130/G23261A.

Schneider, T., Bischoff, T., Haug, G. H., 2014. Migrations and dynamics of the intertropical convergence zone. Nature 513, 45–53,

https://doi.org/10.1038/nature13636.

Schobben, M., Ullmann, C. V., Leda, L., Korn, D., Struck, U., Reimold, W. U., Ghaderi, A., Algeo, T. J., Korte, C., 2016. Discerning primary versus diagenetic signals in carbonate carbon and oxygen isotope records: An example from the Permian–Triassic boundary of Iran. Chemical Geology 422, 94–107, http://dx.doi.org/10.1016/j.chemgeo.2015.12.013.

Schoene, B., Samperton, K. M., Eddy, M. P., Keller, G., Adatte, T., Bowring, S. A., Khadri, S. F. R., Gertsch, B., 2015. U-Pb geochronology of the Deccan Traps and relation to the end-Cretaceous mass extinction. Science 347(6218), 182–184, doi:10.1126/science.aaa0118.

Schott, F. A., McCreary, J. P., 2001. The monsoon circulation of the Indian Ocean. Progress in Oceanography 51(1), 1–123, https://doi.org/10.1016/S0079-6611(01)00083-0.

Schulte, S., Rostek, F., Bard, E., Rullkötter, J., Marchal, O., 1999. Variations of oxygen-minimum and primary productivity recorded in sediments of the Arabian Sea. Earth and Planetary Science Letters 173, 205–221.

Sclater, J. G., Meinke, L., Bennett, A., Murphy, C., 1985. The depth of the ocean through the Neogene. In: Kennett, J. P. (Ed.), The Miocene Ocean: Paleoceanography and Biogeography. Geological Society of America, Memoir 163, p. 1–21.

SELFRAG AG, 2012. Lab v. 2.0 User Manual. Document SELFRAG Lab, SELFRAG AG, Kerzers, Switzerland.

Serra-Kiel, J., Hottinger, L., Caus, E., Drobne, K., Ferrandez, C., Jauhri, A. K., Less, G., Pavlovec, R., Pignatti, J., Samso, J. M., Schaub, H., Sirel, E., Strougo, A., Tambareau, Y., Tosquella, J., Zakrevskaya, E., 1998. Larger foraminiferal biostratigraphy of the Tethyan Paleocene and Eocene. Bulletin de la Societe Geologique de France 169(2), 281–299.

Serra-Kiel, J., Vicedo, V., Razin, P., Grelaud, C., 2016a. Selandian–Thanetian larger foraminifera from the lower Jafnayn Formation in the Sayq area (eastern Oman Mountains). Geologica Acta 14(3), 315–333, doi:10.1344/GeologicaActa2016.14.3.7.

Serra-Kiel, J., Gallardo-Garcia, A., Razin, P., Robinet, J., Roger, J., Grelaud, C., Leroy, S., Robin, C., 2016b. Middle Eocene–Early Miocene larger foraminifera from Dhofar (Oman) and Socotra Island (Yemen). Arabian Journal of Geosciences 9(5), 1–95, doi:10.1007/s12517-015-2243-3.

Shamrock, J. L., Watkins, D. K., 2012. Eocene calcareous nannofossil biostratigraphy and community structure from Exmouth Plateau, Eastern Indian Ocean (ODP Site 762). Stratigraphy 9(1), 1–11.

Sharland, P. R., Archer, R., Casey, D. M., Davies, R. B., Hall, S. H., Heward, A., Horbury, A. D., Simmons, M. D., 2001. Chapter 4: Maximum Flooding Surfaces. In: Aplin, A., Archer, S., Bacon, M., Beck, I., Belopolsky, A., Biteau, J. J., Bjørlykke, K., Buck, S., Burley, S., Christie, M., Craig, J., Deming, D., Doré, A. G., Dromgoole, P. W., Flint, S. S., Geiger, S., Geluk, M., Goulty, N., Green, P. F., Harper, T., Henriquez, A., Hill, D., Japsen, P., Jolley, D. W., Kaldi, J., Larue, D., Lentini, M., Lovell, M., MacDonald, A., Mascle, A., Muggeridge, A., Nadeau, P., Prigmore, J., Ringrose, P., Schollnberger, W. E., Scotchman, I. C., Spitzer, R., Trudgill, B., Turner, J., Vejbæk, O., Whidden, K., Wood, R. (Eds.), Arabian Plate Sequence Stratigraphy. Gulf Petrolink, p. 127–301.

Shenoy, D. M., Suresh, I., Uskaikar, H., Kurian, S., Vidya, P. J., Shirodkar, G., Gauns, M. U., Naqvi, S. W. A., 2020. Variability of dissolved oxygen in the Arabian Sea Oxygen Minimum Zone and its driving mechanisms. Journal of Marine Systems 204, 103310, https://doi.org/10.1016/j.jmarsys.2020.103310.

Shirayama, Y., Thornton, H., 2005. Effect of increased atmospheric CO_2 on shallow water marine benthos. Journal of Geophysical Research C: Oceans 110(9), 1–7, doi:10.1029/2004JC002618.

Siddall, M., Khatiwala, S., van de Flierdt, T., Jones, K., Goldstein, S. L., Hemming, S., Anderson, R. F., 2008. Towards explaining the Nd paradox using reversible scavenging in an ocean general circulation model. Earth and Planetary Science Letters 274, 448–461, doi:10.1016/j.epsl.2008.07.044.

Siedenberg, K., Strauss, H., Podlaha, O. G., van den Boorn, S., 2018. Multiple sulfur isotopes ($\delta^{34}S$, $\Delta^{33}S$) of organic sulfur and pyrite from Late Cretaceous to Early Eocene oil shales in Jordan. Organic Geochemistry 125, 29–40, https://doi.org/10.1016/j.orggeochem.2018.08.002.

Slotnick, B. S., Dickens, G. R., Nicolo, M. J., Hollis, C. J., Crampton, J. S., Zachos, J. C., Sluijs, A., 2012. Large-amplitude variations in carbon cycling and terrestrial weathering during the latest Paleocene and earliest Eocene: The record at Mead Stream, New Zealand. The Journal of Geology 120, 487–505, doi:10.1086/666743.

Sluijs, A., Brinkhuis, H., Stickley, C. E., Warnaar, J., Williams, G. L., Fuller, M., 2003. Dinoflagellate cysts from the Eocene–Oligocene transition in the Southern Ocean: Results from ODP Leg 189. In: Exon, N. F., Kennett, J. P., Malone, M. J. (Eds.), Proceedings of the Ocean Drilling Program, Scientific Results (Vol. 189).

Sluijs, A., Schouten, S., Pagani, M., Woltering, M., Brinkhuis, H., Sinninghe Damsté, J. S., Dickens, G. R., Huber, M., Reichart, G., Stein, R., Matthiessen, J., Lourens, L. J., Pedentchouk, N., Backman, J., Moran, K., 2006. Subtropical Arctic Ocean temperatures during the Palaeocene/Eocene thermal maximum. Nature 441, 610–613, doi:10.1038/nature04668.

Sluijs, A., Brinkhuis, H., Schouten, S., Bohaty, S. M., John, C. M., Zachos, J. C., Reichart, G.-J., Sinninghe Damste, J. S., Crouch, E. M., Dickens, G. R., 2007. Environmental precursors to rapid light carbon injection at the Palaeocene/Eocene boundary. Nature Letters 450, 1218–1221, doi:10.1038/nature06400.

Sluijs, A., Schouten, S., Donders, T. H., Schoon, P. L., Röhl, U., Reichart, G-. J., Sangiorgi, F., Kim, J-. H., Sinninghe Damsté, J. S., Brinkhuis, H., 2009. Warm and wet conditions in the Arctic region during Eocene Thermal Maximum 2. Nature Geoscience 2, 777–780, doi:10.1038/NGEO668.

Sluijs, A., Dickens, G. R., 2012. Assessing offsets between the $\delta^{13}C$ of sedimentary components and the global exogenic carbon pool across early Paleogene carbon cycle perturbations. Global Biogeochemical Cycles 26, 1–14, doi:10.1029/2011GB004224.

Sluijs, A., Van Roij, L., Harrington, G. J., Schouten, S., Sessa, J. A., Levay, L. J., Reichart, G. J., Slomp, C. P., 2014. Warming, euxinia and sea level rise during the Paleocene–Eocene thermal maximum on the gulf coastal plain: Implications for ocean oxygenation and nutrient cycling. Climate of the Past 10(4), 1421–1439, doi:10.5194/cp-10-1421-2014.

Speijer, R. P., Schmitz, B., 2000. A synthesis of biotic and stratigraphic data from the Middle East on late Paleocene global change. GFF 122(1), 152–153.

Speijer, R. P., Wagner, T., 2002. Sea-level changes and black shales associated with the late Paleocene thermal maximum: Organic-geochemical and micropaleontologic evidence from the southern Tethyan margin (Egypt-Israel). Geological Society of America Special Paper 356, 533–549.

Speijer, R. P., Scheibner, C., Stassen, P., Morsi, A. M. M., 2012. Response of marine ecosystems to deep-time global warming: A synthesis of biotic patterns across the Paleocene–Eocene thermal maximum (PETM). Austrian Journal of Earth Sciences 105(1), 6–16.

Spicer, R. A., 2017. Tibet, the Himalaya, Asian monsoons and biodiversity – In what ways are they related? Plant Diversity 39, 233–244, https://doi.org/10.1016/j.pld.2017.09.001.

Spötl, C., Vennemann, T. W., 2003. Continuous flow isotope ratio mass spectrometric analysis of carbonate minerals. Rapid Communications in Mass Spectrometry 17, 1004–1006.

Srivastava, G., Spicer, R. A., Spicer, T. E. V., Yang, J., Kumar, M., Mehrotra, R., Mehrotra, N., 2012. Megaflora and palaeoclimate of a Late Oligocene tropical delta, Makum Coalfield, Assam: Evidence for the early development of the South Asia Monsoon. Palaeogeography, Palaeoclimatology, Palaeoecology 342–343, 130–142, https://doi.org/10.1016/j.palaeo.2012.05.002.

Stap, L., Sluijs, A., Thomas, E., Lourens, L. J., 2009. Patterns and magnitude of deep sea carbonate dissolution during Eocene Thermal Maximum 2 and H2, Walvis Ridge, southeastern Atlantic Ocean. Paleoceanography 24, 1–13, doi:10.1029/2008PA001655.

Steinthorsdottir, M., Vajda, V., Pole, M., 2019. Significant transient pCO_2 perturbation at the New Zealand Oligocene–Miocene transition recorded by fossil plant stomata. Palaeogeography, Palaeoclimatology, Palaeoecology 515, 152–161, https://doi.org/10.1016/j.palaeo.2018.01.039.

Stern, R. J., Johnson, P. R., 2019. Constraining the opening of the Red Sea: Evidence from the Neoproterozoic margins and Cenozoic magmatism for a volcanic rifted margin. In: Rasul, N. M. A., Stewart, I. C. F. (Eds.), Geological Setting, Palaeoenvironment and Archaeology of the Red Sea. Springer Nature, Switzerland, p. 53–79, https://doi.org/10.1007/978-3-319-99408-6_4.

Stewart, J. A., Wilson, P. A., Edgar, K. M., Anand, P., James, R. H., 2012. Geochemical assessment of the palaeoecology, ontogeny, morphotypic variability and palaeoceanographic utility of *“Dentoglobigerina” venezuelana*. Marine Micropaleontology 84–85, 74–86, https://doi.org/10.1016/j.marmicro.2011.11.003.

Stewart, J. A., James, R. H., Anand, P., Wilson, P. A., 2017. Silicate weathering and carbon cycle controls on the Oligocene–Miocene transition glaciation. Paleoceanography 32, 1070–1085, https://doi.org/10.1002/2017PA003115.

Stille, P., Steinmann, M., Riggs, S. R., 1996. Nd isotope evidence for the evolution of the paleocurrents in the Atlantic and Tethys Oceans during the past 180 Ma. Earth and Planetary Science Letters 144, 9–19.

Straume, E. O., Gaina, C., Medvedev, S., Nisancioglu, K. H., 2020. Global Cenozoic Paleobathymetry with a focus on the Northern Hemisphere Oceanic Gateways. Gondwana Research 86, 126–143, https://doi.org/10.1016/j.gr.2020.05.011.

Stap, L., Lourens, L. J., van Dijk, A., Schouten, S., Thomas, E., 2010. Coherent pattern and timing of the carbon isotope excursion and warming during Eocene Thermal Maximum 2 as recorded in planktic and benthic foraminifera. Geochemistry, Geophysics, Geosystems 11, 1–10, doi:10.1029/2010GC003097.

Stewart, J. A., James, R. H., Anand, P., Wilson, P. A., 2017. Silicate weathering and carbon cycle controls on the Oligocene–Miocene transition glaciation. Paleoceanography 32, 1070–1085, https://doi.org/10.1002/2017PA003115.

Sun, X., Wang, P., 2005. How old is the Asian monsoon system? – Palaeobotanical records from China. Palaeogeography, Palaeoclimatology, Palaeoecology 222, 181–222, https://doi.org/10.1016/j.palaeo.2005.03.005.

Sun, J., Ye, J., Wu, W., Ni, X., Bi, S., Zhang, Z., Liu, W., Meng, J., 2010. Late Oligocene–Miocene mid-latitude aridification and wind patterns in the Asian interior. Geology 38(6), 515–518, https://doi.org/10.1130/G30776.1.

Super, J. R., Thomas, E., Pagani, M., Huber, M., O'Brien, C., Hull, P. M., 2018. North Atlantic temperature and pCO_2 coupling in the early–middle Miocene. Geology 46(6), 519–522, https://doi.org/10.1130/G40228.1.

Tachikawa, K., Arsouze, T., Bayon, G., Bory, A., Colin, C., Dutay, J. -C., Frank, N., Giraud, X., Gourlan, A. T., Jeandel, C., Lacan, F., Meynadier, L., Montagna, P., Piotrowski, A. M., Plancherel, Y., Pucéato, E., Roy-Barman, M., Waelbroeck, C., 2017. The large-scale evolution of neodymium isotopic composition in the global modern and Holocene ocean revealed from seawater and archive data. Chemical Geology 457, 131–148, http://dx.doi.org/10.1016/j.chemgeo.2017.03.018.

Tada, R., Zheng, H., Clift, P. D., 2016. Evolution and variability of the Asian

monsoon and its potential linkage with uplift of the Himalaya and Tibetan Plateau. Progress in Earth and Planetary Science 3(4), 1–26, https://doi.org/10.1186/s40645-016-0080-y.

Tanaka, T., Togashi, S., Kamioka, H., Amakawa, H., Kagami, H., Hamamoto, T., Yuhara, M., Orihashi, Y., Yoneda, S., Shimizu, H., Kunimaru, T., Takahashi, K., Yanagi, T., Nakano, T., Fujimaki, H., Shinjo, R., Asahara, Y., Tanimizu, M., Dragusanu, C., 2000. JNdi-1: a neodymium isotopic reference in consistency with LaJolla neodymium. Chemical Geology 168, 279–281.

Tang, H., Micheels, A., Eronen, J. T., Ahrens, B., Fortelius, M., 2013. Asynchronous responses of East Asian and Indian summer monsoons to mountain uplift shown by regional climate modelling experiments. Climate Dynamics 40, 1531–1549, doi:10.1007/s00382-012-1603-x.

Tesfamichael, T., Jacobs, B., Tabor, N., Michel, L., Currano, E., Feseha, M., Barclay, R., Kappelman, J., Schmitz, M., 2017. Settling the issue of “decoupling” between atmospheric carbon dioxide and global temperature: $[CO_2]_{atm}$ reconstructions across the warming Paleogene–Neogene divide. Geology 45(11), 999–1002, https://doi.org/10.1130/G39048.1.

Thomas, E., 1989. Development of Cenozoic deep-sea benthic foraminiferal faunas in Antarctic waters. Geological Society Special Publication No. 47, 283–296.

Thomas, E., Shackleton, N. J., 1996. The Paleocene–Eocene benthic foraminiferal extinction and stable isotope anomalies. In: Knox, R. W. O., Corfield, R. M., Dunay, R. E. (Eds.), Correlation of the Early Paleogene in Northwest Europe. Geological Society Special Publication 101, p. 401–441.

Thomas, E., 1998. Biogeography of the late Paleocene benthic foraminiferal extinction. In: Aubry, M. P., Lucas, S., Berggren, W. A. (Eds.), Late Paleocene–Early Eocene Climatic and Biotic Events in the Marine and Terrestrial Records. Columbia University Press, New York, p. 214–243.

Thomas, E., Zachos, J. C., Bralower, T. J., 2000. Deep-sea environments on a warm earth: latest Paleocene–early Eocene. In: Huber, B. T., MacLeod, K. G., Wing, S. L. (Eds.), Warm Climates in Earth History. Cambridge University Press, Cambridge, UK, p. 132–160.

Thomas, D. J., Bralower, T. J., Jones, C. E., 2003. Neodymium isotopic reconstruction of late Paleocene–early Eocene thermohaline circulation.

Earth and Planetary Science Letters 209, 309–322, doi:10.1016/S0012-821X(03)00096-7.

Thomas, E., 2007. Cenozoic mass extinctions in the deep sea: What perturbs the largest habitat on Earth? The Geological Society of America Special Paper 424, 1–23, doi:10.1130/2007.2424(01).

Thomas, D. J., Korty, R., Huber, M., Schubert, J. A., Haines, B., 2014. Nd isotopic structure of the Pacific Ocean 70–30 Ma and numerical evidence for vigorous ocean circulation and ocean heat transport in a greenhouse world. Paleoceanography 29, 454–469, doi:10.1002/2013PA002535.

Thomas, E., Boscolo-Galazzo, F., Balestra, B., Monechi, S., Donner, B., Röhl, U., 2018. Early Eocene Thermal Maximum 3: Biotic response at Walvis Ridge (SE Atlantic Ocean). Paleoceanography and Paleoclimatology 33, 1–22, https://doi.org/10.1029/2018PA003375.

Thomson, J. R., Holden, P. B., Anand, P., Edwards, N. R., Porchier, C. A., Harris, N. B., 2021. Tectonic and climatic drivers of Asian monsoon evolution. Nature Communications 12(4022), https://doi.org/10.1038/s41467-021-24244-z.

Tomas, S., Frijia, G., Bomelburg, E., Zamagni, J., Perrin, C., Mutti, M., 2016. Evidence for seagrass meadows and their response to paleoenvironmental changes in the early Eocene (Jafnayn Formation, Wadi Bani Khalid, N Oman). Sedimentary Geology 341, 189–202, http://dx.doi.org/10.1016/j.sedgeo.2016.05.016.

Townsend, C. R., Scarsbrook, M. R., Doledec, S., 1997. The intermediate disturbance hypothesis, refugia, and biodiversity in streams. Limnology and Oceanography 42(5), 938–949.

Tripati, A. K., Elderfield, H., 2005. Deep-sea temperature and circulation changes at the Paleocene–Eocene thermal maximum. Science 308, 1894–1898, doi:10.1126/science.1109202.

Tucker, M. E., Wright, V. P., 1990. Carbonate Sedimentology. Blackwell Science Publications, 482 p.

Turner, A. G., Annamalai, H., 2012. Climate change and the South Asian summer monsoon. Nature Climate Change 2, 587–595, https://doi.org/10.1038/NCLIMATE1495.

Ullmann, C. V., Korte, C., 2015. Diagenetic alteration in low-Mg calcite from macrofossils: a review. Geological Quaterly 59(1), 3–20,

http://dx.doi.org/10.7306/gq.1217.

Ullmann, C. V., Gale, A. S., Huggett, J., Wray, D., Frei, R., Korte, C., Broom-Fendley, S., Littler, K., Hesselbo, S. P., 2018. The geochemistry of modern calcareous barnacle shells and applications for palaeoenvironmental studies. Geochimica et Cosmochimica Acta 243, 149–168, https://doi.org/10.1016/j.gca.2018.09.010.

Uthicke, S., Momigliano, P., Fabricius, K. E., 2013. High risk of extinction of benthic foraminifera in this century due to ocean acidification. Scientific Reports 3, 1–5, doi:10.1038/srep01769.

van Andel, T. H., 1975. Mesozoic/Cenozoic calcite compensation depth and the global distribution of calcareous sediments. Earth and Planetary Science Letters 26, 187–194.

van de Flierdt, T., Griffiths, A. M., Lambelet, M., Little, S. H., Stichel, T., Wilson, D. J., 2016. Neodymium in the oceans: a global database, a regional comparison and implications for palaeoceanographic research. Philosophical Transactions of the Royal Society A 374, 1–30, http://dx.doi.org/10.1098/rsta.2015.0293.

van der Wielen, K. P., 2013. Application of high voltage breakage to a range of rock types of varying physical properties (Ph.D. thesis). Camborne School of Mines, University of Exeter, UK.

van Peer, T., Taylor, V., Liebrand, D., Brzelinski, S., Möbius, I., Friedrich, O., Bohaty, S., Xuan, C., Lippert, P., Wilson, P. A., 2020. Eccentricity-paced ice sheet variability and obliquity-driven bottom-water changes during the Oligocene–Miocene. European Geosciences Union 2020, virtual conference, https://doi.org/https://doi.org/10.5194/egusphere-egu2020-15256.

Van Simaeys, S., 2004. The Rupelian–Chattian boundary in the North Sea Basin and its calibration to the international time-scale. Netherlands Journal of Geosciences/Geologie en Mijnbouw 83(3), 241–248.

Vance, D., Scrivner, A. E., Beney, P., Staubwasser, M., Henderson, G. M., Slowey, N. C., 2004. The use of foraminifera as a record of the past neodymium isotope composition of seawater. Paleoceanography 19, 1–17, doi:10.1029/2003PA000957.

Vanderkluysen, L., Mahoney, J. J., Hooper, P. R., Sheth, H. C., Ray, R., 2011. The feeder system of the Deccan Traps (India): Insights from dike

geochemistry. Journal of Petrology 52(2), 315–343, doi:10.1092/petrology.egq082.

Varol, O., 1989. Paleocene calcareous nannofossil biostratigraphy. In: Crux, J. A., van Heck, S. E. (Eds.), Nannofossils and their applications. Ellis Horwood Limited, p. 267–310.

Villa, G., Fiorini, C., Persico, D., Roberts, A. P., Florindo, F., 2014. Middle Eocene to Late Oligocene Antarctic glaciation/deglaciation and Southern Ocean productivity. Paleoceanography 29, 223–237, https://doi.org/10.1002/2013PA002518.

Vogel, N., Uthicke, S., 2012. Calcification and photobiology in symbiont-bearing benthic foraminifera and responses to a high CO_2 environment. Journal of Experimental Marine Biology and Ecology 424–425, 15–24, doi:10.1016/j.jembe.2012.05.008.

von der Heydt, A., Dijkstra, H. A., 2006. Effect of ocean gateways on the global ocean circulation in the late Oligocene and early Miocene. Paleoceanography 21, 1–18, doi:10.1029/20065PA001149.

Wade, B. S., Pälike, H., 2004. Oligocene climate dynamics. Paleoceanography 19, 1–16, https://doi.org/10.1029/2004PA001042.

Wade, B. S., Berggren, W. A., Olsson, R. K., 2007. The biostratigraphy and paleobiology of Oligocene planktonic foraminifera from the equatorial Pacific Ocean (ODP Site 1218). Marine Micropaleontology 62, 167–179, https://doi.org/10.1016/j.marmicro.2006.08.005.

Wade, B. S., Pearson, P. N., Olsson, R. K., Fraass, A. J., Leckie, R. M., Hemleben, C., 2018. Taxonomy, biostratigraphy, and phylogeny of Oligocene and lower Miocene *Dentoglobigerina* and *Globoquadrina*. In: Wade, B. S., Olsson, R. K., Pearson, P. N., Huber, B. T., Berggren, W. A. (Eds.), Atlas of Oligocene Planktonic Foraminifera. Cushman Foundation Special Publication No. 46, p. 331–384.

Wang, E., Shi, F., Manlapig, E., 2012. Mineral liberation by high voltage pulses and conventional comminution with same specific energy levels. Minerals Engineering 27, 28–36.

Webb, A. A. G., Guo, H., Clift, P. D., Husson, L., Müller, T., Constantino, D., Yin, A., Xu, Z.., et al. (2017). The Himalaya in 3D: Slab dynamics controlled mountain building and monsoon intensification. Lithosphere 9(4), 637–651, doi: 10.1130/L636.1.

Wei, H. H., Bordoni, S., 2016. On the Role of the African Topography in the South Asian Monsoon. Journal of Atmospheric Sciences 73, 3197–3212, https://doi.org/10.1175/JAS-D-15-0182.1.

Westerhold, T., Röhl, U., Raffi, I., Fornaciari, E., Monechi, S., Reale, V., Bowles, J., Evans, H. F., 2008. Astronomical calibration of the Paleocene time. Palaeogeography, Palaeoclimatology, Palaeoecology 257, 377–403, doi:10.1016/j.palaeo.2007.09.016.

Westerhold, T., Röhl, U., Donner, B., McCarren, H. K., Zachos, J. C., 2011. A complete high-resolution Paleocene benthic stable isotope record for the central Pacific (ODP Site 1209). Paleoceanography 26(2), 1–13, doi:10.1029/2010PA002092.

Westerhold, T., Röhl, U., 2013. Orbital pacing of Eocene climate during the Middle Eocene Climate Optimum and the chron C19r event: Missing link found in the tropical western Atlantic. Geochemistry, Geophysics, Geosystems 14(11), 4811–4825, doi:10.1002/ggge.20293.

Westerhold, T., Röhl, U., Frederichs, T., Agnini, C., Raffi, I., Zachos, J. C., Wilkens, R. H., 2017. Astronomical calibration of the Ypresian timescale: Implications for seafloor spreading rates and the chaotic behavior of the solar system? Climate of the Past 13, 1129–1152, https://doi.org/10.5194/cp-13-1129-2017.

Westerhold, T., Röhl, U., Donner, B., Zachos, J. C., 2018. Global extent of early Eocene hyperthermal events: A new Pacific benthic foraminiferal isotope record from Shatsky Rise (ODP Site 1209). Paleoceanography and Paleoclimatology 33, 626–642, https://doi.org/10.1029/2017PA003306.

Westerhold, T., Marwan, N., Drury, A. J., Liebrand, D., Agnini, C., Anagnostou, E., Barnet, J. S. K., Bohaty, S. M., De Vleeschouwer, D., Florindo, F., Frederichs, T., Hodell, D. A., Holbourn, A. E., Kroon, D., Lauretano, V., Littler, K., Lourens, L. J., Lyle, M., Pälike, H., Röhl, U., Tian, J., Wilkens, R. H., Wilson, P. A., Zachos, J. C., 2020. An astronomically dated record of Earth’s climate and its predictability over the last 66 million years. Science 369, 1383–1387, doi:10.1126/science.aba6853.

Williams, G. L., Fensome, R. A., MacRae, R. A., 2017. The Lentin and Williams Index of Fossil Dinoflagellates, 2017 Edition. American Association of Stratigraphic Palynologists Foundation, AASP Contributions Series Number 48, 1–1097.

Winguth, A. M. E., Thomas, E., Winguth, C., 2012. Global decline in ocean ventilation, oxygenation, and productivity during the Paleocene–Eocene Thermal Maximum: Implications for the benthic extinction. Geology 40(3), 263–266, doi:10.1130/G32529.1.

Wolfgring, E., Wagreich, M., 2016. A quantitative look on northwestern Tethyan foraminiferal assemblages, Campanian Nierental Formation, Austria. PeerJ 4:e1757, https://doi.org/10.7717/peerj.1757.

Woodhouse, A., Jackson, S. L., Jamieson, R. A., Newton, R. J., Sexton, P. F., Aze, T., 2021. Adaptive ecological niche migration does not negate extinction susceptibility. Scientific Reports 11, 15411, https://doi.org/10.1038/s41598-021-94140-5.

Woodruff, F., Savin, S. M., 1989. Miocene deepwater oceanography. Paleoceanography 4(1), 87–140.

Wouters, H., Dickson, A., Porcelli, D., Hesselbo, S. P., van den Boorn, S., Giraldo Gómez, V. M., Mutterlose, J., 2014. Mo isotopes as redox indicators for the Southern Tethys during the PETM. American Geophysical Union, Fall Meeting 2014, abstract ID: PP51B-1118.

Wright, J. D., Miller, K. G., Fairbanks, R. G., 1992. Early and middle Miocene stable isotopes: implications for deepwater circulation and climate. Paleoceanography 7(3), 357–389.

Wright, N. M., Scher, H. D., Seton, M., Huck, C. E., Duggan, B. D., 2018. No change in Southern Ocean circulation in the Indian Ocean from the Eocene through late Oligocene. Paleoceanography and Paleoclimatology 33, 152–167, https://doi.org/10.1002/2017PA003238.

Xie, S. P., Xu, H., Saji, N. H., Wang, Y., 2006. Role of Narrow Mountains in Large-Scale Organization of Asian Monsoon Convection. Journal of Climate 19, 3420–3429.

Yang, F., Kumar, A., Schlesinger, M. E., Wang, W., 2003. Intensity of hydrological cycles in warmer climates. Journal of Climate 16, 2419–2423, https://doi.org/10.1175/2779.1.

Yang, X., Groeneveld, J., Jian, Z., Steinke, S., Giosan, L., 2020. Middle Miocene intensification of South Asian monsoonal rainfall. Paleoceanography and Paleoclimatology 35, 1–18, https://doi.org/10.1029/2020PA003853.

Young, J. R., 1998. Neogene Nannofossils. In: Bown, P. R. (Ed.), Calcareous Nannofossil Biostratigraphy. Kluwer Academic, p. 225–265.

Young, J. R., Bown, P. R., Lees, J. A., 2019. Nannotax3. International Nannoplankton Association. Accessed: <http://www.mikrotax.org/Nannotax3>.

Yu, Z., Colin, C., Wan, S., Saraswat, R., Song, L., Xu, Z., Clift, P., Lu, H., Lyle, M., Kulhanek, D., Hahn, A., Tiwari, M., Mishra, R., Miska, S., Kumar, A., 2019. Sea level-controlled sediment transport to the eastern Arabian Sea over the past 600 kyr: Clay minerals and Sr–Nd isotopic evidence from IODP site U1457. Quaternary Science Reviews 205, 22–34, https://doi.org/10.1016/j.quascirev.2018.12.006.

Zachos, J. C., Breza, J. R., Wise, S. W., 1992. Early Oligocene ice-sheet expansion on Antarctica: Stable isotope and sedimentological evidence from Kerguelen Plateau, southern Indian Ocean. Geology 20, 569–573, https://doi.org/10.1130/0091-7613(1992)020<0569:EOISEO>2.3.CO;2.

Zachos, J. C., Quinn, T. M., Salamy, K. A., 1996. High-resolution (10^4 years) deep-sea foraminiferal stable isotope records of the Eocene–Oligocene climate transition. Paleoceanography 11(3), 251–255.

Zachos, J. C., Flower, B. P., Paul, H., 1997. Orbitally paced climate oscillations across the Oligocene/Miocene boundary. Nature Letters 388, 567–570.

Zachos, J. C., Pagani, M., Sloan, L., Thomas, E., Billups, K., 2001a. Trends, rhythms, and aberrations in global climate 65 Ma to present. Science 292, 686–693, doi:10.1126/science.1059412.

Zachos, J. C., Shackleton, N. J., Revenaugh, J. S., Pälike, H., Flower, B. P., 2001b. Climate response to orbital forcing across the Oligocene–Miocene boundary. Science 292, 274–278.

Zachos, J. C., Wara, M. W., Bohaty, S., Delaney, M. L., Petrizzo, M. R., Brill, A., Bralower, T. J., Premoli-Silva, I., 2003. A transient rise in tropical sea surface temperature during the Paleocene–Eocene Thermal Maximum. Science 302, 1551–1554.

Zachos, J. C., Röhl, U., Schellenberg, S. A., Sluijs, A., Hodell, D. A., Kelly, D. C., Thomas, E., Nicolo, M., Raffi, I., Lourens, L. J., McCarren, H., Kroon, D., 2005. Rapid acidification of the ocean during the Paleocene–Eocene Thermal Maximum. Science 308, 1611–1615, doi:10.1126/science.1109004.

Zachos, J. C., Kump, L. R., 2005. Carbon cycle feedbacks and the initiation of Antarctic glaciation in the earliest Oligocene. Global and Planetary Change 47, 51–66, doi:10.1016/j.gloplacha.2005.01.001.

Zachos, J. C., Schouten, S., Bohaty, S., Quattlebaum, T., Sluijs, A., Brinkhuis, H., Gibbs, S. J., Bralower, T. J., 2006. Extreme warming of mid-latitude coastal ocean during the Paleocene–Eocene Thermal Maximum: Inferences from TEX_{86} and isotope data. Geology 34(9), 737–740, doi:10.1130/G22522.1.

Zachos, J. C., Dickens, G. R., Zeebe, R. E., 2008. An early Cenozoic perspective on greenhouse warming and carbon-cycle dynamics. Nature 451, 279–283, doi:10.1038/nature06588.

Zachos, J. C., Mccarren, H., Murphy, B., Röhl, U., Westerhold, T., 2010. Tempo and scale of late Paleocene and early Eocene carbon isotope cycles: Implications for the origin of hyperthermals. Earth and Planetary Science Letters 299, 242–249, doi:10.1016/j.epsl.2010.09.004.

Zamagni, J., Mutti, M., Košir, A., 2008. Evolution of shallow benthic communities during the Late Paleocene–earliest Eocene transition in the Northern Tethys (SW Slovenia). Facies 54(1), 25–43, doi:10.1007/s10347-007-0123-3.

Zamagni, J., Mutti, M., Kosir, A., 2012. The evolution of mid Paleocene–early Eocene coral communities: How to survive during rapid global warming. Palaeogeography, Palaeoclimatology, Palaeoecology 317–318, 48–65, doi:10.1016/j.palaeo.2011.12.010.

Zeebe, R. E., Dickens, G. R., Ridgwell, A., Sluijs, A., Thomas, E., 2014. Onset of carbon isotope excursion at the Paleocene–Eocene thermal maximum took millennia, not 13 years. Proceedings of the National Academy of Sciences 111(12), 1062–1063, doi:10.1073/pnas.1321177111.

Zeebe, R. E., Ridgwell, A., Zachos, J. C., 2016. Anthropogenic carbon release rate unprecedented during the past 66 million years. Nature Geoscience 9(4), 325–329, doi:10.1038/NGEO2681.

Zeebe, R. E., Westerhold, T. Littler, K., Zachos, J. C., 2017. Orbital forcing of the Paleocene and Eocene carbon cycle, Paleoceanography, 32, 440–465, doi:10.1002/2016PA003054.

Zeebe, R. E., Lourens, L. J., 2019. Solar system chaos and the Paleocene–Eocene boundary age constrained by geology and astronomy. Science 365(6456), 926–929, doi:10.1126/science.aax0612.

Zeebe, R. E., Tyrrell, T., 2019. History of carbonate ion concentration over the last 100 million years II: Revised calculations and new data. Geochimica et Cosmochimica Acta 257, 373–392, https://doi.org/10.1016/j.gca.2019.02.041.

Zhang, Y. G., Pagani, M., Liu, Z., Bohaty, S. M., DeConto, R., 2013a. A 40-million-year history of atmospheric CO_2. Philosophical Transactions of the Royal Society A 371, 20130096, http://dx.doi.org/10.1098/rsta.2013.0096.

Zhang, Q., Willems, H., Ding, L., 2013b. Evolution of the Paleocene–Early Eocene larger benthic foraminifera in the Tethyan Himalaya of Tibet, China. International Journal of Earth Sciences (Geologische Rundschau) 102, 1427–1445, doi:10.1007/s00531-012-0856-2.

Zhang, Q., Wendler, I., Xu, X., Willems, H., Ding, L., 2017. Structure and magnitude of the carbon isotope excursion during the Paleocene–Eocene thermal maximum. Gondwana Research 46, 114–123, http://dx.doi.org/10.1016/j.gr.2017.02.016.

Zhang, Q., Willems, H., Ding, L., Xu, X., 2018. Response of larger benthic foraminifera to the Paleocene–Eocene thermal maximum and the position of the Paleocene/Eocene boundary in the Tethyan shallow benthic zones: Evidence from south Tibet. The Geological Society of America Bulletin 131(1–2), 84–98, https://doi.org/10.1130/B31813.1.

Zhang, T., Han, W., Fang, X., Song, C., Wang, Y., Tian, Q., Zhang, W., Feng, Z., Tan, M., 2021. Tectonic forcing of environmental transition in Central Asia at ~11–9 Ma. Gondwana Research 89, 19–30, https://doi.org/10.1016/j.gr.2020.08.012.

Zheng, H., Wei, X., Tada, R., Clift, P. D., Wang, B., Jourdan, F., Wang, P., He, M., 2015. Late Oligocene–early Miocene birth of the Taklimakan Desert. Proceedings of the National Academy of Sciences of the United States of America 112(25), 7662–7667, https://doi.org/10.1073/pnas.1424487112.

Ziegler, M. A., 2001. Late Permian to Holocene paleofacies evolution of the Arabian Plate and its hydrocarbon occurrences. GeoArabia 6(3), 445–504.